ONLINE MONITORING OF DISINFECTANTS USING CHEMIRESISTIVE SENSORS

ONLINE MONITORING OF DISINFECTANTS USING CHEMIRESISTIVE SENSORS

By MD ALI AKBAR, B.Sc., M.Sc.

A Thesis Submitted to the School of Graduate Studies in Partial Fulfilment of the Requirement of the Degree of Doctor of Philosophy in Chemistry

McMaster University, DOCTOR OF PHILOSOPHY (2025), Hamilton, Ontario, Canada (Chemistry)

TITLE: Online Monitoring of Disinfectants Using Chemiresistive Sensors
AUTHOR: Md Ali Akbar
BSc. (U. Dhaka, Bangladesh), M.Sc. (Wright State U., USA)
SUPERVISOR: Professor Peter Kruse
NUMBER OF PAGES: xxxv, 261

Lay Abstract

This thesis aims to investigate the scopes of continuous online monitoring of disinfectants using chemiresistive sensors. The study focuses on the methods to enhance selectivity and sensitivity of chemiresistive sensors to detect disinfectants such as free chlorine, chloramines (monochloramine and dichloramine), and permanganate in water. We have developed chemiresistive sensors with increased specificity by modifying the carbon-based substrates. To enhance selectivity of the sensors, the substrate was modified with redox-active molecules using simple methods. The substrates were also modified by changing the deposition strategy to detect wider concentration range of disinfectants. This thesis explores detection of disinfectants over wide range of concentrations; simultaneous detection of disinfectants in the presence of more than one disinfectant; and continuous detection of disinfectants that are pH dependent.

Abstract

To ensure safe and reliable water quality, continuous monitoring of a wide range of water parameters is required. Disinfectants are added to kill the pathogens in water and a sufficient level of disinfectant in water prevents pathogen regrowth. Therefore, monitoring the disinfectant is crucial to prevent waterborne disease. Conventional monitoring techniques rely on colorimetric kits and bulky electrochemical analyzers. These techniques rely either on additional reagents or frequent maintenance. This thesis attempts to solve these issues by incorporating chemiresistive sensor platforms to monitoring of disinfectants. First, the single-walled carbon nanotube (SWCNT) networks were optimized to sense broader range of disinfectants (potassium permanganate) in water. High sensitivity and broader dynamic range of detection were achieved by controlling the density of the SWCNT networks. We have demonstrated that sparce networks (~25 kΩ) are sensitive to trace concentrations (0.01–0.1 mg/L). Medium density networks (~15 kΩ) provided stable responses in the intermediate range (0.2–1.6 mg/L) and highly dense networks (~5 kΩ) were most effective at higher concentrations (1–8 mg/L). Functionalization of the sensors with redox-active molecules further improved the sensitivity and durability. Then, we tackle multivariate sensing of free chlorine at different pHs by utilizing an array of functionalized chemiresistors. We introduced an electrical reset to continuously measure free chlorine in simulated tap water background. Then, we demonstrated the classification and quantification free chlorine and potassium permanganate at different pHs using an array of chemiresistors. Finally, we have demonstrated that this carbon-based chemiresistive array can be extended to graphene-based chemiresistors and to other disinfectants. Differentiation and quantification of monochloramine and free chlorine were demonstrated using few-layer graphene-based functionalized chemiresistors. This thesis advances monitoring of a critical, complex drinking-water parameter and opens an avenue toward multianalyte detection that will ensure safe drinking water.

Acknowledgements

I am immensely grateful to my supervisor, Dr. Peter Kruse, whose wisdom and example have shaped my approach to science. I will remember him as the most humorous academic at McMaster. He was consistently available—even while he was staying in Germany and India—and in some weeks, he met with me as often as three times to discuss the project. Many Friday afternoons that began in frustration ended in new excitement after he found potential in a single plot; I hope to carry that instinct forward in my own work. I also cherish our non-research-related conversations, which always leave me more knowledgeable.

I thank Dr. Ravi Selvaganapathy for serving on my committee and for his contributions to my projects; our conversations taught me a great deal about engineering. I am grateful to Dr. Sarah Styler for her thorough reviews of my committee reports and detailed comments on my research.

I remain deeply grateful to my master's supervisor from Wright State University, Dr. Ioana Emilia Pavel**,** for being an amazing mentor and for consistently inspiring and supporting me to take on new roles. I am thankful to my undergraduate supervisor from University of Dhaka, Dr. A. M. Sarwaruddin Chowdhury, for his encouragement and support during the grad school application process.

I am thankful to my undergraduate students—Rebecca Sun**,** Thomas Kirby**,** Mia Balmforth**,** Mildred Tong**,** Lichen (Bruce) Guan**,** and Adriana Rekas. Specially, Thomas,

who took the lead on a project that started as a side project. I also appreciate the many thoughtful conversations with other students in our lab: Arjun Rego, Lea Hong, Leo (Xianxuan) Huang, and Devanjith Ganepola. I thank Omar Sharif, my junior from the University of Dhaka, who introduced me to this lab.

I am grateful to the graduate students who inspired and motivated me to work hard. I especially thank Dr. Shayan Angizi for encouraging me toward several fruitful avenues; I have not seen a student with his passion and encouragement for doing science. I thank Dr. Dipankar Saha for helping me with many things at McMaster University, and for the comfort of sharing a language in the lab. I am grateful to Johnson Dalmeida for training me when I joined, and Ana Zubiarrain-Lasserna for including me in one of the first collaborative projects. I thank wonderful lab mates Maryam Darestani-Farahani and Nazneen Meethal. I also thank Mehraneh Tavakkoli-Gilavan for helpful conversations and collaboration on several projects. To my friends at Mac (soon-to-be PhD holders) Rishad Arfin and Abu Ilius Faisal: thank you for the excellent breaks. I also thank my closest friends (Sahab, Rubel, Suvro, and Alif) who have encouraged me to stay on track and to complete the degree.

I am deeply grateful to my wife, Sunom, for her unwavering patience and support throughout this journey. Thank you for enduring my late nights and weekends of work, and for always finding ways to make my life easier. To my son, Aaroush Akbar: you are the cutest part of my life and, happily, my biggest distraction during the last three years—I loved every moment. I am forever grateful to my parents, Humayun Kabir and Akhera

Begum, for their sacrifices that made me who I am. I am grateful to my brothers, Sojib and Sharif, for their encouragement. I am thankful to all the relatives who have always encouraged me to pursue higher studies

Table of Contents

List of Figures

Chapter 2 Online monitoring of disinfectants in water

Chapter 4 Optimization of Carbon Nanotube Percolation Networks for Broad Dynamic Range Detection of Permanganate in Water

Chapter 5 Continuous monitoring of free chlorine level and pH using an array of carbon nanotube chemiresistors

Chapter 6 Identification and Quantification of Aqueous Disinfectants Using an Array of Carbon Nanotube-Based Chemiresistors

Chapter 7 Continuous Monitoring of Monochloramine in Water, and Its Distinction from Free Chlorine and Dichloramine Using a Functionalized Graphene-Based Array of Chemiresistors

List of Tables

Chapter 2 Online monitoring of disinfectants in water

Chapter 4 Optimization of Carbon Nanotube Percolation Networks for Broad Dynamic Range Detection of Permanganate in Water

Chapter 5 Continuous monitoring of free chlorine level and pH using an array of carbon nanotube chemiresistors

Chapter 6 Identification and Quantification of Aqueous Disinfectants Using an Array of Carbon Nanotube-Based Chemiresistors

Chapter 7 Continuous Monitoring of Monochloramine in Water, and Its Distinction from Free Chlorine and Dichloramine Using a Functionalized Graphene-Based Array of Chemiresistors

List of Abbreviations

DPD	N,N-diethyl-p-phenylenediamine
FIA	Flow injection analysis
SWCNT	Single Walled Carbon Nanotube
2D	Two-dimensional
FLG	Few-Layer Graphene
H2O2	Hydrogen Peroxide
KMnO4	Potassium Permanganate
LoD	Limit of Detection
OCl−	Hypochlorite
PDMS	Polydimethylsiloxane
ORP	Oxidation Reduction Potential
PCAT	Phenyl-Capped Aniline Tetramer
SEM	Scanning Electron Microscopy
UV-Vis	Ultraviolet-Visible
ClO_2	chlorine dioxide
DOM	Dissolved organic matter
EPS	extracellular polymeric substances
MWCNT	multiwalled carbon nanotube
CVD	chemical vapor deposition
AOPs	advanced oxidation processes
CYA	Cyanuric acid
DO	dissolved oxygen
NH_2Cl	monochloramine
DBP	disinfectant by-product
HOCl	hypochlorous acid
O_2	molecular oxygen
WHO	World Health Organization
$NaClO_2$	sodium chlorite

NDMA	N-nitrosodimethylamine
EPA	Environmental Protection Agency
OBr^-	Hypobromite
THM	trihalomethane
DBS	dodecylbenzenesulfonate
HOBr	hypobromous acid
FC	free chlorine
PLS	Partial least squares
PCA	Principal component analysis
ABTS	2,2′-azino-bis(3-ethylbenzothiazoline-6-sulfonic acid)
TMB	3,3′,5,5′-tetramethylbenzidine
UVT	UV transmittance
MoS_2	molybdenum disulfide
RGO	reduced graphene oxide,
DPPD	*N*, *N*-diethyl-1,4-phenylenediamine
SiO_2	silicon dioxide
BDD	boron-doped diamond BDD
GO	graphene oxide
GLC	graphene-like carbon
CoPc	cobalt phthalocyanine
AQ	anthraquinone
PEDOT: PSS	poly(3,4-ethylenedioxythiophene): poly(styrenesulfonate)

Declaration of Academic Achievements

Chapter 4 is based on the article published in the *Journal of Physical Chemistry C* (Akbar, M. A.; Selvaganapathy, P. R.; and Kruse, P. *Journal of Physical Chemistry C* 129 (32) 14583-14592). The authors' contributions are as follows: M.A.A. was responsible for device fabrication, experimental work, characterizations, and preparation of the original manuscript draft. P.K. conceived and supervised the study, revised the manuscript, and secured funding. P.R.S. revised the manuscript.

Chapter 5 is based on the article published in the journal *ACS Omega* (Akbar, M. A.; Gilavan, M. T.; Selvaganapathy, P. R.; and Kruse, P. *ACS Omega* 10 (27) 29074-29086). The authors' contributions are as follows: M.A.A. and P.K. designed the study. M.A.A. was responsible for device fabrication, experimental work, characterizations, and preparation of the original manuscript draft. P.K. conceived and supervised the study, revised the manuscript, and secured funding. M.T.G. contributed to the optimization of the device fabrication (data shown in table S1). P.R.S contributed to the development of the discussion and revised the manuscript.

Chapter 6 is based on the article published in the journal *ACS Applied Engineering Materials* (Akbar, M. A.; Sharif, O.; Selvaganapathy, P. R.; and Kruse, P. *ACS Appl. Eng. Mater.* 2023, 1, 11, 3040–3052. The authors' contributions are as follows: M.A.A. was responsible for device fabrication, experimental work, characterizations, and preparation of the original manuscript draft. P.K. conceived and supervised the study, revised the manuscript, and secured funding. O.S. synthesized and characterized PCAT and conducted initial experiments at the beginning of the project. O.S. characterized the SWCNT network shown in figure 2. The electrochemical and spectrophotometric characterizations performed by O.S. are shown in figures 4, S1-S35 and table S1-S2. P.R.S contributed to the development of the discussion and revised the manuscript.

Chapter 7 is based on the article published in the journal *ACS ES&T Water* (Akbar, M. A.; Selvaganapathy, P. R.; and Kruse, P. *ACS ES&T Water* 2024, 4, 9, 4041–4051. The authors' contributions are as follows: M.A.A. was responsible for device fabrication, experimental work, characterizations, and preparation of the original manuscript draft. P.R.S. contributed to manuscript revision. P.K. conceived and supervised the study, revised the manuscript, and secured funding.

Chapter 1 Introduction

1.1 Motivation

Even though 71% of the planet's surface is covered by water, 2.1 billion people lack access to safely managed drinking water.[1] In addition to environmental regulations passed worldwide to protect water resources, a significant effort has been dedicated to advancing purification technologies for both centralized treatment plants and resource-limited settings. Safe and reliable water quality requires continuous monitoring of a wide range of parameters, yet, historically, the focus of sensor development has been uneven. Most of the attention has been directed towards biosensors and heavy metal sensors (i.e., lead, arsenic, mercury). Though these parameters are undeniably important, other equally critical analytes such as disinfectants are often overlooked. Disinfectants are essential for inactivating pathogen and suppressing the microbial regrowth. Safe drinking water depends on keeping disinfectant levels in a narrow window.[2,3] The concentration needs to be high enough to suppress pathogen regrowth throughout the distribution network, but low enough to avoid taste, odor, and comply with regulatory limits In real systems, disinfectant residuals are dynamic: temperature swings, biofilm activity, pipe materials, and duration of water staying in the distribution channel continually shift disinfectant demand. Continuous monitoring of disinfectant is therefore an operational necessity.

Standard measurements such as N,N-diethyl-p-phenylenediamine (DPD) colorimetry[4] and amperometry[5] work but carry trade-offs such as additional reagents, waste streams, and interferences (e.g., iron/manganese for DPD), maintenance (calibration) that complicate the widespread deployment of a high number of sensor deployments across large networks or decentralized sites.[6] These constraints create blind spots in time and space, and this is exactly where outbreak and nitrification episodes often start. Chemiresistive sensors, a type of electrical sensors are potential solution for these gaps. These sensors are built from semiconductive materials (graphene, carbon nanotubes), and translate surface redox or adsorption events into current changes.[7] This enables a reagent-free, low-power, and miniaturizable solid-state platform for disinfectant monitoring.[8–10]

1.2 Structure of This Thesis

Chapter 2 begins by discussing the parameters that affect the efficacy of disinfectants such as pH, oxidation-reduction potential, ionic strength, and dissolved oxygen. Then, the disinfectants used in water treatment are discussed such as free chlorine, monochloramine, chlorine dioxide, potassium permanganate, ozone, peroxene, UV-peroxide, and hypobromite/hypobromous acid. Then their applications in drinking water (primary and secondary disinfectants), industrial water, cooling water loops, swimming pools, and wastewater treatment plants are discussed. Finally, the different operating methods of sensors that are in current or proposed future use for detecting and monitoring disinfectants in water are discussed. Optical, electrochemical, and electrical (field effect transistors and chemiresistors) sensors are discussed for the application in disinfectant sensing. Literature reviews of each of the operating principles are also provided after each section.

Chapter 3 shows the optimization of chemiresistive percolation networks for disinfectant sensing. Spectroscopic, microscopic, and electrical characterization of single-walled carbon nanotubes (SWCNTs) for chemiresistive sensing were discussed. The density of the percolation network was shown to directly influence both the detection range and sensitivity for potassium permanganate sensing. Functionalization of the SWCNT networks was demonstrated which provided improvements in selectivity and stability, while extending the long-term performance of the sensors.

Chapter 4 extends chemiresistive disinfectant sensing for a complex scenario where pH dictates the species of the disinfectant and potency of disinfection. The device architecture was modified from earlier prototypes to include features that facilitate scalable fabrication. We then demonstrate continuous monitoring of free chlorine at different pHs utilizing an array of functionalized SWCNT-based chemiresistors. SWCNT films were noncovalently functionalized with cobalt phthalocyanine and anthraquinone. The sensor device was further enhanced by an electronic reset function that enabled repeated use during continuous monitoring. Finally, sensor durability was tested through repeated measurements in simulated tap water. Chemometrics was applied to analyze the sensor array data.

Chapter 5 demonstrates the applicability of functionalized chemiresistors for identification and quantification of disinfectants in different pHs. An array of chemiresistors functionalized specifically to differentiate free chlorine and potassium permanganate in water. Chemometric methods were used to differentiate the two disinfectants across five pH conditions.

In chapter 6, the idea of multiple disinfectant sensing using carbon-based substrates is extended. Two of the most popular disinfectants, monochloramine and free chlorine can be simultaneously present in the water treatment plant. Few layer graphene based chemiresistors were functionalized with redox-active molecules to demonstrate classification of disinfectants, and simultaneous detection of free chlorine and monochloramine. Then, tap water testing of monochloramine is demonstrated and finally, multivariate calibration of the array is utilized to predict unknown concentrations of monochloramine.

Chapter 7 provides an overview of the principal findings from each research study. It also outlines potential avenues for future work to build upon this foundation.

1.3 References

(1) UNICEF. Drinking water https://data.unicef.org/topic/water-and-sanitation/drinking-water/ (accessed Aug 31, 2025).

(2) Sayre, I. M. International Standards for Drinking Water. *J. Am. Water Work. Assoc.* **1988**, *80* (1), 53–60.

(3) US Environmental Protection Agency - Office of Water. *Alternative Disinfectants and Oxidants Guidance Manual*, 1st Ed.; (Washington, DC) US Environmental Agency, 1999.

(4) Gordon, G.; Sweetin, D. L.; Smith, K.; Pacey, G. E. Improvements in the N,N-Diethyl-p-Phenylenediamine Method for the Determination of Free and Combined Residual Chlorine through the Use of FIA. *Talanta* **1991**, *38* (2), 145–149.

(5) Kumar, D. R.; Kesavan, S.; Nguyen, T. T.; Hwang, J.; Lamiel, C.; Shim, J. J.

Polydopamine@electrochemically Reduced Graphene Oxide-Modified Electrode for Electrochemical Detection of Free-Chlorine. *Sensors Actuators, B Chem.* **2017**, *240*, 818–828. https://doi.org/10.1016/j.snb.2016.09.025.

(6) Kruse, P. Review on Water Quality Sensors. *J. Phys. D. Appl. Phys.* **2018**, *51*, 203002.

(7) Zubiarrain-Laserna, A.; Angizi, S.; Akbar, M. A.; Divigalpitiya, R.; Selvaganapathy, P. R.; Kruse, P. Detection of Free Chlorine in Water Using Graphene-like Carbon Based Chemiresistive Sensors. *RSC Adv.* **2022**, *12*, 2485–2496.

(8) Antony, C. E.; K., G.; S. G., P.; Jayakumar, A.; Yadav, A.; Sivakumar, N. S.; Kamath, N.; M. N., S.; Kamble, V. B.; Jaiswal-Nagar, D. Polyvinylpyrrolidone-Stabilized Palladium Nanocrystals as Chemiresistive Sensors for Low-Concentration Hydrogen Gas Detection. *ACS Appl. Nano Mater.* **2021**, *4* (2), 1643–1653.

(9) Zhang, J.; Liu, L.; Yang, Y.; Huang, Q.; Li, D.; Zeng, D. A Review on Two-Dimensional Materials for Chemiresistive- And FET-Type Gas Sensors. *Phys. Chem. Chem. Phys.* **2021**, *23* (29), 15420–15439.

(10) Patel, V.; Saha, D.; Kruse, P.; Selvaganapathy, P. R. Reagent-Free Hydrogen Peroxide Sensing Using Carbon Nanotube Chemiresistors with Electropolymerized Crystal Violet. *ACS Appl. Nano Mater.* **2022**, *5* (3), 3957–3966.

Chapter 2 Online monitoring of disinfectants

This chapter focuses on the review of current literature on the disinfectants applied in the treatment of drinking water. The review starts with a discussion of parameters affecting the efficacy of the disinfectants. Then the disinfectants used in the treatment processes are discussed, followed by their applications. Finally, different methods (current and future) are discussed.

Online monitoring of disinfectants in water

Md. Ali Akbar[¥], and Peter Kruse[¥,*]

[¥] Department of Chemistry and Chemical Biology, McMaster University, 1280 Main
Street West, Hamilton, Ontario L8S 4M1, Canada

[*] pkruse@mcmaster.ca

Abstract :

Online monitoring of disinfectants is essential to ensure a safe supply of water while at the same time limiting by-products and corrosion related issues. Oxidants are reactive and unstable, and occasional testing on discrete samples can leave water without disinfectant. Continuous sensing captures the dynamics of disinfectant concentration variation and speciation due to a shift of parameters. We outline the chemistry that controls performance such as pH, temperature, ionic strength, dissolved oxygen, and oxidation–reduction potential (ORP); and link these to oxidant speciation, kinetics, and residual stability. We survey disinfectants across applications: free chlorine, monochloramine, chlorine dioxide, ozone, potassium permanganate, peroxene (O_3/H_2O_2), UV/H_2O_2, and $HOBr/OBr^-$. We also highlight efficacy and constraints for online measurement. We assess sensing methods covered in this work: optical (traceable but reagent-dependent); electrochemical (fast, reagent-free, but reliant on stable reference electrodes and fouling control); and electrical (chemiresistors and solution-gated FETs), with challenges in selectivity, drift, and in-situ calibration. ORP is a rapid working alternative that must be interpreted with pH and oxidant concentration rather than used as a replacement for residual. Priorities for improvements in future methods include calibration, antifouling and self-verification with automated recalibration, and model-based control linking speciation and ORP to operational needs.

1. Introduction

Access to safe water depends on effective disinfection across many scenarios, such as municipal drinking water, wastewater effluent, industrial and cooling-water circuits, healthcare facilities, and recreational venues such as pools and spas. Disinfection protects public health primarily by inactivating pathogens and suppressing biofilms; it also oxidizes nuisance compounds that cause taste, odour and fouling. Common agents include free chlorine and monochloramine, chlorine dioxide, ozone, and UV/advanced-oxidation processes, each with distinct kinetics, residual behaviour, and by-product profiles. Regulatory and design practice often quantify primary disinfection using CT (disinfectant concentration × contact time) tables that specify organism- and temperature-dependent inactivation targets. Secondary disinfection relies on maintaining a measurable residual through the distribution system to guard against intrusions and regrowth.

The disinfection process targets harmful microorganisms such as *Escherichia coli* (bacteria), enteric viruses (e.g. adenovirus), and protozoa (e.g. *Giardia lamblia*, *Cryptosporidium parvum*). These microorganisms often adhere to surfaces, forming biofilms with extracellular polymeric substances (EPS) on pipe walls, sediments, or particulate matter.[1] It is assumed in disinfection that the disinfectant is uniformly distributed in the water body, and the residual disinfectant is there to prevent the regrowth of the microorganisms as the water is treated during the primary disinfection. These assumptions simplify sensor design and interpretation but may not reflect actual complex water distribution systems. Dissolved organic matter (DOM) composed of humic substances, fulvic acids, and many other natural organic compounds imposes a chlorine demand by reacting with disinfectants.[2] This could lead to a reduction of residual disinfectant.

Each disinfectant involves trade-offs among variety, residual, and by-products. Free chlorine is a broad-spectrum disinfectant and leaves a residual; monochloramine is weaker but longer-lived and thus commonly used for secondary disinfection; chlorine dioxide is potent and pH-independent but must be generated on site; ozone is a powerful primary disinfectant without a residual and requires attention to bromate control in bromide-rich waters. World Health Organization (WHO) guidance and engineering manuals summarize these trade-offs and their implications for safety plans and compliance.[3,4] Maintaining residuals in distribution is important: water temperature, pH, organic and inorganic demand, and pipe conditions all modulate decay. In chloraminated systems, nitrification can lower oxidant efficacy, pH, and aesthetic quality, emphasizing the need for proactive monitoring and control strategies at susceptible locations in the network.[5]

The chemistry and microbiology related to disinfectants in water change on short timescales and require continuous online monitoring to capture pitfalls and protect consumers. Since disinfectants are reactive and - in several cases - short-lived, point samples and lab assays can miss transients**.** Microbiological tests for fecal coliforms/*E. coli* typically take 24–48 h, meaning results often arrive after contaminated water has already reached consumers.[6,7] The 2000 Walkerton tragedy in Canada dramatically illustrated the risk of relying on delayed microbiological confirmation without robust residual maintenance and alarms (7 deaths, ~2,300 illnesses). [8,9] This is why utilities pair continuous online monitoring (free/combined chlorine, chlorine dioxide, ozone, pH, temperature, and oxidation-reduction potential, ORP) at plant and system control points with routine lab verification. ORP is not a substitute for residual measurements, but it provides a fast, integrative indicator of oxidative capacity. ORP is related to the oxidant dosage and pH. ORP is often used for early warning while confirmatory analyses are in process.

In this review, we discuss the parameters that affect the monitoring of disinfectants in water due to their involvement in disinfectant chemistry, including pH, oxidation-reduction potential (ORP), ionic strength, dissolved oxygen (DO) and their contribution in the disinfection efficacy. We discuss commonly used disinfectants in drinking water treatment such as free chlorine (Cl_2/HOCl/OCl^-), monochloramine (NH_2Cl), chlorine dioxide (ClO_2), potassium permanganate ($KMnO_4$), ozone (O_3), peroxene (ozone/H_2O_2), UV-peroxide (UV/H_2O_2), and hypobromous acid/hypobromite (HOBr/OBr^-). Their applications in drinking water (primary and secondary disinfectants), industrial water, cooling water loops, swimming pools, and wastewater treatment plants are also discussed. Finally, this review delves into the different operating principles of sensors that are in current or proposed future use for detecting and monitoring disinfectants in water. Here we limit our discussion to sensing strategies that can operate continuously, in situ, and (ideally) reagent-less. Manual measurements such as field kits, benchtop assays, or grab-sample workflows are out of scope for this review. Many optical techniques (especially colorimetry and fluorescence) depend on added reagents and/or more complex optics, which makes fully autonomous online use difficult.[10] Flow injection analysis (FIA) can automate sampling, but still consumes reagents. We have therefore not included FIA as we also do not cover laboratory-centric optical sensors where turbidity, deposits, or colored interferents shift baselines. Readers seeking broader treatment of handheld/lab methods and emerging materials can consult: Wilson et al. on continuous chlorine detection and practical deployment (fouling, operability),[11] Yang & Ge and Wu et al. on modern colorimetric sensor design,[12,13] and Thakur & Devi on water-quality monitoring devices across optical/electrochemical modalities.[14] A broader discussion on water quality sensors can be found in ref. [10]

2. Parameters impacting disinfectant efficacy

Disinfection serves as a critical step in protecting public health by playing an indispensable role in the water treatment, healthcare sectors, and industrial applications. Successful disinfection processes prevent disease transmission by the inactivation or elimination of pathogenic microorganisms. Water quality parameters such as pH, ORP, ionic strength, dissolved oxygen, and temperature play a role in keeping the disinfection concentration at the desired level with respect to the active disinfectant species.[14] Here these parameters are discussed.

2.1. pH

pH is an important water quality parameter in ensuring disinfectant efficacy. pH is defined as the negative logarithm of hydrogen ion concentration (quantified as $-\log[H^+]$). In the case of disinfectants, pH can directly influence the chemical species present (speciation), redox potential of the solution, stability, and disinfectant biproduct pathways.[15–17] They all influence the chemical behaviour of disinfectants and quality of the drinking water which in turn affects the disinfection efficacy. For certain disinfectants such as free chlorine, pH decides which oxidant species will dominate in water. Depending on the species present due to the pH of water, the redox potential will be different. Disinfectants work by mechanisms such as oxidizing contaminants, disrupting cell structure or by inactivating enzymes. Therefore rate constants for pathogen kill or natural organic matter (NOM) oxidation can change significantly with pH.[15] High pH can shorten the residual effect of disinfectants such as ozone or H_2O_2. For disinfectants such as monochloramine, basic pH increases the stability while acidic pH shortens the life. Lower pH often contributes to increasing disinfectant by-product (DBP) formation due to the increasing reactivity. Because of that, chlorine-based disinfectants show high rates of DBP formation at lower pH.

Drinking water pH is commonly regulated in the range from 6.5 to 9.[10,18–21] The relationship between aqueous pH and disinfectant performance is particularly important for free chlorine-based systems. In the aqueous phase, free chlorine is a mixture of pH dependent species such as hypochlorous acid (HOCl) and hypochlorite ions (OCl^-). These two species show different levels of antimicrobial activity. The pH-dependent behavior of disinfectants extends to their reaction kinetics with organic matter which then can affect microbial inactivation rates and disinfection byproduct formation. Understanding these pH-disinfectant relationships becomes essential for optimizing treatment processes and balancing microbial control with chemical safety in various applications.

Table 2.1. Commonly used disinfectants, their optimal ranges and key notes.

Disinfectant	Target pH for practical applications	Impact of pH changes	Key notes
Free chlorine [16,22,23] ($HOCl/OCl^-$)	7.2 – 7.8	HOCl ($pK_a \approx 7.6$) is 80-100 times more bactericidal than OCl^-.	Keep pH ≤ 7.8 for ≥ 70 % HOCl; let pH rise after contact if trihalomethanes (THMs) are a concern.
Chloramines [22–24]	8.0 – 9.0	Higher pH favours stable monochloramine; lower pH forms dichloramine and trichloramine.	Dose at pH ≈ 8.3 with Cl:N ≈ 4:1; avoid < 7.5 to limit odour & nitrification.
Permanganate[22,23,25]	6.5 – 8.5	Acidic water reduces MnO_4^- to soluble Mn^{2+} (fast metal oxidation); alkaline water drives slower, selective MnO_2 pathways.	Usual dosage at ambient pH; adjust only for special targets (e.g., sulfide).
Hydrogen peroxide[17,22,23]	6.5 – 8.5	Alkaline pH accelerates •OH generation but burns residual; acidic pH helps protozoa control.	Natural pH suits H_2O_2/UV AOP; avoid > pH 9 unless rapid oxidation is worth the loss of residual.

Chlorine dioxide[22,23,26]	6.0 – 9.5	Germicidal power is pH-independent; low pH increases volatilisation, high pH raises chlorite/chlorate.	Effective between 6 and 9.5; no pH change needed for efficacy.
Ozone[22,23,27]	6.0 – 7.0	Alkaline pH speeds decomposition to •OH, erasing residual.	Contact at slightly acidic pH, then raise pH for corrosion control before distribution.

Table 1 lists the commonly applied disinfectants and their targeted pH for optimal disinfection. For free chlorine, pH 6 to pH 7.5 favors the formation of highly bactericidal hypochlorous acid (HOCl), while pH above 7.5 conditions promote the formation of less effective hypochlorite ions (OCl^-). Targeted pH for the free chlorine-based disinfection ranges from 7.2-7.8. Chloramines require slightly alkaline environments to maintain stable monochloramine (NH_2Cl). This also helps to lower dichloramine and trichloramine formation. Permanganate remains effective across a broad pH range, though its oxidation mechanisms vary with pH. The oxidation pathway shifts—from rapid Mn^{2+} production in acid to slower, more selective MnO_2 formation in alkaline water. In the peroxone (O_3/H_2O_2) process, alkaline pH shifts H_2O_2 to HO_2^-, which reacts with ozone and increases hydroxyl radical production[28,29] Ozone on the other hand decomposes more rapidly at higher pH which results in decreasing its residual stability.[30] Chlorine dioxide maintains consistent oxidation potential across pH 6-10, making it uniquely pH-independent. The selection and operation of disinfectants must therefore consider pH as a critical parameter to ensure effective microbial inactivation and system performance.

2.2. Ionic Strength

Ionic strength in an aqueous solution is a measure of the concentration of ionic charge present in that solution.[31] It quantifies the total electrical charge in the solution and reflects the extent of electrostatic interactions between ions and with the solvent. When ionic compounds dissolve in water, they dissociate into ions, and the total concentration of these electrolytes in the solution can affect important properties such as the activitiesof weak acids or bases and the solubility of different salts. The molar ionic strength (I) of a solution is mathematically defined as a function of the concentration of all ions present. The formula for calculating molar ionic strength is given by $I = ½ \Sigma c_i z_i^2$, where c_i represents the molar concentration of ion i (in mol/L), and z_i represents the charge number (valence) of that ion. The summation (Σ) extends over all ionic species present in the solution.[31] The factor of one-half (½) is included because the formula considers both the positively charged cations and the negatively charged anions of each ionic species. Multivalent ions, those with a higher charge (e.g., SO_4^{2-}, Mg^{2+}), contribute more significantly to the ionic strength of a solution because the charge term (z_i) is squared in the formula.

The ionic strength of water samples varies naturally across different aquatic ecosystems.[12] Natural waters, such as seawater and mineral water, typically possess a non-negligible ionic strength due to the presence of various dissolved salts.[13] The ionic strength of freshwater systems can be influenced by factors like watershed urbanization, where reduced permeability of surfaces and storm drain networks efficiently transport ions to surface waters.[12] Other sources such as industrial discharges and agricultural runoff can also contribute significantly to the ion content of water bodies which in result increases the ionic strength. The concentration of ions through evaporation, whether due to anthropogenic activities or natural processes, can also elevate the ionic strength of water.[12] In laboratory settings, the ionic strength of a solution is precisely controlled by the type and concentration of electrolytes that are intentionally added to the water.

Disinfectant performance is affected by the shielding of electrostatic charges and quenching of oxidant species.[32] Shielding electrostatic charges can alter how quickly disinfectant molecules can reach to the cellular membrane and thereby affect the disinfection process. Disinfectants such as HOCl and ozone rely on electrostatic interactions to approach and penetrate cell walls. High ionic strength due to the introduction of counter ions (such as Na^+, Ca^{2+}) results in the formation of an electrostatic shield around the microbial cells. Electrostatic shielding can reduce the attraction between neutral HOCl and negatively charged cell surfaces. Diffusion of the disinfectant inside the cell membrane can therefore be hindered. Halide and carbonate ions can contribute to the quenching or redirecting of active oxidant species. Carbonate (CO_3^{2-}) and bicarbonate (HCO_3^-) ions act as scavengers for free radicals. When in contact with a hydroxyl radical they form a less reactive carbonate radical which reduces the overall disinfection power.[33] Competing reactions can also deplete the disinfectants before achieving the microbial target (free chlorine reacting with ammonia to form chloramines).

2.3. Temperature

Water temperature is crucial in aquatic ecosystems because it influences physical, chemical, and biological processes. External factors like air temperature, climate changes, seasonal shifts, and human activities all affect water temperature. These variations also matter for water treatment, as temperature impacts how well different treatment methods work. It might seem that drinking water distribution systems (DWDS) are protected from high surface temperatures since most pipes are buried underground. However, heat can still transfer quickly to typical buried depths, causing water temperatures to match surface conditions within hours or days.[34]

The efficacy of chemical disinfectants is significantly affected by temperature, which impacts multiple aspects of microbial inactivation. Temperature influences not only the rate of chemical reactions but also the stability of disinfectants and their ability to penetrate and disrupt microbial cells.[35] The impact of temperature on reaction rates is typically modeled using the Arrhenius equation (Eq. 1), where the rate constant (k) depends on temperature (T), activation energy (E_a), the universal gas constant (R), and a pre-exponential factor (A).

$$k = A \exp\left(\frac{-E_a}{RT}\right) \qquad (1)$$

In principle, E_a/R, obtained from experimental results, can help estimate how the decay rate changes from k_1 to k_2 when temperature changes from T_1 to T_2 (Eq. 2).

$$k_2 = k_1 \exp\left[-\frac{E_a}{R}\left(\frac{1}{T_2} - \frac{1}{T_1}\right)\right] \qquad (2)$$

Since disinfectant decay processes are complex, most modeling approaches are empirical and based on experimental data from real water systems.[36] To estimate how temperature affects disinfectant decay, previously measured E_a/R values are used by researchers. This ratio can vary significantly depending on water chemistry.[37] At lower temperatures, disinfection processes generally become less efficient. The reduced kinetic energy of molecules slows down reaction rates between disinfectants and microorganisms. This requires either higher concentrations of the disinfectant or extended contact times to achieve the desired level of microbial inactivation. For example, in cold water systems, disinfectants such as free chlorine exhibit slower disinfection kinetics, necessitating adjustments in dosing or exposure duration to maintain effectiveness. Similarly, chloramines, which are already less reactive than free chlorine, demonstrate even slower microbial inactivation rates in colder conditions, making them more challenging to use in low-temperature environments. High temperatures typically enhance disinfection rates by accelerating chemical reactions. However, this benefit can be offset by increased disinfectant decomposition. Many oxidizing disinfectants, such as chlorine and hydrogen peroxide, degrade more rapidly at higher temperatures which leads to a faster depletion of active disinfectant residuals.[35]

The relationship between temperature and disinfectant efficacy is further complicated by interactions with other water quality parameters. Higher temperatures can increase the oxidation of organic matter which leading to greater demand of the disinfectant. Seasonal changes, geographic location, and system-specific conditions (e.g., indoor vs. outdoor treatment) all play a role in determining the optimal approach. A thorough understanding of temperature effects is therefore important for consistent microbial control over different operational environments. These effects are carefully considered when designing and implementing disinfection protocols, particularly in applications where temperature changes can occur. In water treatment facilities regular monitoring of temperature helps predict and prevent issues like bacterial growth or rapid disinfectant loss.

2.4. Oxidation reduction potential (ORP)

Most commonly used disinfectants are oxidizing agents, and they work by electron transfer. The oxidative ability of a disinfectant is determined by its redox potential, which in a water quality context is referred to as the oxidation-reduction potential (ORP). ORP is defined by the ability of the disinfectant solution to oxidize the contaminants in water. Higher ORP values represent a solution that can oxidize pathogens effectively while lower ORP in solution refers to solution that may not be safe to drink due to the possibility of the proliferation of pathogens. ORP is electrochemically determined by measurement of the potential difference between a platinum working electrode and a reference electrode in an aqueous solution. The basis for ORP behavior is the Nernst equation, where the electrode potential is a function of the activities of the oxidizing and reducing species present in the solution. An ORP sensor operates similar to a standard pH sensor where a potentiometric measurement is conducted using a two-electrode system.[38] The oxidation-reduction potential behaviour of an oxidant at an electrode can be understood from the Nernst equation[39]:

$$E = E_0 + \frac{RT}{nF} \ln \frac{[Oxidizer]}{[Reducer]} \qquad (3)$$

Here E is the measured potential (mV) between the platinum and reference electrode, E_o is the measured potential (mV) between the platinum and the reference electrode at a concentration of [oxidizer] = [reducer] or the standard ORP for the given oxidation-reduction process, R is the universal gas constant (R= 8.314 $\mathrm{Jmol^{-1}K^{-1}}$), T is temperature in Kelvin, n is number of electrons transferred, and F is Faraday's constant (96485 $\mathrm{Cmol^{-1}}$).

The relationship of pH and ORP with the concentration of a disinfectant such as free chlorine can be understood from the discussion of the Nernst equation for the HOCl and

OCl^- reduction reactions. For HOCl, reduction at an acidic pH (for example pH 6.5) can be presented as:

$$HOCl + H^+ + 2\,e^- \longrightarrow Cl^- + H_2O \qquad (4)$$

At a temperature of 298 K, the Nernst equation for the above reaction can be written as:

$$E = E_{0,HOCl} + 29.58\,mV \cdot \log \frac{[HOCl]\cdot[H^+]}{[Cl^-]} \qquad (5)$$

The Nernst equation for OCl^- which is dominating at basic pH (for example 8.5) can be written at 298 K as:

$$OCl^- + H_2O + 2\,e^- \longrightarrow Cl^- + 2\,OH^- \qquad (6)$$

$$E = E_{0,OCl^-} + 29.58\,mV \cdot \log \frac{[OCl^-]}{[Cl^-]\cdot[OH^-]^2} \qquad (7)$$

The ORP response to disinfectants can be explained by the involvement of protons in their redox reactions, which makes the corresponding redox potentials strongly pH dependent. In oxidation–reduction potential (ORP) measurements, this influence is evident from equation (5): a lower pH (higher proton concentration) generally leads to a higher E value (ORP). In the case of equation (7), the increase in $[OH^-]$ with pH drives the potential to more negative values, lowering the ORP. The ORP decreases with increasing pH as the dominant redox couple shifts from proton-dependent HOCl at low pH to hydroxide-dependent OCl^- at high pH, producing the characteristic negative slope of ORP versus pH for free chlorine solutions.

Due to the logarithmic nature of the Nernst equation, the relation between the concentration of the redox species to measured ORP is not linear. Large concentration changes, especially at high levels, may induce relatively small changes in ORP. This has a bearing on interpreting ORP measurements where quantitative analysis is an issue. Above ~25 ppm free chlorine approaches its thermodynamic ceiling (~900 mV at 25 °C). Even doubling the dose of free chlorine does not change the electrode potential in any significant way.[40] Typically, a one-unit pH rise reduces the ORP by ~60 mV at constant mg L^{-1} Cl_2.[41] Rapid consumption of HOCl lowers ORP faster than a colorimetric residual test can be run, giving early warning of breakthrough.[42]

Table 2.2 Maximum oxidation-reduction potential (ORP) values (in volts) as a function of pH and oxidant type.[43]

Oxidant	pH 7	pH 8	pH 9
Oxygen	0.582	0.552	0.508
Monochloramine	0.806	0.716	0.66
Potassium permanganate	0.812	0.795	0.672
Chlorine dioxide	0.98	0.943	0.912
Free chlorine	1.02	0.922	0.769

The data in Table 2 show that the maximum redox potential drops as pH increases for all oxidants tested. Chlorine has the highest redox potential at pH 7 (1.02 V) but loses a significant portion of its potential by pH 9 (0.769 V). Chlorine dioxide also shows a high initial potential but declines more gradually with rising pH. Potassium permanganate maintains relatively stable ORP values between pH 7 and 8 before dropping at pH 9. Oxygen has the lowest ORPs overall, and monochloramine shows a steady decrease across the pH range.

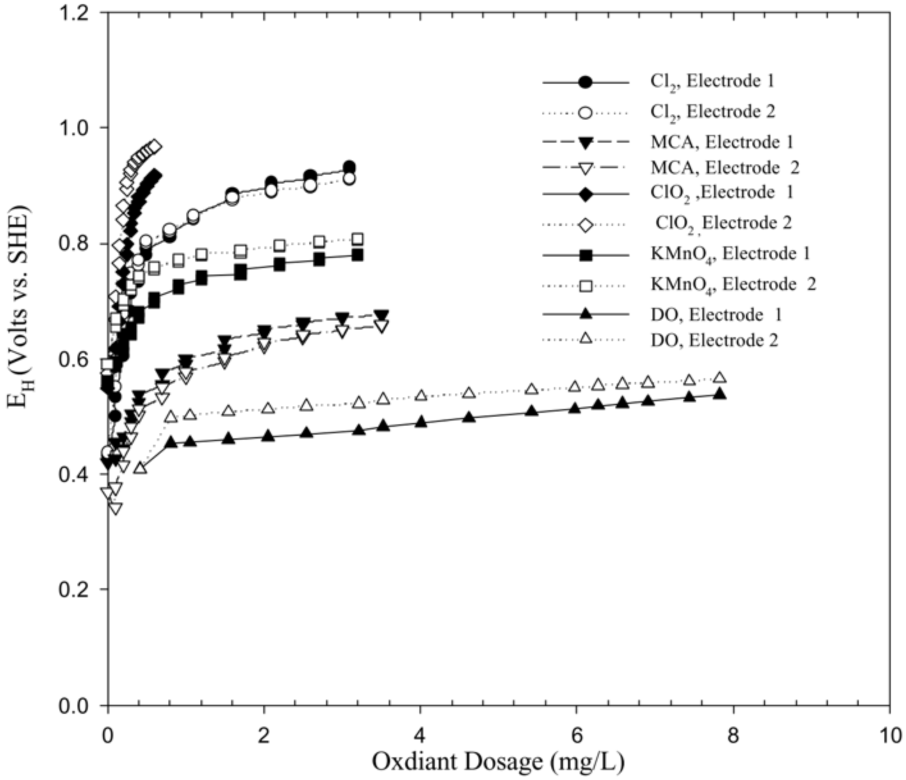

Figure 2.1 The effect of oxidant type on Oxidation–reduction potential (ORP) (5 mg C/L, 23°C, pH 8).[43] ORP(E_H, volts vs SHE) as a function of oxidant dose (mg L^{-1}) for common residual disinfectants, measured with two ORP electrodes (Electrode 1 and Electrode 2). For each oxidant, E_H rises rapidly at low dose and approaches a plateau characteristic of its redox couple: chlorine dioxide and free chlorine reach the highest potentials (~0.9–1.0 V), permanganate is intermediate (~0.75–0.8 V), monochloramine lower (~0.6–0.65 V), and dissolved oxygen the lowest (~0.45–0.55 V). Replicate electrodes exhibit the same ordering with small offsets, reflecting electrode-to-electrode variability under the test conditions. Reprinted with permission from Reference [43]; Copyright 2004 American Water Works Association (AWWA).

Figure 1 shows redox potentials (E_H) measured relative to the Standard Hydrogen Electrode (SHE), the universal 0.00 V reference. A higher redox potential means a more oxidising environment or a strong disinfectant. The figure shows that the redox potential generally increases with oxidant dosage, but the rate of increase and maximum values vary by oxidant. Chlorine and chlorine dioxide reach the highest E_H values, with chlorine showing a gradual rise and chlorine dioxide increasing sharply at low doses before levelling off. Potassium permanganate achieves moderate E_H values and stabilizes quickly after initial dosing. Monochloramine has lower potentials than chlorine-based oxidants but still shows a steady upward trend. Dissolved oxygen records the lowest E_H across all dosages, with only a slight increase as the concentration rises.

Table 3 shows the optimal range of ORP values for the disinfectants used in water treatment. Ozone and chlorine dioxide sit highest (~700–900 mV), free chlorine follows (~650–750 mV), then permanganate and monochloramine (~475–550 mV), with hydrogen peroxide lowest (~250–350 mV). Overall, it is recommended to use ORP (when needed) as a fast operational proxy, tuned to pH and disinfectant demand, not as a substitute for residual measurements.

Table 2.3 Effective ORP ranges and key notes for common disinfectants.

Disinfectant	ORP (mV) window	Key notes
Free chlorine[41,44,45] ($HOCl/OCl^-$)	≈ 650 – 750	≥ 650 mV is the point at which HOCl is present in sufficient quantity to give 30-s inactivation of common enteric bacteria; above ~750 mV more effective in preventing pathogens and begins to approach corrosive conditions.
Monochloramine[5,42,44,46]	≈ 450 – 550	Because NH_2Cl is a weaker oxidant, it leaves a lower ORP; field studies of chloraminated systems report stable residual when bulk ORP stays near 500 mV.
Potassium permanganate[44]	≈ 475 – 550	High-level MnO_4^- dosing for taste and odor or parasite control drives ORP into the upper-400s/low-500s; going much higher adds little benefit and may cause MnO_2 fouling.

Hydrogen peroxide (no UV) [4447]	≈ 250 – 350	H_2O_2 rarely pushes ORP above 300 mV (even at high ppm) and therefore has weak germicidal power; in AOPs this rely on •OH rather than bulk ORP.
Chlorine dioxide[44]	≈ 600 – 900	Maintains high ORP across pH 2-12; control setpoints near 700–800 mV are used to balance rate of microbial inactivation with oxidant consumption.
Ozone[48,49]	≈ 700 – 900	Above ~700 mV, systems generally meet 99% reduction (also known as 2-log credit) in Giardia and virus; values > 900 mV rarely add benefit and indicate excess ozone feed or low demand.

2.5. Dissolved oxygen (DO)

Dissolved oxygen (DO) refers to molecular oxygen (O_2) present in water. The concentration of DO is dependent on temperature, pressure, salinity, and the balance between oxygen production and consumption processes. It is a critical ecological parameter for keeping aerobic organisms alive and is also important in engineered water systems.[50] DO enters and changes within a water system in several ways: it can be present in the source water, introduced or consumed during water treatment. DO continually equilibrates with the surrounding air.[51] DO is a mild oxidant relative to common disinfectants such as ozone or hypochlorous acid (HOCl), with a standard redox potential of $E_{O2/OH^-} \approx 0.401$ V at pH 14.[52,53] This potential increases under acidic conditions. Its reduction in water can occur through one- or two-electron pathways, and will produce species such as hydrogen peroxide (H_2O_2) or hydroxyl ions (OH^-) depending on the environment[54,55]:

$$O_2 + 2H_2O + 2e^- \rightarrow H_2O_2 + 2OH^- \qquad (8)$$

$$H_2O_2 + 2e^- \rightarrow 2OH^- \qquad (9)$$

$$O_2 + 2H_2O + 4e^- \rightarrow 4OH^- \qquad (10)$$

The influence of DO on disinfection efficacy is nuanced. Oxidizing disinfectants act by accepting electrons from microbial components; oxygen can compete weakly for those electrons or reactive intermediates, but its oxidative strength is much lower than that of the disinfectants themselves.[56] In most practical systems, this competition is negligible compared to the direct microbicidal activity of stronger oxidants. In advanced oxidation processes (AOPs), DO can participate indirectly in radical chemistry. Photocatalytic or ozone-based systems can use DO to generate superoxide ($O_2^{\cdot-}$) or promote hydroxyl radical (·OH) formation, thereby enhancing microbial inactivation. On the other hand, oxygen can also scavenge certain reactive radical species, slightly reducing disinfection rates in some photochemical processes.[28,57] High DO levels in chloraminated water can enhance the nitrification process. Nitrifying bacteria use DO as the electron acceptor to oxidise ammonia. This can result in a reduction of the monochloramine residual.

The redox environment of the treated water (which is partly determined by DO) can affect disinfectant stability. Highly oxygenated conditions can influence the disproportionation or side reactions of chlorine species. In cases like this, temperature and pH are the dominant factors.[58]

DO affects growth rates and physiology of bacteria present in water. Aerobic bacteria thrive in oxygen-rich environments, and anaerobic bacteria are inhibited or killed by oxygen. Oxygen gradients within biofilms influence metabolic activity. This makes biofilms more resistant in oxygen-rich zones due to extracellular polymeric substance (EPS) production.[2] DO also contributes to the measured ORP of water, which in turn affects the speciation and reactivity of many dissolved species. In some industrial systems, high DO levels promote corrosion, releasing metal ions that can react with or inactivate disinfectants.[59]

3. Disinfectants

In this section, disinfectants used in water treatments are discussed. The chemistry involved in the use of each of the disinfectants is briefly discussed. The most commonly used disinfectant is free chlorine. Monochloramine is becoming popular and currently second most popular for disinfecting drinking water due to its stability. Other disinfectants used in the disinfection of water are also included: such as potassium permanganate for its roles in iron and manganese control; ozone as a powerful disinfectant; peroxene and UV-peroxide as advanced oxidation pairs, chlorine dioxide for its pH-independent role, and hypobromous acid/hypobromite for its role in saline or high pH applications.

3.1. Free chlorine

Free chlorine (FC) is a powerful disinfectant for both primary disinfection at the plant and residual control in distribution system. In water it exists as hypochlorous acid (HOCl) and hypochlorite (OCl^-), with speciation governed by pH (at 25 °C).[60] As shown in figure 2, Cl_2 exists as a species of FC below pH 3.5. As a primary disinfectant, FC inactivates pathogens; as a residual, it suppresses their regrowth. The World Health Organization recommends maintaining about 0.5–5 mg L^{-1} FC in distribution systems since adequate oxidant levels curb biofilm formation and inhibit pathogen regrowth throughout the network.[11,61,62] . There are two ways to introduce free chlorine in water. One way is to add Cl_2 and the other is to add bleach in powder form $Ca(OCl)_2$ or as solution (NaOCl). Chlorine gas, when added to water, disproportionates into HOCl and HCl at pH above 3.

$$Cl_2 + H_2O \rightarrow HOCl + H^+ + Cl^- \qquad (11)$$

At high pH, HOCl partially dissociates into OCl^- and H^+.[63]

$$HOCl \rightarrow H^+ + OCl^- \quad pKa = 7.6 \qquad (12)$$

The following equation expresses the relationship of the concentrations of the two species with pH:

$$\log\frac{[OCl^-]}{[HOCl]} = \log K_a + pH \qquad (13)$$

The concentrations of HOCl and OCl^- in equilibrium are referred to as [HOCl] and [OCl^-] respectively. The ionization constant of HOCl is K_a, and at 25 °C, the pK_a is 7.54.[1,64–66] The amounts of HOCl at pH 6.5, 7.5, 8.5, and 9.5 are 91.5%, 55%, 11% and 1% of the free chlorine, respectively.[66]

HOCl penetrates cells and oxidizes sulfhydryl groups in enzymes, proteins, and nucleic acids; OCl^- is less membrane-permeant. [67] HOCl is the stronger oxidant (E° $HOCl/Cl^- \approx +1.49$ V vs. SHE) and far more potent than OCl^- (E° $OCl^-/Cl^- \approx +0.90$ V):

$$HOCl + H^+ + 2e^- \rightarrow Cl^- + H_20,\ \ E^0 = 1.49\,V \qquad (14)$$

$$OCl^- + H_20 + 2e^- \rightarrow Cl^- + 2OH^-, E^0 = 0.90\,V \qquad (15)$$

HOCl typically exhibits ~80–100 times higher killing rates for *E. coli* than OCl^- at the same temperature.[44,68–71] HOCl is particularly more effective due to its greater penetration ability to bacterial pathogen surface compared to its counterpart. Free chlorine is broadly effective for bacteria and many viruses.[72]

ORP rises with free chlorine dose and falls with pH. Cyanuric acid (CYA) is used in certain applications alongside FC to shield HOCl from UV photolysis. CYA binds with FC to form chlorinated isocyanurates. This lowers the activity of HOCl and hence the observed ORP.[45] FC can also be combined with UV in sequential approaches for specific pathogen prevention in drinking water distribution systems.[73]

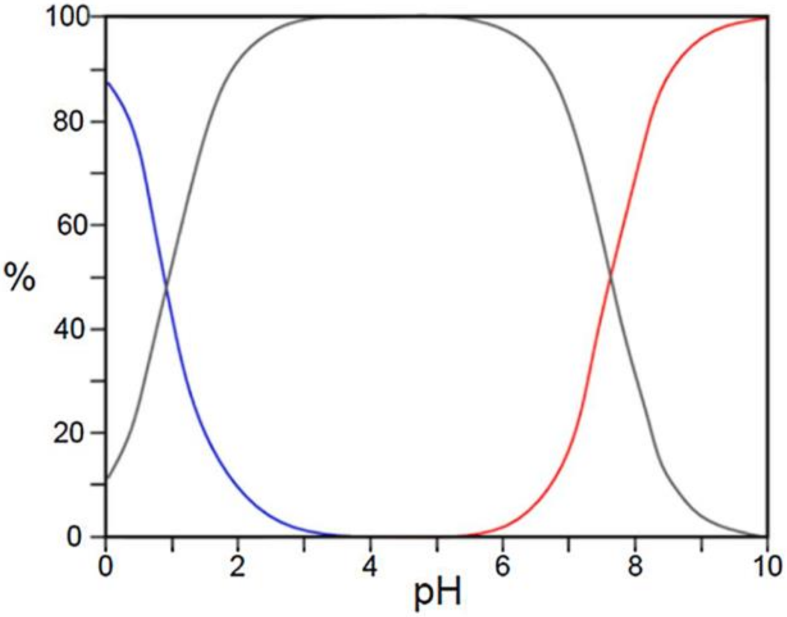

Figure 2.2 Distribution of residual chlorine as a function of pH. The grey line shows HOCl, the red line is OCl^- and the blue line is Cl_2. Reprinted with permission from Reference [74]; Copyright 2020 Elsevier.

3.2. Monochloramine

Two types of chloramines can be formed in water: organic and inorganic. As a result of treatment, three types of inorganic chloramines can be found in water which are monochloramine (NH_2Cl), dichloramine ($NHCl_2$), and trichloramine (NCl_3, also known as nitrogen trichloride).[75] Chloramines form either intentionally by adding ammonia to free chlorine, or unintentionally as a byproduct of chlorination when natural ammonia is present.[76]

Drinking water systems in Canada maintain a residual concentration of <4 mg/L of NH_2Cl, which covers the U.S. Environmental Protection Agency (EPA) regulated maximum value (4 mg/L) and the World Health Organization (WHO) guidance value (3 mg/L).[76]

The chloramines are formed in a series of competing reactions as shown in the equations:

$$NH_3 + HOCl \rightarrow NH_2Cl + H_2O \qquad (16)$$

$$NH_2Cl + HOCl \rightarrow NHCl_2 + H_2O \qquad (17)$$

$$NHCl_2 + HOCl \rightarrow NCl_3 + H_2O \qquad (18)$$

The type of chloramine species and their relative amounts depend on the pH of the solution, chlorine to ammonia weight ratio (Cl_2:N), temperature and contact time. NH_2Cl is the desirable disinfectant in water. It is dominating species when Cl_2: N is kept is less than 5:1. Figure 3 shows the concentrations of the different chloramines with respect to Cl_2: N. As the ratio increases, the NH_2Cl concentration increases up to a ratio of 5:1. When the Cl_2: N ratio is in the range of 5:1 to 7.6:1, $NHCl_2$ is formed. If the ratio goes above 7.6:1, NCl_3 starts to form in solution. Figure 3 explains the zones where each of the chloramines dominate as the ratio of Cl_2:N increases.[77] NH_2Cl is widely used as secondary disinfectant due to its stability and longer-lasting effect. NH_2Cl helps to lower the formation of DBPs in the distribution system due to its lower reactivity compared to FC. $NHCl_2$ and NCl_3 are undesirable because they cause strong, irritating odours and taste complaints.[76] They can also irritate eyes and the respiratory tract, and yield poorer, less stable disinfectant residuals than NH_2Cl.[78] NCl_3 is volatile and can impact air quality by forming aerosols around basins.[79]

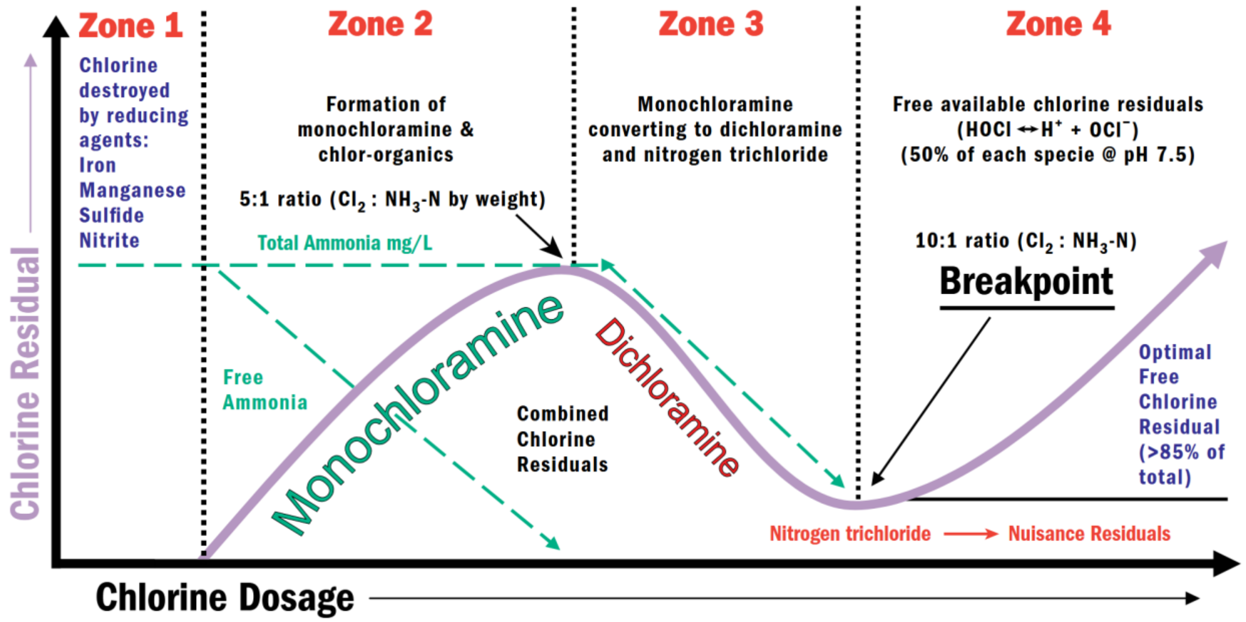

Figure 2.3 Illustration of breakpoint chlorination curve. Breakpoint chlorination progresses through four zones. In Zone 1, the initial chlorine dose is largely consumed by reducing agents (e.g., Fe^{2+}, Mn^{2+}, H_2S, NO_2^-), so little or no residual forms. In Zone 2, added chlorine reacts with available ammonia and reactive organics to build a maximum monochloramine residual while uncombined (free) ammonia is driven toward zero. In Zone 3, further chlorination converts monochloramine to dichloramine and nitrogen trichloride; the total combined chloramine residual falls as the system approaches the breakpoint, where ammonia is essentially exhausted. In Zone 4, a true free chlorine residual develops (typically least odorous when ≥ ~85% of total chlorine is free) though small nuisance combined residuals may persist, and the potential for disinfection by-product formation remains as free chlorine increases. Reprinted with permission from Reference [77]; Copyright 2008 American Water Works Association (AWWA).

3.3. Chlorine dioxide

Chlorine dioxide (ClO_2) is a powerful disinfectant. ClO_2 is a small highly energetic molecule and sanitizes by oxidation without chlorinating the water. It is a free radical with the chlorine atom in a +4 oxidation state. ClO_2 can be kept stable in dilute aqueous solution in a closed container in the dark. It can react violently at high concentrations with the reducing agents present in water. ClO_2 can accept an electron to form chlorite (ClO_2^-). It can take up to five electrons during its complete reduction to form chloride. This makes it 2.5 times more effective than free chlorine on a molar capacity basis. Chlorite ions (ClO_2^-) are in a pH-dependent equilibrium with chlorous acid which has a pK_a of 1.8. Consequently, the dominant species over the entire acceptable pH range of drinking water would be the chlorite ion.[80,81]

$$\cdot ClO_2 + e^- \rightarrow ClO_2^- \qquad Eo = 0.954V \qquad (19)$$

$$ClO_2^- + 2H_2O + 4e^- \rightarrow Cl^- + 4OH^- \quad Eo = 0.76V \qquad (20)$$

$$ClO_3^- + H_2O + 2e^- \rightarrow ClO_2^- + 2OH^- \quad Eo = 0.33V \quad (21)$$

$$ClO_3^- + 2H^+ + e^- \rightarrow \cdot ClO_2 + H_2O \quad Eo = 1.152V \qquad (22)$$

In water, ClO_2 reacts with organic and inorganic materials. ClO_2 particularly targets electron-rich organic compounds such as phenols, amines (secondary and tertiary) and organic sulfides. It works better at a lower dose in applications such as controlling odor and taste-producing compounds and phenolic compounds.[26] It is also a potent disinfectant for removing viruses[82,83] and bacteria[84]. The maximum feed dose for ClO_2 in Canada is 1.2 mg/L (to keep chlorite/chlorate by-products within guidelines).[85]

ClO_2 has high solubility in water compared to free chlorine and remains in water as dissolved gas.[80,86] Despite its high solubility in water, it can be easily removed through aeration. Since it cannot be shipped due to its high reactivity, it is generated on site in the water using sodium chlorite ($NaClO_2$) as a precursor. $NaClO_2$ reacts with Cl_2(g), HOCl or HCl to produce ClO_2.[87]

Overall, ClO_2 is a better disinfectant than free chlorine and monochloramine in the inactivation of viruses. It can effectively oxidize Fe, Mn and sulfides and control taste and odour-causing compounds. The disinfection process is not affected by the pH. However, it requires on-site production, which requires appropriate safety controls and protection from light-driven decomposition.

3.4. Potassium permanganate

Potassium permanganate ($KMnO_4$) is an oxidizing agent, recognized for the application as disinfectant and deodorizer.[88] In water treatment plants $KMnO_4$ is utilized to control odor and taste of water. It is also used to remove color, prevent growth of microorganisms and to reduce manganese and iron concentrations.[89] It is also useful in reducing trihalomethane (THM) and commonly found disinfection by-products as it can be used as a precursor to oxidation and lowering the dosing concentration of other oxidizing agents.[4,80] Chlorine application in the treatment plant often comes in the downstream of the treatment plant while $KMnO_4$ is used at the beginning to control odor, taste, algae, etc. It is not desirable in tap water since it results in a pink color.[80]

Under acidic conditions, $KMnO_4$ is highly reactive and shows better disinfection power.[90] $KMnO_4$ will oxidize a broad range of organic and inorganic materials. MnO_4^- is reduced to MnO_2 and precipitates out of the solution.[4] The half reactions under the acidic conditions are[91]:

$$MnO_4^- + 4\,H^+ + 3\,e^- \longrightarrow MnO_2 + 2\,H_2O \qquad (23)$$

$$MnO_4^- + 8\,H^+ + 5\,e^- \longrightarrow Mn^{2+} + 4\,H_2O \qquad (24)$$

The half reaction under basic conditions is:

$$MnO_4^- + 2\,H_2O + 3\,e^- \longrightarrow MnO_2 + 4\,OH^- \qquad (25)$$

Potassium permanganate inactivates microorganisms mainly by oxidizing critical cell components and disrupting key enzymes. In practice, MnO_4^- is a broad-spectrum disinfectant and can attack bacteria, fungi, viruses, and algae through direct oxidation of cellular material.[92] When $KMnO_4$ is applied, it is reduced to insoluble MnO_2. This freshly formed MnO_2 provides a second, physical route for microorganism removal. The microbes and other particles can adsorb onto MnO_2 surfaces and then be removed by settling or filtration. In colloidal form, the MnO_2 surface has –OH groups that can bind charged species (and even some neutral molecules), thereby increasing capture of microorganisms as the precipitate forms.[93,94] Higher temperature accelerates the deactivation of pathogens such as polio virus and *E. coli.*[94,95]

Overall, $KMnO_4$ is easy to use, store, and transport. It is an effective oxidizer for manganese and iron; odor and taste causing compounds; and inorganic and organic matter. It has been demonstrated to control nuisance organisms and killing viruses. Permanganate treatment has little impact on the other treatment processes that can be employed in the treatment plant.[80] Despite a lot of merits, MnO_4^- requires longer contact time in the treatment and it gives a pink color which is not desirable in drinking water.[80] In conventional plants, the excess MnO_4^- is monitored by observing the pink color and corrected by making sure all MnO_4^- are reduced to solid MnO_2. The MnO_2 solids accumulate (in reducing condition) in filter backwash water and in the settling basin for removal.[80]

3.5. Ozone

Ozone is a powerful oxidant and disinfectant widely used in water treatment. At room temperature, it is a colorless (but highly corrosive and toxic) gas with a sharp, distinctive odor that can be detected at very low concentrations (0.02 to 0.05 mg/L by volume).[96] The two mechanisms through which ozone can react are direct oxidation reaction by the molecular ozone and indirect reaction by hydroxyl radicals.[80,97] Both mechanisms generate different oxidation products.[98] It is produced by reacting an oxygen molecule with an oxygen atom. This reaction is endothermic, and a considerable amount of energy is required. Corona discharge is a common method to produce ozone. This method is also referred to as silent electrical discharge. Briefly, oxygen gas is passed through a channel where two electrodes are separated by a dielectric and a discharge gap. A voltage is applied between the electrodes to generate an electron flow. The electrons break down the oxygen molecules to eventually produce ozone molecules which decompose back to molecular oxygen with a half-life of about 10-80 minutes. The decomposition process is dependent on the pH and temperature of the solution. In bromide-containing waters, ozonation first forms $HOBr/OBr^-$ and can proceed to bromate.[3] Process control (pH, H_2O_2, AOC management) is necessary to limit bromate formation.

3.6. Peroxene

Peroxene is a mixture of ozone and hydrogen peroxide that generates high concentrations of hydroxyl radicals (•OH). Adding H_2O_2 to ozonated water accelerates ozone decomposition and boosts •OH formation. The peroxene process differs from ozonation in that peroxene relies primarily on •OH as the oxidant.[80]

Two concurrent pathways govern oxidation by peroxene: first, via the direct oxidation by ozone in the water and second, oxidation by hydroxyl radicals, which are produced through the dissociation of ozone. These two competing reactions occur for the oxidation of compounds in water. Direct oxidation by molecular ozone is relatively slow, even when the ozone concentration is high. In contrast, reactions with hydroxyl radicals (•OH) are very fast, so despite their low concentration, they can dominate when •OH is generated.[99]

The ozone concentration depletes quickly since peroxide greatly increases the decomposition of ozone. The rapid depletion of ozone is outweighed by the more reactive hydroxyl radicals. Hydroxyl radicals have a higher oxidation potential (+2.8 volts) compared to ozone (+2.07 in pH below 7, +1.24 in pH above 7).

$$\cdot OH + e^- \rightarrow OH^- \quad E_0 = +2.08 \qquad (26)$$

$$O_3 + 2H^+ + 2e^- \rightarrow O_2 + H_2O \quad E_0 = +2.07 \qquad (27)$$

$$O_3 + H_2O + 2e^- \rightarrow O_2 + 2OH^- \quad E_0 = +1.14 \qquad (28)$$

Peroxene is effectively used in oxidizing organics which are not easy to oxidize, such as geosmin and 2-methylisoborneol (MIB), which are compounds that impart odor and taste.[80] It can also oxidize halogenated compounds like trichloroethylene, 1-chloropentane, 1,1-dichloropropene, and 1,2-dichloroethane.[100,101]

Overall, peroxene provides a reactive and faster oxidation process which can effectively oxidize difficult-to-treat organics that contribute to taste and odor related issues. Practical considerations remain: concentrated H_2O_2 is a strong oxidant with handling hazards that degrades in storage. Additionally, the rapid O_3 decay in peroxene means it does **not** provide a measurable disinfectant residual. Peroxene is not as effective in oxidizing iron and manganese as ozone alone.[80]

3.7. UV-peroxide

UV-H_2O_2 is an advanced oxidation process which uses ultraviolet (UV) light in combination with H_2O_2. The combination generates hydroxyl radicals (•OH), which are an extremely reactive species. Organic contaminants break down when exposed to hydroxyl radicals. H_2O_2 absorbs UV light at around 254 nm from low-pressure mercury lamps. The H_2O_2 molecules are split by the UV energy. The hydroxyl radicals oxidize contaminants and convert them to CO_2 and H_2O.[102]

$$H_2O_2 + \mathrm{h\nu} \rightarrow \quad 2 \cdot OH \qquad (29)$$

UV-H_2O_2 is advantageous over the UV-ozone system due to the higher solubility of H_2O_2 in water over the comparatively lower solubility of ozone. This results in larger amounts of hydroxyl radicals in water in a UV-H_2O_2 system than the UV-ozone system for an equal amount of energy provided to the system. High turbidity and nitrate in water can however affect the penetration of UV light in the contaminated water. Additionally, the tubes can be fouled due to scaling. To ensure a high yield of hydroxyl radicals, residual H_2O_2 may need to be removed since H_2O_2 can consume hydroxyl radicals and exert a chlorine demand. In drinking water treatment systems, UV-H_2O_2 is used to destroy trace contaminants like pesticides, pharmaceuticals, 1,4-dioxane, N-nitrosodimethylamine (NDMA), taste and odor.[103] Trojan Technologies has commercialized this type of advanced oxidation process.[104]

3.8. Hypobromite/ hypobromous acid

Hypobromite (OBr^-) is a bromine-based oxidizing agent. Hypobromite acts similar to hypochlorite (OCl^-) in water. It is often formed in water by adding bromide ions that go on to react with oxidants. Commonly free chlorine is used to produce hypobromite in water. When free chlorine reacts with bromide ions, hypobromous acid (HOBr) is produced.

$$Cl_2 + Br^- \rightarrow HOBr + Cl^- \qquad (30)$$

HOBr can then partially dissociate to produce hypobromite.

$$HOBr \Leftrightarrow OBr^{-} + H^{+} \qquad (31)$$

In a swimming pool environment, ozone-bromine treatment is used by introducing ozone to a highly concentrated bromide solution. The ozone and bromide reaction produces HOBr:[105]

$$O_3 + Br^{-} + H_2O \rightarrow HOBr + O_2 + OH^{-} \qquad (32)$$

The undissociated HOBr is the strongly biocidal form, and its fraction is governed by pH and pK_a. Because pK_a(HOBr) ≈ 8.6–8.7, at pH 8.5 HOBr is >50 % undissociated ($\alpha \approx 0.58$), whereas HOCl ($pK_a \approx 7.5$) is only ~9 % undissociated. Therefore, bromine retains higher biocidal potency at alkaline pH, making it attractive for high-pH cooling circuits and saline/marine waters.

The disinfection efficiency of ozone-bromine treatment is comparable to conventional hypochlorous acid procedures. While some research suggests brominated compounds can be more toxic than chlorinated compounds, in vitro testing found no increased toxicity in pool water disinfected with ozone-bromine.[106] Polycyclic aromatic hydrocarbons in the presence of hypobromous acid can generate emerging toxic byproducts in bromide-containing water during chlorination, which accounts for the occurrence of HPAHs and OPAHs in tap water and WWTP effluents. As bromide-containing water more closely simulates real-world conditions than HOCl only systems, the highly reactive HOBr poses new challenges to tracing pollutant transformation and discovering novel DBPs.[107] Brominated pools/spas experience fewer chloramine-related complaints while still meeting the same residual (≈ 1–$3\ \mathrm{mg\,L^{-1}}$ as Br_2). OBr^{-} disinfection is particularly useful where alkaline pH, ammonia, seawater salinity or intense biofouling pressure reduce chlorine's efficacy. Its fast kill kinetics and stable bromamine residuals make it the oxidant of choice for most cooling-water, recreational-water and marine applications.[108–110]

4. Areas of Application

This section discusses how disinfectant chemistry is put into practice across a number of applications. In drinking water, primary disinfection delivers a high degree of pathogen inactivation at the plant, and secondary disinfection provides a protective residual throughout the distribution system. Industrial and cooling-water programs emphasize biofouling control and materials compatibility under variable loading, pH, and temperature. Recreational waters such as swimming pools must balance pathogen control with user (bather) comfort. By-products need to be minimized under sunlight high-organic conditions. Wastewater disinfection is important to monitor due to variable quality and short contact times.

4.1. Primary disinfectants for drinking water

The term "primary disinfectant" refers to disinfectants deployed in water treatment plants to kill or inactivate microorganisms (mainly human pathogens) that are present in water. Primary disinfectants provide rapid and effective disinfection in the initial water treatment process. This disinfection is carried out entirely at the water treatment facility.[111]

Free chlorine, in the form of HOCl, is a very strong disinfectant that can inactivate a wide range of pathogens. Not only is it suitable for primary disinfection, but it also leaves a protective residual in water supply systems (secondary disinfection).[112] However, if the incoming water has ammonia or other nitrogen-containing compounds, and free chlorine is the intended secondary disinfectant, operators should make sure that a minimum of 80% of the total chlorine residual is free chlorine after primary disinfection. In the event of using breakpoint chlorination to remove raw water ammonia, the reaction should be allowed to go to completion before the water is discharged from the disinfection system. Any excess ammonia, otherwise, may initiate other chemical reactions in the distribution system, quickly consuming the chlorine residual and exposing the water to contamination.[111]

Chlorine dioxide, however, must be produced on site, usually by reacting sodium chlorite with chlorine gas, hypochlorous acid, or hydrochloric acid. Alternatively, it is produced electrochemically. The disinfectant is very effective, even more so than chlorine—though not quite as effective as ozone. Furthermore, any chlorine dioxide remaining after initial disinfection can be utilized to provide residual disinfectant levels in sections (or the entirety) of the distribution system.[111]

Ozone is an effective disinfectant as well, created on-site through the electrical charging of dry air or oxygen. Although very effective for microbial inactivation, it has no residual and thus is not suitable for application in maintaining disinfection in distribution pipes. In the absence of some secondary disinfectant (such as chloramines or chlorine dioxide), biofilm growth in the system can be a problem. To counteract this, a biofiltration step is normally suggested following ozone treatment to inhibit microbial regrowth.[111]

Ultraviolet (UV) light can be used as a primary disinfection method. Not all UV reactors, however, are created equal—to be qualified, one specific model will need to show that it is able to achieve the necessary levels of disinfection. This is achieved through testing by biodosimetry with MS-2 bacteriophage or Bacillus subtilis spores in a bid to determine maximum flow rates at various levels of UV transmittance while attaining the intended dose. If the UV technology in question does not utilize the 254 nm wavelength (which approximates the optimal germicidal range of 260-265 nm), certification becomes more complicated. In that situation, then the actual delivered dose must be confirmed by real-world biodosimetry testing. The results would then need to be calculated as an equivalent 254 nm UV dose for proper comparison.[111]

Disinfection monitoring ensures water safety by continuous or daily testing, depending on system type. Municipal residential systems are required to utilize real-time monitoring with alarms, and non-municipal systems that do not have the capability utilize daily grab samples. Free chlorine systems have analyzers that sample at the end of each stage of disinfection (before addition of post-treatment chemicals) and must be correctly calibrated (±0.05 mg/L below 1.0 mg/L or ±5% above). Chlorine dioxide systems have the same installation guidelines but require periodic testing for chlorite/chlorate byproducts. Monochloramine monitoring is the same as free chlorine practices, with the additional test for total chloramines. UV systems are constantly ensuring 254 nm-equivalent dose delivery with failure alarms that are required, and sensors require regular calibration, of particular significance for surface water or groundwater under surface influence. [111]

4.2. Secondary disinfectants for drinking water

Secondary disinfection gives a residual protective disinfectant in water distribution systems. This is done to avoid microbial recontamination, manage biofilm growth, and give an early indication of system breakthrough. Only chlorine, chlorine dioxide, and monochloramine offer this residual disinfection. Regulation stipulates minimum residual concentrations to be held at all points of daily water flow: free chlorine (≥0.05 mg/L at pH ≤8.5), chlorine dioxide (≥0.05 mg/L), or monochloramine (≥0.25 mg/L as combined chlorine). The maximum residual concentrations are 4.0 mg/L for free chlorine, 0.8 mg/L for chlorine dioxide, and 3.0 mg/L for combined chlorine. Minimum targets include 0.2 mg/L free chlorine (pH ≤8.5) or 1.0 mg/L monochloramine for the purpose of effective suppression of bacterial activity - more so nitrification in chloraminated systems. Total chlorine only measurements are a good representation of the combined residual in properly balanced chloramine systems because no free chlorine should be measurable. Monochloramine is a relatively weak disinfectant and, as such, not an acceptable primary disinfectant for most uses. This is because at typical concentrations, it takes too long an exposure time to achieve satisfactory disinfection. But, as it has the ability to remain in water systems, it is often applied as a secondary disinfectant to maintain a steady chlorine residual in the distribution system. When utilized for secondary disinfection, the sequence of addition of chlorine and ammonia does not influence the development of combined chlorine residual. As long as the ratios are correct and mixing is carried out immediately, the chemicals can be added in any sequence or even all at the same time. [111]These residual maintenance strategies provide protection of water quality with optimum operational effectiveness and regulatory compliance all along the distribution system. [111]

4.3. Disinfectants for industrial water, cooling water loops

Bromine in various chemical forms is being commonly applied in industrial water systems like cooling towers and fountains. In these systems, hypobromite can be formed as a secondary oxidant when chlorine or ozone reacts with naturally occurring bromide ions in the water, particularly in seawater.
This renders it of extremely high significance for critical industrial processes like desalination operations, ballast water treatment in vessels, and the continuous running of cooling towers. Electrochemical disinfection systems that efficiently generate hypobromite in situ are finding increasingly broad application in industrial water treatment and ballast water treatment in the shipping industry. Electrochemical systems are known to be very efficient and suitable for large capacities, providing a safe and effective method of disinfecting water.

Microbial control in recirculating cooling water systems is essential to prevent a wide range of serious problems, including the increased risk of Legionnaires' disease, physical blockages due to microbial growth, corrosion under biological masses, and heat exchanger inefficiency. In these applications, biocides like hypobromite play a very significant role in maintaining system integrity and operational efficiency.

4.4. Swimming pools

Swimming pool disinfection is essential for the protection of bathers from pathogens that are water-borne and aerosol-borne. Additionally, it is important to keep the chemical by-products within the safe limit. Commonly free chlorine is used to disinfect the swimming pool water as the primary disinfectant.[113] Often, liquid feed, tablets or gas form of free chlorine (sodium or calcium hypochlorite or onsite electro-generated) is used. The operational target is ≥ 1 mg L^{-1} free Cl_2 in pools and ≥ 3 mg L^{-1} in hot tubs/spas. It is recommended to raise to ≥ 2 mg L^{-1} when cyanuric acid (CYA) is present.[113] CYA is used in outdoor swimming pools as a chlorine stabilizer. CYA forms complexes with free chlorine to generate chlorinated isocyanurates which shield HOCl from UV photolysis.[114] This phenomenon reduces daytime free chlorine loss and chemical consumption. The same complexation lowers the activity of HOCl and depresses ORP; this slows down the pathogen inactivation and oxidation of bather wastes.[115] Hence the need for higher free-chlorine setpoint in the presence of CYA. Trichloroisocyanuric acid and sodium dichloroisocyanurate products inherently add CYA and can lead to seasonal accumulation. CYA is generally discouraged for spas/therapy pools and most indoor venues, and it complicates hyperchlorination responses (e.g., *Cryptosporidium*). Routine monitoring of both CYA and free chlorine is recommended to keep stabilizer within range and to interpret ORP correctly. In warmer water with higher pHs such as spas and therapy pools, HOBr/OBr- is used as primary disinfectant.[116] The operational target of bromine solution is ≥ 3 mg L^{-1} in pools, ≥ 4 mg L^{-1} in hot tubs. [116] Supplementary methods of disinfection that are used in pools include UV (UV-C, 254 nm), ozone, and AOPs (UV/H_2O_2, O_3/ H_2O_2). These methods require especial needs such as quenching before returning to the pool (ozone), or residual chlorine or bromine (UV). AOPs generate hydroxyl radicals that destroy organics and odor producing microorganisms. They are employed in pools where the waste load is high.[117]

Chloramines (mono-, di-, trichloramine) and trihalomethanes (THMs) form when free chlorine reacts with nitrogenous organics from sweat and urine that are released into the swimming pools. Trichloromethane (TCM), Trichloroacetic acid (TCAA) and Dichloroacetic acid (DCAA) are the most toxic DBPs that are formed in the indoor pools.[118] Managing the number of swimmers, free chlorine residual, disinfection strategy, total organic carbon, and water temperature can help curb DBP formation and the related health risks in the pools. [118]

4.5. Wastewater treatment

Waste-water treatment disinfection is the process step (typically following primary settling and secondary biological treatment) during which a physical or chemical agent is used to inactivate disease-causing microbes that are still present in the clarified effluent. Disinfectants destroy fecal bacteria, viruses and protozoan cysts present in wastewater. Treatment helps ensure the plant is in compliance with regulatory microbial limits (e.g., geometric mean ≤126 CFU E. coli 100 mL^{-1} on many North-American permits).[119] Free chlorine is widely used in wastewater treatment. Typical secondary-effluent doses are 5–20 mg/L. The real design driver is CT = C×T (concentration × contact time) and many reuse rules specify minimum CT benchmarks (e.g., CT ≥ 450 mg·min/L for filtered effluent). After chlorination, facilities often dechlorinate to protect aquatic life.[120] UV is a very common disinfectant for plants with good effluent clarity. UV delivers high inactivation of bacteria/viruses and Cryptosporidium/Giardia without forming chlorinated DBPs, but it leaves no residual. Design is based on UV dose (mJ/cm²) and wastewater systems commonly target ~30–100 mJ/cm². Low UV transmittance (UVT), high TSS, and lamp fouling reduce delivered dose.[7,121,122] Ozone is also used where advanced oxidation or reuse goals overlap. However, utilities must control bromate formation when bromide is present. This disinfection process also requires off-gas destruction and careful mass transfer design.[123]

5. Operating Principles of Sensors

Effective monitoring of disinfectants is mainly achieved by one of three distinct means: optical, electrochemical, and electrical sensors. Each method has distinct trade-offs for speed, selectivity, and maintenance. Optical methods (colorimetry, fluorescence) are traceable and sensitive with simple readouts but rely on reagents and can be biased by interferences. Electrochemical approaches (potentiometry, voltammetry, amperometry) are fast and reagent-free. However, they depend on stable reference electrodes which are vulnerable to fouling and cross-reactions. Electrical sensors (chemiresistors and solution-gated FETs) offer compact, low-power, networkable nodes. Their limiting factors are long-term stability and selectivity in complex matrices. The following subsections discuss these methods in more detail along with recently reported approaches to detect and monitor disinfectants.

5.1. Optical sensors

5.1.1. Colorimetric

Colorimetric sensing converts an analyte-driven chemical reaction into a visible color change of a reagent (dye, chromophore, or nanoparticle) in the measurement zone. That change in absorbance or ΔRGB from images of the reagent pad, cuvette, or microfluidic channel is quantified to determine concentration of the analyte. Often an aromatic amine such as N,N-diethyl-p-phenylenediamine (DPD) or 3,3′-dimethylbenzidine (orthotolidine), a π-conjugated dye like 3,3′,5,5′-tetramethylbenzidine (TMB) or 2,2′-azino-bis(3-ethylbenzothiazoline-6-sulfonic acid) (ABTS), or even a plasmonic nanoparticle are used as a colour-forming reagent to react with the disinfectant either stoichiometrically or through catalysis. This interaction changes the dye's electronic structure and, in turn, its molar absorptivity at a specific wavelength. According to the Beer Lambert law $A = \varepsilon bc$, absorbance A (unitless) equals the molar absorptivity ε ($L \cdot mol^{-1} \cdot cm^{-1}$) times the optical path length b (cm) times the analyte concentration c ($mol \cdot L^{-1}$). In a camera or other readout systems, the observed color change, often summarized as ΔRGB, tracks absorbance because $A = \log_{10}(I_0/I)$, so channel intensity decreases as concentration increases. With fixed illumination and path length, a calibration converts ΔRGB (or a single channel such as G) to absorbance and yields a linear concentration response over a defined range. Outside that range, deviations can arise from stray light, turbidity and scattering, reagent depletion, or detector saturation, so the method should report the usable linear interval and the limit of detection. Because most disinfectants are potent oxidants, they quickly oxidise these chromophores or activate peroxidase-like nanozymes, allowing rapid, low-cost measurements easily captured by smartphone cameras or simple photodiodes.[12,13]

5.1.2. Fluorescence

The fluorescence detection method uses reagents like the colorimetric methods and additionally requires sophisticated instruments to capture fluorescence. Fluorescence sensors convert a chemical reaction with the target oxidant into a light signal. A fluorescent probe is transformed into a strongly fluorescent product (turn-on), or a bright dye is quenched (turn-off). In the case of FC, molecular designs typically exploit hypochlorous acid's (HOCl/ClO$^-$) strong electrophilic/oxidizing character to cleave or oxidize protecting groups, restore conjugation, or suppress intramolecular charge transfer. Similar strategies have also been demonstrated for H_2O_2. These mechanisms enable high sensitivity and fast response suitable for tracking disinfectants at sub-micromolar to micromolar levels.

Table 2.4 Optical sensors

Material	Disinfectant	Parameters/note	References
Colorimetric			
Starch-stabilized silver nanoprisms (AgNPrs)	H_2O_2	1.57 µM can be recognized by naked-eye; good accuracy, stability and reproducibility.	[124]
DPD	FC	linear range of 0.8–14 µM and LoD of 0.23 µM.	[125]
Azobenzene acid	FC		[126]
DPD	FC	0.7 -56 µmoll^{-1}; effective approach when interference chemical (Fe^{3+}) is present; PLS has been employed to increase selectivity	
Fenton-DPD method	H_2O_2	0-12 µM; LoD 0.05 µM; Oxidative coloration reaction of DPD via Fenton reactions	[127]
PBA and ARS complex	H_2O_2	50 – 500 µM	[128]
LGB and HRP	ClO_2	0.25 to 1.8 mgL^{-1}	[129]
Fluorescence			

GQDs	FC	0.05 to 10 µM; LoD 0.05 µM	130
	FC	LoD 37.56 nM, rapid response time (<30 s); 6-(2-benzothiazolyl)-2-naphthol as the fluorophore and N,N-dimethylthiocarbamate as the recognition group	131
Carbazole	MnO_4^-		132
BPCN-SSPy	FC		133.
GQDs	FC	0.5 µM to 1.0 mM; LoD 0.3 µM	134
CS, PVA, and TPA	H_2O_2	LoD of 0.1 µM and LoQ of 0.33 µM	135
Rhodamine S	ClO_2	0.0060–0.450 µgmL^{-1}; LoD of 0.0030 µgmL^{-1}.	136

GQDs = graphene quantum dots, Zn(Hmim)$_2$, DPD = *N*,*N*-diethyl-*p*-phenylenediamine, PBA= phenylboronic acid, ARS = Alizarin Red S, LGB = lissamine green B, HRP = horseradish peroxidase, CS = chitosan, PVA = polyvinyl alcohol, TPA = terephthalic acid,

5.2. Electrochemical sensors

Electrochemical sensors are commonly used for the detection of redox active analytes. These sensors transduce redox processes at electrodes into measurable potentials or currents. Electrochemical techniques such as potentiometry, voltammetry, and amperometry have been used to measure disinfectants in water. Depending on the technique, they may use two electrodes (e.g., potentiometric: indicator and reference) or three electrodes (e.g., amperometry/voltammetry: working, reference, counter) for potential control.

For reliable, continuous use, the reference electrode must remain stable over long periods to minimize recalibration, be durable enough for repeated use, and tolerate the complex chemistry of real water samples. Meeting all three requirements (stability, reusability, and broad chemical compatibility) is a central challenge. Additionally, the fabrication process of the reference electrode needs to be simple and cost effective. Commonly used reference electrodes are the saturated calomel electrode (SCE, Hg/Hg_2Cl_2), the standard hydrogen electrode (SHE, $H_2/H^+|Pt$), and the silver/silver chloride (Ag/AgCl) electrode. According to the Nernst equation, the oxidation-reduction potential (ORP) of the solution depends on the concentrations of the chemicals participating in the reaction. The reference electrodes depend on maintaining a steady concentration of the participating species to generate a constant electrochemical potential.

5.2.1. Voltammetry

Voltammetric measurements require three electrodes (working, counter and reference) in the solution. An electrical potential is applied between the counter electrode and the working electrode until the potential difference between reference electrode and working electrode reaches a set value. The resulting current flowing through the counter and working electrodes is measured over time. As the potential of the working electrode relative to the reference electrode is swept from a negative to a positive value, depending on the oxidation or reduction reaction that takes place at the working electrode, an oxidation (positive current) peak or a reduction (negative current) peak will occur at a specific voltage. Both, LSV and CV work by sweeping the voltage linearly, however, in the case of CV the voltage reverses back to the starting point in a cyclic manner. The peaks generated from this technique can be used for the quantification of the analyte by integrating the current measured as a measure of charge transferred (ignoring side reactions). The analyte species are characterized by locating the peaks at their characteristic voltages.

5.2.2. Amperometry

Amperometry measurements are carried out by three electrode systems where the potential at the working electrode is maintained at a constant value (relative to the reference electrode) while the current flows between the working and counter electrodes. The current measured from this method is the result of the disinfectants undergoing an electrochemical reduction reaction. The potential that needs to be applied is decided based on the peak identified in the voltametric analysis. A specific potential is fixed on the working electrode with respect to the reference electrode. Pt, Au or carbon-based working electrodes are often used. The current generated during the measurement can be directly correlated to the bulk concentration of the disinfectant. Amperometry can be used to identify electroactive redox species by employing different electrode materials at specific potentials identified by voltametric methods. To avoid interfering ions that may be reduced around similar potentials as the redox species, the potential needs to be carefully selected. One problem that arises from amperometric sensing of free chlorine is that the electrode surface may adsorb the products that are formed after the reduction takes place. This results in sensitivity loss over time. Depending on the movement of the solution, amperometric methods can be categorized as chronoamperometry and hydrodynamic amperometry. In the chronoamperometric methods, the solution does not need to be stirred, whereas in hydrodynamic amperometry, the solution is stirred.

5.2.3. Potentiometry

Standard potentiometric measurements involve a working electrode made of materials that are sensitive the analyte and a reference electrode. Commonly, Ag/AgCl is used as a reference electrode. In a solution, the circuit potential of working and reference electrode linearly correlates to the log concentration of the analyte species in the solution. Potentiometric sensors measure disinfectants such as free chlorine by a buffered iron solution. The potential change due to the reduction reaction of free chlorine and iron ion is measured in this type of method. Since using an iron ion buffer is challenging this method did not become as popular as the DPD-based colorimetric methods.[137,138]

Electrochemical techniques suffer from the fact that their working electrodes, usually noble metals like platinum (Pt) and gold (Au), can become poisoned on the surface, e.g., by manganese salt depositions. This may lead to the generation of electrochemically active surface oxides, destabilizing the measured signals.[139,140] Table 5 lists the electrochemical sensors reported for disinfectant sensing.

Table 2.5 Electrochemical sensors.

Material	Disinfectant	Parameters	References
Voltammetric			
Gold electrode	FC	1 mg/L to 5 mg/L; LoD of 0.04 mg/L	141
Boron-doped diamond	O_3 and FC	Simultaneous detection of O_3 (3 mg/L) and FC (100 mg/L)	142
PdNPs, p1,5-DAN, CPE	H_2O_2	detecting hydrogen peroxide (H2O2) with linear ranges of 0.1 to 250 μM and 0.2 to 300 μM as well as detection limits (S/N = 3) of 1.0 and 5.0 nM	143
Cl microelectrode	NH_2Cl	(0.1–30.0 mg Cl_2/L) at an applied potential of +550 mV	144
Zeolite modified CPE	MnO_4^-	35 to 80 nmol/L; LoD of 0.40 nmol/L	145
Potentiometric			
Stainless steel vs. Pt	FC	Linear range (1 mg/L-10 mg/L)	146
Silver nanoparticles decorated on porous silicon	H_2O_2	1.65 μmol L^{-1}–0.5 mmol L^{-1}; LoD of 0.45 μmol L^{-1}.	147
Silicon-chip with Pt and Au	NH_2Cl	1 - 10 mg/L; LoD 0.03 mg/L; *in-situ* pH control to eliminate oxygen interference	148

Au interdigitated microelectrode array	FC	0.35-1.85 mg/L; *in-situ* pH control	[149]
Au, Pt, and carbon fiber microelectrode	NH_2Cl	(0–4.2 mg Cl2/L); no DO interference for Au and Pt	[150]
Pt and Au electrode	NH_2Cl	Behavior of chloramine was studied	[151]
Amperometric			
Graphite (pencil trace)	FC	7-500 mg/L; LoD 6600 ppb	[152]
Free chlorine and total chlorine microelectrodes (5−10 µm tip size)	NH_2Cl	studied the fate/penetration of disinfectant	[153]
Carbon black	ClO_2	0.05–20 mg/L; LoD of 0.01 mg/L; screen-printed electrode	[154]
Glassy carbon	FC	0.009-10 range; 9ppb	[155]
Glassy carbon	FC	0.7-16 range; 3 ppb	[156]
Graphite (pencil trace)	FC	0.4-6 range; 400 ppb	[157]
Asparagine-GO	FC	0 – 8 mg/L	[158]
Pt and glassy carbon	ClO_2	Measured over pH range 2-10	[159]

FC = free chlorine, p1,5-DAN = Poly 1,5-Diaminonaphthalene, PdNPs = palladium nanoparticles, CPE = carbon paste electrode, GO = graphene oxide.

5.3. Electrical sensors

Electrical sensors are semiconductor device-based platforms that have emerged as a popular choice for chemical and biological sensing. Their sensing capability comes from the ability to transduce physical and chemical interactions that take place near or at their gate surface.[160] These sensors are simple in design and robust in operation in a continuous format. Furthermore, chemiresistors provide an advantage of detecting analytes without the reference electrode, and field effect transistors have high sensitivities in detection.[10]

5.3.1. Field effect transistors

Field effect transistor (FET) based sensors can detect an analyte by its effect on the electric field at the gate. When chemicals interact with the gate, the electric field changes which then modulates the conductivity of the channel. The conductivity change is measured as signal.[161] When a positive electric field is applied it attracts electrons and repulses holes. In a p-type materials (where holes are the majority charge carriers), the positive field repulses holes and leaves fewer charge carriers, therefore the conductivity of the channel decreases. In an n-type material (electrons as the majority charge carrier), a positive field attracts more electrons into the channel, thus increasing the conductivity. Operationally, a FET sensor combines a sensor and an amplifier.[161] A minor change in the potential can cause a significant change in the channel's current.[162] This effect is like applying an external voltage to gate electrode of a standard FET device where electrical conductivity changes in real time. This change in conductivity corresponds to the presence of the analyte.[162] FETs are advantageous since they can be integrated with standard electronics and high sensitivity. However, they are more complex to build compared to chemiresistors.[10] In the case of back gated FETs, the gate is built into the substrate. Often the gate is made of silicon with a layer of dielectric silicon dioxide (SiO_2) which electrically insulates it from the channel. In solution-gated FETs, a reference electrode is used to apply the gate voltage through the solution.[18]

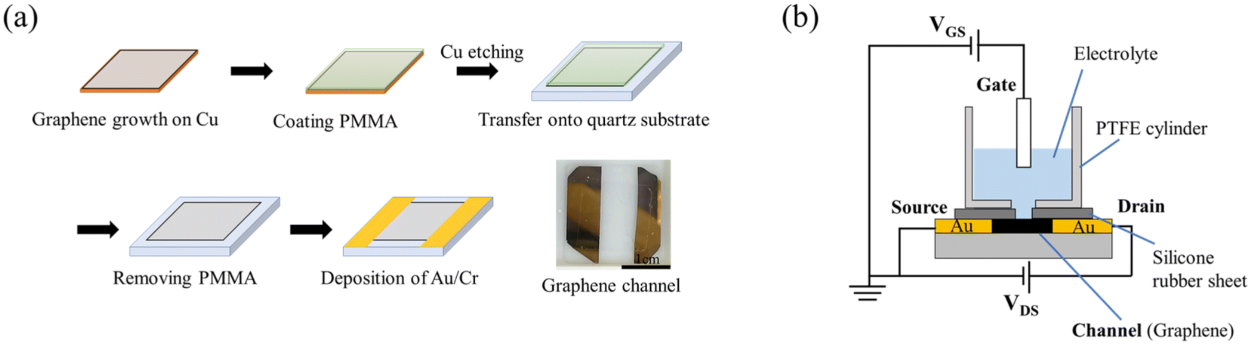

Figure 2.4 (a) Fabrication of graphene film for FET on a Cu Substrate using CVD. (b) Schematic diagram of a solution gated graphene FET. Reprinted with permission from Reference [140]; Copyright 2024 Royal Society of Chemical (RSC).

All FET-based free chlorine sensors reported in the literature are solution-gated FETs prepared using single layer graphene. Table 6 shows the FET based disinfectant sensors that were reported in the literature. Typically, conductive channel fabrication of FET sensors is a multistep process as shown in figure 2.4a. The monolayer graphene is deposited using chemical vapor deposition (CVD) which yields precise growth of graphene. The final channel has a length of 7.5 mm and a width of 15 mm.[140] Figure 2.4b shows a schematic of a graphene FET sensor. Ag/AgCl is a common gate electrode used for the free chlorine sensing using graphene based FETs.[163,164] Sugawara et al. systematically studied the impact of the gate electrode in the measurement of free chlorine, and compared the effects of gold, boron-doped diamond (BDD) and graphene.[140] They concluded that gate electrodes with lower surface redox activity can produce the best sensors. In this case, they found that FET devices with graphene and BDD had lower limits of detection (LoD) compared to the Au electrodes.

Figure 2.5a presents the transfer characteristics (drain-source current I_{DS} versus gate-source voltage V_{GS}) collected from the graphene channel with a gold gate electrode. I_{DS} is the electrical current flowing through the transistor channel from drain to source when a small, fixed drain–source voltage (V_{DS}) is applied. I_{DS} is the output that gets measured. V_{GS} is the control voltage applied to the gate relative to the source. The observed ambipolar behavior in all curves demonstrates continuous modulation of charge carriers in graphene from hole-dominated to electron-dominated conduction through field-effect control.[140] Using the gate to source voltage ($V_{GS)}$ values for similar transfer curves, a schematic representation of graphene's electronic states has been shown in figure 2.5b. [140] Different concentrations of NaClO were then analyzed for the corresponding $V_{GS.}$ [140] At the Dirac point, graphene's valence and conduction bands meet with no band gap. At the Dirac point, the number of charge carriers is at minimum, and the current in the graphene channel would be the lowest.[165] The Dirac point voltage (V_{DP}) increases significantly from 0.09 V to 0.70 V for concentration changes from 0 to 5 mg/L of NaClO. [140] Therefore it has been demonstrated that free chlorine can modulate the graphene Dirac point and V_{DP} shows concentration dependent shifts. [140]

Figure 2.5c shows graphene-based FET's free chlorine selectivity over the commonly found ions in water. The device demonstrated exceptional selectivity for hypochlorite ions (ClO^-), with a normalized current response (NCR) of 1.21±0.21 to just 0.71 mg/L as free chlorine. Common interfering ions at 100 times higher concentrations (1 mM) produced negligible responses: chloride (Cl^-), nitrate (NO_3^-), sulfate (SO_4^{2-}), and ammonium (NH_4^+) showed NCR values below -0.0063; 200 times weaker than the ClO^- response. Phosphate (PO_4^{3-}) and carbonate (CO_3^{2-}) showed slightly higher interference (NCR = -0.0078 to -0.014), but still 100 times smaller than for ClO^-. Calcium ions (Ca^{2+}) produced the strongest interference (NCR = -0.0197), which was 60 times smaller than the hypochlorite response.[163] When these devices were tested for NaClO in tap water they showed excellent recovery rates ranging from 80% to 110% as shown in figure 5d. Therefore, the graphene-based FETs can be a great alternative to standard methods used for free chlorine measurements.

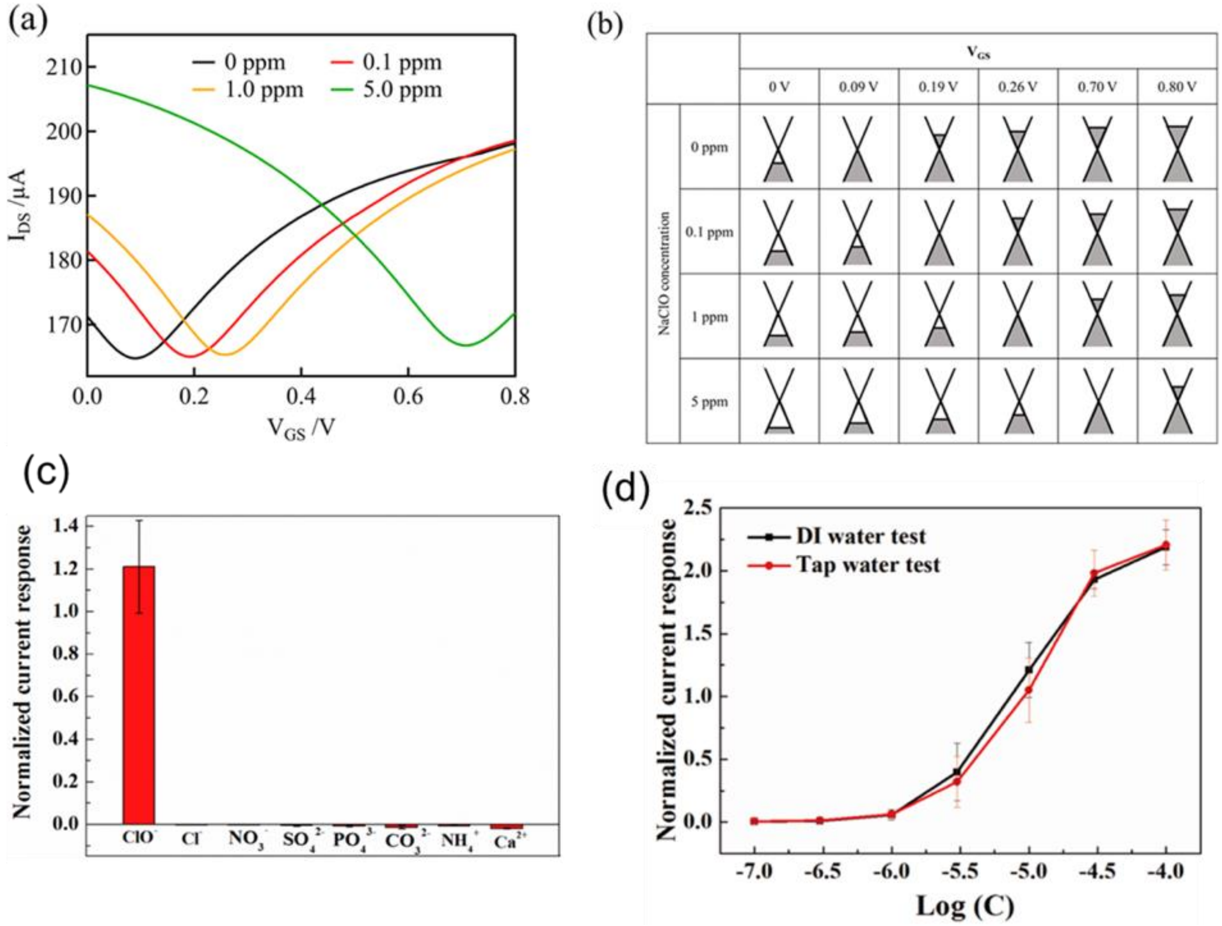

Figure 3.5 (a) Current-voltage characteristics of graphene FETs with Au gate electrodes measured for free chlorine levels (0 to 5 mg/L) in phosphate-buffered saline buffer (pH 7). **(b)** Diagram showing how graphene's electronic properties change with sodium hypochlorite (NaClO) concentration and applied gate voltage (V_{GS}). Reprinted with permission from Reference [140]; Copyright 2024 Royal Society of Chemical (RSC). **(c)** The sensor's current response to 10 μM hypochlorite (ClO^-) was compared with various interfering ions (1 mM each): chloride (Cl^-), nitrate (NO_3^-), sulfate (SO_4^{2-}), phosphate (PO_4^{3-}), carbonate (CO_3^{2-}), ammonium (NH_4^+), and calcium (Ca^{2+}). Standard deviation of 3 measurements was shown as error bar. **(d)** Normalized current response of sensors for a range of NaClO concentrations carried out in DI water and tap water. Standard deviation

of 3 measurements was shown as error bar. Reprinted with permission from Reference [163]; Copyright 2018 Elsevier.

FET sensors have been explored extensively as pH, heavy metals, and biosensors.[10,18,166] Even though it has been demonstrated that disinfectants such as free chlorine can be detected, other commonly used disinfectants, such as monochloramine or potassium permanganate have not been explored for this type of device. FET-based sensors show shorter device lifetime, and lower sensitivity and selectivity in complex media are the major challenges in FET-based monitoring[167]. An extended-gate geometry offers better durability (reduced fouling and corrosion) in continuous monitoring by spatially separating the sensing surface and the gate of the FET while keeping them electrically connected. The gate can thus be cleaned or replaced without impacting the electronics.[168] In the case of interfering redox species being present in the water, the response of the FET to free chlorine can be adjusted by tuning the gate electrode surface with free chlorine-sensitive species containing amine groups.[169,170] This addition has been demonstrated to stabilize the electrode potential and thereby decrease the variations in free chlorine responses.[140] Another approach that could be taken to enhance accuracy and robustness is a dual gate configuration with materials of different sensitivity. This will generate different signals, which could be used for multivariate analysis or machine learning. FET-based chlorine gas sensing[171] and hydrogen peroxide detection[172] for biosensing applications have not been discussed here.

Table 2.6 Field effect transistor (FET) sensors.

Material	Disinfectant	Parameters	References
Graphene	FC	0 to 5 mg/L	140
Graphene	FC	100 nM to 100 µM	163
MoS2/RGO, MoS_2	H_2O_2	LoD 1 pM,	166
Graphene	FC	0-29.3 mg/L	164

FC = free chlorine, RGO = reduced graphene oxide, MoS_2 = molybdenum disulfide

5.3.2. Chemiresistive sensors

Chemiresistors are solid-state electrical devices containing an active layer the conductivity of which changes upon interaction with an analyte. Typically, the active (conductive) layer of material is deposited in between two contacts (or electrodes), and the contacts are connected to a set of control electronics to generate a small bias potential across the layer while measuring the resulting current.[173] Other approaches are possible, including the use of an AC driving potential.[174] The change in the conductivity of the active layer is correlated with the concentration of the analyte. Chemiresistive sensors are often categorized according to the active layers used for fabrication. Common materials used for the active layer include semiconducting metal oxides[175–178], conducting polymers[179–182], metal nanoparticles[183–186], and carbon-based materials[18,187–189]. Their low cost, ease of device fabrication, and compatibility with conventional DC circuits make them very popular in gas sensing.[190,191]Although chemiresistive gas sensing has been demonstrated for more than fifty years, aqueous sensing is a relatively new area of research. There has been an increasing number of reports of chemiresistive sensors for detecting pH, ions, and disinfectants.[192–195] Figure 2.6a shows a fabrication schematic of a recently reported chemiresistive sensor. A glass microscope slide was used as a substrate where a conductive layer of single-walled carbon nanotube (SWCNT) was deposited, overlapping two pencil patches. Cu tapes were placed on the pencil contacts to facilitate the attachment of electrical components. The Cu contacts were finally masked with a dielectric material, such as polydimethylsiloxane (PDMS). Figure 2.6b shows a typical current vs time graph when sensors interact with chemicals. In this case, MnO_4^- was added to water and increasing sensor responses were achieved as SWCNT networks were hole-doped. This curve was further processed to create a calibration graph (Figure 2.6c) where the percent change (% change) sensor response was plotted against the concentration of MnO_4^- (mg/L).[196]

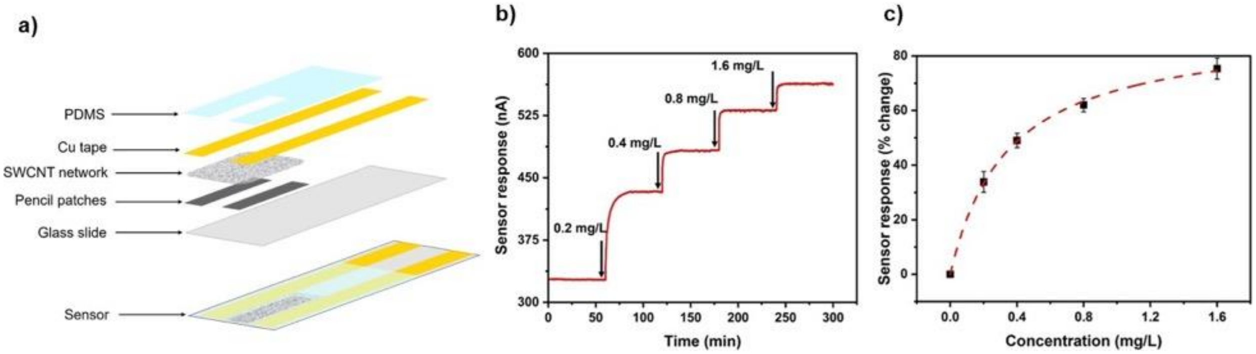

Figure 2.6 Fabrication and characterization of chemiresistive sensors. (a) Schematic of each of the basic components of the device (top) and the device geometry (bottom). (b) Characterization of chemiresistive device in permanganate (MnO_4^-) solution. Raw sensor response of a 15 kΩ resistance device as current change (nA) plotted against time (minutes) for the spiking of MnO_4^-. The arrow shows the points of MnO_4^- addition. 0.2 mg/L MnO_4^- was added in the background solution with 0 mg/L MnO_4^-. Other concentrations were added in the stirring sample. (c) Calibration graph of three devices as percent change (% change) sensor response plotted against concentration of MnO_4^- (mg/L). The dots show average values and error bars represent the standard deviation of the responses to corresponding concentrations. The dotted line is the Langmuir adsorption isotherm fit. The model parameters for the sensor are A = 90.53±1.82% and B = 2.92±0.17 $mg^{-1}L$ for an R^2 value of 0.99. Reprinted with permission from Reference [[196]]; Copyright 2025 American Chemical Society (ACS).

Four disinfectants that have been tested are free chlorine, hydrogen peroxide, potassium permanganate, and monochloramine. Table 7 tabulates the reports on the disinfectant sensors using this platform. One of the first reports on disinfectant chemiresistive sensors was carried out with a polypyrrole-multiwalled carbon nanotube (MWCNT) composite functionalized with dodecylbenzenesulfonate (DBS) for the detection of H_2O_2.[197] The simple design of chemiresistors attracted attention because it does not need a reference electrode and with the reversible dopant molecule, it can detect an analyte in a continuous manner. A number of chemiresistive H_2O_2 sensors have been introduced for the sole purpose of detecting biological analytes.[172] We reviewed only the studies for the application in water quality monitoring, unlike the disinfectant gas sensors reviewed in ref. 163. Free chlorine detection with a SWCNT substrate was reported utilizing the switchable doping behavior of molecules present in the functionalized semiconducting nanotubes.[198,199] Here, an aniline oligomer phenyl capped aniline tetramer (PCAT) was noncovalently adsorbed on a SWCNT network. When PCAT is oxidized by $HOCl/OCl^-$ some of the charges are removed from the network, resulting in an increase in conductivity of the PCAT-SWCNT network. The range of detection was reported from 0.06 mg/L to 60 mg/L of free chlorine with a thicker network (thickness of 100 μm). The thickness of the substrate plays a crucial role in the chemiresistive response. The response time and sensitivity of the device are improved with a thinner substrate. This is because analytes can diffuse through the thin film at a quicker rate than through a thicker film and thinner networks have fewer active spots where the analyte can interact.[10] Making the sensing film thinner shortens the time to reach equilibration because the analyte can diffuse more quickly into the sensing layer from the surrounding solution. When transport in the sensing layer is diffusion-limited, the characteristic response time scales with thickness squared ($t \propto L^2/D$). Here, t is the response time, L is the diffusion path length (in sensing film, L is the film thickness), and D is the diffusion coefficient of the analyte in the sensing layer.[200,201] Sparser, near-percolation-threshold networks also have fewer parallel paths, so small changes at a few junctions produce a larger overall resistance change (higher $\Delta R/R$).[202,203] Active sites in sparser networks are exposed to the solution rather than buried in the bulk, which increases the fraction of material that participates in sensing.[204] Together, these effects result quicker responses and higher sensitivity, though extremely thin films can become noisy or unstable, so there is an application-dependent optimum density A recent study optimized the SWCNT networks for chemiresistive sensors to accommodate a wide range of concentrations of MnO_4^- in water.[196] It was demonstrated that sparser network-based sensors detected low concentrations, while denser network-based sensors was able to detect higher concentrations.

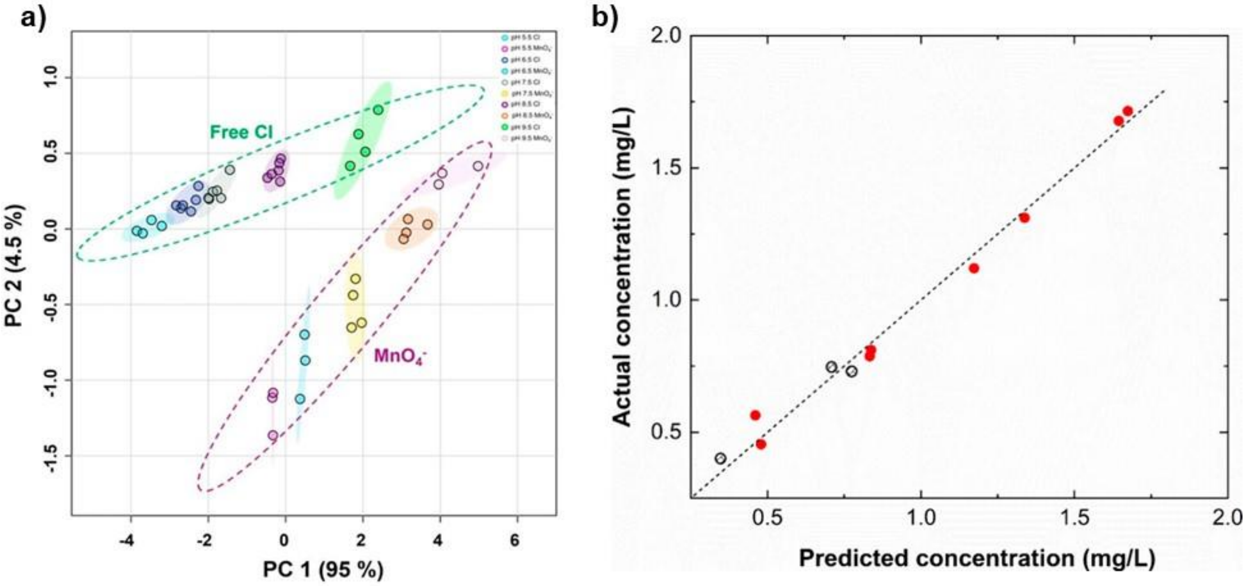

Figure 2.7 Chemometrics in chemiresistive sensing array. (**a)** Principal component analysis (PCA) of the sensor responses for 1 ppm of free chlorine (FC) and permanganate (MnO_4^-) in five pHs: 5.5, 6.5, 7.5, 8.5, and 9.5. The dotted regions represent FC and MnO_4^-. The colored regions inside represent the pH regions for the corresponding analyte. The colored ellipses characterize a 95% confidence level. Reprinted with permission from Reference [192]; Copyright 2023 American Chemical Society (ACS). **(b)** Regression graph from partial least squares (PLS) model showing the predicted concentration from the model and actual concentration measured by the DPD method. The solid red dots represent the training data set from the known spiking of monochloramine in tap water. The open circles represent the testing data set for three unknown tap water samples. The dashed line represents the ideal comparison line. The model parameters, R^2 and root mean squared error value using leave-one-out cross-validation (RMSELOOCV) method values are 0.99 and 0.012. Reprinted with permission from Reference [205]; Copyright 2024 American Chemical Society (ACS).

The devices are of particular interest where rapid prototyping is necessary because they are easy to fabricate. There are wide variety of techniques to incorporate sensing materials, in addition to the utilization of macroscale features, which makes this platform specifically useful for initial testing when material morphology has yet to be optimized or whenever minimization of fabrication cost is required. Chemiresistive sensors consume low power, show good sensitivity, and good reproducibility[188]. Chemometric analysis (Figure 2.7) addresses the selectivity issues that are commonly associated with chemiresistors. Here, an array of SWCNT-based chemiresistors (functionalized and un-functionalized) was utilized to differentiate FC and MnO_4^- over a range of pHs.[192] The sensor data were analyzed with principal component analysis (PCA) to separate the analyte at different pHs (Figure 2.7a). Figure 2.7b shows the regression graph from a partial least squares (PLS) model applied to a few-layer graphene-based array for monitoring of monochloramine in tap water.[205] This model was applied to predict the concentration of unknown concentrations of the sample and showed good predictability.

Table 2.7 Chemiresistive sensors.

Material	Disinfectant	Parameters	Reference
Graphene-amino pyrene	FC	0.01–1.0 mg/L; 0.003	169
SWCNT-PCAT	FC	0.06–60 mg/L; 0.06 mg/L (lowest measured)	198
GLC-PCAT	FC	0.01–1.4 mg/L; 0.001mg/L	173
Graphene-PEDOT:PSS	FC	0.1–500 mg/L; 0.18 mg/L	206
SWCNT-CoPc-AQ array	FC	0.015–10 mg/L; 0.001 mg/L	207
Graphene-array	FC NH_2Cl $NHCl_2$	(0-2.45 mg/L) (0 – 2.08 mg/L) (0-2.25 mg/L)	205
SWCNT-array	FC MnO_4^-	(0 – 2 mg/L) (0 – 1.33 mg/L)	192
Graphene/graphitic composite- CNT	FC	(0-0.59) mg/L	208
Pencil lead- PCAT	FC	0 – 12 mg/L	209

Pencil drawn film	FC	0.06 – 60 mg/L	210
MWCNT-array	FC	0-1 mg/L over the pH (5.5-9)	211,212
SWCNT-crystal violet	H_2O_2		213
Polypyrrol-CNT	H_2O_2		197
GLC-PCAT	FC	0.05-1.75 mg/L	214
SWCNT -DPPD	MnO_4^-	lower range concentrations (0.01− 0.1 mg/L, limit of detection, LoD 0.0001 mg/L), medium range concentrations (0.2 −1.6 mg/L, LoD 0.002 mg/L) and high range concentrations (1− 8 mg/L, LoD 0.03 mg/L)	196
SWCNT	FC	(0.05 – 1.2 mg/L)	215

FC = free chlorine, NH_2Cl = monochloramine, $NHCl_2$ = dichloramine, GO = graphene oxide, GLC = graphene-like carbon, DPPD = *N*, *N*-diethyl-1,4-phenylenediamine, PCAT = phenyl-capped aniline tetramer, PEDOT: PSS = poly(3,4-ethylenedioxythiophene): poly(styrenesulfonate), CoPc = cobalt phthalocyanine, AQ = anthraquinone, SWCNT = single-walled carbon nanotube, MWCNT = multi-walled carbon nanotube.

6. Conclusion

Effective disinfection is a dynamic situation where oxidant speciation shifts with pH and temperature, requiring adjustment with changing organic and inorganic loads, and residual disinfectant level drops as water moves through treatment and distribution. This review showed that online monitoring provides the progressive solution needed to keep systems under control where breakthrough events will be swiftly recognized for corrective action, and DPBs will be minimized. Among the parameters that can be monitored, ORP offers a fast, integrative signal of oxidative strength. However, ORP must be interpreted in the context of chemistry (such as $HOCl/OCl^-$ level, chloramine formation, bromide reactions) and additives that suppress the oxidative reactivity (such as cyanuric acid in recreational water). pH, ionic strength, dissolved oxygen, and temperature add crucial information to ensure effective disinfection. Free chlorine remains the most popular disinfectant in drinking water applications with increasing popularity of monochloramine usage as secondary disinfectant due to its long-lasting residual effect. Other disinfectants are increasingly used in AOPs to find innovative solutions to disinfect water and wastewater.

Sensing technologies are slowly moving toward multi-parameter, reagent-less systems. Colorimetric platforms, however, are still the most used detection method due their reliability despite the need for reagents. Electrochemical techniques are the most researched methods with rapid, low-cost deployment but requiring attention to reference electrode stability (due to fouling, and cross-sensitivity issues). Emerging electrical approaches (chemiresistors and FETs) promise simple architectures and truly continuous operation. With the increasing use of chemometrics and potential of simple fabrication methods of chemiresistors, the scientific community has challenges to solve in making the chemiresistive arrays more durable and commercially ready to be applied in treatment plants.

Future research should concentrate on: (i) standardized calibration and intercomparison protocols for online sensors across realistic matrices; (ii) antifouling, self-verification, and in-situ recalibration to extend maintenance intervals; (iii) model-based control that links measured ORP/speciation to CT targets under varying temperature and pHs; and (iv) secure data pipelines that feed alarms. Utility officials and operators can move from chasing residuals to proactively managing risk of contamination in water if these advancements are achieved.

References

(1) Deborde, M.; von Gunten, U. Reactions of Chlorine with Inorganic and Organic Compounds during Water Treatment-Kinetics and Mechanisms: A Critical Review. *Water Res.* **2008**, *42* (1–2), 13–51.

(2) Stewart, P. S.; Franklin, M. J. Physiological Heterogeneity in Biofilms. *Nat. Rev. Microbiol.* **2008**, *6* (3), 199–210. https://doi.org/10.1038/nrmicro1838.

(3) Morrison, C. M.; Hogard, S.; Pearce, R.; Mohan, A.; Pisarenko, A. N.; Dickenson, E. R. V; Gunten, U. Von; Wert, E. C. Critical Review on Bromate Formation during Ozonation and Control Options for Its Minimization. *Environ. Sci. Technol.* **2023**, *57*, 18393–18409. https://doi.org/10.1021/acs.est.3c00538.

(4) Hazen and Sawyer. *Disinfection Alternatives for Safe Drinking Water*; Van Nostrand Reinhold: New York, NY, 1992.

(5) Hossain, S.; Chow, C. W. K.; Cook, D.; Sawade, E.; Hewa, G. A. Review of Nitrification Monitoring and Control Strategies in Drinking Water System. *Int. J. Environ. Res. Public Heal.* **2022**, *19*, 4003.

(6) Banna, M. H.; Imran, S.; Francisque, A.; Najjaran, H.; Sadiq, R.; Rodriguez, M.; Hoorfar, M. Online Drinking Water Quality Monitoring: Review on Available and Emerging Technologies. *Crit. Rev. Environ. Sci. Technol.* **2014**, *44* (12), 1370–1421.

(7) APHA; AWWA; AEF. Standards Methods for the Examination of Water and Wastewater; Washington, DC, 2005.

(8) Hrudey, S. E.; Payment, P.; Huck, P. M.; Gillham, R. W.; Hrudey, E. J. A Fatal Waterborne Disease Epidemic in Walkerton, Ontario: Comparison with Other Waterborne Outbreaks in the Developed World. *Water Sci. Technol.* **2003**, *47* (3), 7–14.

(9) Salvadori, M. I.; Sontrop, J. M.; Garg, A. X.; Moist, L. M.; Suri, R. S.; Clark, W. F. Factors That Led to the Walkerton Tragedy. *Kidney Int.* **2009**, *75* (112), S33–S34.

(10) Kruse, P. Review on Water Quality Sensors. *J. Phys. D. Appl. Phys.* **2018**, *51*, 203002.

(11) Wilson, R. E.; Stoianov, I.; O'Hare, D. Continuous Chlorine Detection in Drinking Water and a Review of New Detection Methods. *Johnson Matthey Technol. Rev.* **2019**, *63* (2), 103–118.

(12) Yang, F.; Ge, L. Colorimetric Sensors : Methods and Applications. *Sensors* **2023**, *23*, 9887.

(13) Wu, Y.; Feng, J.; Hu, G.; Zhang, E.; Yu, H.-H. Colorimetric Sensors for Chemical and Biological Sensing Applications. *Sensors* **2023**, *23*, 2749.

(14) Thakur, A.; Devi, P. A Comprehensive Review on Water Quality Monitoring Devices: Materials Advances, Current Status, and Future Perspective. *Crit. Rev. Anal. Chem.* **2024**, *54* (2), 193–218.

(15) Krupinska, I. Impact of the Oxidant Type on the Efficiency of the Oxidation and Removal of Iron Compounds Fromgroundwater Containing Humic Substances. *Molecules* **2020**, *25*, 3380.

(16) Mehendale, F. V.; Clayton, G.; Homyer, K. M.; Reynolds, D. M. HOCl vs OCl−: Clarification on Chlorine-Based Disinfectants Used within Clinical Settings. *J. Glob. Heal. Reports* **2023**, *7*, 1–7. https://doi.org/10.29392/001c.84488.

(17) Ikai, H.; Nakamura, K.; Shirato, M.; Kanno, T.; Iwasawa, A.; Sasaki, K.; Niwano, Y.; Kohno, M. Photolysis of Hydrogen Peroxide , an Effective Disinfection System via Hydroxyl Radical Formation ო. *Antimicrob. Agents Chemother.* **2010**, *54* (12), 5086–5091. https://doi.org/10.1128/AAC.00751-10.

(18) Zubiarrain-Laserna, A.; Kruse, P. Review—Graphene-Based Water Quality Sensors. *J. Electrochem. Soc.* **2020**, *167* (3), 037539.

(19) US Environmental Protection Agency. *National Primary Drinking Water Regulations: Long Term 2 Enhanced Surface Water Treatment Rule Fed. Regist*; 2006.

(20) Health Canada. *Guidelines for Canadian Drinking Water Quality—Summary Table (Ottawa, Ontario: Water and Air Quality Bureau, Healthy Environments and Consumer Safety Branch, Health Canada)*; 2017.

(21) The Council of the European Union. *European Union Council Directive 98/83/EC of 3 November 1998 on the Quality of Water Intended for Human Consumption Official Journal of the European Communities*; 1998.

(22) World Health Organization. *PH in Drinking-Water Revised Background Document for Development of Who Guidelines of Drinking-Water Quality*; Geneva, 2007.

(23) Suter II, G.; Cormier, S.; Schofield, K.; Gilliam, J.; Barbour, C. *PH*; U.S. Environmental Protection Agency: Washington, DC, 2025.

(24) Organization, W. H. *Monochloramine in Drinking-Water Background Document for Development of WHO Guidelines for Drinking-Water Quality*; Geneva, 2004.

(25) Wang, Y.; Zheng, K.; Guo, H.; Tian, L.; He, Y.; Wang, X.; Zhu, T.; Sun, P.; Liu, Y. Potassium Permanganate-Based Advanced Oxidation Processes for Wastewater Decontamination and Sludge Treatment : A Review. *Chem. Eng. J.* **2023**, *452*, 139529. https://doi.org/10.1016/j.cej.2022.139529.

(26) Haida, U.; Mohamed, N.; Khan, A.; Lim, Y. C.; Lee, K. S.; Liew, K. Bin; Kassab, Y. W. A Systematic Review on Chlorine Dioxide as a Disinfectant. *J. Med. Life* **2022**, *15* (March), 313–318. https://doi.org/10.25122/jml-2021-0180.

(27) Ozone decomposition https://www.lenntech.com/library/ozone/decomposition/ozone-decomposition.htm? (accessed Aug 1, 2025).

(28) Gunten, U. Von. Ozonation of Drinking Water: Part I. Oxidation Kinetics and Product Formation. *Water Res.* **2003**, *37*, 1443–1467.

(29) Merényi, G.; Lind, J.; Naumov, S.; Sonntag, C. Von. Reaction of Ozone with Hydrogen Peroxide (Peroxone Process): A Revision of Current Mechanistic Concepts Based on Thermokinetic and Quantum-Chemical Considerations. *Environ. Sci. Technol.* **2010**, *44* (9), 3505–3507. https://doi.org/10.1021/es100277d.

(30) Staehelin, J.; Holgné, J. Decomposition of Ozone in Water: Rate of Initiation by Hydroxide Ions and Hydrogen Peroxide. *Environ. Sci. Technol.* **1982**, *16* (10), 676–681. https://doi.org/10.1021/es00104a009.

(31) Ziegler, R.; Suter II, G.; Kefford, B. J.; Schofield, K.; Pond, G. *Ionic Strength*; U.S. Environmental Protection Agency: Washington, DC, 2025.

(32) Liao, C. Hydroxyl Radical Scavenging Role of Chloride and Bicarbonate Ions in the H2O2 / UV Process. *Chemosphere* **2001**, *44*, 1193–1200.

(33) How ozone generators effectively remove 1,4-dioxane from water supplies https://pinnacleozone.com/resources/whitepapers/how-ozone-generators-effectively-remove-14-dioxane-from-water-supplies/#_toc_Ozone_combined_with_other_chemicals_and_treatments.

(34) Furst, K. E.; Graham, K. E.; Weisman, R. J.; Adusei, K. B. It's Getting Hot in Here: Effects of Heat on Temperature, Disinfection, and Opportunistic Pathogens in Drinking Water Distribution Systems. *Water Res.* **2024**, *260* (March), 121913.

(35) Health Canada. Guidance on the Temperature Aspects of Drinking Water; 2021.

(36) Fisher, I.; Kastl, G.; Sathasivan, A.; Jegatheesan, V. Suitability of Chlorine Bulk Decay Models for Planning and Management of Water Distribution Systems. *Crit. Rev. Environ. Sci. Technol.* **2011**, *41* (20), 1843–1882.

(37) Fisher, I.; Kastl, G.; Sathasivan, A. A Suitable Model of Combined Effects of Temperature and Initial Condition on Chlorine Bulk Decay in Water Distribution Systems. *Water Res.* **2012**, *46* (10), 3293–3303.

(38) Bier, A. W. *Introduction to Oxidation Reduction Potential Measurement*.

(39) CHANG, C.-N.; CHENG, H.-B.; CHAO, A. C. Applying the Nernst Equation To Simulate Redox Potential Variations for Biological Nitrification and Denitrification Processes. *Environ. Sci. Technol.* **2004**, *38* (6), 1807–1812.

(40) Suslow, T. V. *Using Oxidation Reduction Potential (ORP) for Water Disinfection Monitoring , Control and Documentation*; California.

(41) Liao, L. B.; Chen, W. M.; Xiao, X. M. The Generation and Inactivation Mechanism of Oxidation – Reduction Potential of Electrolyzed Oxidizing Water. *J. Food Eng.* **2007**, *78*, 1326–1332. https://doi.org/10.1016/j.jfoodeng.2006.01.004.

(42) Haute, S. Van; Zhou, B.; Luo, Y.; Sampers, I.; Vanhaverbeke, M.; Millner, P. The Use of Redox Potential to Estimate Free Chlorine in Fresh Produce Washing Operations : Possibilities and Limitations. *Postharvest Biol. Technol.* **2019**, *156*, 110957. https://doi.org/10.1016/j.postharvbio.2019.110957.

(43) James, C. N.; Copeland, R. C.; Lytle, D. A. Relationships between Oxidation-Reduction Potential, Oxidant, and PH in Drinking Water. *Water Work. Assoc.* **2004**, 1–13.

(44) Copeland, A.; Lytle, D. A. Measuring the Oxidation-Reduction Potential of

Important Oxidants in Drinking Water. *J. Am. Water Work. Assoc.* **2014**, *106* (1), E10–E20.

(45) Bastian, T.; Brondum, J. Do Traditional Measures of Water Quality in Swimming Pools and Spas Correspond with Beneficial Oxidation Reduction Potential ? *Public Health Rep.* **2009**, *124* (April), 255–261.

(46) Devkota, L. M.; Williams, D. S.; Matta, J. H.; Albertson, O. E.; Grasso, D.; Fox, P. Variation of Oxidation – Reduction Potential Along the Breakpoint Curves in Low-Ammonia Effluents. *Water Environ. Res.* **2000**, *72* (5), 610–617. https://doi.org/10.2175/106143000X138193.

(47) Wyk, S. J. P. Van; Boutigny, A.; Pathology, P.; X, P. B. Sanitation of a South African Forestry Nursery Contaminated with Fusarium Circinatum Using Hydrogen Peroxide at Specific Oxidation Reduction Potentials. **2012**, No. June, 875–880.

(48) Nghi, N. H.; Cuong, L. C.; Dieu, T. V.; Ngu, T.; Thi, D.; Oanh, Y. Ozonation Process and Water Disinfection. *Vietnam J. Chem.* **2018**, *56* (6), 717–720. https://doi.org/10.1002/vjch.201800076.

(49) Lo, G. Evaluation of Current Operating Standards for Chlorine Dioxide in Disinfection of Dump Tank and Flume for Fresh Tomatoes 3. *J. Food Prot.* **2012**, *75* (2), 304–313. https://doi.org/10.4315/0362-028X.JFP-11-347.

(50) BERNHARDT, D.; II, J. F. R. Dissolved Oxygen. In *Handbooks for Water-Resources Investigations*; 2020.

(51) U.S. Environmental Protection Agency. Dissolved Oxygen https://www.epa.gov/caddis/dissolved-oxygen? (accessed Jul 24, 2025).

(52) Li, S.; Shi, L.; Guo, Y.; Wang, J.; Liu, D.; Zhao, S. Selective Oxygen Reduction Reaction: Mechanism Understanding, Catalyst Design and Practical Application. *Chem. Sci.* **2024**, *15* (29), 11188–11228. https://doi.org/10.1039/d4sc02853h.

(53) Dutton, A. S.; Fukuto, J. M.; Houk, K. N.; Energetics, C.; Calculations, C. P. C. M. S.; Chem, D. A. J. P. Theoretical Reduction Potentials for Nitrogen Oxides from Reduction Potentials Are as Follows : *Inorg. Chem.* **2005**, *44* (21), 7687–7688.

(54) Null, S. E.; Mouzon, N. R.; Elmore, L. R. Dissolved Oxygen, Stream Temperature, and Fish Habitat Response to Environmental Water Purchases. *J. Environ. Manage.* **2017**, *197*, 559–570. https://doi.org/10.1016/j.jenvman.2017.04.016.

(55) Li, D.; Zou, M.; Jiang, L. Dissolved Oxygen Control Strategies for Water Treatment: A Review. *Water Sci. Technol.* **2022**, *86* (6), 1444–1466. https://doi.org/10.2166/wst.2022.281.

(56) Corporation, B. & V. *White's Handbook of Chlorination and Alternative Disinfectants*, 5th ed.; Black & Veatch Corporation, 2010.

(57) Andrés, C. M. C.; Lastra, J. M. P. de la; Andrés Juan, C.; Plou, F. J.; Pérez-Lebeña, E. Chlorine Dioxide: Friend or Foe for Cell Biomolecules? A Chemical Approach.

Int. J. Mol. Sci. **2022**, *23*, 15660. https://doi.org/10.3390/ijms232415660.

(58) Gordon, G.; Rosenblatt, A. A. Chlorine Dioxide: The Current State of the Art. *Ozone Sci. Eng.* **2005**, *27* (3), 203–207. https://doi.org/10.1080/01919510590945741.

(59) Jung, H.-R.; Kim, U.-J.; Seo, G.-T.; Lee, H.-D.; Lee, C.-S. Effect of Dissolved Oxygen (DO) on Internal Corrosion of Water Pipes. *Environ. Eng. Res.* **2009**, *14* (3), 195–199. https://doi.org/10.4491/eer.2009.14.3.195.

(60) Feng, Y.; Smith, D. W.; Bolton, J. R. Photolysis of Aqueous Free Chlorine Species (HOCl and OCl–) with 254 Nm Ultraviolet Light. *J. Environ. Eng. Sci.* **2007**, *6*, 277–284.

(61) World Health Organization. *Guidelines for Drinking-Water Quality: Fourth Edition Incorporating the First Addendum*, Fourth edi.; Geneva: World Health Organization, 2017.

(62) Sayre, I. M. International Standards for Drinking Water. *J. Am. Water Work. Assoc.* **1988**, *80* (1), 53–60.

(63) Qin, Y.; Kwon, H. J.; Howlader, M. M. R.; Deen, M. J. Microfabricated Electrochemical PH and Free Chlorine Sensors for Water Quality Monitoring: Recent Advances and Research Challenges. *RSC Adv.* **2015**, *5* (85), 69086–69109.

(64) Carrell, J.; Morris, J. C. The Acid Ionization Constant of HOCI from 5 to 35°. *J. Phys. Chem.* **1966**, *70* (12), 3798–3805.

(65) Choi, H.; Chatterjee, P.; Lichtfouse, E.; Martel, J. A.; Hwang, M.; Jinadatha, C.; Sharma, V. K. Classical and Alternative Disinfection Strategies to Control the COVID-19 Virus in Healthcare Facilities: A Review. *Environ. Chem. Lett.* **2021**, *19* (3), 1945–1951.

(66) Spencer, M. *Water Quality Instrumentation*, 1st ed.; Water Environment Federation: Alexandria, 2022.

(67) McGuire, M. J. Drinking Water Chlorination. *Am. Chem. Counc.* **2018**, 38.

(68) Lide, D. R. *Handbook of Chemistry and Physics*, 85th Edn.; CRC Press LLC: Boca Raton, USA, 2004.

(69) Morris, J. C. Future of Chlorination. *J. / Am. Water Work. Assoc.* **1966**, *58* (11), 1475–1482.

(70) Butterfield, C. T.; Wattie, E.; Megregian, S.; Chambers, C. W. Influence of PH and Temperature on the Survival of Coliforms and Enteric Pathogens When Exposed to Free Chlorine. *Public Health Rep.* **1943**, *58* (51), 1837–1866.

(71) Marks, H. C.; Strandskov, F. B. Halogens and Their Mode of Action. *Ann. N. Y. Acad. Sci.* **1950**, *53* (1), 163.

(72) Wang, L.; Bassiri, M.; Najafi, R.; Najafi, K.; Yang, J. Hypochlorous Acid as a Potential Wound Care Agent Part I . Stabilized Hypochlorous Acid : A Component of the Inorganic Armamentarium of Innate Immunity. *J. Burns Wounds* **2007**, *6*, 65–

79.
(73) Liu, L.; Xing, X.; Hu, C.; Wang, H.; Lyu, L. Effect of Sequential UV/Free Chlorine Disinfection on Opportunistic Pathogens and Microbial Community Structure in Simulated Drinking Water Distribution Systems. *Chemosphere* **2019**, *219*, 971–980. https://doi.org/10.1016/j.chemosphere.2018.12.067.
(74) Seymour, I.; O'Sullivan, B.; Lovera, P.; Rohan, J. F.; O'Riordan, A. Electrochemical Detection of Free-Chlorine in Water Samples Facilitated by in-Situ PH Control Using Interdigitated Microelectrodes. *Sensors Actuators, B Chem.* **2020**, *325* (August), 128774.
(75) City of Hamilton. *Drinking Water Systems Annual Water Quality and Summary Report*; 2021.
(76) Health Canada. Chloramines in Drinking Water - Guideline Technical Document for Public Consultation; 2018.
(77) Spon, R. Do You Really Have a Free Chlorine Residual. *Am. Water Work. Assoc.* **2008**, *34* (6), 24–27.
(78) Engelhardt, T. L.; Malkov, V. B. Chlorination, Chloramination and Chlorine Measurement. *Hach Company*; Loveland, Colorado, 2015.
(79) Jacobs, J. H.; Spaan, S.; van Rooy, G. B. G. J.; Meliefste, C.; Zaat, V. A. C.; Rooyackers, J. M.; Heederik, D. Exposure to Trichloramine and Respiratory Symptoms in Indoor Swimming Pool Workers. *Eur. Respir. J.* **2007**, *29*, 690–698.
(80) US Environmental Protection Agency - Office of Water. *Alternative Disinfectants and Oxidants Guidance Manual*, 1st Ed.; (Washington, DC) US Environmental Agency, 1999.
(81) Aieta, E. M.; Berg, J. D. A Review of Chlorine Dioxide in Drinking Water Treatment. *J. Am. Water Works Assoc.* **1986**, *78* (6), 62–72.
(82) Girard, M.; Mattison, K.; Fliss, I.; Jean, J. International Journal of Food Microbiology Ef Fi Cacy of Oxidizing Disinfectants at Inactivating Murine Norovirus on Ready-to-Eat Foods. *Int. J. Food Microbiol.* **2016**, *219*, 7–11. https://doi.org/10.1016/j.ijfoodmicro.2015.11.015.
(83) Anfruns-estrada, E.; Bottaro, M.; Pint, R. M.; Guix, S. Effectiveness of Consumers Washing with Sanitizers to Reduce Human Norovirus on Mixed Salad. *Foods* **2019**, *8*, 637.
(84) Noszticzius, Z.; Wittmann, M.; Kály-kullai, K.; Beregvári, Z.; Kiss, I.; Szegedi, J. Chlorine Dioxide Is a Size-Selective Antimicrobial Agent. *PLoS One* **2013**, *8* (11), 1–10.
(85) Health Canada. Guidelines for Canadian Drinking Water Quality: Guideline Technical Document – Chlorite and Chlorate; 2014.
(86) Wang, Y.; Liu, H.; Xie, Y.; Ni, T.; Liu, G. Oxidative Removal of Diclofenac by

Chlorine Dioxide : Reaction Kinetics and Mechanism. *Chem. Eng. J.* **2015**, *279*, 409–415. https://doi.org/10.1016/j.cej.2015.05.046.

(87) Mzinyathi, M.; Muthuraj, V.; Ajala, E. O.; Kakavandi, B.; van Rensburg, S. J.; Nkambule, T. T. I.; Mamba, G. Chlorine Dioxide Drinking Water Pre-Oxidation and Disinfection: A Review of Its Effectiveness, Mechanisms, and Disinfection by-Products. *Desalin. Water Treat.* **2025**, *323* (May), 101340. https://doi.org/10.1016/j.dwt.2025.101340.

(88) Fang, H.; Dai, L.; Wang, S.; Shi, W.; Ma, D. Application of Permanganate/Bisulfite Process for Treatment of Sulfamerazine Contaminated Water. *Desalin. Water Treat.* **2021**, *241*, 124–134.

(89) Qiu, Y.; Luo, Y.; Zhang, T.; Du, X.; Wang, Z.; Liu, F.; Liang, H. Comparison between Permanganate Pre-Oxidation and Persulfate/Iron(II) Enhanced Coagulation as Pretreatment for Ceramic Membrane Ultrafiltration of Surface Water Contaminated with Manganese and Algae. *Environ. Res.* **2021**, *196*, 110942. https://doi.org/10.1016/j.envres.2021.110942.

(90) Yahya, M. T.; Landeen, L. K.; Gerba, C. P. Inactivation of Legionella Pneumophila by Potassium Permanganate. *Environ. Technol. (United Kingdom)* **1990**, *11* (7), 657–662. https://doi.org/10.1080/09593339009384908.

(91) Lide, D. R. *CRC Handbook of Chemistry and Physics*, seventy fi.; CRC Press: Boka Raton, FL, 1990.

(92) Webber, W. J. J.; Posselt., H. S. . . *"Disinfection." Physicochemical Processes in Water Quality Control.*; Webber, W. J., Ed.; John Wiley & Sons: New York, NY., 1972.

(93) Cleasby, J. .; Baumann, E. R.; Black, C. D. Effectiveness of Potassium Permanganate for Disinfection. *J. Am. Water Works Assoc.* **1964**, *56* (4), 466–474.

(94) Murray, J. W. The Surface Chemistry of Hydrous Manganese Dioxide. *J. Colloid Interface Sci.* **1974**, *46* (3), 357–371.

(95) Lund, E. The Significance of Oxidation in Chemical Inactivation of Poliovirus. *Arch. Virol.* **1963**, *12*, 648–660.

(96) Properties, P.; Ozone, O. F.; Mechanism, T. H. E.; Ozone, O. F. OZONE AS AN ALTERNATIVE DISINFECTANT – A REVIEW. *Pol. J. Food Nutr. Sci.* **2006**, *15/56* (1), 3–8.

(97) Epelle, E. I.; Macfarlane, A.; Cusack, M.; Burns, A.; Okolie, J. A.; Mackay, W.; Rateb, M.; Yaseen, M. Ozone Application in Different Industries : A Review of Recent Developments. *Chem. Eng. J.* **2023**, *454* (P2), 140188. https://doi.org/10.1016/j.cej.2022.140188.

(98) Liu, Z.; Demeestere, K.; Hulle, S. Van. Comparison and Performance Assessment of Ozone-Based AOPs in View of Trace Organic Contaminants Abatement in Water

and Wastewater : A Review. *J. Environ. Chem. Eng.* **2021**, *9* (4), 105599. https://doi.org/10.1016/j.jece.2021.105599.

(99) Hoigne, J.; Bader, H. Ozonation of Water: Kinetics of Oxidation of Ammonia by Ozone and Hydroxyl Radicals. *Environ. Sci. Technol.* **1978**, *12* (1), 79–84. https://doi.org/10.1021/es60137a005.

(100) Glaze, W. H.; Kang, J. Advanced Oxidation Processes for Treating Groundwater Contaminated With TCE and PCE: Laboratory Studies. *J. AWWA* **1988**, *80* (5), 57–63. https://doi.org/10.1002/j.1551-8833.1988.tb03038.x.

(101) Masten, S. J.; Jürg, H. Comparison of Ozone and Hydroxyl Radical-Induced Oxidation of Chlorinated Hydrocarbons in Water. *Ozone Sci. Eng.* **1992**, *14* (3), 197–214. https://doi.org/10.1080/01919519208552475.

(102) Wang, C.; Moore, N.; Bircher, K.; Andrews, S.; Hofmann, R. Full-Scale Comparison of UV/H2O2 and UV/Cl2 Advanced Oxidation: The Degradation of Micropollutant Surrogates and the Formation of Disinfection Byproducts. *Water Res.* **2019**, *161*, 448–458. https://doi.org/10.1016/j.watres.2019.06.033.

(103) Wang, C.; Moore, N.; Bircher, K.; Andrews, S.; Hofmann, R.; Ma, L.; Liu, J. Advances in the Removal of Precursors of Disinfection By-Products by Ultraviolet-Coupled Advanced Oxidation Processes. *Desalin. Water Treat.* **2021**, *231*, 297–314. https://doi.org/10.1016/j.watres.2019.06.033.

(104) Technologies, T. About UV Advanced Oxidation https://www.trojantechnologies.com/en/technologies/uv-advanced-oxidation-process? (accessed Aug 1, 2025).

(105) Von Gunten, U. Ozonation of Drinking Water: Part II. Disinfection and by-Product Formation in Presence of Bromide, Iodide or Chlorine. *Water Res.* **2003**, *37* (7), 1469–1487. https://doi.org/10.1016/S0043-1354(02)00458-X.

(106) El-Athman, F.; Zehlike, L.; Kämpfe, A.; Junek, R.; Selinka, H. C.; Mahringer, D.; Grunert, A. Pool Water Disinfection by Ozone-Bromine Treatment: Assessing the Disinfectant Efficacy and the Occurrence and in Vitro Toxicity of Brominated Disinfection by-Products. *Water Res.* **2021**, *204*. https://doi.org/10.1016/j.watres.2021.117648.

(107) Liu, Q.; Xu, X.; Fu, J.; Du, Y.; Lin, L.; Bai, L.; Wang, D.; Ximenes, V. F.; Morgon, N. H.; De Souza, A. R.; Fujioka, T.; Yoshikawa, H.; Eguchi, M.; Boivin, S.; Kodamatani, H. Role of Hypobromous Acid in the Transformation of Polycyclic Aromatic Hydrocarbons during Chlorination. *Water Res.* **2021**, *146* (October), 117787. https://doi.org/10.1016/j.watres.2021.117648.

(108) Chlorine And Chlorine Alternatives https://www.watertechnologies.com/handbook/chapter-27-chlorine-and-chlorine-alternatives (accessed Jul 21, 2025).

(109) Disinfectants Bromine https://www.lenntech.com/processes/disinfection/chemical/disinfectants-bromine.htm (accessed Jul 15, 2025).

(110) Lenninger, M.; Wiemeyer, F.; Kopp, E.; Aguiló-Aguayo, N.; Pham, T.; Bechtold, T. Reduction of Bromate Formation in Electrochemical Production of Hypobromite for Water Disinfection. *J. Water Process Eng.* **2023**, *55* (July). https://doi.org/10.1016/j.jwpe.2023.104264.

(111) Ministry of the Environment, conservation and P. Procedure for Disinfection of Drinking Water in Ontario https://www.ontario.ca/page/procedure-disinfection-drinking-water-ontario#section-3 (accessed May 25, 2025).

(112) Collivignarelli, M. C.; Abbà, A.; Benigna, I.; Sorlini, S.; Torretta, V. Overview of the Main Disinfection Processes for Wastewater and Drinking Water Treatment Plants. *Sustainability* **2018**, *10* (86). https://doi.org/10.3390/su10010086.

(113) Home Pool and Hot Tub Water Treatment and Testing https://www.cdc.gov/healthy-swimming/about/home-pool-and-hot-tub-water-treatment-and-testing.html? (accessed Jul 20, 2025).

(114) Askins, A. Cyanuric Acid in Commercial Swimming Pools and Its Effects on Chlorine's "Staying Power" And Oxidation Reduction Potentials, 2013.

(115) Bastian, T. Do Traditional Measures of Water Quality in Swimming Pools and Spas Correspond with Beneficial Oxidation Reduction Potential ? *Public Health Rep.* **2009**, *124* (April), 255–261.

(116) Operating and Managing Public Pools, Hot Tubs and Splash Pads https://www.cdc.gov/healthy-swimming/toolkit/operating-public-pools-hot-tubs-and-splash-pads.html?

(117) World Health Organization. *Guidelines for Safe Recreational Water Environments. Volume 2: Swimming Pools and Similar Environments*; 2006.

(118) Hussain, G.; Mian, H. R.; Hewage, K.; Macneill, A. J.; Sadiq, R. Disinfection By-Products in Indoor Swimming Pools : A Critical Review to Prioritize Commonly Occurring Species and Influencing Factors. *J. Hazard. Mater.* **2025**, *495*, 138739.

(119) Wastewater Technology Fact Sheet: Disinfection for Small Systems; United States Environmental Protection Agency.

(120) United States Environmental Protection Agency. *Wastewater Technology Fact Sheet Chlorine Disinfection*; Washington, D.C., 1999.

(121) United States Environmental Protection Agency. *Wastewater Technology Fact Sheet- Ultraviolet Disinfection*; Washington, D.C., 1999.

(122) United States Environmental Protection Agency. Summary of California's Water Reuse Guideline or Regulation for Impoundments https://www.epa.gov/waterreuse/summary-californias-water-reuse-guideline-or-

regulation-impoundments? (accessed Aug 19, 2025).

(123) United States Environmental Protection Agency. *Wastewater Technology Fact Sheet Ozone Disinfection*; Washington, D.C., 1999.

(124) Nitinaivinij, K.; Parnklang, T.; Thammacharoen, C.; Ekgasit, S.; Wongravee, K. Colorimetric Determination of Hydrogen Peroxide by Morphological Decomposition of Silver Nanoprisms Coupled with Chromaticity Analysis. *Anal. Methods* **2014**, *6* (24), 9816–9824. https://doi.org/10.1039/c4ay02339k.

(125) Dou, J.; Shang, J.; Kang, Q.; Shen, D. Field Analysis Free Chlorine in Water Samples by a Smartphone-Based Colorimetric Device with Improved Sensitivity and Accuracy. *Microchem. J.* **2019**, *150* (June), 104200. https://doi.org/10.1016/j.microc.2019.104200.

(126) Lou, X.; Zhang, Y.; Qin, J.; Li, Z. Colorimetric Hypochlorite Detection Using an Azobenzene Acid in Pure Aqueous Solutions and Real Application in Tap Water. *Sensors Actuators, B Chem.* **2012**, *161* (1), 229–234. https://doi.org/10.1016/j.snb.2011.10.024.

(127) Zou, J.; Cai, H.; Wang, D.; Xiao, J.; Zhou, Z.; Yuan, B. Spectrophotometric Determination of Trace Hydrogen Peroxide via the Oxidative Coloration of DPD Using a Fenton System. *Chemosphere* **2019**, *224*, 646–652. https://doi.org/10.1016/j.chemosphere.2019.03.005.

(128) Sun, X.; Odyniec, M. L.; Sedgwick, A. C.; Lacina, K.; Xu, S.; Qiang, T.; Bull, S. D.; Marken, F.; James, T. D. Reaction-Based Indicator Displacement Assay (RIA) for the Colorimetric and Fluorometric Detection of Hydrogen Peroxide. *Org. Chem. Front.* **2017**, *4* (6), 1058–1062. https://doi.org/10.1039/c6qo00448b.

(129) Pepich, B. V.; Dattilio, T. A.; Fair, P. S.; Munch, D. J.; Gordon, G.; Körtvélyesi, Z. An Improved Colorimetric Method for Chlorine Dioxide and Chlorite Ion in Drinking Water Using Lissamine Green B and Horseradish Peroxidase. *Anal. Chim. Acta* **2007**, *596*, 37–45.

(130) Y, D.; G, L.; N, Z.; R, W.; Y, C.; G, C. Graphene Quantum Dot as a Green and Facile Sensor for Free Chlorine in Drinking Water. *Anal. Chem.* **2012**, *84*, 8378–8382.

(131) Hu, W.; Zhao, M.; Gu, K.; Xie, L.; Liu, M.; Lu, D. Fluorescent Probe for the Detection of Hypochlorous Acid in Water Samples and Cell Models. *RSC Adv.* **2021**, *12* (2), 777–784. https://doi.org/10.1039/d1ra08116k.

(132) Shi, G.; Shahid, M. A.; Yousuf, M.; Mahmood, F.; Rasheed, L.; Bielawski, C. W.; Kim, K. S. A “Turn-on” Fluorescent Probe for the Detection of Permanganate in Aqueous Media. *Chem. Commun.* **2019**, *55* (10), 1470–1473. https://doi.org/10.1039/c8cc08958b.

(133) Liu, Z.; Yan, Y.; Wang, H.; Wang, X.; Xue, B. Sequential Detection of H2S and HClO Fluorescence Probes and Their Applications in Real Sample Detection,

Smartphone Sensing Development, and Bioimaging. *Anal.* **2025**, *150* (12), 2591–2599. https://doi.org/10.1039/d5an00382b.

(134) Hallaj, T.; Amjadi, M.; Manzoori, J. L.; Shokri, R. Chemiluminescence Reaction of Glucose-Derived Graphene Quantum Dots with Hypochlorite, and Its Application to the Determination of Free Chlorine. *Microchim. Acta* **2015**, *182* (3–4), 789–796. https://doi.org/10.1007/s00604-014-1389-0.

(135) Karimi, K.; Gharachorloo, M.; Fallah, A. Highly Sensitive Photoluminescence Sensor Based on Chitosan Biopolymer Film for Determination of Hydrogen Peroxide. *Int. J. Biol. Macromol.* **2025**, *296*, 139735. https://doi.org/10.1016/j.ijbiomac.2025.139735.

(136) Jiang, Z.; Zhang, B.; Liang, A. A New Sensitive and Selective Fluorescence Method for Determination of Chlorine Dioxide in Water Using Rhodamine S. *Talanta* **2005**, *66*, 783–788. https://doi.org/10.1016/j.talanta.2004.12.037.

(137) Zdrachek, E.; Bakker, E. Potentiometric Sensing. *Anal. Chem.* **2019**, *91*, 2–26. https://doi.org/10.1021/acs.analchem.8b04681.

(138) Kimmel, D. W.; Leblanc, G.; Meschievitz, M. E.; Cli, D. E. Electrochemical Sensors and Biosensors. *Anal. Chem.* **2012**, *84*, 685–707.

(139) Qin, Y.; Kwon, H. J.; Howlader, M. M. R.; Deen, M. J. Microfabricated Electrochemical PH and Free Chlorine Sensors for Water Quality Monitoring: Recent Advances and Research Challenges. *RSC Adv.* **2015**, *5* (85), 69086–69109.

(140) Sugawara, M.; Watanabe, T.; Einaga, Y.; Koh, S. Impact of Gate Electrode on Free Chlorine Sensing Performance in Solution-Gated Graphene Field-Effect Transistors. *RSC Adv.* **2024**, *14* (11), 7867–7876.

(141) Saputro, S.; Takehara, K.; Yoshimura, K.; Matsuoka, S.; Narsito. Differential Pulse Voltammetric Determination of Free Chlorine for Water Disinfection Process. *Electroanalysis* **2010**, *22* (23), 2765–2768. https://doi.org/10.1002/elan.201000322.

(142) Peng, Z.; Irkham, N.; Akai, K.; Murata, M.; Tomisaki, M.; Einaga, Y. Simultaneous Electrochemical Detection of Ozone and Free Chlorine with a Boron-Doped Diamond Electrode. *Analyst* **2022**, *147* (8), 1655–1662. https://doi.org/10.1039/d1an02347k.

(143) Khalifa, Z.; Oura, M. F. A.; Hathoot, A.; Azzem, M. A. Voltammetric Determination of Hydrogen Peroxide at Decorated Palladium Nanoparticles/Poly 1,5-Diaminonaphthalene Modified Carbon-Paste Electrode. *R. Soc. Open Sci.* **2024**, *11* (6). https://doi.org/10.1098/rsos.231894.

(144) Lee, W. H.; Pressman, J. G.; Wahman, D. G.; Bishop, P. L. Characterization and Application of a Chlorine Microelectrode for Measuring Monochloramine within a Biofilm. *Sensors Actuators, B Chem.* **2010**, *145* (2), 734–742.

(145) Nosuhi, M.; Nezamzadeh-Ejhieh, A. Voltammetric Determination of Trace

Amounts of Permanganate at a Zeolite Modified Carbon Paste Electrode. *New J. Chem.* **2017**, *41* (24), 15508–15516. https://doi.org/10.1039/c7nj03076b.

(146) Kato, N.; Hirano, N.; Okazaki, S.; Matsushita, S.; Gomei, T. Development of an All-Solid-State Residual Chlorine Sensor for Tap Water Quality Monitoring. *Sensors Actuators, B Chem.* **2017**, *248* (September), 1037–1044.

(147) Ensafi, A. A.; Rezaloo, F.; Rezaei, B. Electrochemical Sensor Based on Porous Silicon/Silver Nanocomposite for the Determination of Hydrogen Peroxide. *Sensors Actuators, B Chem.* **2016**, *231*, 239–244. https://doi.org/10.1016/j.snb.2016.03.018.

(148) Seymour, I.; O'Sullivan, B.; Lovera, P.; Rohan, J. F.; O'Riordan, A. Elimination of Oxygen Interference in the Electrochemical Detection of Monochloramine, Using in Situ PH Control at Interdigitated Electrodes. *ACS Sensors* **2021**, *6* (3), 1030–1038.

(149) Seymour, I.; O'Sullivan, B.; Lovera, P.; Rohan, J. F.; O'Riordan, A. Electrochemical Detection of Free-Chlorine in Water Samples Facilitated by in-Situ PH Control Using Interdigitated Microelectrodes. *Sensors Actuators, B Chem.* **2020**, *325* (August), 128774. https://doi.org/10.1016/j.snb.2020.128774.

(150) Lee, W. H.; Wahman, D. G.; Pressman, J. G. Monochloramine-Sensitive Amperometric Microelectrode: Optimization of Gold, Platinum, and Carbon Fiber Sensing Materials for Removal of Dissolved Oxygen Interference. *Ionics (Kiel).* **2015**, *21* (9), 2663–2674. https://doi.org/10.1007/s11581-015-1454-7.

(151) Piela, B.; Wrona, P. K. Electrochemical Behavior of Chloramines on the Rotating Platinum and Gold Electrodes. *J. Electrochem. Soc.* **2003**, *150* (5), E255. https://doi.org/10.1149/1.1560951.

(152) Islam, J.; Shao, H.; Badal, M. R.; Razeeb, K. M.; Jamalid, M. Pencil Graphite as Electrode Platform for Free Chlorine Sensors and Energy Storage Devices. *PLoS One* **2021**, *16* (3 March), 1–20. https://doi.org/10.1371/journal.pone.0248142.

(153) Lee, W. H.; Wahman, D. G.; Bishop, P. L.; Pressman, J. G. Free Chlorine and Monochloramine Application to Nitrifying Biofilm: Comparison of Biofilm Penetration, Activity, and Viability. *Environ. Sci. Technol.* **2011**, *45* (4), 1412–1419. https://doi.org/10.1021/es1035305.

(154) Tomei, M. R.; Marcoccio, E.; Neagu, D.; Moscone, D.; Arduini, F. A Miniaturized Carbon Black-Based Electrochemical Sensor for Chlorine Dioxide Detection in Swimming Pool Water. *Electroanalysis* **2020**, *32* (5), 986–991. https://doi.org/10.1002/elan.201900667.

(155) Salazar, P.; Martín, M.; García-garcía, F. J.; González-mora, J. L.; González-elipe, A. R. A Novel and Improved Surfactant-Modified Prussian Blue Electrode for Amperometric Detection of Free Chlorine in Water. *Sensors Actuators B. Chem.* **2015**, *213*, 116–123.

(156) Kumar, D. R.; Kesavan, S.; Nguyen, T. T.; Hwang, J.; Lamiel, C.; Shim, J.

Polydopamine @ Electrochemically Reduced Graphene Oxide-Modified Electrode for Electrochemical Detection of Free-Chlorine. *Sensors Actuators B. Chem.* **2017**, *240*, 818–828.

(157) Pan, S.; Deen, M. J.; Ghosh, R. Low-Cost Graphite-Based Free Chlorine Sensor. *Anal. Chem.* **2015**, *87* (21), 10734–10737. https://doi.org/10.1021/acs.analchem.5b03164.

(158) Siddiqui, J.; Jamal Deen, M. Biodegradable Asparagine-Graphene Oxide Free Chlorine Sensors Fabricated Using Solution-Based Processing. *Analyst* **2022**, *147* (16), 3643–3651.

(159) Ivaska, A.; Forsberg, P.; Heikka, R. Application of an Amperometric Sensor to In-Line Monitoring of Pulp Bleaching with Chlorine Dioxide. *Anal. Chim. Acta* **1990**, *238* (C), 223–229. https://doi.org/10.1016/S0003-2670(00)80540-1.

(160) Errachid, A.; Zine, N.; Samitier, J.; bausells, J. FET-Based Chemical Sensor Systems Fabricated with Standard Technologies. *Electroanalysis* **2004**, *16* (22), 1843–1851.

(161) Zhang, A.; Lieber, C. M. Nano-Bioelectronics. *Chemcial Rev.* **2016**, *115*, 215–257. https://doi.org/10.1021/acs.chemrev.5b00608.

(162) Buth, F.; Kumar, D.; Stutzmann, M.; Garrido, J. A. Electrolyte-Gated Organic Field-Effect Transistors for Sensing Applications. *Appl. Phys. Lett.* **2011**, *98*, 153302.

(163) Xiong, C.; Zhang, T.; Wang, D.; Lin, Y.; Qu, H.; Chen, W.; Luo, L.; Wang, Y.; Zheng, L.; Fu, L. Highly Sensitive Solution-Gated Graphene Transistor Based Sensor for Continuous and Real-Time Detection of Free Chlorine. *Anal. Chim. Acta* **2018**, *1033*, 65–72. https://doi.org/10.1016/j.aca.2018.06.041.

(164) Mopoung, K.; Suwanyangyaun, P.; Odanaka, R.; Kosuga, S.; Watanabe, T.; Koh, S.; Sanorpim, S. A Real-Time Free Chlorine Monitoring by Graphene Field-Effect Transistor. *Proc. 14th Annu. IEEE Int. Conf. Nano/Micro Eng. Mol. Syst. NEMS 2019* **2019**, 64–67. https://doi.org/10.1109/NEMS.2019.8915664.

(165) Geim, A. K.; Novoselov, K. S. The Rise of Graphene. *Nat. Mater.* **2007**, *6*, 183–191.

(166) Zheng, C.; Jin, X.; Li, Y.; Mei, J.; Sun, Y.; Xiao, M.; Zhang, H.; Zhang, Z.; Zhang, G. J. Sensitive Molybdenum Disulfide Based Field Effect Transistor Sensor for Real-Time Monitoring of Hydrogen Peroxide. *Sci. Rep.* **2019**, *9* (1), 1–9. https://doi.org/10.1038/s41598-018-36752-y.

(167) Elli, G.; Hamed, S.; Petrelli, M.; Ibba, P.; Ciocca, M.; Lugli, P.; Petti, L. Field-Effect Transistor-Based Biosensors for Environmental and Agricultural Monitoring. *Sensors* **2022**, *22*, 4178.

(168) Janićijević, Ž.; Nguyen-Le, T.-A.; Baraban, L. Extended-Gate Field-Effect Transistor Chemo- and Biosensors : State of the Art and Perspectives ˇ. *Next Nanotechnol.* **2023**, *3–4* (September), 100025.

https://doi.org/10.1016/j.nxnano.2023.100025.

(169) Angizi, S.; Selvaganapathy, P. R.; Kruse, P. Graphene-Silicon Schottky Devices for Operation in Aqueous Environments: Device Performance and Sensing Application. *Carbon N. Y.* **2022**, *194*, 140–153.

(170) Mikami, T.; Yamamoto, T.; Tomisaki, M.; Einaga, Y. Amine-Functionalized Diamond Electrode for Boosting CO2 Reduction to CO. *ACS Sustain. Chem. Eng.* **2022**, *10*, 14685–14692. https://doi.org/10.1021/acssuschemeng.2c02532.

(171) Trung, N. T.; Hossain, M. I.; Alam, M. I.; Ando, A.; Kitakami, O.; Kikuchi, N.; Takaoka, T.; Sainoo, Y.; Arafune, R.; Komeda, T. In Situ Study of Molecular Doping of Chlorine on MoS2field Effect Transistor Device in Ultrahigh Vacuum Conditions. *ACS Omega* **2020**, *5* (43), 28108–28115. https://doi.org/10.1021/acsomega.0c03741.

(172) Patel, V.; Kruse, P.; Selvaganapathy, P. R. Solid State Sensors for Hydrogen Peroxide Detection. *Biosensors* **2021**, *11* (9).

(173) Zubiarrain-Laserna, A.; Angizi, S.; Akbar, M. A.; Divigalpitiya, R.; Selvaganapathy, P. R.; Kruse, P. Detection of Free Chlorine in Water Using Graphene-like Carbon Based Chemiresistive Sensors. *RSC Adv.* **2022**, *12*, 2485–2496.

(174) Li, Z.; Ausri, I. R.; Zilberman, Y.; Tang, X. S. Towards Label-Free, Wash-Free and Quantitative B-Type Natriuretic Peptide Detection for Heart Failure Diagnosis. *Nanoscale* **2019**, *11*, 18347–18357. https://doi.org/10.1039/c9nr05386g.

(175) Li, J.; Wang, X.; Tang, J.; Li, F.; Wang, X.; Muhammad, T. A. D.; Hu, Z.; Wang, D.; Gong, Z.; Fan, M. Fingerprinting and Differentiation of Landfill Leachate and Domestic Sewage in Surface Water with Machine Learning Based Surface Enhanced Raman Spectroscopy. *ACS ES&T Water* **2024**, *4* (3), 1146–1154.

(176) Imbault, A.; Wang, Y.; Kruse, P.; Strelcov, E.; Comini, E.; Sberveglieri, G.; Kolmakov, A. Ultrathin Gas Permeable Oxide Membranes for Chemical Sensing: Nanoporous Ta2O5 Test Study. *Materials (Basel).* **2015**, *8* (10), 6677–6684. https://doi.org/10.3390/ma8105333.

(177) John, A. T.; Murugappan, K.; Nisbet, D. R.; Tricoli, A. An Outlook of Recent Advances in Chemiresistive Sensor-Based Electronic Nose Systems for Food Quality and Environmental Monitoring. *Sensors* **2021**, *21* (7). https://doi.org/10.3390/s21072271.

(178) Kumar, A.; Mazumder, J. T.; Joyen, K.; Favier, F.; Mirzaei, A.; Kim, J. Y.; Kwoka, M.; Bechelany, M.; Jha, R. K.; Kumar, M.; Kim, H. W.; Kim, S. S. Defect Engineering Approaches for Metal Oxide Semiconductor-Based Chemiresistive Gas Sensing. *Coord. Chem. Rev.* **2025**, *541* (March). https://doi.org/10.1016/j.ccr.2025.216836.

(179) Rahman, A.; Kumar, P.; Park, D.; Shim, Y. Electrochemical Sensors Based on

Organic Conjugated Polymers. *Sensors (Switzerland)* **2008**, *8*, 118–141.

(180) Zamiri, G.; Haseeb, A. S. M. A. Recent Trends and Developments in Graphene/Conducting Polymer Nanocomposites Chemiresistive Sensors. *Materials (Basel).* **2020**, *13* (15). https://doi.org/10.3390/ma13153311.

(181) Hangarter, C. M.; Chartuprayoon, N.; Hernández, S. C.; Choa, Y.; Myung, N. V. Hybridized Conducting Polymer Chemiresistive Nano-Sensors. *Nano Today* **2013**, *8* (1), 39–55. https://doi.org/10.1016/j.nantod.2012.12.005.

(182) Dube, A.; Malode, S. J.; Alodhayb, A. N.; Mondal, K.; Shetti, N. P. Conducting Polymer-Based Electrochemical Sensors: Progress, Challenges, and Future Perspectives. *Talanta Open* **2025**, *11* (November 2024), 100395. https://doi.org/10.1016/j.talo.2024.100395.

(183) Tomeček, D.; Fitl, P.; Vlček, J.; Marešová, E.; Vrňata, M. Detection of Taggants in Explosives on Nanostructured Metal/Silver Phthalocyanine Chemiresistors: Influence of Analyte Photoactivation. *Sensors Actuators, B Chem.* **2017**, *239*, 147–156. https://doi.org/10.1016/j.snb.2016.07.033.

(184) Sun, Y.; Wang, B.; Hou, Y.; Suematsu, K.; Zhao, Z.; Zhang, W.; Shimanoe, K.; Hu, J. Noble Metal Nanoparticles Functionalized Conductive Co3(Hexaiminotriphenylene)2 Chemiresistor for Hydrogen Sulfide Detection at Room-Temperature. *Chem. Eng. J.* **2023**, *465* (March), 142818. https://doi.org/10.1016/j.cej.2023.142818.

(185) Milyutin, Y.; Abud-Hawa, M.; Kloper-Weidenfeld, V.; Mansour, E.; Broza, Y. Y.; Shani, G.; Haick, H. Fabricating and Printing Chemiresistors Based on Monolayer-Capped Metal Nanoparticles. *Nat. Protoc.* **2021**, *16* (6), 2968–2990. https://doi.org/10.1038/s41596-021-00528-y.

(186) Hubble, L. J.; Cooper, J. S.; Sosa-Pintos, A.; Kiiveri, H.; Chow, E.; Webster, M. S.; Wieczorek, L.; Raguse, B. High-Throughput Fabrication and Screening Improves Gold Nanoparticle Chemiresistor Sensor Performance. *ACS Comb. Sci.* **2015**, *17* (2), 120–129. https://doi.org/10.1021/co500129v.

(187) Meng, Z.; Stolz, R. M.; Mendecki, L.; Mirica, K. A. Electrically-Transduced Chemical Sensors Based on Two-Dimensional Nanomaterials. *Chem. Rev.* **2019**, *119* (1), 478–598.

(188) Schroeder, V.; Savagatrup, S.; He, M.; Lin, S.; Swager, T. M. Carbon Nanotube Chemical Sensors. *Chem. Rev.* **2019**, *119* (1), 599–663.

(189) Cho, G.; Azzouzi, S.; Zucchi, G.; Lebental, B. Electrical and Electrochemical Sensors Based on Carbon Nanotubes for the Monitoring of Chemicals in Water—a Review. *Sensors* **2022**, *22* (1). https://doi.org/10.3390/s22010218.

(190) Chiu, S. W.; Tang, K. T. *Towards a Chemiresistive Sensor-Integrated Electronic Nose: A Review*; 2013; Vol. 13. https://doi.org/10.3390/s131014214.

(191) Neri, G. First Fifty Years of Chemoresistive Gas Sensors. *Chemosensors* **2015**, *3* (1), 1–20. https://doi.org/10.3390/chemosensors3010001.

(192) Akbar, M. A.; Sharif, O.; Selvaganapathy, P. R.; Kruse, P. Identification and Quantification of Aqueous Disinfectants Using an Array of Carbon Nanotube-Based Chemiresistors. *ACS Appl. Eng. Mater.* **2023**, *1* (11), 3040–3052.

(193) Angizi, S.; Huang, X.; Hong, L.; Akbar, M. A.; Selvaganapathy, P. R.; Kruse, P. Defect Density-Dependent PH Response of Graphene Derivatives: Towards the Development of PH-Sensitive Graphene Oxide Devices. *Nanomaterials* **2022**, *12*, 1801.

(194) Patel, V.; Akbar, M. A.; Kruse, P.; Selvaganapathy, P. R. A Reagent-Free Phosphate Chemiresistive Sensor Using Carbon Nanotubes Functionalized with Crystal Violet. *Analyst* **2023**, *148*, 3551–3558.

(195) Kirby, T.; Akbar, M. A.; Tavakkoli Gilavan, M.; Selvaganapathy, P. R.; Kruse, P. Carbon Nanotube-Based Chemiresistive Sensor Array for Dissolved Gases. *ACS Omega* **2024**, *9* (47), 46986–46996.

(196) Akbar, M. A.; Selvaganapathy, P. R.; Kruse, P. Optimization of Carbon Nanotube Percolation Networks for Broad Dynamic Range Detection of Permanganate in Water. *J. Phys. Chem. C* **2025**, *129* (30).

(197) Teh, K.; Lin, L. MEMS Sensor Material Based on Polypyrrole – Carbon Nanotube Nanocomposite : Film Deposition and Characterization. *J. Micromechanics Microengineering* **2005**, *15*, 2019–2027. https://doi.org/10.1088/0960-1317/15/11/005.

(198) Hsu, L. H. H.; Hoque, E.; Kruse, P.; Ravi Selvaganapathy, P. A Carbon Nanotube Based Resettable Sensor for Measuring Free Chlorine in Drinking Water. *Appl. Phys. Lett.* **2015**, *106*, 063102.

(199) Hoque, E.; Chowdhury, T.; Kruse, P. Chemical in Situ Modulation of Doping Interactions between Oligoanilines and Nanocarbon Films. *Surf. Sci.* **2018**, *676*, 61–70.

(200) Teverovsky, A. A Rapid Technique for Moisture Diffusion Characterization of Molding Compounds in PEMs. *EEE Links, NASA/GSFC* **2003**, *January*, *V*.

(201) Li, J. C.; Han, X. B.; Jiang, Y. H.; Ba, D. C. Theoretical Study of the Gas Sensitivity and Response Time of Metal Oxide Thin Films. *Thin Solid Films* **2011**, *520* (2), 881–886. https://doi.org/10.1016/j.tsf.2011.04.163.

(202) Khnykov, A. Y.; Vdovichenko, A. Y.; Chvalun, S. N. Nanostructured Materials for Gas Sensors. *Nanobiotechnology Reports* **2025**, *20* (2), 101–117. https://doi.org/10.1134/S2635167625600051.

(203) Thanihaichelvan, M.; Browning, L. A.; Dierkes, M. P.; Reyes, R. M.; Kralicek, A. V.; Carraher, C.; Marlow, C. A.; Plank, N. O. V. Metallic-Semiconducting Junctions

Create Sensing Hot-Spots in Carbon Nanotube FET Aptasensors near Percolation. *Biosens. Bioelectron.* **2019**, *130* (July 2018), 408–413. https://doi.org/10.1016/j.bios.2018.09.021.

(204) Wang, C.; Yin, L.; Zhang, L.; Xiang, D.; Gao, R. Metal Oxide Gas Sensors: Sensitivity and Influencing Factors. *Sensors* **2010**, *10* (3), 2088–2106. https://doi.org/10.3390/s100302088.

(205) Akbar, M. A.; Selvaganapathy, P R.; Kruse, P. Continuous Monitoring of Monochloramine in Water, and Its Distinction from Free Chlorine and Dichloramine Using a Functionalized Graphene-Based Array of Chemiresistors. *ACS ES&T Water* **2024**, *4* (9), 4041–4051.

(206) Yen, Y. K.; Lee, K. Y.; Lin, C. Y.; Zhang, S. T.; Wang, C. W.; Liu, T. Y. Portable Nanohybrid Paper-Based Chemiresistive Sensor for Free Chlorine Detection. *ACS Omega* **2020**, *5* (39), 25209–25215.

(207) Akbar, M. A.; Gilavan, M. T. Selvaganapathy, P R.; Kruse, P. Continuous Monitoring of Free Chlorine Level and PH Using an Array of Carbon Nanotube Chemiresistors. *ACS omega* **2025**, *10* (27), 29074–29086. https://doi.org/10.1021/acsomega.5c01256.

(208) Wu, R.; Gilavan, M. T.; Akbar, M. A.; Fan, L.; Selvaganapathy, P. R. Direct Transformation of Polycarbonate to Highly Conductive and Superhydrophobic Graphene/Graphitic Composite by Laser Writing and Its Applications. *Carbon N. Y.* **2024**, *216*, 118597.

(209) Mohtasebi, A.; Broomfield, A. D.; Chowdhury, T.; Selvaganapathy, P. R.; Kruse, P. Reagent-Free Quantification of Aqueous Free Chlorine via Electrical Readout of Colorimetrically Functionalized Pencil Lines. *ACS Appl. Mater. Interfaces* **2017**, *9* (24), 20748–20761.

(210) Hoque, E.; Hsu, L. H. H.; Aryasomayajula, A.; Selvaganapathy, P. R.; Kruse, P. Pencil-Drawn Chemiresistive Sensor for Free Chlorine in Water. *IEEE Sensors Lett.* **2017**, *1* (4), 4500504.

(211) Lebental, B.; Perrin, G. Uncertainty-Based Performance Evaluation of a Carbon Nanotube-Based Sensor Array Monitoring PH and Active Chlorine in Drink Water. *Int. Symp. Olfaction Electron. Nose, ISOEN 2022 - Proc.* **2022**, 1–3. https://doi.org/10.1109/ISOEN54820.2022.9789680.

(212) Perrin, G.; Lebental, B. Uncertainty-Based Calibration Method for Environmental Sensors - Application to Chlorine and PH Monitoring With Carbon Nanotube Sensor Array. *IEEE Sens. J.* **2023**, *23* (5), 5146–5155. https://doi.org/10.1109/JSEN.2023.3238900.

(213) Patel, V.; Saha, D.; Kruse, P.; Selvaganapathy, P. R. Reagent-Free Hydrogen Peroxide Sensing Using Carbon Nanotube Chemiresistors with Electropolymerized

Crystal Violet. **2022**. https://doi.org/10.1021/acsanm.1c04540.

(214) Patel, V.; Kruse, P.; Selvaganapathy, P. R. Flexible Chemiresistive Sensor with Xurographically Patterned Gold Leaf as Contact Electrodes for Measuring Free Chlorine . *2021 IEEE Int. Conf. Flex. Printable Sensors Syst.* **2021**, 1–4. https://doi.org/10.1109/FLEPS51544.2021.9469787.

(215) Tavakkoli Gilavan, M.; Igun, O.; Akbar, M. A.; Jahangirifard, S.; Kruse, P.; Selvaganapathy, P. R. Patterning of Nano and Micromaterials on Polymer Substrates Using Spraying, Selective Laser Treatment, and Adhesive Delamination for Sensing Applications. *Adv. Mater. Interfaces* **2025**, 2500027.

Chapter 3 Chemometrics

Chemometrics is the application of mathematical and statistical methods to chemical data to extract relevant information. It is used to build predictive models and guide experimental design. It is particularly valuable in handling multivariate datasets such as spectra, chromatograms, or sensor array responses, where univariate analysis cannot capture the underlying complexity. Chemometric tools such as principal component analysis (PCA), partial least squares regression (PLS), and clustering methods are used to transform raw measurements into meaningful chemical and process information.

3.1 Principal Component Analysis (PCA): Principal Component Analysis (PCA) is one of the most widely used multivariate statistical techniques in chemometrics and related fields. It provides a mathematical framework for reducing the dimensionality of complex datasets while keeping the most relevant information. It projects high-dimensional data onto a smaller number of orthogonal components and shows patterns, trends, and clusters that are often obscured in the raw measurements.[1] In the field of chemical sensing, spectroscopy, and materials characterization, researchers frequently deal with large datasets containing correlated variables. For example, absorbance values measured across hundreds of wavelengths, or sensor responses across multiple conditions, form high-dimensional datasets. Interpreting these data is not straightforward. PCA addresses this challenge by transforming the original correlated variables into new uncorrelated variables called principal components (PCs). The PCs are ordered such that the first few capture most of the variance in the dataset.[2]

3.1.1 Theory and Interpretation

The mathematical foundation of PCA lies in linear algebra and statistics. Consider a dataset represented as a matrix X with observations in rows and variables in columns. PCA decomposes X into the product of two smaller matrices and a residual error:

$$X = T P^T + E \tag{1}$$

Here, T is the score matrix, containing the projections of the original observations onto the

PCs. P is the loading matrix, containing the directions (eigenvectors) along which the variance is maximized. E represents the residual matrix, capturing unexplained variance.[1] The PCs are obtained by solving the eigenvalue problem of the covariance matrix of X. The first PC corresponds to the eigenvector associated with the largest eigenvalue and it captures the greatest variance in the data. Each subsequent PC captures the maximum remaining variance under the constraint of being orthogonal to the previous components. Scores provide information on how samples relate to each other, and loadings provide information on how variables contribute to observed patterns.

Score plots and loading plots are used to interpret PCA. Score plots reveal relationships among samples, such as clustering, grouping, or trends along process conditions. In sensing studies, for example, samples with different analytes exposures may form separate clusters along the first or second PC. Loading plots show how original variables contribute to each PC. In spectroscopy, loadings can highlight specific wavelength regions that drive the main variation. In sensor arrays, loadings may identify which sensors dominate the discrimination of certain analytes. Another key tool is the scree plot, which displays the explained variance for each component. This helps determine the number of components to retain. Typically, the first few components explain most of the variance, while the remaining ones capture noise.

3.1.2. Applications

PCA is widely used across chemistry, analytical sciences, and process monitoring. Its usage spans exploratory analysis, quality control, and data preprocessing. PCA simplifies interpretation of infrared, Raman, UV-Vis, and NMR spectra by highlighting key spectral features. For example, overlapping bands can be resolved into patterns that separate sample types or concentrations. Arrays of sensors functionalized with different materials often produce correlated responses.[3] PCA can reveal how different analytes separate in the score space, demonstrating the discriminating ability of the array. Loadings further indicate which sensors are most sensitive to specific compounds. In industrial chemistry and pharmaceuticals, PCA is used to detect deviations from normal operation by comparing real-time data against historical models. This provides early warnings about process drift or equipment faults. PCA also acts as a noise-reduction method by retaining only the major components and discarding minor ones dominated by random fluctuations.

As sensing technologies generate increasingly large and complex datasets, PCA is still a valuable first step in exploratory analysis. However, its integration with more advanced machine learning methods is growing. PC can also be used to predict concentration using principal component regression (PCR). PCA can serve as a dimensionality reduction technique before applying supervised algorithms like Partial Least Squares (PLS), Support Vector Machines (SVM), or Neural Networks. This hybrid approach enhances predictive modeling while ensuring interpretability.[4]

3.2 Partial Least Squares (PLS): Partial Least Squares (PLS) is one of the most important methods in chemometrics, especially when dealing with high-dimensional, noisy, or collinear datasets. Unlike multiple linear regression, which requires predictor variables to be independent, PLS can handle strongly correlated predictors and still produce robust, interpretable models. This makes it particularly valuable in analytical chemistry, spectroscopy, process monitoring, and sensor applications, where measurements often generate hundreds of interdependent variables.[5]

3.2.1 Theory and Interpretation: PLS models the relationship between two data matrices: X (predictor variables, such as spectral intensities or sensor responses) and Y (response variables, such as concentrations or properties). By projecting both X and Y into a shared low-dimensional latent variable space, PLS not only predicts Y from X but also captures the structure of both datasets.[6] Mathematically, the PLS decomposition can be written as:

$$X = T P^T + E \qquad (2)$$

$$Y = U Q^T + F \qquad (3)$$

Here, T and U are the score matrices representing projections of X and Y. P and Q are the loading matrices that describe how the original variables contribute. E and F are residuals not explained by the model. An important property of PLS is that the latent variables (T) are constructed to maximize the covariance between X and Y. This ensures that extracted components are not only good summaries of X but are also directly relevant for predicting Y.

Partial Least Squares Regression (PLSR) differs from PCR. In PCR, components are chosen to maximize variance in X only, while PLS selects components that simultaneously capture variance in X and their ability to predict Y.[7]

Interpretation of a PLS model is carried out using score, weights and loadings plot. Score plots (t-scores vs. u-scores) show how samples are distributed in the latent variable space, revealing clusters, trends, or outliers. Weight and loading plots indicate which predictors contribute most to the model; Y-weights (c) show how responses align with components.

Variable Importance in Projection (VIP) plot summarizes the contribution of each X-variable to explain Y across all components. Residual analysis also plays a critical role. Y-residuals indicate the predictive quality of the model, while X-residuals highlight outliers or samples that do not conform to the modeled relationship.

3.3.2 Applications

PLSR has become a standard tool in chemometrics, with applications ranging from laboratory analysis to industrial scale-up.[4] PLS is widely used in near-infrared (NIR), Raman, and UV-Vis spectroscopy to build calibration models that predict concentrations of analytes from spectral data. PLS relates molecular descriptors to chemical properties or biological activity, enabling rational design of compounds. In manufacturing, PLS enables real-time monitoring and control by linking multivariate sensor data (X) to quality attributes (Y).

In sensor networks, PLS models can disentangle overlapping responses and enable quantitative predictions. Validation is critical to ensure predictive reliability. It is done either by cross-validation when the data set is small or external validation with an independent data set. Iteratively leaves out subsets of data to estimate predictive performance. The predictive residual sum of squares (PRESS) and cross-validated R^2 (Q^2) are standard metrics.

An important extension of PLS is Partial Least Squares Discriminant Analysis (PLS-DA). While PLSR is used for quantitative prediction, PLS-DA is adapted for classification tasks, where the response variable Y encodes class membership rather than continuous values. By projecting X into latent variables that maximize separation between classes. PLS-DA is widely applied in metabolomics, food chemistry, and sensor-based classification.[8]

VIP (Variable Importance in Projection) plots are often used in both PLSR and PLS-DA to highlight which predictor variables contribute the most to explaining the variation in Y. A VIP score greater than 1 usually indicates a variable of high importance, while scores below 0.5 are often considered uninformative. These plots are valuable tools for variable selection, simplifying models, and improving interpretability.[9]

PLSR is a versatile and robust method for relating multivariate predictor and response spaces. Its ability to manage collinearity, noise, and multiple responses makes it indispensable in chemometrics, spectroscopy, and process monitoring. PLS links experimental measurement and predictive modeling by providing both interpretability and practical utility.

References

(1) Bro, R.; Smilde, A. K. Principal Component Analysis. *Anal. Methods* **2014**, *6* (9), 2812–2831.

(2) Tefas, A.; Pitas, I. Principal Component Analysis. *Intelligent Systems*. 2016. https://doi.org/10.2307/1270093.

(3) Yu, X.; Fu, L.; Wang, T.; Liu, Z.; Niu, N.; Chen, L. Multivariate Chemical Analysis: From Sensors to Sensor Arrays. *Chinese Chem. Lett.* **2024**, *35* (7), 109167. https://doi.org/10.1016/j.cclet.2023.109167.

(4) Martynko, E.; Kirsanov, D. Application of Chemometrics in Biosensing: A Brief Review. *Biosensors* **2020**, *10* (8). https://doi.org/10.3390/bios10080100.

(5) Roemer, E. A Tutorial on the Use of PLS Path Modeling in Longitudinal Studies. *Ind. Manag. Data Syst.* **2016**, *116* (9), 1901–1921. https://doi.org/10.1108/IMDS-07-2015-0317.

(6) Wold, S.; Sjöström, M.; Eriksson, L. PLS-Regression: A Basic Tool of Chemometrics. *Chemom. Intell. Lab. Syst.* **2001**, *58* (2), 109–130. https://doi.org/10.1016/S0169-7439(01)00155-1.

(7) Wentzell, P. D.; Montoto, L. V. Comparison of Principal Components Regression and Partial Least Squares Regression through Generic Simulations of Complex Mixtures. *Chemom. Intell. Lab. Syst.* **2003**, *65* (2), 257–279. https://doi.org/10.1016/S0169-7439(02)00138-7.

(8) Brereton, R. G.; Lloyd, G. R. Partial Least Squares Discriminant Analysis: Taking the Magic Away. *J. Chemom.* **2014**, *28* (4), 213–225.

(9) Lee, J.; Wang, J.; Flores-Cerrillo, J.; He, Q. P. Improving Featured-Based Soft Sensing through Feature Selection. *IFAC-PapersOnLine* **2020**, *53* (2), 11338–11343. https://doi.org/10.1016/j.ifacol.2020.12.542.

Chapter 4 Optimization of Carbon Nanotube Percolation Networks for Broad Dynamic Range Detection of Permanganate in Water

This chapter demonstrates the tunability of percolation networks of single-walled carbon nanotubes (SWCNTs) for chemiresistive sensing, with a focus on how network density influences detection range and sensitivity. By adjusting the density of the SWCNT film, three resistance regimes were identified, each suited to a specific concentration range of potassium permanganate. High resistance networks (∼25 kΩ) showed the highest sensitivity to trace concentrations (0.01–0.1 mg/L, LoD 0.0001 mg/L). Medium resistance networks (∼15 kΩ) provided stable responses in the intermediate range (0.2–1.6 mg/L, LoD 0.002 mg/L). Low resistance networks (∼5 kΩ) were most effective at higher concentrations (1–8 mg/L, LoD 0.03 mg/L). Spectroscopic pre-screening of the films was used to ensure reproducibility in fabrication and to guide the choice of network density for a desired application. In addition to density control, functionalization of the SWCNT networks was shown to enhance selectivity, stability, and long-term performance.

Reprinted with permission from the *J. Phys. Chem. C* **2025**, *129*, 32, 14583-14592, Md Ali Akbar, Ponnambalam Ravi Selvaganapathy, and Peter Kruse.

DOI:10.1021/acs.jpcc.5c03233

THE JOURNAL OF PHYSICAL CHEMISTRY C
A JOURNAL OF THE AMERICAN CHEMICAL SOCIETY
pubs.acs.org/JPCC
Article

Optimization of Carbon Nanotube Percolation Networks for Broad Dynamic Range Detection of Permanganate in Water

Published as part of The Journal of Physical Chemistry C special issue "Jacek Lipkowski Festschrift".

Md Ali Akbar, Ponnambalam Ravi Selvaganapathy, and Peter Kruse*

Cite This: *J. Phys. Chem. C* 2025, 129, 14583−14592
Read Online

ACCESS | Metrics & More | Article Recommendations | Supporting Information

ABSTRACT: Percolation networks of single-walled carbon nanotubes (SWCNTs) are widely used in chemiresistive sensors due to their tunable electronic properties, which control the sensitivity of the devices. This study explores the tunability of the electronic properties of SWCNT-based chemiresistive films by controlling the percolation network density. We demonstrate that simple spectroscopic measurements can ensure repeatability in the sensor fabrication process and that optimizing the percolation network can expand the useful detection range for the desired analyte. We show that percolation networks within three resistance ranges can be utilized to detect a disinfectant (permanganate), which has applications over a wide concentration range. Devices fabricated with the highest resistance (~25 kΩ) were shown to detect lower range concentrations of permanganate (0.01−0.1 mg/L, limit of detection, LoD 0.0001 mg/L), medium resistance devices (~15 kΩ) can detect midrange concentrations (0.2−1.6 mg/L, LoD 0.002 mg/L), and low-resistance devices (~5 kΩ) can detect high-range concentrations (1− 8 mg/L, LoD 0.03 mg/L), depending on the specific application. SWCNT networks can also be further functionalized to enhance the sensitivity, selectivity, and stability of the devices. This study highlights the potential of SWCNT percolation networks for customizable chemiresistive sensing in environmental monitoring and industrial applications.

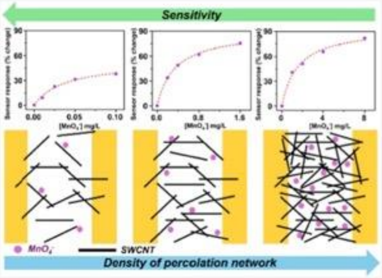

■ INTRODUCTION

Percolation networks are systems of randomly distributed conductive particles that form interconnected electrical pathways. The density of the conductive particles must reach a critical threshold to form a continuous conductive pathway for the electrical current to flow which is known as the percolation threshold.[1] As the particle density increases in the network, it transitions from an insulator (OFF state) to a conductor (ON state). The development and applications of conductive stick-like particles such as carbon nanotubes (CNTs) have been of great interest. Typically, different forms of CNT-based percolation networks are either incorporated in composites[1−4] or dispersed in thin films.[5,6] The electrical conductivity of a percolation network is dependent on the density of the CNTs[7,8] and the geometry[9] of the CNT film. One common application of percolation networks of 1D and 2D materials is in the active layers of electric transduction-based sensors such as chemiresistors[10−12] and field effect transistors[13−15] where the conductivity is monitored to detect the presence of an analyte. Chemiresistors work by changing the conductivity of the active layer when interaction occurs with the analyte. Owing to the ease of depositing single-walled carbon nanotubes (SWCNTs), they are a widely used material for percolation networks.

The electronic properties of an SWCNT percolation network can be tuned to enhance the performance of chemiresistive sensors. The density of the network plays a crucial role in the performance of the sensors. In the case of nanotubes, a lower density results in a lower conductance in the baseline due to fewer interconnected pathways. Sensors operating at lower conductance may result in high current gain relative to the baseline when exposed to analyte.[16,17] Gas sensing with polymer/carbon black composites showed that repeatability becomes an issue with thinner films despite higher gain.[16,17] This can be explained by the reduced mechanical robustness of the film/network as the number of conductive pathways in the network is reduced. The trade-off between sensitivity and robustness needs to be considered when designing sensors for specific applications that require low detection limits. The CNT percolation network can thus be

Received: May 11, 2025
Revised: July 25, 2025
Accepted: July 28, 2025
Published: July 31, 2025

tuned to specific requirements of different sensing applications.[18,19]

Permanganate (MnO_4^-) is an oxidant frequently used in water treatment in the form of potassium permanganate ($KMNO_4$). In the treatment plant, permanganate is used to oxidize dissolved iron (Fe^{2+}) and manganese (Mn^{2+}) into insoluble forms, which are then filtered and removed.[20,21] It is also used to remove phenol-type contaminants and odorous compounds from water.[22,23] Furthermore, permanganate is used to remove hydrogen sulfide by converting it to sulfur and sulfate compounds.[24,25] In a water treatment plant, dosing of MnO_4^- must be precisely optimized to ensure complete oxidation of Mn^{2+} such that no residual permanganate is left in the treated water.[26] Excess permanganate could lead to "pink water" complaints if it exits the plant. On the other hand, incomplete oxidation can cause precipitation of MnO_2 in the distribution pipes, which can lead to discoloration of water and consumer concerns.[26] Current techniques for detecting permanganate primarily rely on spectrophotometric measurements, both direct and indirect. At concentrations above 0.05 mg/L, MnO_4^- imparts a distinct purple color in water, allowing its direct colorimetric detection. The direct methods, even though they avoid additional chemicals, are not sufficiently reliable for samples with MnO_4^- concentrations below 0.75 mg/L.[27] Commercial real-time permanganate monitoring systems use direct UV–vis measurements with multiple wavelengths to accommodate a wide range of concentrations in municipal water.[28] This method requires expensive electronic accessories and can only detect down to about 0.02 mg/L of MnO_4^-.[28] Indirect methods offer high sensitivity but are time sensitive due to the use of unstable reagents like 2,2′-azino-bis(3-ethylbenzothiazoline-6-sulfonic acid (ABTS).[27] A sensitive single-particle detection (SPD) method utilizing dark-field optical microscopy on graphene nanoplatelet silver (GNP@Ag) core–shell nanoparticles has been reported. However, this approach is complex and requires sample preparation before analysis.[29] Additionally, these methods are not ideal for the online monitoring of disinfectants in a treatment plant setting. Therefore, a sensing platform is needed that can continuously monitor permanganate in water for a wide range of concentrations. To tackle this issue, we propose chemiresistive percolation networks of SWCNTs with tunable densities for a wide range (low-to-high) of permanganate detections in water.

We demonstrate a simple and effective method to characterize the density of the SWCNT networks to enhance the repeatability of chemiresistive device fabrication. We used the resistance/conductance of the channel of the sensors to gauge the density of the percolation network, as correlated to the optical density of the network is the visible-light range. Furthermore, we tuned the electronic properties of the chemiresistors by varying the density of the percolation network to detect a wider dynamic range of the analyte. The primary goal of this study was to optimize the SWCNT percolation networks for chemiresistive sensing through optical, electrical, and microscopic characterization. Permanganate ion sensing in water was chosen to illustrate an application of thickness-dependent chemiresistive sensing. We demonstrate that 0.001 mg/L permanganate can be detected by lowering the density of the networks (closer to the percolation threshold) and high concentrations (up to 8 mg/L) can be detected by increasing the density of the network. SWCNTs show nonspecific responses to analytes in water. We further demonstrate that functionalization of the SWCNT network with conjugated, planar, redox-active molecules could successfully enhance the sensor response of different densities of SWCNT networks.

■ EXPERIMENTAL SECTION

Materials. Potassium permanganate 99% $KMnO_4$ crystals, single-walled carbon nanotubes (SWCNTs, chirality (6,5), average diameter 0.78 nm, 95% carbon basis), sodium chloride (NaCl), sodium bicarbonate ($NaHCO_3$), *N*,*N*-diphenyl-1,4-phenylenediamine (DPPD), and methanol (CH_3OH) were purchased from MilliporeSigma. Type 1 ultrapure water (resistivity 18.2 MΩ·cm) was obtained from a Millipore Simplicity UV water purification system. Glass slides (VWR VistaVision, 75 × 25 × 1 mm^3, Cat. No. 16004418) were purchased from VWR. Copper tape (3M EMI Copper Foil Shielding Tape #1181, 1 in. wide) was purchased from 3M. Polydimethylsiloxane (PDMS, Sylgard 184 Silicon Elastomer) was purchased from Dow Chemicals.

Characterization. SWCNT networks were analyzed with a JEOL JSM-7000F scanning electron microscope (SEM) at 3.0 kV beam voltage. 1 × 1 cm^2 sized chips of Si/SiO_2 were used to prepare the samples for the microscopy analysis. The images of the sensing layers were captured on a Nikon Ni-E Eclipse upright microscope in transmitted bright-field mode with a 10*x*/0.3 air objective and a Hamamatsu flash 4.0 camera. All images were taken using NIS-Elements using the large image tool.

A ThermoScientific Orion Aquamate 8000 UV–vis spectrophotometer was used to analyze the SWCNT films on glass slides and solutions (permanganate and DPPD) in quartz cuvettes. For the film characterization, a clean glass slide was used as a blank, and the smooth side of the slides were used for the deposition of SWCNT. The contacts were drawn with silver paste (PELCO Conductive Silver Paint from Ted Pella Inc.). For solution measurements, solvents were used for blanks.

A Nanometrics HL 5500PC Hall effect measurement system was used to measure the Hall mobility of the SWCNT films.

Chemiresistive Sensor Fabrication. Sensors were fabricated using a slight modification of a previously reported method.[11,30] At first, a suspension of SWCNTs was prepared by combining 2–5 mg of SWCNTs with 15 mL of methanol in a glass vial. The suspension was then sonicated using an Elmasonic P30H Ultrasonic Cleaner at 37 kHz for 6 h. The sonicator was operated in sweep mode at 100% power while maintaining the water bath temperature at 30 °C. The suspension was stored at room temperature and sonicated for an additional 30 min immediately before each subsequent use.

The components of the sensors are shown in Figure 1. The glass slides were initially cleaned with methanol and air-dried. Two pencil patches were drawn on the frosted side using a 9B pencil. The slides were then heated on a hot plate to 100 °C. The SWCNT suspension was airbrushed over and between the pencil patches until the desired resistance was achieved. After allowing the slides to cool to room temperature, two pieces of adhesive copper tape were applied to the pencil patches. The contacts were then covered with a thick layer of partially cured PDMS. PDMS was partially cured at room temperature for 5–6 h until the desired viscosity for coating was achieved. The sensors were then fully cured at 60 °C for 1 h. After cooling the sensors on the hot plate, the sensors were stored inside a glass

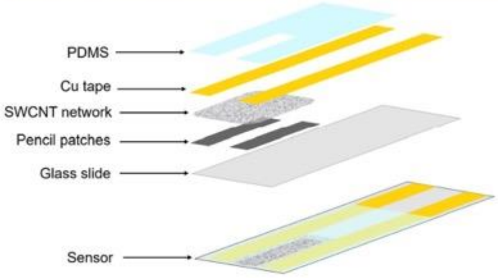

Figure 1. Fabrication of the SWCNT chemiresistive device. (a) Schematic of each of the basic components of the device (top) and the device geometry (bottom).

container in a nitrogen atmosphere. The exposed sensing area was found to be 0.9 × 1.5 cm^2 after the fabrication steps. A photograph of an actual device is shown in Figure S1.

Functionalization. A saturated solution of DPPD was first prepared by dissolving solid DPPD in methanol. Then, one part of the saturated solution was diluted by adding 9 parts (by volume) of methanol to prepare a 10% saturated DPPD solution. After connecting the sensors to the eDAQ electronics, they were functionalized by submerging them in a DPPD solution for 2–3 h. The evaporation of the solvent was minimized by covering the container around the sensor. The current passing through the channel during functionalization was monitored. After a stable response was reached, the sensors were then cleaned with methanol to remove excess molecules from the surface. Then, the surface of the sensors was dried for 5 min in air before placing them in the background solution (for 12–16 h) for sensor equilibration.

Device Fabrication for Hall Measurements. Hall measurement samples were prepared by using Van der Pauw patterns and clover-leaf contact positions. Silicon wafers (Virginia Semiconductor) were thermally oxidized to grow a 1 μm thick layer of silicon dioxide (SiO_2) for electrical insulation. After the oxidation, the wafers were diced into 1 × 1 cm^2 pieces by using a dicing saw. The wafer pieces were then cleaned by rinsing with acetone, followed by methanol and deionized water, and dried with nitrogen gas before being stored in a nitrogen box for future experiments. To reduce contact resistance, Cr (20 nm)/Au (200 nm) pads, measuring 3 × 3 mm^2, were sputter-deposited onto the four corners of each sample (Figure S2). The SWCNT film is airbrushed onto the substrate, such that a uniform density is achieved.

Sensor Characterization. Sensor data was acquired using several eDAQ Quad Multi-Function isoPod (EPU452) setups. Each setup allowed us to connect two eDAQ units to a single computer, with each eDAQ providing four channels. A 10 mV potential bias was applied across the sensor film, and the current was monitored over time. The instrument was configured to Biosensor mode with a data acquisition rate of either 10 or 15 measurements per minute and a current range of 20 μA. A pH electrode (Fisherbrand accumet Gel-Filled Polymer Body Single-junction pH Combination Electrode) and an ORP electrode (Ionode IJ-64) were connected. The pH electrode was calibrated before each experiment using buffer solutions with pH values of 7 and 10. All chemiresistive sensing measurements were carried out in phosphate buffer background prepared by dissolving phosphate-buffered saline (PBS) tablets (Sigma-Aldrich) in ultrapure water. In all cases, a 0.005 M phosphate buffer background was maintained.

Data Analysis. Raw sensor responses were measured as current (nA) using the eDAQ. The data from the last 2 min were averaged for each of the MnO_4^- concentrations and compared to the baseline current, I_0 (0 mg/L MnO_4^-). The sensor response (% change) was determined by calculating the change in current ($\Delta I = I - I_0$) and dividing this by the baseline current (I_0).

$$\text{Response (\% change)} = \frac{I - I_o}{I_o} \times 100\% \quad (1)$$

The fitting parameters were generated using the Origin Pro 2025 software. The average percent changes were fed into the software to fit into a model.

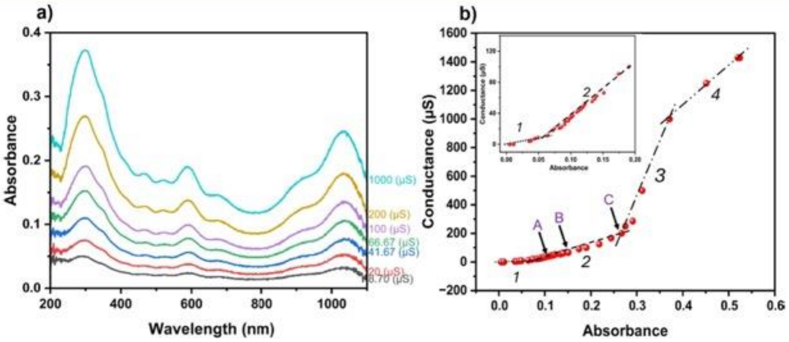

Figure 2. Optical characterization of the SWCNT networks using UV–vis spectroscopy. (a) Absorbance spectra of SWCNT networks with conductances ranging from 6.7 μS to 1000 μS, plotted as a function of wavelength (nm). The data highlight the optical absorption properties of the networks across the wavelength range of 200 to 1100 nm. (b) Film conductance plotted as a function of absorbance at a wavelength of 305 nm. Here, the SWCNT suspension was airbrushed onto the channel between two contacts to cover the range from the conductor to insulator. The inset shows a zoomed-in version of the graph at low absorbances, highlighting the range up to 0.3. The resistances of the channel measured under the same condition ranged from 234 kΩ to 0.7 kΩ. Representative conductance values (A, B, C) are shown for key sensor ranges: (A) 24 kΩ (high), (B) 15 kΩ (medium), and (C) 5 kΩ (low).

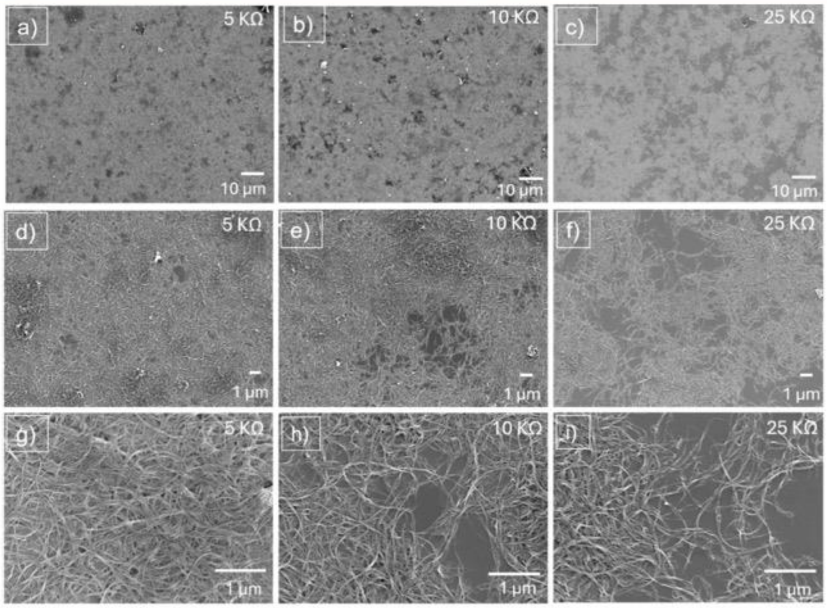

Figure 3. SEM images of the SWCNT films with different resistances (5, 15, and 25 kΩ). First row images (a, b, and c) were taken at ×1000 magnification, second row images (d, e, and f) represent × 5000 magnification, and third row shows images (g, h, and i) taken at ×22000 magnification. The CNT networks were prepared on Si wafer in a similar way as deposited on to the sensors.

RESULTS AND DISCUSSION

Characterization of the SWCNT Percolation Network.

SWCNTs are widely used for solid-state electrical sensors such as chemiresistive and FET devices, where the electrical properties of SWCNTs are modulated by the analyte. The density of nanotubes grown or deposited on a substrate contributes to the electrical properties (conductivity). Facile fabrication methods such as drop casting, spray casting, and spin coating are most commonly used to make conductive percolation networks. Uniformity and homogeneity of the network are desired to achieve a more repeatable outcome (sensor response) from the interactions of CNTs and analytes. The thickness of the CNT networks is challenging to measure, since the networks are not uniform and loosely packed. The two properties that can be monitored to control the percolation networks are resistance/conductivity and transmittance/absorbance. Here, we studied the relationship of the conductance and absorbance to gauge the properties of percolation networks used for the chemiresistive sensor. The selected geometry of the chemiresistive film (0.9×1.5 cm^2) was previously reported by us as optimized for free chlorine sensors.[31] For ease of comparison, we use the same geometry here to conduct optical characterization of networks with a varied density. We utilized a simple setup consisting of a UV−vis spectrometer (to record the absorbance) and a two-probe configuration (with a multimeter) to study the optical and electrical properties of networks consisting of 95% semiconducting SWCNTs. Figure 2a shows the absorbance spectra collected in the wavelength range of 200 to 1100 nm for percolation networks with different conductances. The characteristic SWCNT peaks were present in the UV−vis spectra.[31,32] With increasing nanotube density in the network, the absorbance also increased. The electrical conductance of the networks was found to increase along with the optical absorbance of the networks.

The maximum peak intensities of the networks at 305 nm can be related to their conductance (Figure 2b). As more and more SWCNTs were airbrushed on to the substrate, the channel between the contacts became more conductive due to the addition of interconnected pathways for the flow of charge carriers. The conductivity of the network is related to the density of the nanotubes by the following standard percolation theory of power law eq 2,

$$\sigma \propto (N - N_c)^{\alpha} \tag{2}$$

where σ refers to the conductivity in three dimensions and N is the nanotube density. N_c is the critical nanotube density at which the network shows the first conductive pathway, also known as the percolation threshold.[33] α is the critical exponent, with a theoretical value of 1.33 for a 2D network and 1.94 for a 3D network.[34] Therefore, the conductivity increases faster in 3D networks. The sharp increase in the conductivity represents the transition of a highly insulating channel into a conductive network. In our date, a sharp increase in conductance can be observed when the absorbance increases from 0.035 to 0.059. This suggests that this range of conductance marks the percolation threshold for this geometry. Four dotted lines are drawn (1 to 4) to represent four slopes exhibiting four regimes of the conductance curve. A conductive pathway was first observed at an absorbance value of 0.035 with a conductance of 4.27 μS (resistance = 234 kΩ). Therefore, region 1 is below the percolation threshold of the network. Region 2 represents the formation of a 2D network as

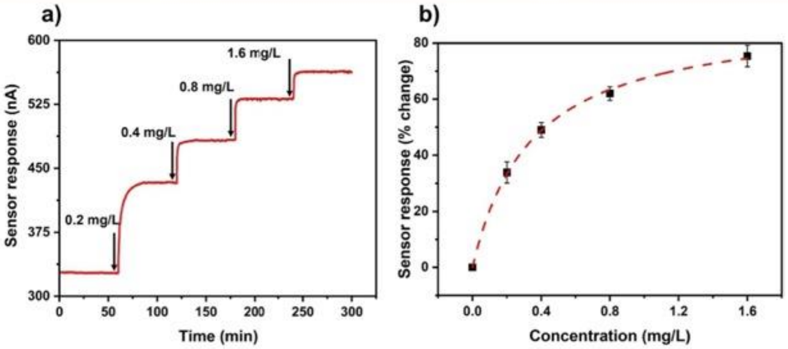

Figure 4. Characterization of the chemiresistive device in permanganate (MnO_4^-) solution. (a) Raw sensor response of a 15 kΩ resistance device as current change (nA) plotted against time (minutes) for the spiking of MnO_4^-. The arrow represents the point of MnO_4^- addition. 0.2 mg/L MnO_4^- was added in the background solution with 0 mg/L MnO_4^-. (b) Calibration graph of three devices as the percent change (% change) sensor current response plotted against the concentration of MnO_4^- (mg/L). The dots represent average values and error bars represent the standard deviation of the responses to corresponding concentrations. The dotted line is the Langmuir adsorption isotherm fit. The model parameters for the sensor are $A = 90.5 \pm 1.8\%$ and $B = 2.92 \pm 0.17$ mg^{-1} L for an R^2 value of 0.99.

the density of the stick-like particles increases in the 2D plane. A third slope (region 3) arises in the conductance curve where the conductance changes 10 times with each doubling of the absorbance, likely due to the network growth transitioning to 3-dimensional. The onset of region 4 represents the transition from a percolation network to a bulk material. Fabricating electrical devices just above the percolation threshold can enhance the sensitivity of the electrical transduction at the expense of the mechanical stability of the channel. Water-quality monitoring chemiresistors operating in aqueous environments experience harsher conditions and more mechanical stress than chemiresistive gas sensors; hence, a lack of stability of the channel poses significant challenges with repeatability during continuous online operation. This straightforward characterization of the network provides a yardstick to follow to stay away from the percolation threshold while fabricating devices exhibiting greater stability at the aqueous interface.

To investigate the morphology of the percolation networks, varying CNT network densities were characterized by SEM. We chose three types of networks based on the measured resistances due to their relevance in the fabrication of chemiresistors; they were labeled as low (5 kΩ), medium (15 kΩ), and high (25 kΩ). We used the same method to deposit the SWCNT networks on the Si/SiO_2 substrate. Figure 3 represents three columns for the three types of networks: left column (5 kΩ), middle column (15 kΩ), and right column (25 kΩ). The first row (Figure 3a, b, and c) shows the 1000× magnified images of the three types of networks. Figure 3a shows a network appearing like a continuous film. As this is the densest film out of the three, we see the most densely packed network here compared with 3b and 3c. Figure 3c shows that the 25 kΩ network has more openings in the film than the lower resistance films (10 and 5 kΩ). Figures 3d, e, and f show the 5000× magnified SEM images of the three networks. Here, it is clearly visible that the films are mostly uniform with patches present in the film. CNTs are randomly distributed on the substrate with no apparent preference in orientation. At the lower resistances (Figures 3d, 5 kΩ), agglomeration of the nanotubes is also visible. This could be because of rearrangements of the nanotubes at higher density. 22000× magnified SEM images (Figure 3g, h, i) show that the CNT networks are made of bundles of CNTs. Occasional CNT thick spots represent agglomeration of the CNTs. These spots are more commonly seen in films with lower resistance due to the overall larger amount of CNTs sprayed to achieve the desired resistance. The 25 kΩ film has a network with the least number of interconnections between the nanotubes leading to a low conductance. The CNT network with the lowest resistance has more uniformity and homogeneity than the high resistance ones. This could have impacts on the stability of the film in aqueous media. We have provided images of the sensing layer in Figure S4. Overall, percolation networks of CNTs can be modified to tune the electrical properties from a highly resistive network (by staying closer to the percolation threshold) to a conductive film (by moving away from the threshold).

Chemiresistors Using a Percolation Network of CNTs. Percolation networks of carbon nanotubes (CNTs) are tunable and useful in devices where electrical changes enable distinct functional responses, such as chemiresistors and ChemFETs. In this study, we fabricated chemiresistive devices by airbrushing SWCNT networks onto glass slides. Resistance was monitored in real time during deposition using a multimeter. The exposed portion of the CNT network (0.9 × 1.5 cm^2) was immersed in water, and current was continuously measured under a constant bias.

A representative chemiresistive response graph collected using an unfunctionalized device with 15 kΩ is shown in Figure 4a. The baseline response was achieved by keeping the devices in a stirred water background to reach equilibrium. Then, 0.2 mg/L of MnO_4^- was added from a stock solution of $KMnO_4$. The sensors showed an increase in current as MnO_4^- was added which is consistent with previous studies on oxidant sensing with chemiresistive devices.[11,35] This increase in current is due to the doping induced by the MnO_4^-.[36] The surface of the SWCNT is inherently p-doped due to the adsorption of oxygen functionalities upon exposure to air. MnO_4^- is an oxidizing agent, and when in contact with the SWCNT network, it withdraws electrons from the surface. As MnO_4^- takes electrons from the surface, the concentration of holes increases in the film, increasing the conductivity measured across the network. As we add more MnO_4^- in the solution (Figure 4a), the sensor response increases. The saturation of the response at higher concentration is lower due to the surface reaching maximum coverage with MnO_4^-. To create a calibration graph of the device, the percent change of the sensor response is calculated using eq 1 and then plotted against the concentration of MnO_4^-. Figure 4b shows a typical calibration graph where the percent change in response is shown as a function of the concentration of MnO_4^- present in the solution. The data points are fitted with a Langmuir adsorption isotherm-style equation:[12,37]

$$\% \text{ Response} = \frac{\text{ABc}}{1 + \text{Bc}} \tag{3}$$

Here, c is the concentration of MnO_4^- (mg/L). A and B are fitting parameters. Parameter A is the maximum theoretical response that can be achieved from the sensor, and parameter B is the binding constant (also known as the equilibrium constant) of the analyte (MnO_4^-) to the surface of the active element (SWCNT). Parameter A refers to the upper limit of detection for a particular density/resistance of the SWCNT network, representing the response (% change) when all available sites are fully occupied. A higher B value signifies that the particular SWCNT network reaches its maximum response faster than the one with a lower value. Both parameters give insights about the sensitivity of a chemiresistive sensor to a particular analyte and depend on the thickness or density of the transducing film.[37] This Langmuir adsorption-like model assumes that the functionalized SWCNT network can accommodate no more than a monolayer coverage of MnO_4^-, which is a plausible assumption, given its negative charge. For Figure 4b, the fitting parameters are $A = 90.53 \pm 1.82\%$ and $B = 2.92 \pm 0.17$ mg^{-1} L, and the maximum detectable concentration can be calculated for a 95% coverage to be 6.51 mg/L.

We conducted Hall measurements to determine the sheet Hall resistance coefficient, which provides insights into the type (n-type or p-type) and density of charge carriers in the semiconducting SWCNT network. This determines whether the dominant charge carriers are electrons (expressed by a negative coefficient, n-type) or holes (expressed by a positive coefficient, p-type). The Hall coefficient R_H can be calculated by using the following equation:

$$R_H = \frac{V_h \cdot t}{I \cdot B} \tag{4}$$

Here, V_h is the Hall voltage measured, I is the current applied, B is the magnetic field, and t is the density of the network layer. For the purpose of the Hall measurements, gold contacts were sputtered on a Si wafer. $I-V$ measurements confirmed that the contacts were Ohmic in nature. The data reported here was taken with samples that showed a good linear relationship and the same slope on the graphs for the different contact pairs (Table S1). As expected, the bare SWCNT network has a positive sheet Hall resistance coefficient of $+0.49 \pm 0.01$ m^2/C, which indicates that holes are the dominant charge carrier. When the SWCNTs were exposed to methanol, the coefficient decreased to $+0.30 \pm 0.01$ m^2/C because n-doping by the methanol partially counteracted the p-doping of the SWCNTs. The increase in the sheet resistance upon exposure to methanol is in agreement with the data gathered from the chemiresistive devices. When the SWCNT network is exposed to 4 mg/L of aqueous MnO_4^-, an increase in the Hall resistance coefficient is observed, consistent with the sensor data indicating p-doping when exposed to MnO_4^-.

Hall mobility is indicative of how quickly electrons or holes (charge carriers) move through the SWCNT network when an electric field is applied. Hall mobility (μH) can be calculated from the sheet Hall coefficient (R_{Hs}) and the sheet resistivity (ρ_s) as shown in eq 5.

$$\mu \text{H} = \frac{R_{Hs}}{\rho_s} \tag{5}$$

Hall mobility is independent of the sample geometry and the density of the layer. The Hall mobility data in Table S1 shows that methanol significantly reduces the hole mobility in the SWCNT network from 20.67 ± 0.61 $cm^2/(V \cdot s)$ to 11.38 ± 0.48 $cm^2/(V \cdot s)$. MnO_4^- increased the mobility to 24.20 ± 1.61 $cm^2/(V \cdot s)$.

MnO_4^- Sensing Using Different Percolation Network Densities. Percolation networks with different densities were fabricated by controlling the deposition of the SWCNTs between the pencil patches to investigate the effect of the network density on MnO_4^- sensing. Previously reported chemiresistors were based on SWCNT networks with resistances ranging from 10 to 20 kΩ.[11,30] Here, we aimed to achieve three resistances (5 kΩ, 15 kΩ, 25 kΩ) by limiting the CNT deposition at the beginning of the fabrication step. The actual resistances of the devices for the low range were 4.9 kΩ, 5.0 kΩ, and 5.0 kΩ; for the medium range were 15.0 kΩ, 15.0 kΩ, and 15.1 kΩ; and for the high range, 24.8 kΩ, 25.1 kΩ, and 25.1 kΩ. For the following discussion, the ranges will be referred to as low (or 5 kΩ), medium (15 kΩ), and high (25 kΩ). The sensors are then tested for three concentration ranges of MnO_4^- solutions. The sensors with 25 kΩ are considered to have the sparsest network; therefore, a lower concentration range (0.01−0.1 mg/L) is tested. Figure S5 shows the Langmuir-adsorption-fitting calibration graph for the 25 kΩ sensors. The sensors detected low concentrations (0.01 mg/L) of MnO_4^- with a $9.0 \pm 1.8\%$ current response; however, they could potentially saturate at 0.71 mg/L MnO_4^- when 95% of the surface is occupied with an analyte. Parameter A for the calibration graph provides the maximum saturation of the sensor response, and 95% of the sensor response was used to calculate the maximum detectable concentration for the 25 kΩ sensors. However, the sensitivity decreases at higher concentrations. Utilizing fitting parameters A (maximum theoretical response) and B (equilibrium binding constant), the limit of detection (LOD) was calculated for the 25 kΩ sensor to be 0.0004 mg/L. Figures S6 and S7 show the calibration graphs for the sensors with 15 kΩ detecting midrange concentrations (0.2−1.6 mg/L) and 5 kΩ measuring high-range concentrations (1−8 mg/L). With an increase in the SWCNT density in the channel, the saturation response (parameter A) increased upon exposure to high concentrations. Parameter B for the three fitted graphs decreased with decreasing resistance of the network. This decrease in parameter B with increasing network density causes the detection range to extend to higher concentration, at the cost of a decrease in sensitivity of the sensors. Comparing the sensor responses for 0.1 mg/L MnO_4^- across all three sensor types reveals that denser networks yield lower responses: the high-range sensor gives 38.46%, the medium-range sensor 20.6%, and the low-range sensor only 6.01%. The difference in

https://doi.org/10.1021/acs.jpcc.5c03233
J. Phys. Chem. C 2025, 129, 14583−14592

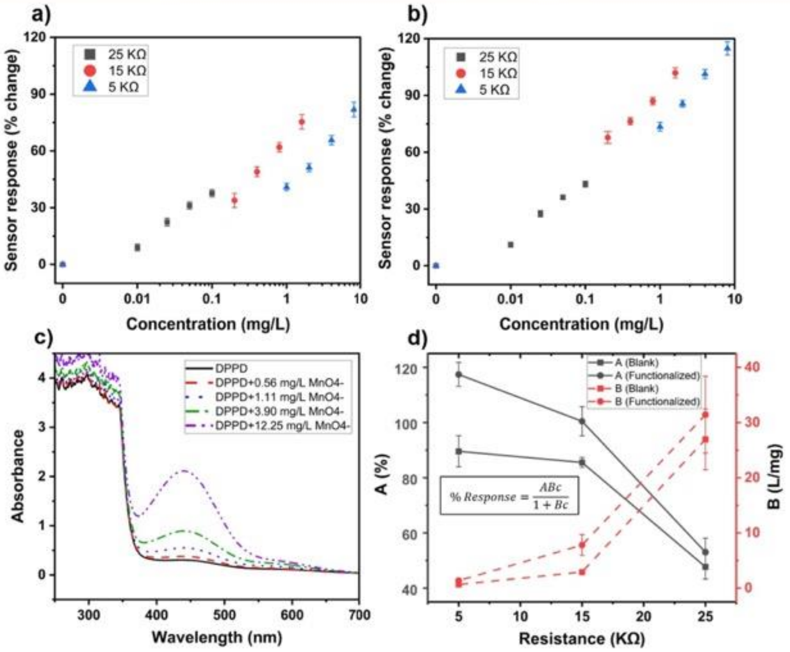

Figure 5. Electrical and spectrophotometric characterization of devices (unfunctionalized and functionalized) and DPPD solution with permanganate ions. (a) Unfunctionalized sensor responses as the percent change (% change) plotted as a function of the concentration of permanganate. (b) DPPD-functionalized sensor responses as the percent change (% change) plotted against the concentration of permanganate. The error bars in the sensor responses in Figure 5a and b are the standard deviations of the responses of three devices and the data points are average responses of the three devices for specific concentrations. The wide concentration ranges are accommodated by using a log scale to visualize the difference. The data points are also visualized separately in the Supporting Information (Figures S4–S6, S8–S10). (c) UV–vis spectra of DPPD only, and DPPD with increasing concentrations of MnO_4^-. In all cases, methanol was used as the solvent. (d) The A and B parameters of the Langmuir adsorption isotherm model fitted to the data points shown in Figure 5a and b are plotted against the resistance of the sensor. The equation in the graph is the Langmuir adsorption isotherm-like model where % response is the sensor response and c is the permanganate concentration. Parameters A and B were calculated after fitting the sensor responses of unfunctionalized and functionalized sensors. The error bars in Figure 5a and b represent standard deviation of the responses from three devices. The error bars in Figure 5d represent the deviation of the parameters generated when the Langmuir model was fitted by cross validating the data points.

sensitivity of the networks can be explained by the available number of conductive pathways. When less dense networks are exposed to low concentrations of MnO_4^-, fewer analyte–network interactions can have a larger impact on the network conductance due to the smaller number of pathways. Denser networks (lower resistance) require more analyte interactions for the same degree of current modulation. Furthermore, in a 3D network, parts of the network may become inaccessible to the analyte and an unmodulated shunt current will pass through the bulk of the network while only the surface interacts with the analyte. Less dense networks provide better sensitivity but saturate at low concentrations of the analyte due to limited charge carrier capacity. Denser networks perform better at higher concentrations as the analytes can percolate through the networks. Therefore, the density of the network needs to be tuned to cover the appropriate concentration range for each specific application.

We investigated the functionalization of SWCNT networks to enhance the sensitivity of sensors to MnO_4^-. Here, we selected DPPD, a molecule that shows reversible redox characteristics in oxidizing and reducing environments through the two amine groups.[11,38] Its planar and conjugated structure is appropriate for noncovalent functionalization of SWCNT networks. The inherently p-doped SWCNT surface shows a decrease in current when the sensor is placed in methanol (Figure S8) due to charge transfer from methanol to SWCNTs, counteracting p-doping with an n-doping effect. Further counteraction of p-doping of the SWCNTs is observed as a current change in Figure S8 when DPPD is introduced. This is due to more electron donation from the reduced form of DPPD to the SWCNTs as DPPD molecules are adsorbed onto the surface through π–π interactions. The current stabilizes as the sensor film approaches complete coverage of DPPD molecules. The sensor response can be explained by a charge transfer mechanism where the conductivity of the SWCNTs is influenced by the transfer of electron density from the DPPD layer in its reduced form. When permanganate ions interact with DPPD, the amine groups are oxidized to the imine groups. This switches the molecules from n-dopants (amine) to p-dopants (imine) of the inherently p-doped SWCNT network, thereby increasing the conductivity of the network. Figure 5b shows the sensor responses for the

https://doi.org/10.1021/acs.jpcc.5c03233
J. Phys. Chem. C 2025, 129, 14583–14592

functionalized sensors. Figures S9−S11 show the sensor responses fitted with Langmuir adsorption isotherms. Though the trend of the sensor responses does not differ from the unfunctionalized sensors, the functionalized sensors show an overall higher response. DPPD, when exposed to oxidizing chemicals, can transform into a fully oxidized phenyl terminated dimer, also known as *N*,*N*′-diphenyl-1,4-benzoquinone-diimine (B2Q1) from its fully reduced state.[11] The redox reaction is a reversible two-electron process (Figure S12). The fully reduced form of DPPD with two amine groups can be half-oxidized to an intermediate semiquinoid form with one amine and one imine group. The semiquinoid form can then be oxidized to the fully reduced form B2Q1 with two imine groups. The redox process can be characterized by UV−vis spectroscopy (Figure 5c). The solid line showed the curve for the completely reduced DPPD. As MnO_4^- was added, the oxidized state of DPPD (B2Q1) started to form, and a band started appearing at ∼439 nm. This band is associated with the presence of quinoid (− N =) rings in B2Q1.[39] Increasing the concentration of MnO_4^- increases the intensity of the band, representing more DPPD being oxidized to B2Q1. The typical peaks for MnO_4^- were not observed in the spectra when DPPD was added, as shown in Figure S13.

The fitting parameters (A and B) of the data points shown in Figure 5a and b can be used to elucidate the effect of the density of the network. Figure 5d presents the parameters plotted as a function of the resistance of the sensing layer. The maximum sensor response (parameter A), which is a modifier of the sensor response in the Langmuir adsorption model (eq 3), decreased with increasing resistance (less dense network). A denser network (low range resistance) therefore provides a higher sensor response compared with the less dense network (high range resistance). On the other hand, parameter B as a modifier of the concentration in the model increases with increasing resistance, thus shortening the useful concentration range at the higher end for higher resistance networks. However, high values for parameter B improve the sensor responses at low concentrations (eq 3). The sensitivity of the devices thus depends on a combination of both parameters.

The effect of functionalization of the sensing device can also be noticed in the resulting increase of fitting parameters A and B (Figure 5d). The functionalization of the SWCNTs with DPPD created more active sites on the network for the analyte to interact, resulting in an overall larger response (parameter A) and more facile interaction with the analyte (parameter B). The sensitivity of the devices is thus improved by functionalization as a result of both of these parameter changes. Tuning the parameters can be used to engineer sensors for specific applications. To detect low concentrations of the analyte, less dense films can be used. We have tested the sparser networks for 0.001 mg/L (or 1 ppb) of permanganate, and a good sensor response was achieved (Figure S14a), while no response was noticed with the standard detection method (S14b). The limit of detection (LoD) for the sparser networks (25 kΩ) was calculated to be 0.0001 mg/L for the unfunctionalized devices. For higher concentrations, thicker films are desired. Assuming that a response of 95% of A is achieved, using parameters A and B values for a specific sensor and eq 3, we can calculate the concentration that can be measured by a unfunctionalized sensor (25 kΩ), which is 0.71 mg/L. The maximum concentration that can be detected by a 15 kΩ sensor is 6.51 mg/L and by a 5 kΩ sensor is 29.01 mg/L. Therefore, the ability to tune the network density opens the opportunity for a wide range of sensing applications. This principle can be applied to any analyte that meaningfully alters the electrical response of a suitably functionalized chemiresistive sensor.

■ CONCLUSION

Controlling the density of a percolation network is crucial in the fabrication of sensitive and durable chemiresistive devices for aqueous measurements. In this study, we examined percolation networks of carbon nanotubes to fabricate devices to accommodate wide detection ranges. We characterized the SWCNT percolation networks by UV−vis for optical density. With increasing density of the SWCNT networks, their transmittance decreased due to increasing optical density. SEM confirmed that lowering the resistance by depositing nanotubes increased the interconnectivity between the SWCNTs. The microscopy images showed that the connection density among the nanotube layer varies with the amount of SWCNT deposited, and the deposition method produces good quality networks. Hall measurements were used to characterize the electronic property changes in the devices. We showed that aqueous MnO_4^- p-dopes the SWCNTs of the sensors resulting in an increase in current. The sensor responses fit a Langmuir adsorption isotherm-like model showing that sensor responses can saturate at higher concentrations. We modified the percolation network of SWCNTs to incorporate a wide range of detections of MnO_4^-. The resistance of the network is utilized for quality control of the networks for different detection ranges. We show that low-range concentrations (0.01 mg/L−0.1 mg/L) can be detected by high-resistance (25 kΩ) sensor films (in the given geometry), midrange concentrations (0.2 mg/L−1.6 mg/L) can be detected by medium resistance (10 kΩ) films, and high-range concentrations (1 mg/L−8 mg/L) can be detected using low-resistance (5 kΩ) sensors. Correlation of the Langmuir adsorption parameters and resistance/density has been observed, and it has been demonstrated that thinner networks are more sensitive to a low concentration of analytes. Continuing on our previous work with these type of devices that showed stability to measure disinfectants for at least 6−8 weeks,[11] and continuous monitoring of multivariate analytes in simulated tap water,[30] we have demonstrated that the percolation network of nanocarbons can be tuned to cover a wide detection range for specific water quality applications. Sensitivity and selectivity can be increased by functionalizing the percolation network by adding selective molecules.[40,41] Simple noncovalent functionalization with molecules was shown to enhance sensor performance and stability during the 6−8 weeks of measurements.[11,30] Here, we have demonstrated that functionalization of the networks with redox-active molecules (DPPD) can enhance the performance of sensors covering the three different targeted concentration ranges of MnO_4^-. This cost-effective modification technique to accomplish a broader range of detection could be implemented to other analytes and platforms[42] where a similar transduction method is used as a sensing principle.

■ ASSOCIATED CONTENT

Supporting Information

The Supporting Information is available free of charge at https://pubs.acs.org/doi/10.1021/acs.jpcc.5c03233.

Additional experimental details, including photographs of the devices, Hall measurement data, UV−vis spectra, chemiresistive measurement data, and calibration curves (PDF)

AUTHOR INFORMATION

Corresponding Author

Peter Kruse − *Department of Chemistry and Chemical Biology, McMaster University, Hamilton, Ontario L8S 4M1, Canada;* orcid.org/0000-0003-4051-4375;
Email: pkruse@mcmaster.ca

Authors

Md Ali Akbar − *Department of Chemistry and Chemical Biology, McMaster University, Hamilton, Ontario L8S 4M1, Canada;* orcid.org/0000-0002-1809-8232
Ponnambalam Ravi Selvaganapathy − *Department of Mechanical Engineering and School of Biomedical Engineering, McMaster University, Hamilton, Ontario L8S 4L7, Canada;* orcid.org/0000-0003-2041-7180

Complete contact information is available at:
https://pubs.acs.org/10.1021/acs.jpcc.5c03233

Notes

The authors declare no competing financial interest.

ACKNOWLEDGMENTS

We thank the Centre for Emerging Device Technologies (CEDT) for the access to the Hall system and Dr. Nebile Isik Goktas for the training on the instrument. We thank Jhoynner Martinez from the Canadian Centre for Electron Microscopy (CCEM) for assistance with SEM imaging. Electron microscopy was performed at the Canadian Centre for Electron Microscopy (also supported by NSERC and other government agencies). We thank Dr. Mouhanad Babi from the Centre for Advanced Light Microscopy (CALM) for assistance with the images of the sensing layers. The authors acknowledge financial support from the Natural Sciences and Engineering Research Council of Canada through the Discovery Grant Program (award number RGPIN-2023-04927).

REFERENCES

(1) Dong, S.; Wang, X. Alignment of Carbon Iron into Polydimethylsiloxane to Create Conductive Composite with Low Percolation Threshold and High Piezoresistivity: Experiment and Simulation. *Smart Mater. Struct.* **2017**, *26*, 045027.

(2) Krause, B.; Boldt, R.; Häußler, L.; Pötschke, P. Ultralow Percolation Threshold in Polyamide 6.6/MWCNT Composites. *Compos. Sci. Technol.* **2015**, *114*, 119−125.

(3) Vasanthkumar, M. S.; Bhatia, R.; Arya, V. P.; Sameera, I.; Prasad, V.; Jayanna, H. S. Characterization, Charge Transport and Magnetic Properties of Multi-Walled Carbon Nanotube-Polyvinyl Chloride Nanocomposites. *Phys. E (Amsterdam, Neth.)* **2014**, *56*, 10−16.

(4) Sharma, M.; Bhatia, R.; Sameera, I. Low Temperature Charge Transport Study of MWCNT/PEDOT: PSS Composites: Insulating to Metallic Regime. *J. Phys. D Appl. Phys.* **2023**, *56*, 475306.

(5) Cardenas, J. A.; Catenacci, M. J.; Andrews, J. B.; Williams, N. X.; Wiley, B. J.; Franklin, A. D. In-Place Printing of Carbon Nanotube Transistors at Low Temperature. *ACS Appl. Nano Mater.* **2018**, *1* (4), 1863−1869.

(6) Jang, H. K.; Jin, J. E.; Choi, J. H.; Kang, P. S.; Kim, D. H.; Kim, G. T. Electrical Percolation Thresholds of Semiconducting Single-Walled Carbon Nanotube Networks in Field-Effect Transistors. *Phys. Chem. Chem. Phys.* **2015**, *17* (10), 6874−6880.

(7) Simoneau, L. P.; Villeneuve, J.; Rochefort, A. Electron Percolation in Realistic Models of Carbon Nanotube Networks. *J. Appl. Phys.* **2015**, *118*, 124309.

(8) Snow, E. S.; Novak, J. P.; Campbell, P. M.; Park, D. Random Networks of Carbon Nanotubes as an Electronic Material. *Appl. Phys. Lett.* **2003**, *82* (13), 2145−2147.

(9) Behnam, A.; Ural, A. Computational Study of Geometry-Dependent Resistivity Scaling in Single-Walled Carbon Nanotube Films. *Phys. Rev. B*−*Condens. Matter Mater. Phys.* **2007**, *75* (12), 125432−125438.

(10) Patel, V.; Akbar, M. A.; Kruse, P.; Selvaganapathy, P. R. A Reagent-Free Phosphate Chemiresistive Sensor Using Carbon Nanotubes Functionalized with Crystal Violet. *Analyst* **2023**, *148*, 3551−3558.

(11) Akbar, M. A.; Sharif, O.; Selvaganapathy, P. R.; Kruse, P. Identification and Quantification of Aqueous Disinfectants Using an Array of Carbon Nanotube-Based Chemiresistors. *ACS Appl. Eng. Mater.* **2023**, *1* (11), 3040−3052.

(12) Akbar, M. A.; Selvaganapathy, P. R.; Kruse, P. Continuous Monitoring of Monochloramine in Water, and Its Distinction from Free Chlorine and Dichloramine Using a Functionalized Graphene-Based Array of Chemiresistors. *ACS ES&T Water* **2024**, *4* (9), 4041−4051.

(13) Rother, M.; Schießl, S. P.; Zakharko, Y.; Gannott, F.; Zaumseil, J. Understanding Charge Transport in Mixed Networks of Semiconducting Carbon Nanotubes. *ACS Appl. Mater. Interfaces* **2016**, *8* (8), 5571−5579.

(14) Kim, T. H.; Lee, J.; Hong, S. Highly Selective Environmental Nanosensors Based on Anomalous Response of Carbon Nanotube Conductance to Mercury Ions. *J. Phys. Chem. C* **2009**, *113* (45), 19393−19396.

(15) Kumawat, R. L.; Jena, M. K.; Pathak, B. Individual Identification of Amino Acids on an Atomically Thin Hydrogen Boride System Using Electronic Transport Calculations. *J. Phys. Chem. C* **2020**, *124* (49), 27194−27202.

(16) Snow, A. W.; Perkins, F. K.; Ancona, M. G.; Robinson, J. T.; Snow, E. S.; Foos, E. E. Disordered Nanomaterials for Chemielectric Vapor Sensing: A Review. *IEEE Sens. J.* **2015**, *15* (3), 1301−1320.

(17) Sisk, B. C.; Lewis, N. S. Vapor Sensing Using Polymer/Carbon Black Composites in the Percolative Conduction Regime. *Langmuir* **2006**, *22* (18), 7928−7935.

(18) Li, J.; ZhangÖstling, Z. B.M.; Zhang, S. L.; Zhang, S. L. Improved Electrical Performance of Carbon Nanotube Thin Film Transistors by Utilizing Composite Networks. *Appl. Phys. Lett.* **2008**, *92*, 133103.

(19) Benda, R.; Cancès, E.; Lebental, B. Effective Resistance of Random Percolating Networks of Stick Nanowires: Functional Dependence on Elementary Physical Parameters. *J. Appl. Phys.* **2019**, *126*, 044306.

(20) Cleasby, J. L.; Wiley, P.; C, L. Iron and Manganese A Case Study. *J. Am. Water Works Assoc.* **1975**, *67* (3), 147−149.

(21) Yu, W.; Campos, L.; Shi, T.; Li, G.; Graham, N. Enhanced Removal of Manganese in Organic-Rich Surface Water by Combined Sodium Hypochlorite and Potassium Permanganate during Drinking. *RSC Adv.* **2015**, *5* (35), 27970−27977.

(22) Jiang, J.; Gao, Y.; Pang, S. Y.; Wang, Q.; Huangfu, X.; Liu, Y.; Ma, J. Oxidation of Bromophenols and Formation of Brominated Polymeric Products of Concern during Water Treatment with Potassium Permanganate. *Environ. Sci. Technol.* **2014**, *48* (18), 10850−10858.

(23) Omoike, A. I.; Harmon, D. Slow-Releasing Permanganate Ions from Permanganate Core-Manganese Oxide Shell Particles for the Oxidative Degradation of an Algae Odorant in Water. *Chemosphere* **2019**, *223*, 391−398.

(24) Goldnik, E.; Turek, T. Removal of Hydrogen Sul Fi de by Permanganate Based Sorbents: Experimental Investigation and Reactor Modeling. *Chem. Eng. Sci.* **2016**, *151*, 51−63.

(25) Fu, Q.; Xu, Q.; Liu, Z.; Wang, D.; Liu, X.; He, D.; He, Y.; Li, Y.; Yang, J.; Duan, A. Insights into Potassium Permanganate Reducing

H2S Generation from Anaerobic Fermentation of Sludge. *Chem. Eng. J.* **2022**, *430* (4), 133150.

(26) Health Canada. *Guidelines for Canadian Drinking Water Quality: Guideline Technical Document–Manganese*, 2019.

(27) McBeath, S. T.; Wilkinson, D. P.; Graham, N. J. D. Analytical Quantification of Aqueous Permanganate: Direct and Indirect Spectrophotometric Determination for Water Treatment Processes. *Chemosphere* **2020**, *251*, 126626.

(28) UviTec Permanganate Sensor https://new.abb.com/products/measurement-products/analytical/continuous-water-analysis/permanganate/uvitec-permanganate-sensor (accessed 05 5, 2025).

(29) Ye, Z.; Weng, R.; Ma, Y.; Wang, F.; Liu, H.; Wei, L.; Xiao, L. Label-Free, Single-Particle, Colorimetric Detection of Permanganate by GNPs@Ag Core-Shell Nanoparticles with Dark-Field Optical Microscopy. *Anal. Chem.* **2018**, *90* (21), 13044–13050.

(30) Akbar, M. A.; Tavakkoli Gilavan, M.; Selvaganapathy, P. R.; Kruse, P. Continuous Monitoring of Free Chlorine Level and PH Using an Array of Carbon Nanotube Chemiresistors. *ACS omega* **2025**, *10* (27), 29074–29086.

(31) Alafogianni, P.; Dassios, K.; Farmaki, S.; Antiohos, S. K.; Matikas, T. E.; Barkoula, N. M. On the Efficiency of UV-Vis Spectroscopy in Assessing the Dispersion Quality in Sonicated Aqueous Suspensions of Carbon Nanotubes. *Colloids Surfaces A Physicochem. Eng. Asp.* **2016**, *495*, 118–124.

(32) Liu, P.; Khan, A. T.; Ding, E. X.; Zhang, Q.; Xu, Z.; Bai, X.; Wei, N.; Tian, Y.; Li, D.; Jiang, H.; et al. Direct Synthesis of Semiconducting Single-Walled Carbon Nanotubes Toward High-Performance Electronics. *Adv. Electron. Mater.* **2023**, *9* (7), 2300196.

(33) Hu, L.; Hecht, D. S.; Gruner, G. Percolation in Transparent and Conducting Carbon Nanotube Networks. *Nano Lett.* **2004**, *4* (12), 2513–2517.

(34) Stauffer, D.; Aharony, A. *Introduction to Percolation Theory*, 2nd Revise.; Taylor & Francis: London, 2003.

(35) Kirby, T.; Akbar, M. A.; Tavakkoli Gilavan, M.; Selvaganapathy, P. R.; Kruse, P. Carbon Nanotube-Based Chemiresistive Sensor Array for Dissolved Gases. *ACS Omega* **2024**, *9* (47), 46986–46996.

(36) Shin, D. W.; Meng, X.; Lee, J. H.; Yu, S. M.; Yoo, J. H.; Lim, K. S.; Patole, S. P.; Yoo, J. B. Doping and Dedoping in SWCNT Film by the Spontaneous Redox Process. *J. Phys. Chem. C* **2011**, *115* (37), 18327–18332.

(37) Zubiarrain-Laserna, A.; Angizi, S.; Akbar, M. A.; Divigalpitiya, R.; Selvaganapathy, P. R.; Kruse, P. Detection of Free Chlorine in Water Using Graphene-like Carbon Based Chemiresistive Sensors. *RSC Adv.* **2022**, *12*, 2485–2496.

(38) Chowdhury, T.; Hoque, E.; Mohtasebi, A.; Kruse, P. Nature of the Interaction of N,N′-Diphenyl-1,4-Phenylenediamine with Iron Oxide Surfaces. *J. Phys. Chem. C* **2017**, *121* (5), 2721–2729.

(39) Hoque, E.; Chowdhury, T.; Kruse, P. Chemical in Situ Modulation of Doping Interactions between Oligoanilines and Nanocarbon Films. *Surf. Sci.* **2018**, *676*, 61–70.

(40) Angizi, S.; Huang, X.; Hong, L.; Akbar, M. A.; Selvaganapathy, P. R.; Kruse, P. Defect Density-Dependent PH Response of Graphene Derivatives: Towards the Development of PH-Sensitive Graphene Oxide Devices. *Nanomaterials* **2022**, *12*, 1801.

(41) Angizi, S.; Selvaganapathy, P. R.; Kruse, P. Graphene-Silicon Schottky Devices for Operation in Aqueous Environments: Device Performance and Sensing Application. *Carbon N. Y.* **2022**, *194*, 140–153.

(42) Tavakkoli Gilavan, M.; Igun, O.; Akbar, M. A.; Jahangirifard, S.; Kruse, P.; Selvaganapathy, P. R. Patterning of Nano and Micro-materials on Polymer Substrates Using Spraying, Selective Laser Treatment, and Adhesive Delamination for Sensing Applications. *Adv. Mater. Interfaces* **2025**, *12*, 2500027.

https://doi.org/10.1021/acs.jpcc.5c03233
J. Phys. Chem. C 2025, 129, 14583–14592

Supporting Information

Optimization of Carbon Nanotube Percolation Networks for Broad Dynamic Range Detection of Permanganate in Water

Md Ali Akbar[1], Ponnambalam Ravi Selvaganapathy[2, 3], Peter Kruse[1]*

[1]Department of Chemistry and Chemical Biology, McMaster University, 1280 Main St. W., Hamilton, Ontario L8S 4M1, Canada.

[2]Department of Mechanical Engineering, McMaster University, 1280 Main St. W., Hamilton, Ontario L8S 4L7, Canada.

[3]School of Biomedical Engineering, McMaster University, 1280 Main St. W., Hamilton, Ontario L8S 4L7, Canada.

* Email: pkruse@mcmaster.ca

Figure S1. Photograph of a fabricated chemiresistive sensing device.

Figure S2. Photographic image of SiO_2 substrate (1×1 cm^2) with gold contacts in the four corners for the four-probe measurement.

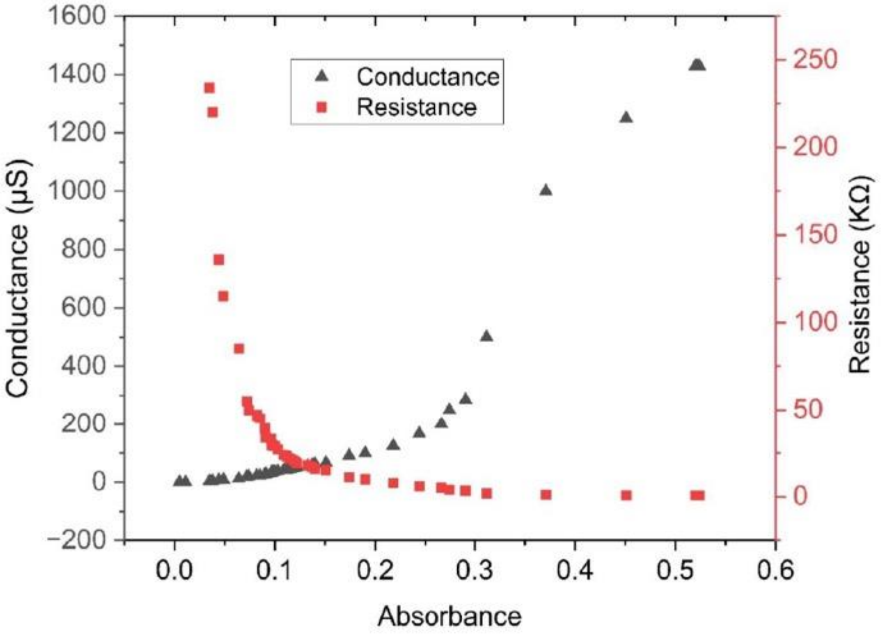

Figure S3. Film conductance and resistance plotted as a function of absorbance at the 305 nm wavelength. Here the channel between two contacts was airbrushed with SWCNT suspension to map out the transition from conductor to insulator. The resistance was measured by a two-probe multimeter and conductance was calculated from the measured resistance.

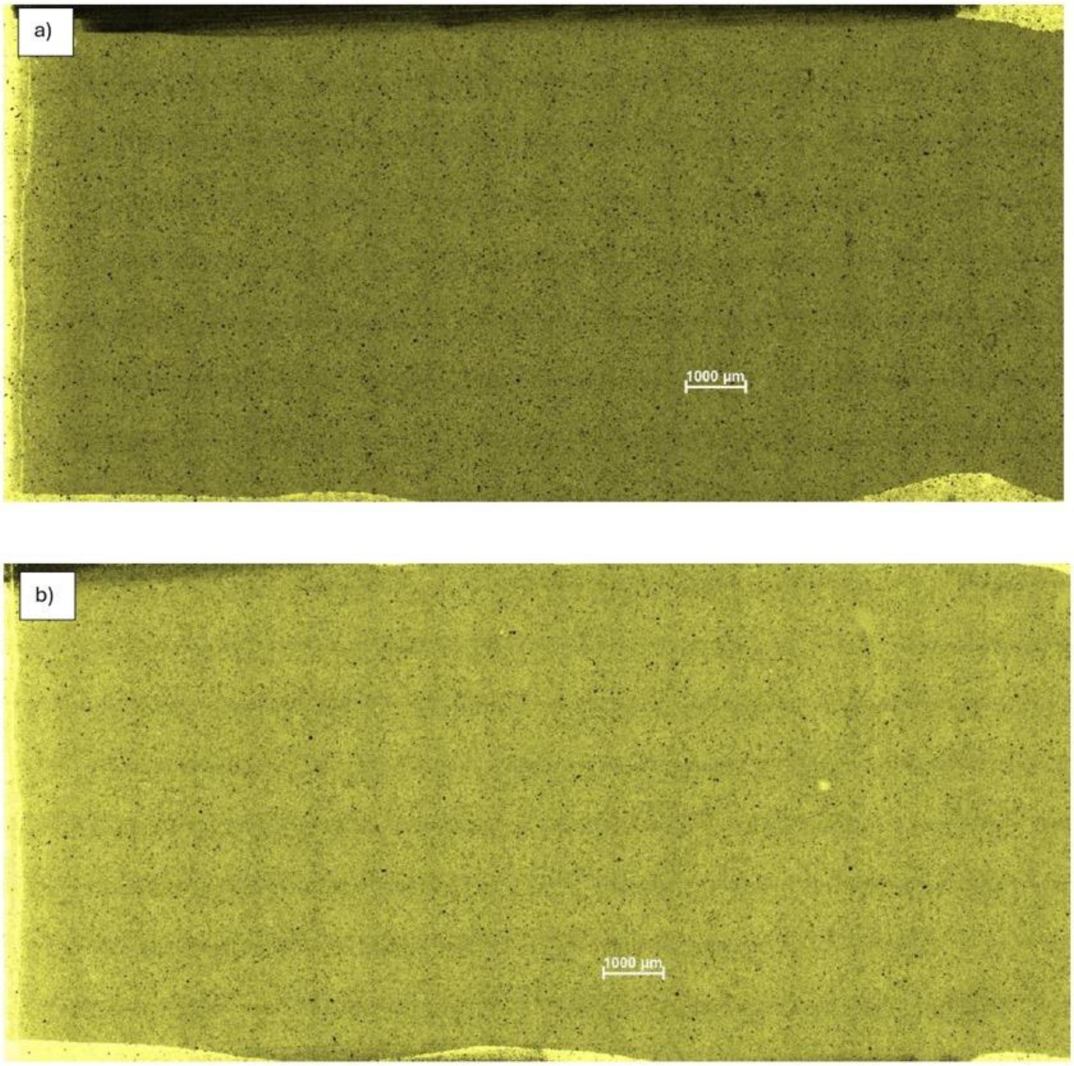

S4

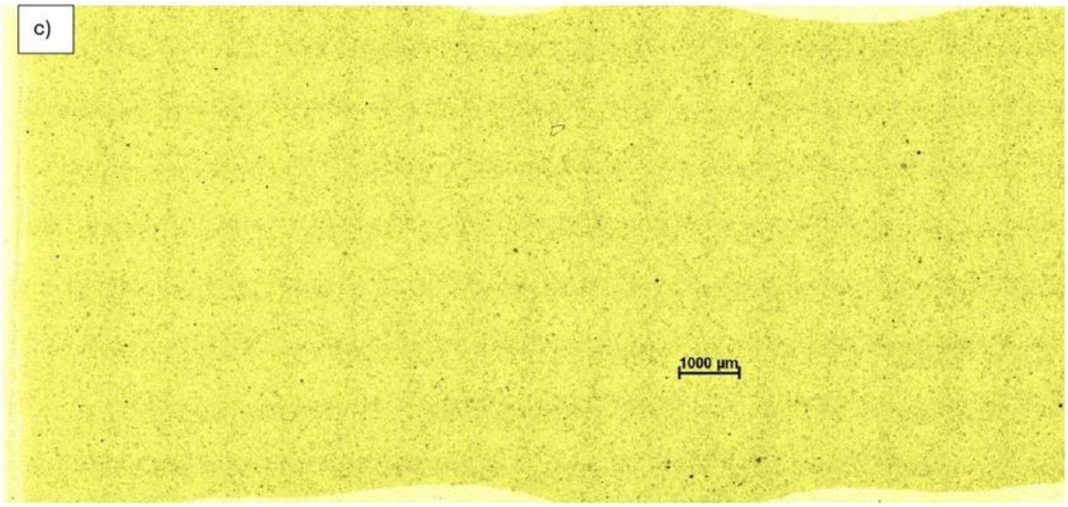

Figure S4. Film images of the sensing layer in the actual devices. a) Sensor film with the resistance of 5 kΩ, b) resistance of 15 kΩ, c) resistance of 25 kΩ. Yellow background was added for contrast only.

Table 1. Hall meaurement data from a four probe device. The data was collected on a Si/SiO$_2$ substrate. The gold contacts were deposited by sputtering. The SWCNT networks were deposited by airbrush. Several individual sample were prepared, and each sample measured after each step. This table lists complete data for two of the samples. Each sample of SWCNT was exposed to methanol, DPPD, and then MnO$_4^-$. The errors in the meaurements represent the standard deviation of three measurements of the sample device in each of the exposures.

	SWCNT	SWCNT + Methanol	SWCNT + DPPD	SWCNT+ DPPD MnO$_4^-$
		Sample 1		
Sheet resistivity [Ω/sq]	230.9±0.8	269.5±0.3	303.8±1.3	267.9±1.6
Sheet Hall resistance coef. [m^2/C]	+0.49±0.01	+0.30±0.01	+0.50±0.01	+0.62±0.06
Hall mobility [cm^2/(V·s)]	21.4±0.61	11.38±0.48	22.80±0.08	24.20±1.61
Charge concentration [cm^{-2}]	$+1.25\times10^{15}\pm 9.43\times10^{12}$	$+1.75\times10^{15}\pm 1.23\times10^{14}$	$+7.53\times10^{14}\pm 1.74\times10^{14}$	$+9.34\times10^{14}\pm 4.9\times10^{12}$
		Sample 2		
Sheet resistivity [Ω/sq]	649.1±0.9	652.1±2.6	654.0±3.9	661.2±2.7
Sheet Hall resistance coef. [m^2/C]	+6.84±0.3	+6.63±0.9	+6.61±0.9	+7.02±0.4
Hall mobility [cm^2/(V·s)]	91.0±1.3	89.8±1.2	89.8±1.0	102±3.4
Charge concentration [cm^{-2}]	$+3.37\times10^{16}\pm 1.7\times10^{16}$	$+3.91\times10^{15}\pm 1.25\times10^{13}$	$+4.31\times10^{15}\pm 2.6\times10^{15}$	$+5.2\times10^{16}\pm 3.82\times10^{16}$

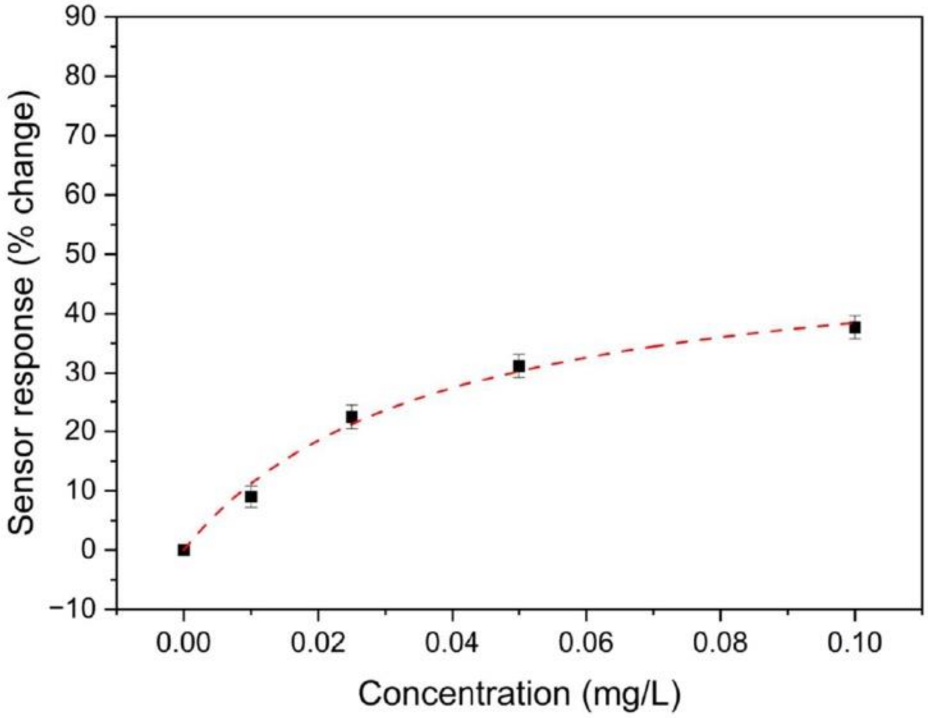

Figure S5. Characterization of the blank sensor (25 KΩ) in a low concentration range (0.01 mg/L to 0.1 mg/L) of permanganate solution. Calibration graph of three devices as percent change (% change) sensor response plotted against concentration of permanganate (mg/L). The dots represent average values and error bars represent the standard deviation of the responses to corresponding concentrations. The dotted line is the Langmuir adsorption isotherm fit. The model parameters for the sensor are A = 52.73±4.46% and B = 26.95±5.50 $mg^{-1}L$ for an R^2 value of 0.99.

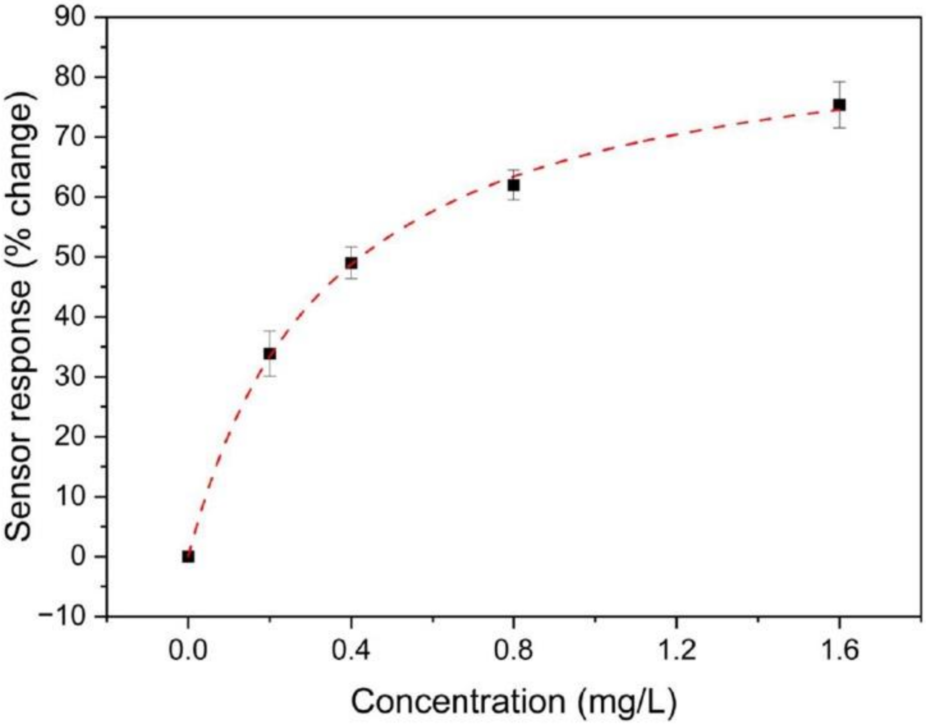

Figure S6. Characterization of the blank sensor (15 KΩ) in a medium concentration range (0.2 mg/L to 1.6 mg/L) of permanganate solutions. Calibration graph of three devices as percent change (% change) sensor response plotted against concentration of permanganate (mg/L). The dots represent average values and error bars represent the standard deviation of the responses to corresponding concentrations. The dotted line is the Langmuir adsorption isotherm fit. The model parameters for the sensor are A = 90.53±1.82% and B = 2.92±0.17 $mg^{-1}L$ for an R^2 value of 0.99.

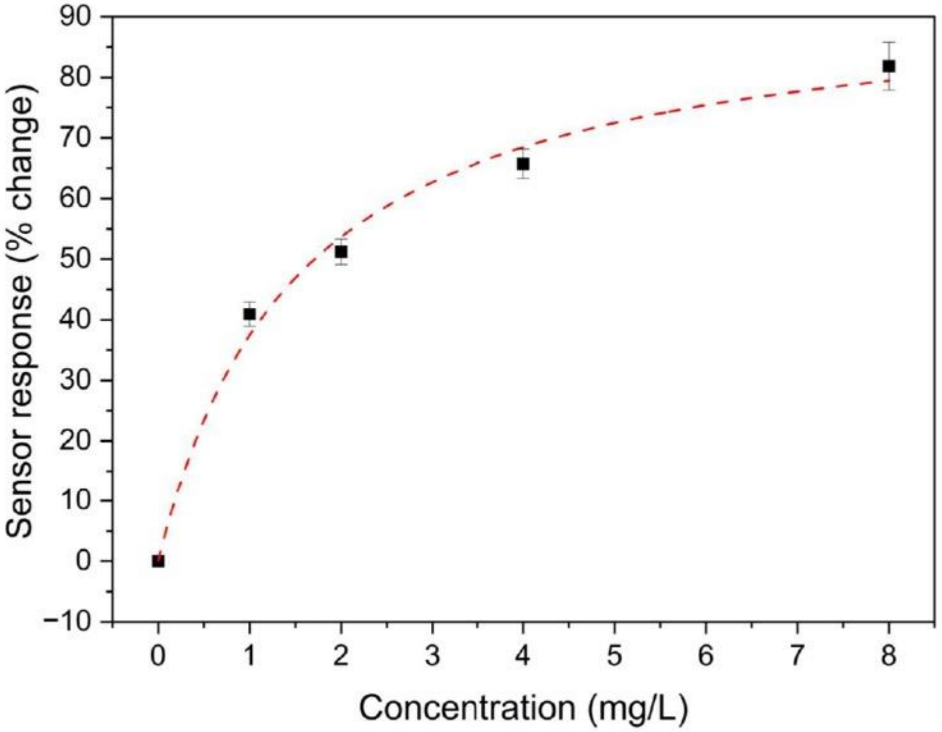

Figure S7. Characterization of the blank sensor (5 KΩ) in a high concentration range (1 mg/L to 8 mg/L) of permanganate solutions. Calibration graph of three devices as percent change (% change) sensor response plotted against concentration of permanganate (mg/L). The dots represent average values and error bars represent the standard deviation of the responses to corresponding concentrations. The dotted line is the Langmuir adsorption isotherm fit. The model parameters for the sensor are A = 94.59±5.64% and B = 0.65±0.12 $mg^{-1}L$ for an R^2 value of 0.99.

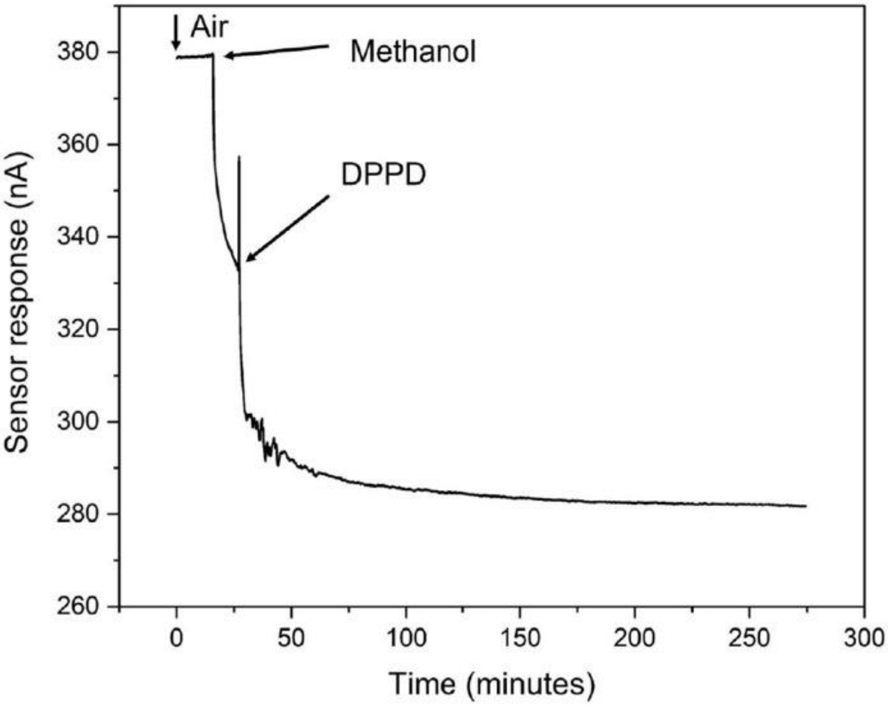

Figure S8. Functionalization of chemiresistive devices with DPPD. Dry sensor is rinsed with methanol and then dipped in methanolic solution of DPPD.

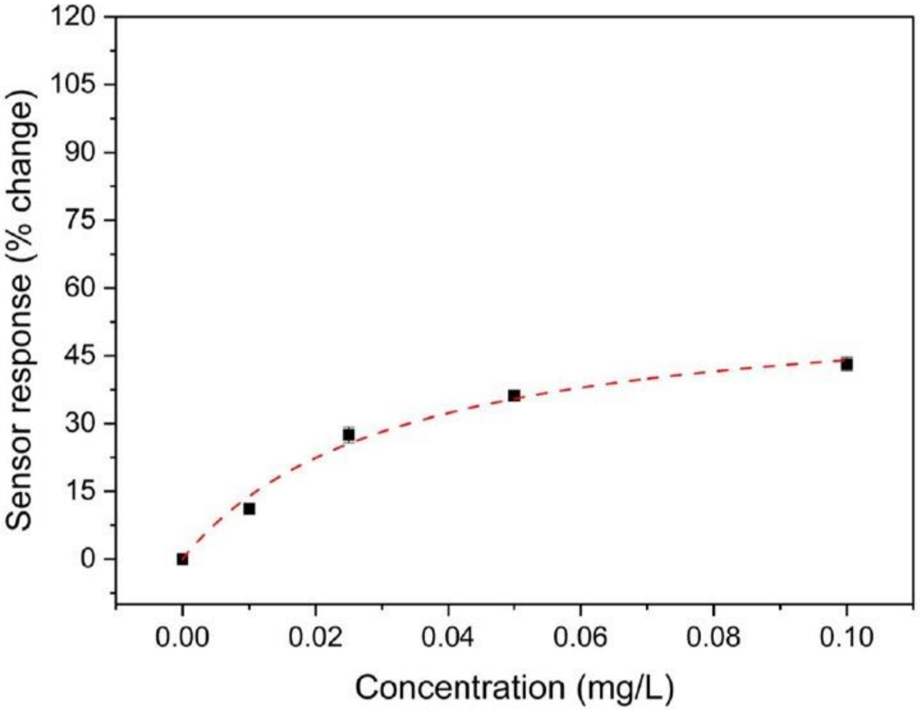

Figure S9. Characterization of the functionalized sensor (25 KΩ) in a low concentration range (0.01 mg/L to 0.1 mg/L) of permanganate solution. Calibration graph of three devices as percent change (% change) sensor response plotted against concentration of permanganate (mg/L). The dots represent average values and error bars represent the standard deviation of the responses to corresponding concentrations. The dotted line is the Langmuir adsorption isotherm fit. The model parameters for the sensor are A = 58.02±5.02% and B = 31.42±6.96 $mg^{-1}L$ for an R^2 value of 0.99.

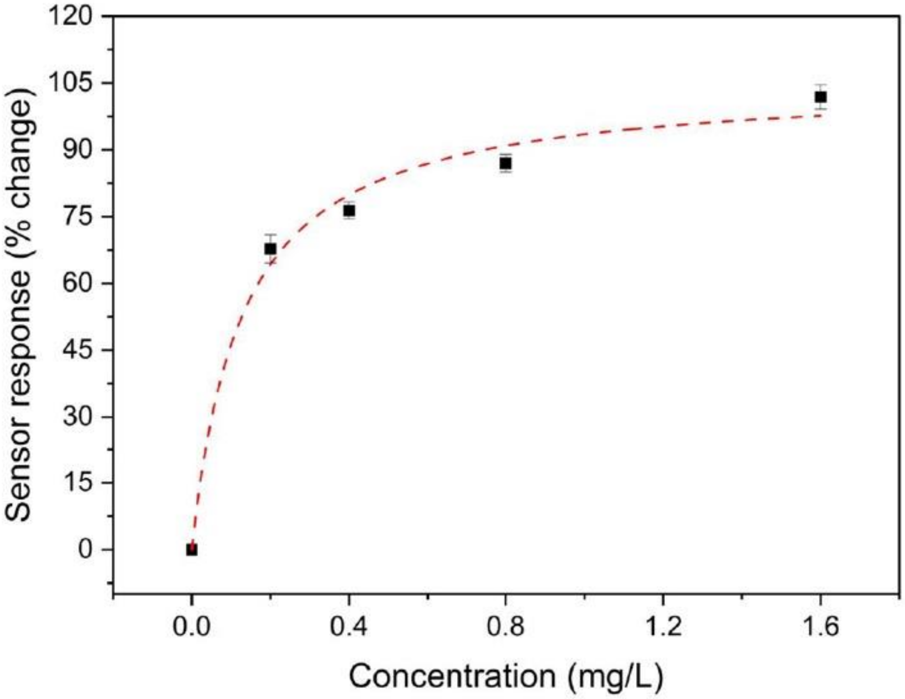

Figure S10. Characterization of the functionalized sensor (15 KΩ) in a medium concentration range (0.2 mg/L to 1.6 mg/L) of permanganate solution. Calibration graph of three devices as percent change (% change) sensor response plotted against concentration of permanganate (mg/L). The dots represent average values and error bars represent the standard deviation of the responses to corresponding concentrations. The dotted line is the Langmuir adsorption isotherm fit. The model parameters for the sensor are A = 105.45±5.26% and B = 7.81±1.89 mg^{-1}L for an R^2 value of 0.99.

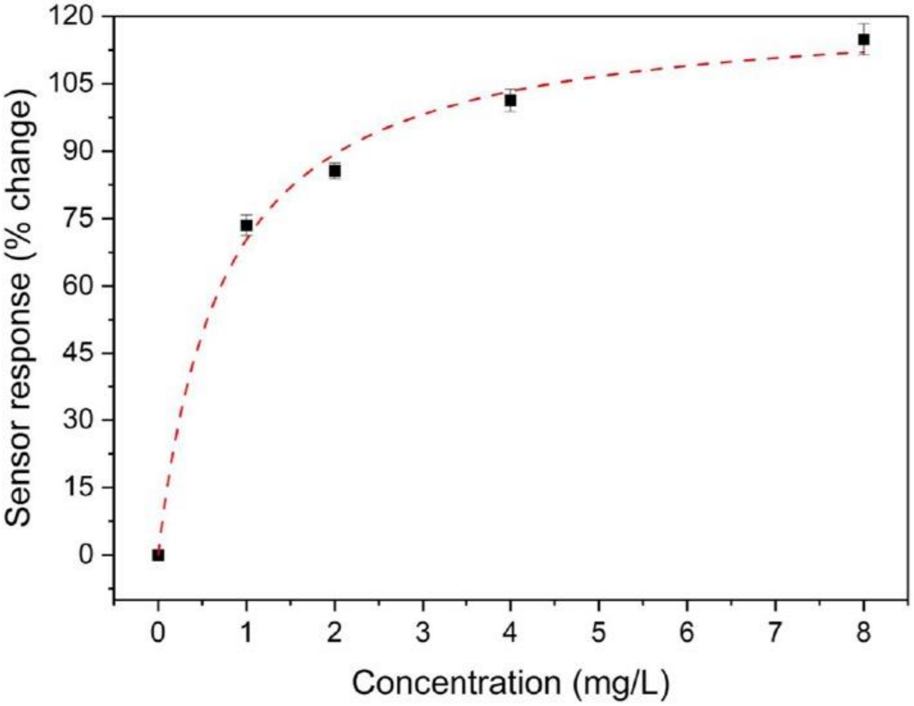

Figure S11. Characterization of the functionalized sensor (5 KΩ) in a high concentration range (1 mg/L to 8 mg/L) of permanganate solution. Calibration graph of three devices as percent change (% change) sensor response plotted against concentration of permanganate (mg/L). The dots represent average values and error bars represent the standard deviation of the responses to corresponding concentrations. The dotted line is the Langmuir adsorption isotherm fit. The model parameters for the sensor are A = 122.43±4.35% and B = 1.35±0.21 $mg^{-1}L$ for an R^2 value of 0.99.

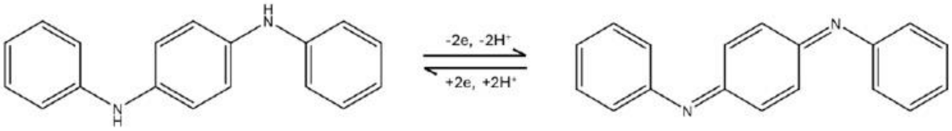

Figure S12. Reversible redox process of N, N-Diphenyl-1, 4-phenylenediamine (DPPD) and N,N′-diphenyl-1,4-benzoquinone- diimine (B2Q1).

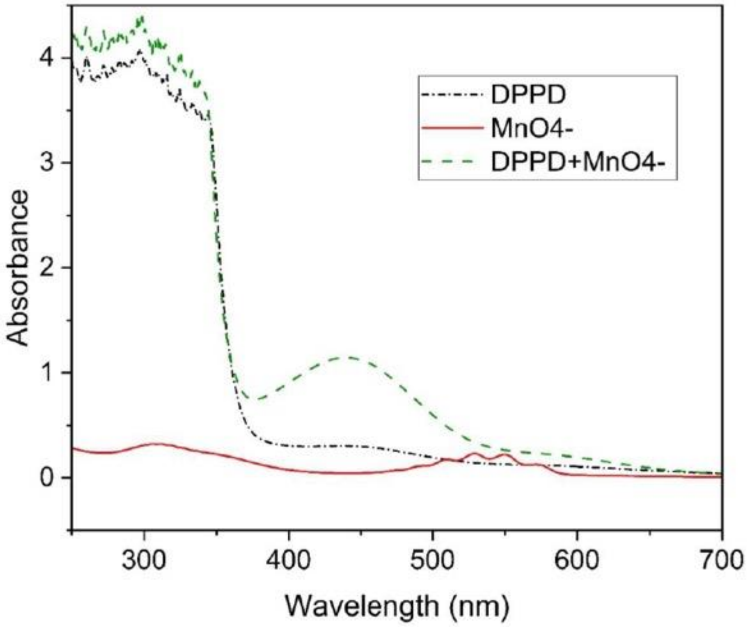

Figure S13. UV-vis spectra of 10% saturated DPPD (black dotted line), 0.8 mg/L MnO_4^- (red solid line) and 10% saturated DPPD with 6.0 mg/L MnO_4^- (green dashed line). In all cases methanol was used as the solvent.

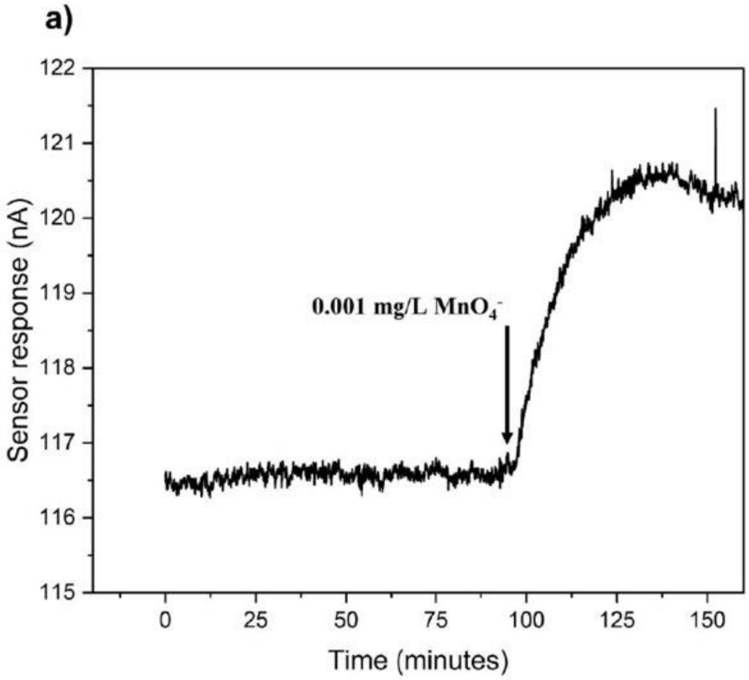
a)
0.001 mg/L MnO_4^-
Sensor response (nA)
Time (minutes)
115
116
117
118
119
120
121
122
0
25
50
75
100
125
150

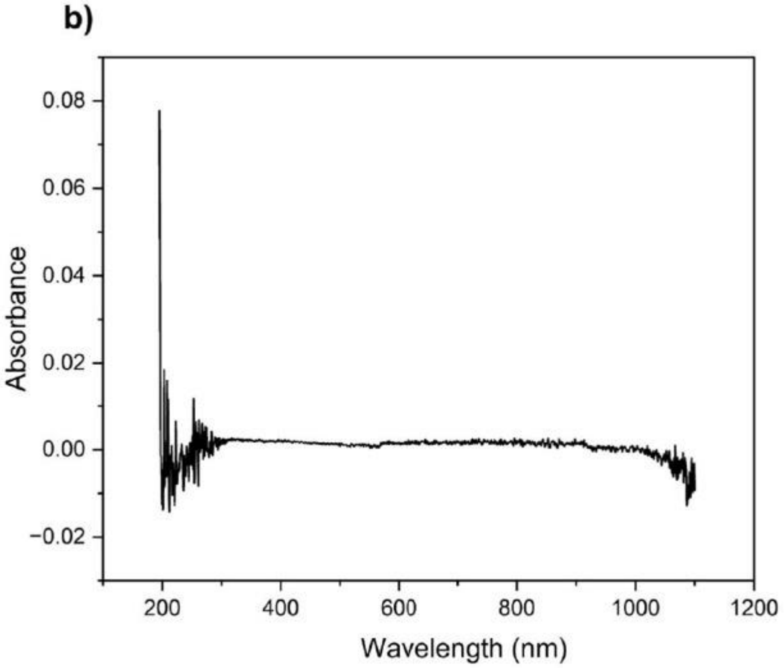

Figure S14. Characterization of an aqueous 0.001 mg/L MnO_4^- solution using a chemiresistor and UV-vis spectrophotometer. a) Sensor response of a device with a resistance of 25 KΩ plotted against time. At the 99th minute 0.001 mg/L of MnO_4^- was added to phosphate buffered water background. b) UV-vis spectra of 0.001 mg/L of MnO_4^- in water. No absorbance was recorded in the range of 200 – 1100 nm wavelengths.

Chapter 5 Continuous monitoring of free chlorine level and pH using an array of carbon nanotube chemiresistors

This chapter describes an array of single-walled carbon nanotube (SWCNT) chemiresistors developed for continuous monitoring of free chlorine (FC) under different pH conditions. The SWCNT films were noncovalently functionalized with cobalt phthalocyanine and anthraquinone to enhance their interaction with FC. The sensor array distinguished concentrations in the range of 0.03–2.1 mg/L across pH values from 6.5 to 9.5. The device design was also modified from earlier prototypes to incorporate features that enable large-scale fabrication, and performance was demonstrated over an extended concentration range of 0.015–10 mg/L. The array achieved a detection limit of 0.001 mg/L and included an electronic reset function to allow repeated use in continuous monitoring. Sensor durability was tested through repeated measurements in simulated tap water. Reprinted with permission from *ACS Omega* **2025**, *10*, 27, 29074–29086, Md Ali Akbar, Mehraneh Tavakkoli Gilavan, Ponnambalam Ravi Selvaganapathy, and Peter Kruse.

DOI: 10.1021/acsomega.5c01256

ACS OMEGA

Open Access

http://pubs.acs.org/journal/acsodf

Article

Continuous Monitoring of Free Chlorine Level and pH Using an Array of Carbon Nanotube Chemiresistors

Md Ali Akbar, Mehraneh Tavakkoli Gilavan, Ponnambalam Ravi Selvaganapathy, and Peter Kruse*

Cite This: https://doi.org/10.1021/acsomega.5c01256 Read Online

ACCESS | Metrics & More | Article Recommendations | Supporting Information

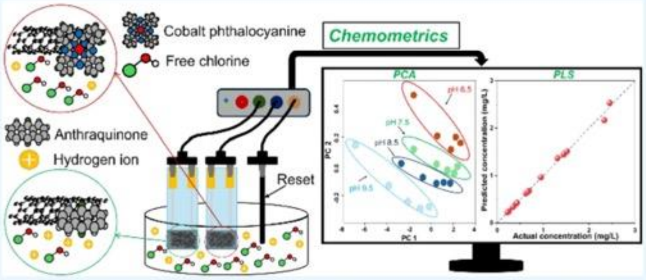

ABSTRACT: Free chlorine (FC) is the most commonly used disinfectant in water treatment plants, both as a primary disinfectant for pathogen removal and as a secondary disinfectant to suppress pathogen growth in the distribution system. The "disinfectant power" is dependent on the concentration of FC as well as the pH of the water. Continuous monitoring of FC level and pH is crucial to ensure safe drinking water; however, currently used methods involve either frequent calibration or reagents. Here, an array of single-walled carbon nanotube (SWCNT) chemiresistors is demonstrated for the continuous monitoring of FC at different pHs. The SWCNT chemiresistors were noncovalently functionalized with cobalt phthalocyanine and anthraquinone. The array has been shown to differentiate FC concentrations ranging from 0.03 to 2.1 mg/L within a pH range of 6.5 to 9.5. In addition, sensor design has been improved from our previous devices to incorporate components to facilitate mass fabrication. This design was tested over a wide range (0.015−10 mg/L) of FC. The limit of detection (LOD) of the sensor was calculated to be 0.001 mg/L. An electronic reset function is incorporated into the sensors to be able to continuously monitor the concentration of FC. The durability of the sensors is demonstrated with repeated measurements in simulated tap water. Overall, this study presents electrical sensor-based continuous monitoring of FC.

■ INTRODUCTION

Disinfectants such as free chlorine (FC) are added to water to keep it safe for drinking. FC is used as a primary disinfectant in the water treatment facility and as a residual disinfectant in the distribution system. As a primary disinfectant, FC removes pathogens from water, and as the residual disinfectant, it prevents the regrowth of the pathogens. An FC concentration of 0.5−5 mg/L is recommended by the World Health Organization (WHO) in the distribution system.[1] The continuous monitoring of FC is essential to maintain an adequate level of oxidant in water as pathogens can regrow in the distribution system when the disinfectant concentration decreases.[2,3] Aqueous FC is a pH-dependent mixture of hypochlorous acid (HOCl, dominant below pH 7.5) and hypochlorite ions (OCl^-, dominant above pH 7.5).[4] With increasing pH, the oxidation−reduction potential (ORP) of FC decreases, and therefore the disinfection power declines for the same concentration of FC as that at lower pH. This is partially because HOCl is a stronger oxidant (E_0 = 1.49 V) than OCl^- (E_0 = 0.9 V), and partially because the reduction reactions of these species themselves involve protons. Therefore, the measurement of FC in water should be complemented with a measurement of pH of the solution to get a better picture of the disinfectant efficacy in water and assist in preventing pathogen outbreaks such as the Walkerton (Canada) incident which resulted in the deaths of seven individuals due to an *Escherichia coli* outbreak.[5,6]

Standard methods are available to measure the chlorine levels in water. Colorimetry is the most commonly used and well-established technique to test the FC concentration; it uses

Received: February 10, 2025
Revised: June 1, 2025
Accepted: June 26, 2025

either *N*, *N*-diethyl-*p*-phenylenediamine (DPD)[7−10] or other[11,12] reagents.[1,13,14] This method is carried out manually by operators in the water treatment plant to measure the level of FC. Additionally, these methods can suffer from issues with interference by other oxidants such as dissolved oxygen or chloramine. Currently, the measurement of FC is carried out on discrete samples using reagents and spectroscopic readout devices. This makes the measurement process expensive and not suitable for the continuous monitoring of the disinfectant.[3] Other methods like amperometric titration need reagents and are not suitable for continuous measurement.[7] Fluorescence-based measurements of FC require reagents and instruments.[15,16] Electrochemical methods reported for FC sensors are based on voltammetry[17,18] or amperometry.[19−21] These methods are suitable for continuous monitoring and do not require reagents; however, they need reference electrodes that need frequent calibration.[22,23]

In contrast to electrochemical methods, electrical methods such as chemiresistive sensing possess the potential for continuous monitoring without the use of a reference electrode.[24] Chemiresistors are electrical-transduction-based sensors based on probing the conductivity of an active (chemiresistive) material via two electrical contacts. The conductivity (or resistance) of the active layer changes quantitatively when analytes interact with it; therefore, the changes in conductivity can be used for concentration measurement. Simple design, low fabrication cost, and compatible design to integrate with DC circuits make chemiresistive sensors a popular choice for sensing applications.[25−28] Previously, carbon nanotubes (CNT),[29] graphite,[30,31] graphene,[32,33] and graphene-like carbon[24] -based chemiresistors have been reported for FC sensing. Other electrical-transduction-based methods such as Schottky diodes and field-effect transistors (FET) provide excellent sensitivity to FC; however, the fabrication process is time-consuming and expensive.[34,35] We have made a series of improvements in the chemiresistive sensing of FC to achieve continuous monitoring of FC in water.[24,29−31] Previous versions of these sensors were suitable only for FC measurement in a constant pH background. SWCNTs are widely used in chemiresistive films due to their ease of processing to prepare a percolation network and excellent sensitivity to external stimuli.[36] However, the lack of selectivity limits the use of a bare SWCNT in chemiresistive sensors. Functionalization provides a way to limit the interference to tailor the sensing layer for specific applications. Recently, we have overcome the issue of correlated sensor responses when exposed to different oxidizing agents (FC and permanganate) by applying chemometric methods to the data from an array of functionalized single-walled carbon nanotube (SWCNT) chemiresistors.[37] Though this study presented a proof of principle in deconvoluting sensor responses, it did not focus on implementing continuous FC and pH sensing in real samples. Previous studies on gas sensing showed that phthalocyanine can be attached on the SWCNTs through $\pi-\pi$ stacking.[38−40] Even though cobalt phthalocyanine-doped SWCNT sensors have been successfully demonstrated for gaseous Cl_2,[41] Cl_2 as a species is not present in aqueous FC above pH 4, meaning that these studies do not directly translate to determining FC levels in drinking water at relevant pHs.

Here, we have introduced an array of two functionalized SWCNT chemiresistors specifically optimized for FC and pH measurements. The chemiresistive devices were functionalized with commercially available cobalt phthalocyanine (CoPc) and anthraquinone (AQ) using a simple noncovalent functionalization method. The chemiresistor design has been improved over our previous studies[37] to introduce scalable steps for mass fabrication of the devices and to enhance the range of detection. This improved study reports an array with a smaller number of sensors in the array (blank, CoPc, and AQ) with a wider range of concentrations (0.03−2.1 mg/L) of FC at a range of pHs (6.5−9.5). Chemometric analysis was carried out to evaluate the sensor array performance to distinguish FC in the pHs tested. Importantly, we have introduced an electronic reset mechanism to enable the continuous detection of heavily fluctuating levels of FC. Furthermore, the sensors were tested in simulated tap water (well-defined composition prepared in the lab) over an extended FC concentration range (0.015−10 mg/L). Lastly, the sensor array was demonstrated to measure FC in simulated tap water in a continuous monitoring format.

■ MATERIALS AND METHODS

Chemicals. Single-walled carbon nanotubes (SWCNT, chirality (6,5), average diameter 0.78 nm, 95% carbon basis), cobalt phthalocyanine (CoPc), anthraquinone (AQ), sodium hypochlorite (NaOCl) solution (reagent grade, 10−15%), sodium chloride (NaCl), sodium bicarbonate ($NaHCO_3$) potassium phosphate monobasic (KH_2PO_4), calcium chloride ($CaCl_2$), magnesium sulfate ($MgSO_4$), methanol (CH_3OH), dimethylformamide (DMF), and acetonitrile (ACN) were purchased from Sigma-Aldrich. Type 1 ultrapure water (resistivity 18.2 MΩ·cm) was obtained from a Millipore Simplicity UV water purification system.

Free Chlorine Measurement. The DPD colorimetric method was used to measure the FC level with a Thermo Scientific Orion Aquamate 8000 ultraviolet−visible (UV−vis) spectrophotometer and a Hach Pocket Colorimeter II. The reagents used were DPD FC Reagent Powder Pillows (Hach 1407099-CA) for the pocket colorimeter measurements and Orion AC4P71 Powder Chemistry Packs for the benchtop Aquamate.

Sensor Fabrication. SWCNT suspensions were prepared by adding 2−5 mg of SWCNT to 15 mL of methanol in a glass vial. The methanolic mixture was then sonicated in an Elmasonic P30H Ultrasonic Cleaner at 37 kHz for 6 h in sweep mode at 30 °C.

Sensors for the initial experiments were fabricated using a previously reported procedure.[37] Briefly, the frosted sides of the glass slides (VWR VistaVision, 75 × 25 × 1 mm^3, Cat. No. 16004418) were first cleaned with methanol and then dried in the air. A 9B pencil was used to draw two pencil pads on the frosted end of each glass slide, and then the slides were placed on a hot plate at a temperature of 100 °C. The SWCNT suspension in methanol was then airbrushed over and between the pencil patches until a uniform film was achieved making sure that the film overlaps the pencil contacts. The resistance of each film was kept in the range of 7−12 kΩ. The slides were then cooled to room temperature. Two pieces of adhesive copper tape (3M EMI Copper Foil Shielding Tape 1181, 1/4 in. wide) were attached on the pencil pads. The copper tape contacts were masked with a thick layer of partially cured (5−6 h at room temperature) polydimethylsiloxane (PDMS -Sylgard 184 Silicon Elastomer from Dow Corning) to be used as a dielectric. The sensors were then placed on the hot plate to cure at 60 °C for 1 h.

Characterization of the Molecules and Film. CoPc and AQ were used for their saturated solutions. CoPc was dissolved in DMF, and AQ was dissolved in ACN. Using quartz cuvettes, the molecule solutions were analyzed over a scanning range of 190−1100 nm with a Thermo Scientific Orion Aquamate 8000 UV−vis spectrophotometer. Pure solvents used for the molecular solution were used as blanks. A Renishaw inVia Raman spectrometer was used to characterize the SWCNT films using a 532 nm solid-state continuous wave laser (50 mW) over a range of 100−3500 cm^{-1} at 5% power. Spectra were recorded on at least three spots of each sample to ensure reproducibility. The spectra were normalized to the highest peak. The SWCNT film was also characterized by a JEOL JSM-7000F scanning electron microscope (SEM) at 3.0 kV, 20,000×, and a working distance of 6.0 mm. The SWCNT sample for SEM was prepared on 1 × 1 cm^2 sized chips of silicon/silicon dioxide (thermally grown).

Experimental Setup. For data collection, the sensors were connected to a 4-channel eDAQ Quad Multi-Function isoPod (EPU452) to measure continuous responses in "biosensor" mode. Using one channel of this instrument per chemiresistor, a constant potential bias of 10 mV was applied across each SWCNT film between the contacts. A pH electrode (Fisherbrand Accumet Gel-Filled Polymer Body Single-junction pH Combination Electrode) and an ORP electrode (Ionode IJ-64) were used to measure the pH and ORP of the solution. Two buffer solutions (pH 4 and 10) were used to calibrate the pH electrode before every experiment. An image of the experimental setup is shown in Figure S1. Clean glassware was soaked in aqueous 0.1 mg/L FC for 1 h as a pretreatment before every experiment. Our previous reports have detailed experimental procedures for each of the steps.[37,42] The sensors were first cleaned with ACN and then exposed to DMF for 5 min. The functionalized sensors were then placed in the molecule solutions. After functionalization, the sensors were rinsed with DMF to remove excess molecules from the surface, followed by an ACN rinse to displace DMF from the surface. After functionalization, the sensors and electrodes were placed in ultrapure water with a salt background. For the initial experiments, NaCl (1.71 mmol) and $NaHCO_3$ (0.59 mmol) were used as background. A stock solution of FC is made by diluting NaOCl solution with ultrapure water. The FC concentration in the stock solution was checked twice before each experiment using DPD chemistry on the AquaMate. The FC concentration range used for the experiments was 0−1.9 mg/L for four pHs (6.5, 7.5, 8.5, 9.5). 0.01 M NaOH and 0.01 M HCl were added as required to keep the pH constant throughout the experiment. FC concentrations are measured 25 min after each spike in concentration. After each experiment, ascorbic acid (0.1 mg/L) is added as a reducing agent to reset the sensors. After 20 min, the sensors are rinsed in fresh DI water for 5 min to remove excess ascorbic acid. Ultrapure water is then replenished in the vessel to achieve a stable baseline for the next experiment. Sensors are always stored in ultrapure water with the same background as used for the experiment. For the simulated tap water experiments, commonly present cations and anions were added to the ultrapure water, namely, 0.04 mM KH_2PO_4, 0.6 mM $CaCl_2$, 0.3 mM $MgSO_4$, and 1 mM $NaHCO_3$. After mixing, the solution was left for 2 h before being used for experimentation.

Data Analysis. Sensor responses are collected as current (nA) vs. time. To process the data, the averaged current over the last 2 min of the current response is converted into a percent change response using eq 1. This represents the current change due to FC addition relative to the baseline current when exposed to the background electrolyte without FC.

$$\text{response (\% change)} = \frac{I - I_0}{I_0} \times 100\% \qquad (1)$$

Here, I refers to the sensor current (in nA) for each spike of FC in water and I_0 is the baseline current (in nA) in just water (0 mg/L FC).

After plotting percent changes against concentrations of FC, the data points are fitted with a Langmuir adsorption isotherm-style equation, as shown in eq 2.

$$y = \frac{abx}{1 + bx} \qquad (2)$$

Here, the sensor's maximum theoretical response is represented by the parameter a. Parameter b is related to the binding constant of FC to the sensor surface. Parameters a and b together reflect the sensitivity of the chemiresistive sensors to a particular analyte. This isotherm was discussed for free chlorine responses in our previous studies.[24,37] To estimate the dynamic range of FC sensing, a linearized Langmuir adsorption isotherm model is implemented by plotting 1/(% sensor response) vs. 1/(FC concentration).

The limit of detection (LOD) is calculated as three times the standard deviation (3σ) of the sensor response. Using eq 2 with corresponding fitting parameters, the concentration that can correspond to a 3σ sensor response is then calculated and reported as the LOD. The reported LOD is the value that can be achieved for any one of the sensors in the array. Principal component analysis (PCA) was performed on the sensing array data using MetaboAnalyst 6.0.[43] Linear discriminant analysis (LDA) and partial least-squares regression (PLSR) were carried out using OriginPro 10.0. For the PLSR analysis, sensor data (% sensor response) and FC concentration were first converted to 1/(% sensor response) and 1/(FC concentration). The converted data were then used for PLSR analysis. The singular value decomposition (SVD) method and standardization of variables were chosen from the built-in functions of the software to carry out the PLSR analysis. After the analysis, sensor data and FC concentration were restored to their original form for visualization.

■ RESULTS AND DISCUSSION

Sensor Design Optimization. The simple design of chemiresistive sensors allows for faster and cheaper fabrication. We modified the design of our sensors to achieve optimum output and facilitate the mass fabrication of the devices. Deposition methods play a crucial role in achieving a uniform film, which is required for effective sensing. Methods such as drop-casting and airbrushing were compared for the SWCNT layer deposition of the sensors. Table S1 tabulates the data for the optimization of sensor fabrication. The airbrushed films required less time for fabrication of the film (40−85 min) compared to drop-cast films (100−140 min). The introduction of sensors in water for the first time requires a considerable wait time to stabilize the sensors in water. Sensors fabricated with the airbrush method yielded less wait time (3−12 h) for stabilization in tap water than the ones fabricated with the drop-casting method (12−48 h). Two electrical contacts are used to measure the conductance changes in the SWCNT film.

https://doi.org/10.1021/acsomega.5c01256
ACS Omega XXXX, XXX, XXX−XXX

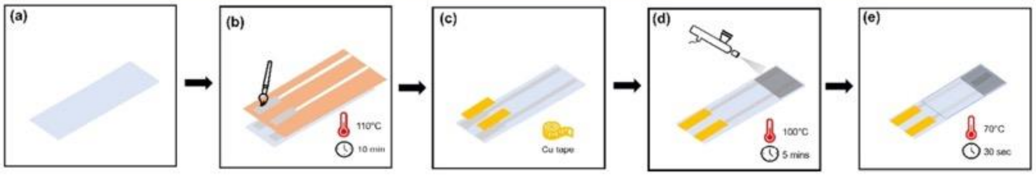

Figure 1. Fabrication of a chemiresistive device. (a) Glass slide was cleaned with DI water and methanol. (b) Fast-drying silver paste was applied to the mask using a brush. Two layers of silver paste were applied for appropriate thickness and then dried at 110 °C for 10 min to remove the solvent. (c) Copper tape was placed on top of the silver contacts. (d) SWCNT was airbrushed on the frosted side at 100 °C. (e) Parafilm is applied on top of the contacts as a dielectric at 70 °C.

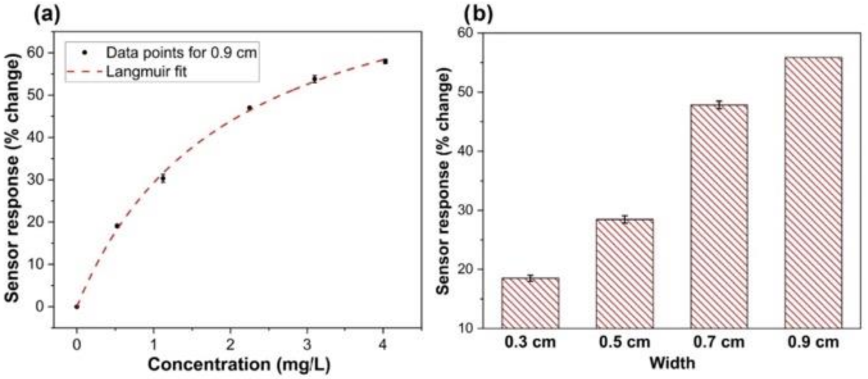

Figure 2. Sensor (blank) response when exposed to FC water with a background of NaCl and $NaHCO_3$ and at a pH of 8. (a) A blank sensor with an optimized exposed width (0.9 cm) was subjected to a range of FC concentrations (0.53−4.0 mg/L). The Langmuir isotherm fitting parameters are $a = 87.13 \pm 2.96\%$ and $b = 0.51 \pm 0.04$ $mg^{-1}L$. The error bars in the data points represent the standard deviation of the 30 data points of the last 2 min of the measurement. (b) Comparison of sensor responses for the blank sensors with different exposed widths for the FC concentration of 3.5 mg/L. Sensor responses are shown for 1.5 cm long sensors with exposed widths of 0.3, 0.5, 0.7, and 0.9 cm. The error bars in the bars represent the standard deviation of the 30 data points of the last 2 min of 3.5 mg/L addition. The response for the 0.9 cm sensor was derived from the fit shown in panel (a); therefore, no error bars in the bar for 0.9 cm.

We investigated the performance of three types of materials for contact fabrication: silver, gold, and carbon. They were combined with airbrushed and drop-cast films. Though sensors with gold contacts were faster to prepare, they showed the largest drift and lowest response compared to those made with silver and carbon. Additionally, airbrushed SWCNT films with silver and carbon contacts had the shortest stabilization time and the least amount of drift.

The optimized sensor fabrication steps are shown in Figure 1. We used a benchtop cutter (Cricut Explore) to design and cut masks to apply silver paste on the clean glass slide (Fisherbrand Microscope slides with frosted tabs, #22−034486). For the mask material, transparent adhesive polyethylene terephthalate (PET) sheet (thickness of 60 ± 8 μm, Uline) was chosen due to the ease of fabrication. After carefully placing the mask, silver paste (Fast-drying, #16040−30, Ted Pella) was brushed onto the surface. Subsequently, copper tape (3M EMI Copper Foil Shielding Tape 1181, 1/4 in wide) was used as the contact pads to improve the connection between the sensors and the measurement equipment. The SWCNT suspension was then airbrushed in between the contacts at 100 °C. An image of the SWCNT network deposited on a Si/SiO_2 substrate in a similar fashion has been shown in Figure S2. The sensors were then left on the hot plate at 70 °C.

The sensitivity of the sensors is dependent on the fraction of the surface area of the chemiresistive films exposed to the analyte. To increase the sensitivity and evaluate the effect of a larger fraction of exposed surface area, a set of sensors were prepared by using the gold contacts and copper tape connection pads. The total area of the SWCNT film deposited was 1.5×1.5 cm^2 (Figure S3). Since we need to leave some space next to each contact to prevent electrical shortage, three widths were selected for the opening of the exposed film. Four different sensor openings (0.3×1.5 cm^2, 0.5×1.5 cm^2, 0.7×1.5 cm^2, and 0.9×1.5 cm^2) for the analyte to interact with the active element have been selected for the experiment. Parafilm was cut specifically to ensure the aforementioned widths while keeping the lengths constant for all four sensors. Figure 2a shows the graph for the sensor with a 0.9 cm wide opening, and Figure S4 shows the calibration graphs of the other three sensors with smaller openings. The data points were calculated from the sensor responses using eq 1. The percent change in the current response was calculated by comparing the FC responses with the baseline current. The graph shows the Langmuir isotherm fit (dotted lines) of the actual data points. Equation 2 was used to fit the responses. The maximum response from the sensor with 0.3 cm exposed width was 18.5%, for the FC concentration of 3.53 mg/L, which is the lowest of the four sensors. For the same concentration, the

https://doi.org/10.1021/acsomega.5c01256
ACS Omega XXXX, XXX, XXX−XXX

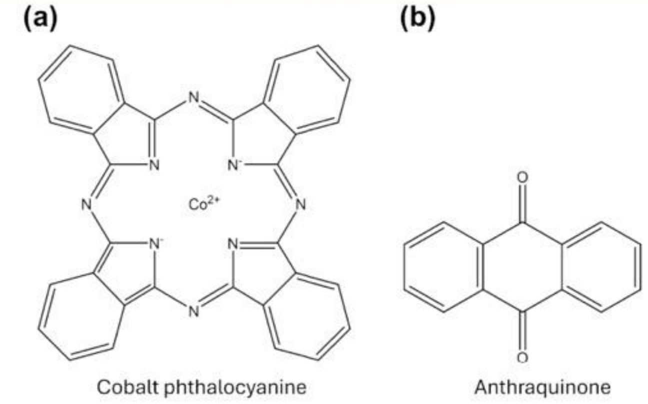

Figure 3. Molecules for the functionalization of the SWCNT surface. (a) Cobalt phthalocyanine (CoPc) and (b) anthraquinone (AQ).

sensor with 0.5 cm exposed width showed 28.5% sensor response, while the sensor with 0.7 cm exposed width gave 48%. As the width of the sensor film increases, parameter *a* increases for the corresponding fit (Figure S4). Since increasing the fraction of exposed surface area leads to higher sensitivity, using the highest possible exposed surface area is desirable. We have chosen 0.9 cm for the width of the opening (0.9×1.5 cm^2) of the sensor element for the optimized design, resulting in a 56% response to 3.53 mg/L FC (Figure 2b). The calibration graph for the sensor with a 0.9 cm opening is shown in Figure 2a. 0.9 cm is the maximum feasible exposed width of the sensing element to safely prevent leakage of the analyte to the contacts and avoid durability issues of the film. To cover the contacts, the xurographically patterned parafilm was placed on the sensors and attached to the sensors by applying pressure for 15−30 s at 70 °C. Sensors were then removed from the hot plate for further use. Parafilm was chosen over PDMS due to its easy and quick application process compared to PDMS's longer curing time. In addition, parafilm was easier to cut xurographically to control the surface area exposed in water. This optimized sensor design can be more easily scaled up to mass fabrication. In this work, the previous design was employed for the optimization of molecule concentration and validation of the molecule for pH detection due to its simple design. The optimized sensor design was then used for simulated tap water experiments.

Functionalization of SWCNT Films. Cobalt phthalocyanine (CoPc) and anthraquinone (AQ) were selected for the components of the array. Both molecules show reversible redox behavior when exposed to oxidizing or reducing chemicals. CoPc shows redox characteristics through the central cobalt ion or the phthalocyanine ligand, and AQ is redox-active through conversion between its quinone and hydroquinone forms. Previous studies showed that CoPc and AQ can be noncovalently adsorbed onto carbon nanotubes.[44−46] These planar molecules (Figure 3) were noncovalently attached to the SWCNT films by dipping the sensors in molecule solutions. We have previously demonstrated that airbrushed SWCNT films can be modified by this method.[37,47] The inherently p-doped nature of the SWCNT sensors was partially counteracted by the n-doping during the functionalization process as CoPc and AQ are adsorbed through $\pi-\pi$ interactions (Figures S5 and S6). This reduced the overall doping level and led to an increase in the film resistivity. The progress of the functionalization process was monitored by measuring the resistance changes across the film. The changes in the electronic properties of the SWCNT films were also characterized by Raman spectroscopy. A shift in the 2D peak can be observed when the doping level changes in the SWCNTs.[48] An upshift in the 2D peak corresponds to p-doping, and a downshift is indicative of n-doping. Upon analyzing SWCNT samples functionalized with CoPc and AQ, downshifts of the 2D peaks were observed for CoPc and AQ demonstrating successful functionalization (Figure S7). The concentration of the molecule solution affects the adsorption of the molecules onto the SWCNT network and needs to be optimized to avoid sparse surface coverage (at low concentrations) and adsorption of aggregates instead of monolayers due to dimer formation in solution (at high concentrations).[49] To select the appropriate concentration for each molecule, different dilutions (1, 3, 10, and 30%) of a saturated solution of the dopant molecules in appropriate solvents (CoPc in DMF and AQ in ACN) were used to functionalize the sensors. Film conductance was monitored during the doping procedure. A stable current is achieved after 1 h of molecule exposure. Doping is followed by 5−10 min rinsing with pure solvents to remove excess molecules from the film surface. In the case of CoPc, ACN is used as a second solvent to displace DMF which has a low volatility. This was done since residual solvent in the SWCNT film may contribute to baseline drift. The functionalized sensors were then tested against different FC concentrations, and the responses were compared to choose the optimum concentration for functionalization. The sensor responses were fitted with Langmuir adsorption isotherms. To choose the best concentration, sensitivity, and stability of the responses were taken into consideration. Figure S8 shows the responses for CoPc, and Figure S9 shows the AQ responses. CoPc responses show that 1% and 10% result in similar sensitivity; however, 10% shows a better coefficient of determination (R^2) value (0.99) than 1% (0.95). The SWCNT surface may not have been fully covered at 1%, causing erratic sensor behavior at high concentrations of FC. Thus, 10% solution was chosen for CoPc functionalization for all other experiments. For AQ, 3

https://doi.org/10.1021/acsomega.5c01256

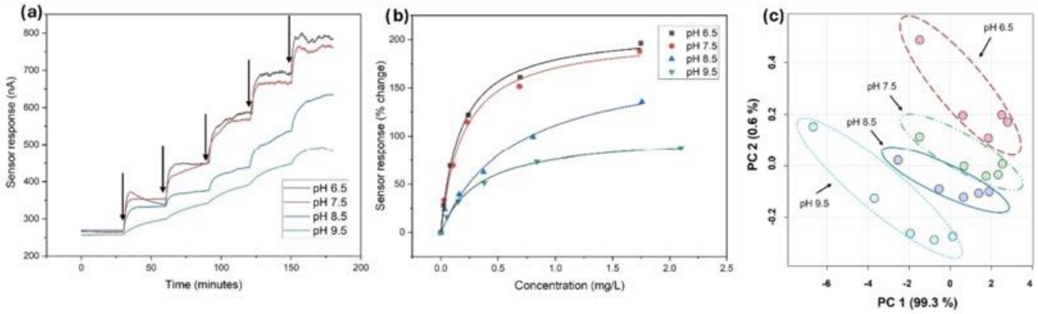

Figure 4. (a) Sensor responses of CoPc as current (nA) plotted against time. FC was added at a 30 min interval (black arrows represent the points of chlorine addition) in water with a background of NaCl and $NaHCO_3$. (b) Langmuir fitted curves for corresponding pH for increasing FC concentrations of the CoPc sensor. The Langmuir adsorption isotherm model fitting parameters are for pH 6.5, $a = 209.8 \pm 5.6\%$ and $b = 5.84 \pm 0.56\ mg^{-1}L$; for pH 7.5, $a = 204.8 \pm 7.5\%$ and $b = 5.11 \pm 0.63\ mg^{-1}L$; for pH 8.5, $a = 182.3 \pm 5.6\%$ and $b = 1.55 \pm 0.44\ mg^{-1}L$; and for pH 9.5, $a = 101.3 \pm 2.7\%$ and $b = 2.98 \pm 0.24\ mg^{-1}L$. (c) PCA score plot showing the regions of FC responses of CoPc, AQ, and blank sensors at different pH. Each pH region is circled and labeled.

and 10% showed the most stable response, while 1 and 30% were not stable at high concentrations of FC. The 10% AQ-functionalized sensor showed the best sensitivity and a good R^2 (0.97). Therefore, 10% was selected for functionalization of the sensors for all the other experiments.

Sensor Characterization. The functionalized (CoPc and AQ) and blank sensors were first kept in an aqueous background solution containing 100 mg/L of NaCl and 50 mg/L of $NaHCO_3$ to approximate the conductivity and pH of typical tap water.[24] Then, FC is added to the solution, and the resulting sensor response current as a function of time is shown in Figure 4a for the CoPc sensor. The FC concentration range tested was from 0.03 to 2.1 mg/L. This range covers the commonly found FC concentrations in water distribution systems.[50] Upon exposure to FC, all three sensors showed an increase in the current due to p-doping. The p-doping due to the interaction of oxidants with SWCNT networks is in agreement with previous reports.[37,51] This doping effect also manifested itself as an upshift in the 2D peaks of the Raman spectra (Figure S7) of functionalized and blank SWCNT samples when exposed to FC. Two forms of FC (HOCl and OCl^-) can coexist. Chlorine gas, when added to water, disproportionates into HOCl and HCl at pH values above 3. HOCl is a weak acid and at sufficiently high pH partially dissociates into OCl^- and H^+.[52]

$$HOCl \rightarrow OCl^- + H^+ \tag{3}$$

We can express the relationship between the concentrations with the following equation

$$\log\frac{[OCl^-]}{[HOCl]} = \log K_a + pH \tag{4}$$

Here, the equilibrium concentrations of HOCl and OCl^- are referred to as [HOCl] and $[OCl^-]$, respectively. K_a is the HOCl ionization constant, and at 25 °C, the pK_a is 7.54.[53] Therefore, the percent composition of the two species (HOCl and OCl^-) at a specific temperature is dependent on the pH of the solution. For instance, at 25 °C ($pK_a = 7.54$) and pH 9.5, eq 4 can be used to calculate the HOCl and OCl^- content. The HOCl content is 1.1%, while OCl^- makes up 98.9%. At pH 6.5, [HOCl] is 91.6%, and $[OCl^-]$ is 8.4%. Chemiresistive sensors respond to these two species via different mechanisms, as reported previously.[37] HOCl interacts with the blank chemiresistive film (SWCNT) through direct adsorption, resulting in a concentration-dependent response. Since HOCl is still present in basic solution (11% of total FC at pH 8.5 and 1% of total FC at pH 9.5), a blank sensor response is expected at all pHs.[37] HOCl also interacts with molecule-functionalized films through a redox reaction of the molecule. The negatively charged OCl^- interacts exclusively through redox-active moieties at the film surface, such as adsorbed CoPc or AQ, with the defects on the surface of the film. Therefore, the pH of the solution needs to be accounted for during measurements of FC in water. Another parameter of the water that contributes in chemiresistive sensing is the oxidation–reduction potential (ORP, a.k.a. redox potential) of the aqueous analyte. The HOCl and OCl^- reductions follow the reaction eqs 5 and 6.

$$HOCl + H^+ + 2e^- \rightarrow Cl^- + H_2O \tag{5}$$

$$OCl^- + H_2O + 2e^- \rightarrow Cl^- + 2OH^- \tag{6}$$

The concentration-dependent ORP of a redox reaction is governed by the Nernst equation

$$E = E_0 - 2.3\frac{RT}{nF}\log\frac{[\text{reducer}]}{[\text{oxidizer}]} \tag{7}$$

Here, E is the redox potential, E_0 is the standard redox potential, R is the universal gas constant, T is the temperature, n is the number of electrons transferred per mole of reaction, and F is the Faraday constant. For reactions 5 and 6, the Nernst equations can be expressed by

$$E = E_{0,\text{HOCl}} - 2.3\frac{RT}{nF}\log\frac{[Cl^-]}{[HOCl]\cdot[H^+]} \tag{8}$$

$$E = E_{0,\text{OCl}^-} - 2.3\frac{RT}{nF}\log\frac{[Cl^-]\cdot[OH^-]^2}{[OCl^-]} \tag{9}$$

eqs 8 and 9 show that increasing $[H^+]$ or decreasing pH will increase the E (ORP) of the solution. Additionally, increasing the concentration of FC will result in a higher ORP. HOCl, being the stronger oxidizing species (higher standard redox potential), will result in an ORP higher than the same concentration of OCl^-. Our devices will respond to the ORP

https://doi.org/10.1021/acsomega.5c01256
ACS Omega XXXX, XXX, XXX−XXX

change of the solution when FC is added. The overall response will increase at lower pH and decrease at higher pH. We tested the response to FC in 4 different pH's ranging from 6.5 to 9.5; this range covers the recommended pH range for drinking water by the World Health Organization (WHO).[1] Figure 4b shows calibration graphs of the FC responses shown in Figure 4a. The raw responses from Figure 4a are processed by taking an average of the last 2 min of current to get the data points, which are then plotted against the FC concentration measured by the standard DPD method. The data points were fitted with the Langmuir adsorption isotherm model. The sensor responses increase with decreasing pH. The fitting parameter *b*, which is indicative of the sensitivity of these chemiresistive devices, was found to increase with decreasing pH. Furthermore, our sensors also respond to a change just in pH (no FC present) as shown in Figure S10a at about 1% change in sensor response per unit of pH (Figure S10b). The same sensor when exposed to FC gives an 80% sensor response for 2 mg/L of FC (Figure S10c). Therefore, the sensors individually cannot detect the FC concentration and pH. Despite the difference in sensitivity of a single sensor toward changes in pH, their correlated responses make it impossible to measure FC level and pH using a single sensor. Hence, we proposed an array of sensors to improve our previously demonstrated individual sensors for pH[26] and FC.[24]

To illustrate the use of the sensor array, a set of three freshly made sensors were exposed to FC over a range of pHs. The responses are shown in Figures S11−S13. Functionalization does not necessarily result in an overall larger response of the individual sensor but changes the nature of the interactions between the sensors and the different analytes relative to each other, such that each sensor response contributes an independent parameter to the array, allowing for chemometric analysis and elucidation of individual analyte concentrations from the responses of the array components. CoPc was found to be more responsive to FC than AQ. CoPc functionalized chemiresistors are known to be redox-active when exposed to Cl_2 gas due to their redox-active metal centers.[44] This does not translate directly to the sensing of aqueous FC species (HOCl and OCl^-) since the chemiresistive film is in contact with a complex aqueous environment (including the electrochemical double layer), where redox activity is associated with both charged and uncharged species. Higher responses from the CoPc sensor may be attributable to the cobalt center getting oxidized. The oxidation of cobalt modulates the charge distribution of the phthalocyanine ring structure which in turn modulates doping of the SWCNT network. In contrast, AQ interacts through the redox reaction that takes place at the carbonyl groups (positions 9 and 10). Furthermore, AQ can show measurable pH responses due to the protonation and deprotonation of the molecule.[45,54,55] In the array, AQ acts like a pH sensor while also responding to FC. To distinguish the pH regions from the correlated sensor responses, routinely used chemometric approaches like PCA and LDA were used.[37] Recently, we have demonstrated the use of chemometric methods in differentiating analytes in water.[42,56] The sensor array data (as percent changes) are first normalized with autoscaling and log-transformation methods to uniformly distribute the data set (Figure S14) and to avoid bias in the chemometric analysis. Upon analysis with PCA, a total of three principal components (PCs) are generated from the three variables (sensors), and each of the PCs represents a linear combination of the original variables. The first two principal components were plotted to show the distribution of the scores in Figure 4c. The first two components accounted for 99.9% of the total variance ($R^2 = 0.99$). Therefore, we can assume that most of the variance was captured by the two components. Each of the 20 scores (coordinates) in the score plot represents an observation with multivariate responses, and the distance between the scores represents the difference in the observations. The circled region represents different pH regions tested. Each score in a circle represents a different FC concentration. HOCl is predominant in acidic environments and dominates the sensor responses. Though there were some overlaps in the pH 7.5 and 8.5 ellipses, the data points are well separated. This demonstrated that the responses were distinct from each other. Considering the wide range of concentrations (0.03−2.1 mg/L) tested for the extreme pHs (6.5−9.5), the array demonstrates potential applicability in the water distribution system. PCA was also carried out using only two variables (CoPc and AQ) and the responses are shown in Figure S15. The PCA score plot shows distinct pH regions of the correlative sensor responses from the CoPc and AQ sensors. This demonstrates that functionalization of the sensors was successful, modifying their responses to be distinct and separable, which would not be possible for a set of blank sensors.

To complement the unsupervised PCA, LDA (a supervised method) analysis was carried out on the data set. Figure S14 shows the plot of the two canonical variables generated from the original data set. The plot (Figure S16) shows that the pH regions are well separated along the first canonical variable. In addition to better discrimination, LDA recognizes the label and can be implemented to cross-validate the data points. Leave-one-out cross-validation method (LOOCV) was chosen for the data set to avoid overfitting of the model. This method treats each data point as test data and predicts a class based on the rest of the data set (training data set). The LDA analysis showed 95% accuracy for the data set. In both PCA and LDA, the scores are representations of the responses generated by the sensors. For two different sensor responses from one variable, two distinct scores should be generated. When calibrated for a range of pHs and FC concentrations, a multivariate map can be created through which pH can be monitored. In a practical setup, these kinds of plots (Figures 4c, S15, and S16) can be used to detect pHs from the sensor array responses. Then, a multivariate regression model such as principal component regression (PCR) or partial least-squares regression (PLSR) can be used to quantify the concentration of FC in solution. Therefore, it is demonstrated that arrays of three or two sensors can be used for the detection of pHs with a range of FC concentrations.

Electrical Reset-Assisted Continuous Monitoring. Real-time monitoring of fast decreases in FC levels with chemiresistive sensors requires resetting of the sensors. While this could be achieved by adding a reducing agent,[24] this would complicate the application for continuous monitoring in drinking water distribution systems. Here, as an improvement, we intermittently reduced the film through an electrical reset pulse applied to the sensors. This allows the sensors to quickly respond to changes at the FC level. A graphite electrode was used to cathodically polarize the sensors, notably without the need for a reference electrode. The electrode was connected to the negative contact of one of the eDAQ channels, and the positive contact of the channel was then connected to the positive contacts of the sensors. A small voltage pulse of −10

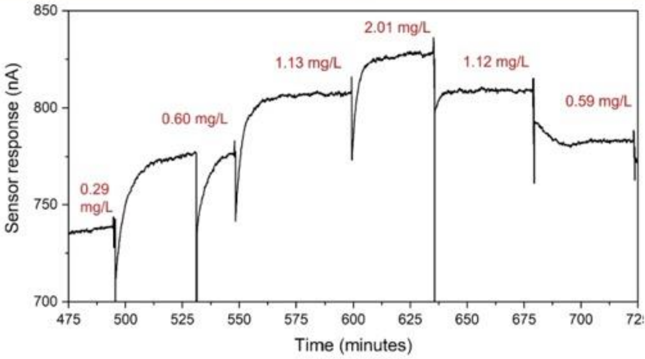

Figure 5. Electrical reset of the CoPc sensor in water with a background of NaCl (1.71 mmol) and $NaHCO_3$ (0.59 mmol). The sensor response is presented as the current change against time. Each of the sharp current changes represents the reset pulse. The concentrations labeled above the curve represent the actual FC concentrations measured by the commercial DPD reagent.

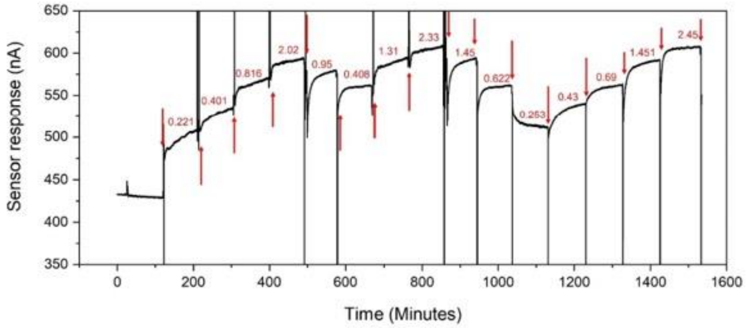

Figure 6. Continuous measurement of FC in simulated tap water (0.04 mmol of KH_2PO_4, 0.6 mmol of $CaCl_2$, 0.3 mmol of $MgSO_4$, and 1 mmol of $NaHCO_3$) using the electrical reset. Raw sensor response of CoPc when exposed to varying concentrations of FC. The arrows represent the FC concentration change, and the concentration for each spike is labeled on top. After every concentration change, an electrical reset was applied.

mV was applied between the electrode and the positive contact of the sensor. This cathodic polarization was carried out for 2–4 s. As shown in Figure 5, the reset pulse was applied at the 495th minute of the 0.29 mg/L response, and more FC was added. During the reset pulse, the measured current across the SWCNT film dropped sharply, and then the current increased to 775 nA corresponding to 0.60 mg/L of FC. This was observed in both functionalized and blank sensors (Figure S17). To evaluate how the reset affects the sensor response, another reset was applied while maintaining 0.60 mg/L FC at 530th minute. Again, the current dropped sharply and then increased back up to the previous level of 775 nA after 12–15 min. After resetting the sensor, 1.13 and 2.01 mg/L FC were spiked to demonstrate its potential application in water. Then, another reset pulse was applied immediately after exposing the sensor to a lower level of FC (mg/L) at the 635th minute to 1.12 mg/L. Subsequently, the concentration was further decreased to 0.59 mg/L at the 678th minute. The current showed a downward trend to track the lower concentration of FC. While the sensors will themselves respond to a decrease in FC concentration, it will be over a much longer time frame.[24] Therefore, this electronic reset accelerates the response of the sensors to sudden drops in FC concentration, which could constitute an emergency in a drinking water distribution system.

Interferences from the analyte matrix can affect sensor measurement. With the intention to model a real tap water matrix, we prepared a simulated tap water solution to test the sensors. The sensors used for continuous measurement were fabricated with optimized parameters. For reference, the annual water quality report by the City of Hamilton (Ontario, Canada) was followed.[50] To prepare the background we included all the major ions present in the tap water of the City of Hamilton by adding 0.04 mmol of KH_2PO_4, 0.6 mmol of $CaCl_2$, 0.3 mmol of $MgSO_4$, and 1 mmol of $NaHCO_3$. After the ions were added to ultrapure water, the solution was monitored to reach a stable pH. The simulated tap water showed comparable pH (~8) and conductivity (0.29 mS/cm) as the NaCl and $NaHCO_3$ background (pH ~8 and conductivity 0.32 mS/cm) used for the previous experiment. After 2 h, the pH stabilized, and then the sensors were placed to obtain a stable baseline, and then FC was added to the simulated tap water. The actual FC concentration of the solution was measured by the DPD method to range from 0.22 to 2.45 mg/L. The pH of the solution remained stable at 8 ± 0.02 during the experiment. Figure 6 shows the raw sensor

https://doi.org/10.1021/acsomega.5c01256
ACS Omega XXXX, XXX, XXX−XXX

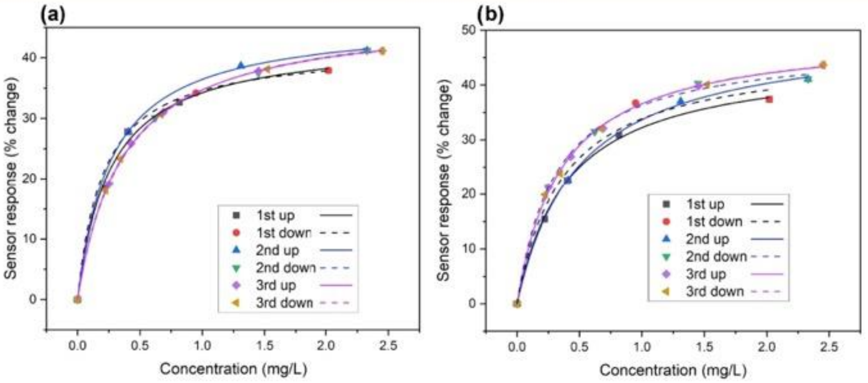

Figure 7. Calibration graphs of the CoPc (a) and AQ (b) sensors in simulated tap water from the responses in continuous measurement. Actual sensor responses (dots) are fitted with Langmuir adsorption isotherms. The fitted lines are presented as solid lines for the upward cycle and dashed lines for the downward cycle. The fitting parameters are provided in the Supporting Information (Table S2).

responses of the CoPc sensor in simulated tap water. The raw data for the AQ and blank sensors are provided in the Supporting Information (Figures S18 and S19). The raw responses show multiple cycles, including first up, first down, second up, second down, and third up. Electronic resets were applied for both increasing and decreasing concentrations of FC. It should be noted that the blank sensor was only stable until the end of the third up cycle, while the functionalized sensors remain stable even after the third down cycle. Sensor responses stabilized more quickly after the first cycle. We repeatedly observed that the first cycle acts like a pretreatment of the sensors.[24] This could be because of the interaction of FC with adventitious carbon on the SWCNT film. As the surface is cleaned by the oxidizing agent, the sensors respond faster. In a real scenario, residual FC level monitoring is needed after chlorination at the treatment plant and in the distribution system. Therefore, the measurement of FC in simulated tap water with commonly found ions demonstrates the use of the array to continuously monitor the FC level. While other oxidizing and reducing agents can interfere with the sensor response, since the sensors are sensitive to these types of chemicals, this is unlikely to occur in actual drinking water applications where the nature of the disinfectant is known and constant.

The raw sensor responses for the continuous measurement were fitted with Langmuir adsorption isotherms with the corresponding FC concentrations for each cycle (upward/downward). Figure 7 represents the curves for the fitted sensor responses for CoPc and AQ sensors. The calibration graph for the blank sensor can be found in the Supporting Information (Figure S20). The sensor responses fit better from the second upward trend. We found that the fitting parameters (Table S2) show a narrow range, demonstrating the applicability of the system for continuous measurement. Since the blank sensor is prone to fouling and durability issues, the blank sensor is excluded from the multivariate regression analysis. The use of only the CoPc and AQ sensors is found to retain full functionality of the array in separating FC level and pH. Figure S21 shows blank sensors from different batches with repeat measurements. It should be noted that though our sensor absolute response can be different in values from sensors from different batches, sensors can be calibrated and can be implemented to detect FC. Fitting parameters for the data collected from the different batches are presented in Table S3. Figure S21 shows that sensors from different batches can be used multiple times for FC sensing.

We analyzed the sensor array responses (AQ and CoPc) for the continuous measurement in simulated tap water with a multivariate regression method called partial least-squares (PLS). Partial least-squares regression (PLSR) is a commonly used method for multivariate quantification, and especially advantageous for a situation where the variables are highly colinear.[42] Here, we present the output of the model as a PLSR plot (Figure 8) using the data from the second and third cycles. Actual concentrations of the solutions were plotted against the predicted concentrations generated from the model based on the sensor responses. The solid line shows the ideal

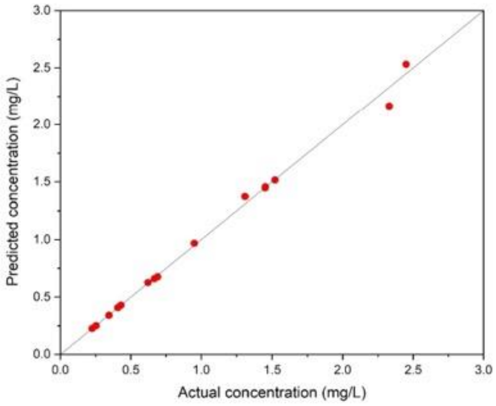

Figure 8. Regression graph for the continuous simulated tap water measurements by the CoPc and AQ sensors from the second and third cycles. PLS model showing the predicted concentration from the model and actual concentration measured by the DPD colorimetric method. The dashed line represents the ideal comparison line. The R^2 value for the model is 0.999, and the RMSELOOCV value is 0.0231.

Table 1. Comparison of Recently Reported Aqueous Free Chlorine Sensors[a]

sensing method	sensing material	range of detection (mg/L)	limit of detection (mg/L)	pH detection (integrated, separate, No)	ref
colorimetric	methyl orange	1−10		separate	59
	DPD	0.04−6.07	0.015	separate	60
electrochemical	CuO-ZIF-8	0.25−60	0.012	separate	61
	Au thin film	0−6	0.8 (lowest measured)	separate	62
	Au interdigitated array	0.5−4.5	0.01	no	63
	asparagine-GO	0−8	0.9 (lowest measured)	no	64
schottky diode	graphene	0.01−1.0	0.003	separate	34
FET	graphene	0.07−7	0.007	no	35
	graphene	0−5.0	0.1 (lowest measured)	separate	65
	graphene	0−3.0	0.56 (lowest measured)	no	66
chemiresistive	SWCNT-PCAT	0.06−60	0.06 (lowest measured)	no	29
	GLC-PCAT	0.01−1.4	0.001	separate	24
	graphene-PEDOT:PSS	0.1−500	0.18	no	32
	SWCNT-CoPc-AQ array	0.015−10	0.001	integrated	this work

[a] GO = graphene oxide, GLC = graphene-like carbon, ZIF-8 = zeolitic imidazolate frameworks, $Zn(Hmim)_2$, DPD = *N*,*N*-diethyl-*p*-phenylenediamine, PCAT = phenyl-capped aniline tetramer, PEDOT:PSS = poly(3,4-ethylenedioxythiophene):poly(styrenesulfonate), CoPc = cobalt phthalocyanine, AQ = anthraquinone.

responses for the array. The PLSR model was evaluated by indicators for regression analysis such as R^2 and root mean squared error leave-one-out cross-validation (RMSELOOCV). RMSELOOCV validates the model's performance by systematically excluding a data point from the data set and then training the model on the remaining data. Then, it predicts the left-out data, and the whole process is repeated to the full data set. Therefore, this gives a complete measure of model performance. The R^2 value for the model in Figure 8 was calculated to be 0.999 and RMSELOOCV of 0.0231. The close to 1 R^2 value and low RMSELOOCV value indicate that the model fits the data well. PLSR carried out on the full data set (including first cycle) showed that the fit is less predictive with deviation from the linearity (shown in Figure S22). The R^2 value for the model with all of the cycles for AQ and CoPc was calculated to be 0.988 and RMSELOOCV of 0.0822. Therefore, including the first cycle makes the model less predictive and inefficient. In a practical scenario, the first cycle can be excluded to calibrate the sensors for continuous measurements.

The conductivity of the water sample matters because the ions in the solution can affect the electrical double layer formed on the surfaces of the SWCNT network through the arrangement of dissolved ions in water. To investigate the effect of conductivity change, we modified the conductivity of the simulated tap water background, which has a conductivity of 0.29 mS/cm. The conductivity measured for Hamilton tap water ranged from 0.29 to 0.34 mS/cm. To increase the conductivity of the simulated water, NaCl was added to the background solution, with the sensor responses shown in Figure S23. After the conductivity was doubled to 0.58 mS/cm, we noticed a slight decrease in the sensor responses. This further drops (less than 0.5%) after increasing the conductivity to 0.95 mS/cm. This reduced p-type doping agrees with our previous studies with nanocarbon film (graphene) where high conductivity led to a decrease in current (−4.5% for 1.0 mS/cm).[49] This decrease in current can be attributed to electrostatic gating of the p-type SWCNT surface. When the ionic strength is high, this layer becomes more compact, and the counterions are packed closely to the SWCNT surface, thereby reducing the charge carriers on the surface which then leads to decreased current. The FC response in high conductivity was then evaluated by adding 0.47 mg/L FC. The sensor response measured for the 0.47 mg/L FC was 27.89% for AQ, 33.15% for CoPc, and 23.04% for blank, which are considerably higher than the sensor response due to doubling or tripling the solution conductivity. This demonstrates that the sensors can perform well in the background water within commonly reported ranges of ionic strength. We further increased the conductivity to 3.69 mS/cm, while FC was present in the solution to mimic a practical scenario where residual FC will be present. The sensors only showed less than 1% change to the conductivity change, demonstrating that the sensors can be used to monitor the FC level in cases of high ionic strength. To cover the range of detection, we tested the sensors for 0.015−10 mg/L of FC concentrations in simulated tap water background to cover lower- and higher-end FC concentrations (Figure S24a). The sensors showed an excellent limit of detection (LOD) of 0.001 mg/L. Figure S24b shows the Langmuir fit, and Figure S24c shows the linearized version of the Langmuir adsorption isotherm. Therefore, the sensor array can be implemented for a wide range of FC concentrations after careful calibration in the proper background.

■ CONCLUSIONS

Drinking water safety depends on the disinfection level in the water distribution system. Knowing the pH of the water is necessary to ensure water quality and disinfectant power to prevent the growth of disease-causing microorganisms. In this study, we present an improved sensor design to facilitate mass-scale fabrication through systematic optimization. The surface area of the active layer was extended to increase the sensor responses, and silver electrodes were incorporated to improve the sensor quality. We have proposed and validated an array to measure the pH and FC level by including sensors functionalized with CoPc and AQ. Functionalization affects the nature of the interactions between the sensors and the different analytes relative to each other, such that chemometric analysis can determine individual analyte concentrations from the array response. We found that CoPc renders the sensor somewhat more responsive toward FC than to pH while AQ functionalization results in a sensor that is somewhat more responsive to pH change and less to FC. Though individually both sensors still respond to both pH and FC, their combined responses were able to distinctly determine pH and FC. PCA was employed to demonstrate that the pH of the solution (6.5 to 9.5) can be detected/monitored in the presence of FC. PCA has been used for monitoring processes;[57,58] therefore, it can be easily incorporated in the distribution system to monitor pH. Once the pH is determined, multivariate regression such as PLSR can be used to quantify the concentration. Knowing both pH and FC concentration, one can measure the level of disinfection in water to ensure drinking water quality. We have demonstrated a continuous monitoring approach using just two SWCNT chemiresistive sensors functionalized with AQ and CoPc, respectively. We have introduced an electrical reset to detect upward and downward changes in the FC level in a continuous fashion. To demonstrate the performance of the sensors in a practical setup, we tested the sensor array in a simulated water background. The sensor array demonstrated an effective calibration for this specific water matrix without interference from ions commonly present in drinking water. In cases in which real-world water samples contain free chlorine as a residual disinfectant, this chemiresistive array can be applicable following calibration in a matching background. The incorporation of an improved sensor design and electrical reset component allows for more repeatable sensing performance compared to previous studies.[24] Surface modification with selective membranes or antifouling coatings may also be incorporated with chemiresistive sensor arrays to mitigate the variations in sensor responses due to matrix impact. The sensor response is not instantaneous, but it is fast enough to detect sudden drops in free chlorine (FC) levels or track continuous fluctuations over time (from hours to days). This enables real-time monitoring, long-term trend analysis, and early warning of water quality changes.

The sensor array reported in this article compares favorably with other recently reported methods for aqueous FC detection (Table 1). Colorimetric and electrochemical methods are in common use for FC monitoring. They have low detection limits, however, require either reagents (colorimetric) or reference electrodes (electrochemical). In contrast to other studies, our sensor array provides an integrated solution for continuous monitoring of both FC concentration and pH without using reagents or reference electrodes. We tested FC concentrations ranging from 0.22 to 2.45 mg/L in a continuous manner. This range can be extended to 0.015−10 mg/L as demonstrated, covering in excess of the range commonly used in water distribution systems. The LOD was calculated to be 0.001 mg/L. Lastly, we showed that the CoPc and AQ sensor responses can be incorporated as a predictive model through PLSR. Overall, this low-cost chemiresistive array-based method is key for monitoring multivariate analytes.

■ ASSOCIATED CONTENT

Supporting Information

The Supporting Information is available free of charge at https://pubs.acs.org/doi/10.1021/acsomega.5c01256.

> Experimental details, including photographs of the experimental setup, characterization data (SEM, Raman), functionalization process data, fitting parameters, and chemometric data (PDF)

■ AUTHOR INFORMATION

Corresponding Author

Peter Kruse − *Department of Chemistry and Chemical Biology, McMaster University, Hamilton, Ontario L8S 4M1, Canada;* orcid.org/0000-0003-4051-4375;
Email: pkruse@mcmaster.ca

Authors

Md Ali Akbar − *Department of Chemistry and Chemical Biology, McMaster University, Hamilton, Ontario L8S 4M1, Canada;* orcid.org/0000-0002-1809-8232
Mehraneh Tavakkoli Gilavan − *School of Biomedical Engineering, McMaster University, Hamilton, Ontario L8S 4L7, Canada*
Ponnambalam Ravi Selvaganapathy − *School of Biomedical Engineering and Department of Mechanical Engineering, McMaster University, Hamilton, Ontario L8S 4L7, Canada;* orcid.org/0000-0003-2041-7180

Complete contact information is available at:
https://pubs.acs.org/10.1021/acsomega.5c01256

Notes

The authors declare no competing financial interest.

■ ACKNOWLEDGMENTS

We thank Dr. Axel Kramer and Sylvio R. Laplante from ABB for fruitful discussions. We thank Thomas Kirby and Dr. Dipankar Saha for their discussion on preparing samples for SEM and Raman spectroscopy. We thank Dr. Adronov group for granting access to a Raman spectrometer and Mokhamed Ranne for training on the instrument. Jhoynner Martinez's assistance with SEM imaging at CCEM is appreciated. Electron microscopy was performed at the Canadian Centre for Electron Microscopy (also supported by NSERC and other government agencies). Funding for this work was provided by the National Science and Engineering Research Council of Canada (NSERC) through the Discovery Grant Program (RGPIN-2018-06145 and RGPIN-2023-04927) and an Alliance Grant (ALLRP 566183−21) as well as by ABB, Inc.

■ REFERENCES

(1) *Guidelines for Drinking-Water Quality, 4 Edition, Incorporating the 1 Addendum* World Health Organization: Geneva; 2017.

(2) Sayre, I. M. International Standards for Drinking Water. *J. AWWA* **1988**, *80* (1), 53−60.

(3) Wilson, R. E.; Stoianov, I.; O'Hare, D. Continuous Chlorine Detection in Drinking Water and a Review of New Detection Methods. *Johnson Matthey Technol. Rev.* **2019**, *63* (2), 103−118.

(4) Feng, Y.; Smith, D. W.; Bolton, J. R. Photolysis of Aqueous Free Chlorine Species (HOCl and OCl−) with 254 Nm Ultraviolet Light. *J. Environ. Eng. Sci.* **2007**, *6*, 277−284.

(5) Hrudey, S. E.; Payment, P.; Huck, P. M.; Gillham, R. W.; Hrudey, E. J. A Fatal Waterborne Disease Epidemic in Walkerton, Ontario: Comparison with Other Waterborne Outbreaks in the Developed World. *Water Sci. Technol.* **2003**, *47* (3), 7−14.

(6) Salvadori, M. I.; Sontrop, J. M.; Garg, A. X.; Moist, L. M.; Suri, R. S.; Clark, W. F. Factors That Led to the Walkerton Tragedy. *Kidney Int.* **2009**, *75* (112), S33−S34.

(7) Jensen, J. N.; Johnson, D. J. Specificity of the DPD and Amperometric Titration Methods for Free Available Chlorine: A Review. *J. AWWA* **1989**, *81* (12), 59−64.

(8) Palin, A. T.; Journal, S.; Water, A.; Association, W.; July, N. The Determination of Free and Combined Chlorine in Water by the Use of Diethyl-p- Phenylene Diamine. *J. AWWA* **1957**, *49* (7), 873−880.

(9) Gordon, G.; Sweetin, D. L.; Smith, K.; Pacey, G. E. Improvements in the N,N-Diethyl-p-Phenylenediamine Method for the Determination of Free and Combined Residual Chlorine through the Use of FIA. *Talanta* **1991**, *38* (2), 145−149.

(10) Moberg, L.; Karlberg, B. An Improved N,N′-Diethyl-p-Phenylenediamine (DPD) Method for the Determination of Free Chlorine Based on Multiple Wavelength Detection. *Anal. Chim. Acta* **2000**, *407*, 127−133.

(11) Verma, K. K.; Jain, A.; Townshend, A. Determination of Free and Combined Residual Chlorine by Flow-Injection Spectrophotometry. *Anal. Chim. Acta* **1992**, *261*, 233−240.

(12) van den Berg, A.; Grisel, A.; Verney-Norberg, E.; van der Schoot, B. H.; Koudelka-Hep, M.; de Rooij, N. F. On-Wafer Fabricated Free-Chlorine Sensor with Ppb Detection Limit for Drinking-Water Monitoring. *Sens. Actuators, B* **1993**, *13* (1−3), 396−399.

(13) US Environmental Protection Agency - Office of Water. *Alternative Disinfectants and Oxidants Guidance Manual*, 1st Ed; US Environmental Agency: Washington, DC; 1999.

(14) Palin, A. T. The Determination of Free and Combined Chlorine in Water by the Use of Diethyl-p- Phenylene Diamine. *J. AWWA* **1957**, *49* (7), 873−880.

(15) Fang, Q.; Wang, Q.; Lin, W.; You, X.; Dong, Y.; Chi, Y. High Photoluminescent TPA and the Ratiometric Sensor for Free Chlorine. *Sens. Actuators, B* **2017**, *244*, 771−776.

(16) Dong, Y.; Li, G.; Zhou, N.; Wang, R.; Chi, Y.; Chen, G. Graphene Quantum Dot as a Green and Facile Sensor for Free Chlorine in Drinking Water. *Anal. Chem.* **2012**, *84*, 8378−8382.

(17) Jović, M.; Cortés-Salazar, F.; Lesch, A.; Amstutz, V.; Bi, H.; Girault, H. H. Electrochemical Detection of Free Chlorine at Inkjet Printed Silver Electrodes. *J. Electroanal. Chem.* **2015**, *756*, 171−178.

(18) Yin, J.; Gao, W.; Yu, W.; Guan, Y.; Wang, Z.; Jin, Q. A Batch Microfabrication of a Self-Cleaning, Ultradurable Electrochemical Sensor Employing a BDD Film for the Online Monitoring of Free Chlorine in Tap Water. *Microsyst. Nanoeng.* **2022**, *8*, No. 39, DOI: 10.1038/s41378-022-00359-1.

(19) Pan, S.; Deen, M. J.; Ghosh, R. Low-Cost Graphite-Based Free Chlorine Sensor. *Anal. Chem.* **2015**, *87* (21), 10734−10737.

(20) Kumar, D. R.; Kesavan, S.; Nguyen, T. T.; Hwang, J.; Lamiel, C.; Shim, J. Polydopamine @ Electrochemically Reduced Graphene Oxide-Modified Electrode for Electrochemical Detection of Free-Chlorine. *Sens. Actuators, B* **2017**, *240*, 818−828.

(21) Muñoz, J.; Céspedes, F.; Baeza, M. Modified Multiwalled Carbon Nanotube/Epoxy Amperometric Nanocomposite Sensors with CuO Nanoparticles for Electrocatalytic Detection of Free Chlorine. *Microchem. J.* **2015**, *122*, 189−196.

(22) Siddiqui, J.; Deen, M. J. Biodegradable Asparagine−Graphene Oxide Free Chlorine Sensors Fabricated Using Solution-Based Processing. *Analyst* **2022**, *147* (16), 3643−3651.

(23) Kruse, P. Review on Water Quality Sensors. *J. Phys. D:Appl. Phys.* **2018**, *51*, No. 203002.

(24) Zubiarrain-Laserna, A.; Angizi, S.; Akbar, M. A.; Divigalpitiya, R.; Selvaganapathy, P. R.; Kruse, P. Detection of Free Chlorine in Water Using Graphene-like Carbon Based Chemiresistive Sensors. *RSC Adv.* **2022**, *12*, 2485−2496.

(25) Meng, Z.; Stolz, R. M.; Mendecki, L.; Mirica, K. A. Electrically-Transduced Chemical Sensors Based on Two-Dimensional Nanomaterials. *Chem. Rev.* **2019**, *119* (1), 478−598.

(26) Angizi, S.; Huang, X.; Hong, L.; Akbar, M. A.; Selvaganapathy, P. R.; Kruse, P. Defect Density-Dependent PH Response of Graphene Derivatives: Towards the Development of PH-Sensitive Graphene Oxide Devices. *Nanomaterials* **2022**, *12*, No. 1801.

(27) Thokala, N.; Vankayala, K.; Gaonkar, A. D.; Periyasamy, G.; Fazl-Ur-Rahman, K.; Valle, K.; DMello, M. E.; Basavaiah, K.; Kalidindi, S. B. An Exfoliated Redox Active Imide Covalent Organic Framework for Metal Free Hydrogen Gas Sensing. *Sens. Diagn.* **2023**, *2* (5), 1176−1180.

(28) Kumar, S.; Kushwaha, C. S.; Singh, P.; Kanojia, K.; Shukla, S. K. Chemiresistive Sensor for Breath Frequency and Ammonia Concentration in Exhaled Gas over a PVA/PANI/CC Composite Film. *Sens. Diagn.* **2023**, *2* (5), 1256−1266.

(29) Hsu, L. H. H.; Hoque, E.; Kruse, P.; Selvaganapathy, P. R. A Carbon Nanotube Based Resettable Sensor for Measuring Free Chlorine in Drinking Water. *Appl. Phys. Lett.* **2015**, *106*, No. 063102.

(30) Hoque, E.; Hsu, L. H. H.; Aryasomayajula, A.; Selvaganapathy, P. R.; Kruse, P. Pencil-Drawn Chemiresistive Sensor for Free Chlorine in Water. *IEEE Sens. Lett.* **2017**, *1* (4), No. 4500504.

(31) Mohtasebi, A.; Broomfield, A. D.; Chowdhury, T.; Selvaganapathy, P. R.; Kruse, P. Reagent-Free Quantification of Aqueous Free Chlorine via Electrical Readout of Colorimetrically Functionalized Pencil Lines. *ACS Appl. Mater. Interfaces* **2017**, *9* (24), 20748−20761.

(32) Yen, Y. K.; Lee, K. Y.; Lin, C. Y.; Zhang, S. T.; Wang, C. W.; Liu, T. Y. Portable Nanohybrid Paper-Based Chemiresistive Sensor for Free Chlorine Detection. *ACS Omega* **2020**, *5* (39), 25209−25215.

(33) Wu, R.; Gilavan, M. T.; Akbar, M. A.; Fan, L.; Selvaganapathy, P. R. Direct Transformation of Polycarbonate to Highly Conductive and Superhydrophobic Graphene/Graphitic Composite by Laser Writing and Its Applications. *Carbon* **2024**, *216*, No. 118597.

(34) Angizi, S.; Selvaganapathy, P. R.; Kruse, P. Graphene-Silicon Schottky Devices for Operation in Aqueous Environments: Device Performance and Sensing Application. *Carbon* **2022**, *194*, 140−153.

(35) Xiong, C.; Zhang, T.; Wang, D.; Lin, Y.; Qu, H.; Chen, W.; Luo, L.; Wang, Y.; Zheng, L.; Fu, L. Highly Sensitive Solution-Gated Graphene Transistor Based Sensor for Continuous and Real-Time Detection of Free Chlorine. *Anal. Chim. Acta* **2018**, *1033*, 65−72.

(36) Schroeder, V.; Savagatrup, S.; He, M.; Lin, S.; Swager, T. M. Carbon Nanotube Chemical Sensors. *Chem. Rev.* **2019**, *119* (1), 599−663.

(37) Akbar, M. A.; Sharif, O.; Selvaganapathy, P. R.; Kruse, P. Identification and Quantification of Aqueous Disinfectants Using an Array of Carbon Nanotube-Based Chemiresistors. *ACS Appl. Eng. Mater.* **2023**, *1* (11), 3040−3052.

(38) Su, H. C.; Tran, T. T.; Bosze, W.; Myung, N. V. Chemiresistive Sensor Arrays for Detection of Air Pollutants Based on Carbon Nanotubes Functionalized with Porphyrin and Phthalocyanine Derivatives. *Sens. Actuators Rep.* **2020**, *2* (1), No. 100011.

(39) Ivanova, V.; Şenocak, A.; Klyamer, D.; Demirbas, E.; Makhseed, S.; Krasnov, P.; Basova, T.; Durmuş, M. 3D Hybrid Materials Based on Zinc and Cobalt Phthalocyanine Derivatives Bearing Terminal Ethynyl Substituents as Active Layers for Chemiresistive Gas Sensors. *Sens. Actuators, B* **2024**, *398*, No. 134733.

(40) Wang, Y.; Hu, N.; Zhou, Z.; Xu, D.; Wang, Z.; Yang, Z.; Wei, H.; Kong, E. S. W.; Zhang, Y. Single-Walled Carbon Nanotube/Cobalt Phthalocyanine Derivative Hybrid Material: Preparation, Characterization and Its Gas Sensing Properties. *J. Mater. Chem.* **2011**, *21* (11), 3779−3787.

(41) Sharma, A. K.; Mahajan, A.; Kumar, S.; Debnath, A. K.; Aswal, D. K. Tailoring of the Chlorine Sensing Properties of Substituted Metal Phthalocyanines Non-Covalently Anchored on Single-Walled Carbon Nanotubes. *RSC Adv.* **2018**, *8* (57), 32719−32730.

(42) Akbar, M. A.; Selvaganapathy, P. R.; Kruse, P. Continuous Monitoring of Monochloramine in Water, and Its Distinction from Free Chlorine and Dichloramine Using a Functionalized Graphene-Based Array of Chemiresistors. *ACS ES&T Water* **2024**, *4* (9), 4041−4051.

(43) Pang, Z.; Lu, Y.; Zhou, G.; Hui, F.; Xu, L.; Viau, C.; Spigelman, A. F.; MacDonald, P. E.; Wishart, D. S.; Li, S.; Xia, J. MetaboAnalyst 6.0: Towards a Unified Platform for Metabolomics Data Processing, Analysis and Interpretation. *Nucleic Acids Res.* **2024**, *52*, No. gkae253.

(44) Sharma, A. K.; Mahajan, A.; Bedi, R. K.; Kumar, S.; Debnath, A. K.; Aswal, D. K. CNTs Based Improved Chlorine Sensor from Non-Covalently Anchored Multi-Walled Carbon Nanotubes with Hexa-Decafluorinated Cobalt Phthalocyanines. *RSC Adv.* **2017**, *7* (78), 49675−49683.

(45) Bourourou, M.; Elouarzaki, K.; Lalaoui, N.; Agnès, C.; Le Goff, A.; Holzinger, M.; Maaref, A.; Cosnier, S. Supramolecular

Immobilization of Laccase on Carbon Nanotube Electrodes Functionalized with (Methylpyrenylaminomethyl)Anthraquinone for Direct Electron Reduction of Oxygen. *Chem. - A Eur. J.* **2013**, *19* (28), 9371–9375.

(46) Brousse, T.; Cougnon, C.; Bélanger, D. Grafting of Quinones on Carbons as Active Electrode Materials in Electrochemical Capacitors. *J. Braz. Chem. Soc.* **2018**, *29* (5), 989–997.

(47) Patel, V.; Akbar, M. A.; Kruse, P.; Selvaganapathy, P. R. A Reagent-Free Phosphate Chemiresistive Sensor Using Carbon Nanotubes Functionalized with Crystal Violet. *Analyst* **2023**, *148*, 3551–3558.

(48) Moonoosawmy, K. R.; Kruse, P. Cause and Consequence of Carbon Nanotube Doping in Water and Aqueous Media. *J. Am. Chem. Soc.* **2010**, *132* (5), 1572–1577.

(49) Dalmieda, J.; Zubiarrain-Laserna, A.; Ganepola, D.; Selvaganapathy, P. R.; Kruse, P. Chemiresistive Detection of Silver Ions in Aqueous Media. *Sens. Actuators, B* **2021**, *328*, No. 129023.

(50) City of Hamilton. Drinking Water Systems Annual Water Quality and Summary Report. 2021.

(51) Patel, V.; Saha, D.; Kruse, P.; Selvaganapathy, P. R. Reagent-Free Hydrogen Peroxide Sensing Using Carbon Nanotube Chemiresistors with Electropolymerized Crystal Violet. *ACS Appl. Nano Mater.* **2022**, *5* (3), 3957–3966.

(52) Qin, Y.; Kwon, H. J.; Howlader, M. M. R.; Deen, M. J. Microfabricated Electrochemical PH and Free Chlorine Sensors for Water Quality Monitoring: Recent Advances and Research Challenges. *RSC Adv.* **2015**, *5* (85), 69086–69109.

(53) Carrell, J.; Morris, J. C. The Acid Ionization Constant of HOCl from 5 to 35°. *J. Phys. Chem. A* **1966**, *70* (12), 3798–3805.

(54) Rohland, P.; Schreyer, K.; Hager, M. D.; Schubert, U. S. Anthraquinone-2,6-Disulfamidic Acid: An Anolyte with Low Decomposition Rates at Elevated Temperatures. *RSC Adv.* **2021**, *11* (61), 38759–38764.

(55) Turcanu, A.; Bechtold, T. PH Dependent Redox Behaviour of Alizarin Red S (1,2-Dihydroxy-9,10- Anthraquinone-3-Sulfonate) - Cyclic Voltammetry in Presence of Dispersed Vat Dye. *Dye. Pigm.* **2011**, *91* (3), 324–331.

(56) Kirby, T.; Akbar, M. A.; Gilavan, M. T.; Selvaganapathy, P. R.; Kruse, P. Carbon Nanotube-Based Chemiresistive Sensor Array for Dissolved Gases. *ACS Omega* **2024**, *9* (47), 46986–46996.

(57) Gao, S.; Tian, R.; Chen, P. Principal Component Analysis for Process Monitoring in Distributed System Environment. *Concurr. Comput. Pract. Expr.* **2019**, *34* (8), No. e5309, DOI: 10.1002/cpe.5309.

(58) Bezergianni, S.; Kalogianni, A. Application of Principal Component Analysis for Monitoring and Disturbance Detection of a Hydrotreating Process. *Ind. Eng. Chem. Res.* **2008**, *47* (4), 6972–6982.

(59) Elmas, S.; Pospisilova, A.; Sekulska, A. A.; Vasilev, V.; Nann, T.; Thornton, S.; Priest, C. Photometric Sensing of Active Chlorine, Total Chlorine, Pool Monitoring. *Sensors* **2020**, *20* (11), No. 3099.

(60) Zhou, M.; Li, T.; Zu, M.; Zhang, S.; Liu, Y.; Zhao, H. Membrane-Based Colorimetric Flow-Injection System for Online Free Chlorine Monitoring in Drinking Water. *Sens. Actuators, B* **2021**, *327*, No. 128905.

(61) Jafari, S.; Pourmortazavi, S. M.; Ehsani, A.; Mirsadeghi, S. CuO-ZIF-8 Modified Electrode Surface as a New Electrochemical Sensing Platform for Detection of Free Chlorine in Aqueous Solution. *Sci. Rep.* **2024**, *14*, No. 18961.

(62) Alam, A. U.; Clyne, D.; Lush, W.; Deen, M. J. A Reusable, Reagent-Less Free Chlorine Sensor Using Gold Thin Film Electrode. *Analyst* **2021**, *146* (8), 2626–2631.

(63) Seymour, I.; O'Sullivan, B.; Lovera, P.; Rohan, J. F.; O'Riordan, A. Electrochemical Detection of Free-Chlorine in Water Samples Facilitated by in-Situ PH Control Using Interdigitated Microelectrodes. *Sens. Actuators, B* **2020**, *325*, No. 128774.

(64) Siddiqui, J.; Deen, M. J. Biodegradable Asparagine-Graphene Oxide Free Chlorine Sensors Fabricated Using Solution-Based Processing. *Analyst* **2022**, *147* (16), 3643–3651.

(65) Sugawara, M.; Watanabe, T.; Einaga, Y.; Koh, S. Impact of Gate Electrode on Free Chlorine Sensing Performance in Solution-Gated Graphene Field-Effect Transistors. *RSC Adv.* **2024**, *14* (11), 7867–7876.

(66) Mopoung, K.; Suwanyangyaun, P.; Odanaka, R.; Kosuga, S.; Watanabe, T.; Koh, S.; Sanorpim, S. *A Real-Time Free Chlorine Monitoring by Graphene Field-Effect Transistor*IEEE 14th International Conference on Nano/Micro Engineered and Molecular Systems (NEMS);IEEE, 2019; pp 64–67.

Supporting Information

Continuous Monitoring of Free Chlorine Level and pH Using an Array of Carbon Nanotube Chemiresistors

Md Ali Akbar[1], Mehraneh Tavakkoli Gilavan[2], Ponnambalam Ravi Selvaganapathy[2, 3], Peter Kruse[1]*

[1] Department of Chemistry and Chemical Biology, McMaster University, 1280 Main St. W., Hamilton, Ontario, L8S 4M1, Canada

[2] School of Biomedical Engineering, McMaster University, 1280 Main St. W., Hamilton, Ontario L8S 4L7, Canada

[3] Department of Mechanical Engineering, McMaster University, 1280 Main St. W., Hamilton, Ontario, L8S 4L7, Canada

* Email: pkruse@mcmaster.ca

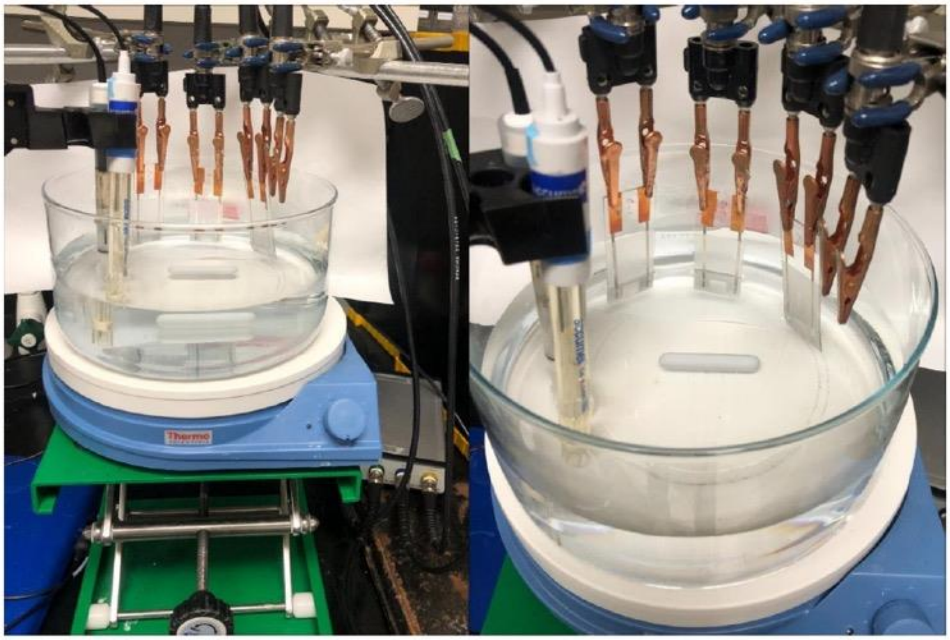

Figure S1. Photographic images of experimental setup.

Table S1. All extracted parameters for different ways of sensor fabrication.

Sensor type	Deposition method	Electrical contact	Fabrication time per sensor (min)	Resistance (kΩ)	Free chlorine		Tap water	
					Max response change (%)	Response time (min)	Stabilization time (hour)	Drift (%)
1	Drop-casted CNT	Silver	140	6.98 ± 0.44	92.17 ± 1.07	>30	48	5.88
2	Drop-casted CNT	Carbon paste	110	7.38 ± 0.54	82.44 ± 1.63	>30	24	1.53
3	Drop-casted CNT	Gold Leaf	100	7.05 ± 0.33	93.94 ± 1.71	20	12	-25.23
4	Airbrushed CNT	Silver	85	8.50 ± 0.25	112.44 ± 0.93	15	3	-0.87
5	Airbrushed CNT	Carbon paste	50	8.55 ± 0.66	98.68 ±1.18	12	4	-3.36
6	Airbrushed CNT	Gold Leaf	40	4.25 ± 0.29	72.7 ± 1.94	20	12	-31.81

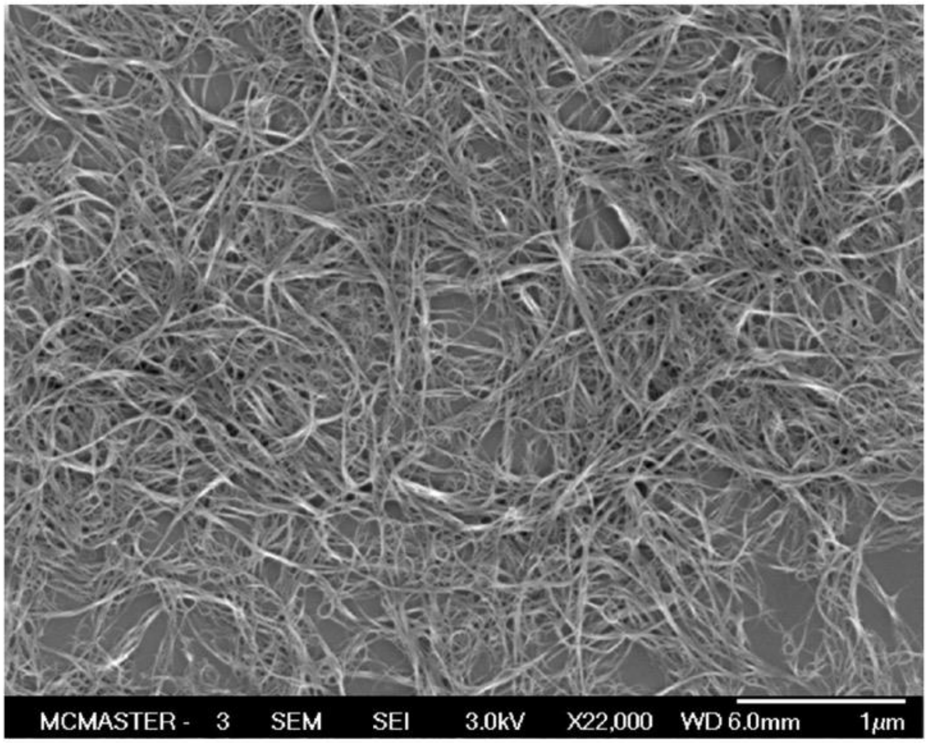

Figure S2. Scanning electron microscope (SEM) image of SWCNT film airbrushed on a silicon/silicon dioxide substrate.

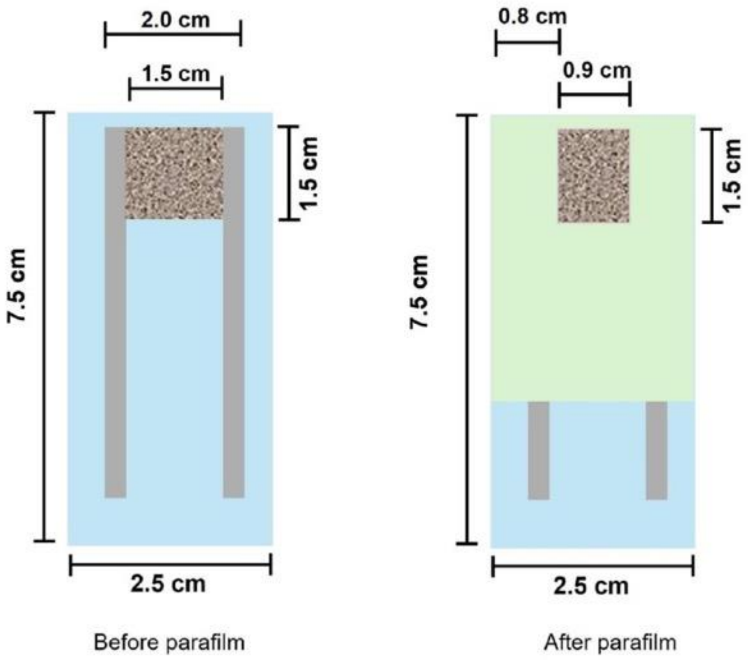

Figure S3. Schematic of the dimensions of the sensor components. The left schematic shows the sensor components before masking with parafilm. The right schematic shows the exposed area after attaching the parafilm.

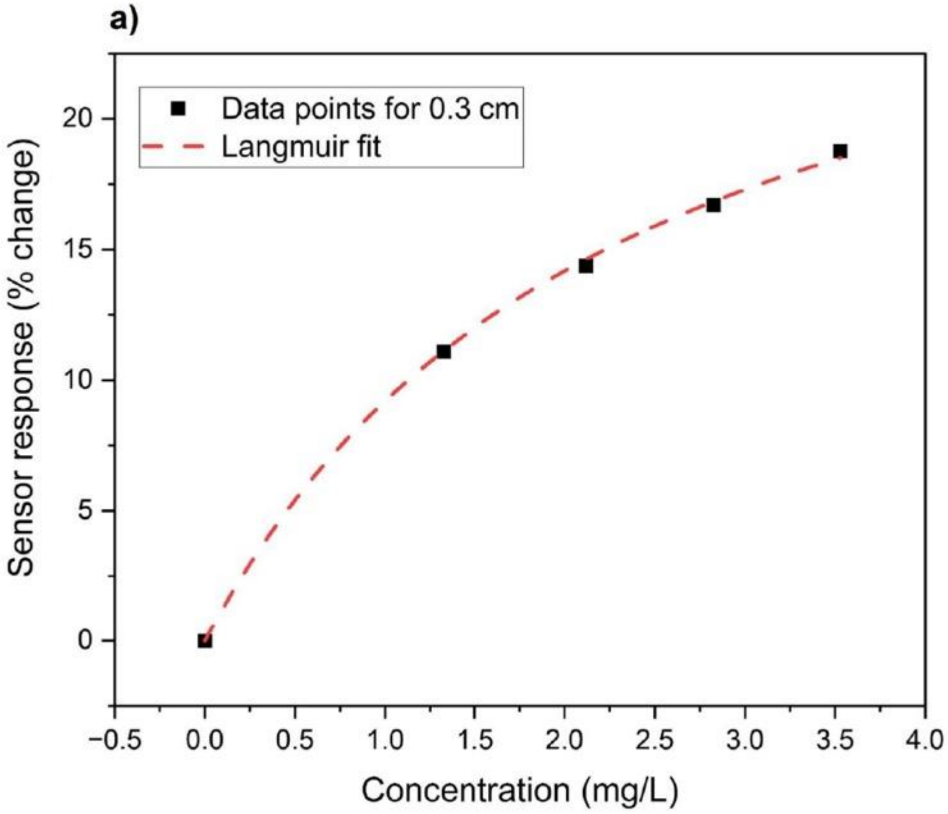
a)
■ Data points for 0.3 cm
Langmuir fit
Sensor response (% change)
20
15
10
5
0
−0.5
0.0
0.5
1.0
1.5
2.0
2.5
3.0
3.5
4.0
Concentration (mg/L)

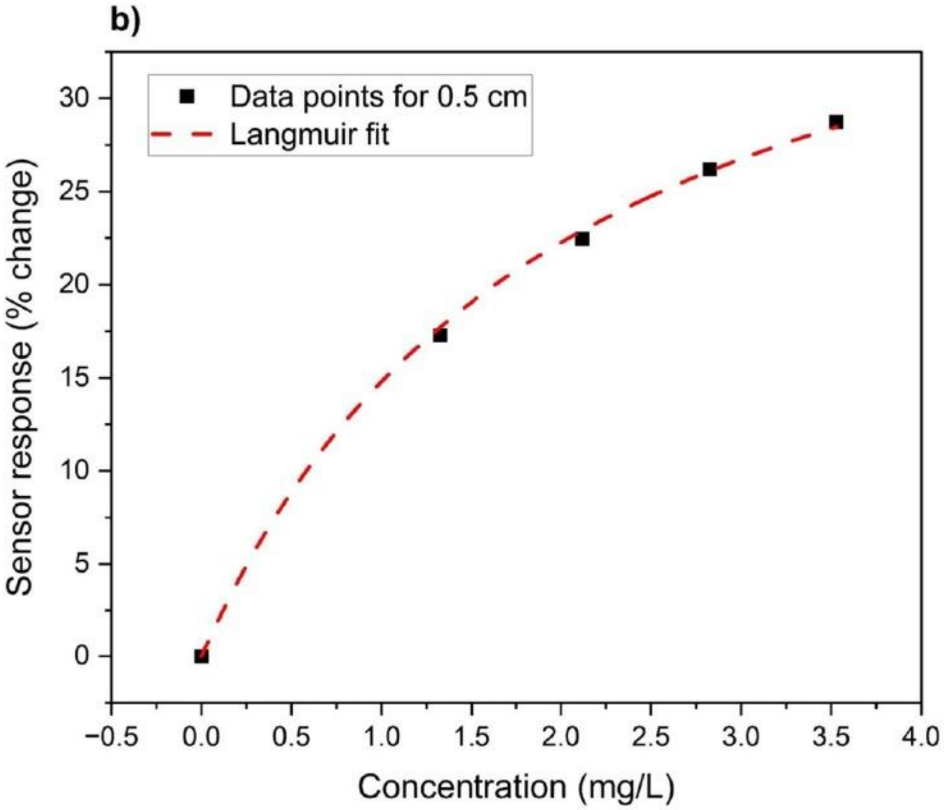
b)
■ Data points for 0.5 cm
Langmuir fit
Sensor response (% change)
0
5
10
15
20
25
30
−0.5
0.0
0.5
1.0
1.5
2.0
2.5
3.0
3.5
4.0
Concentration (mg/L)

S7

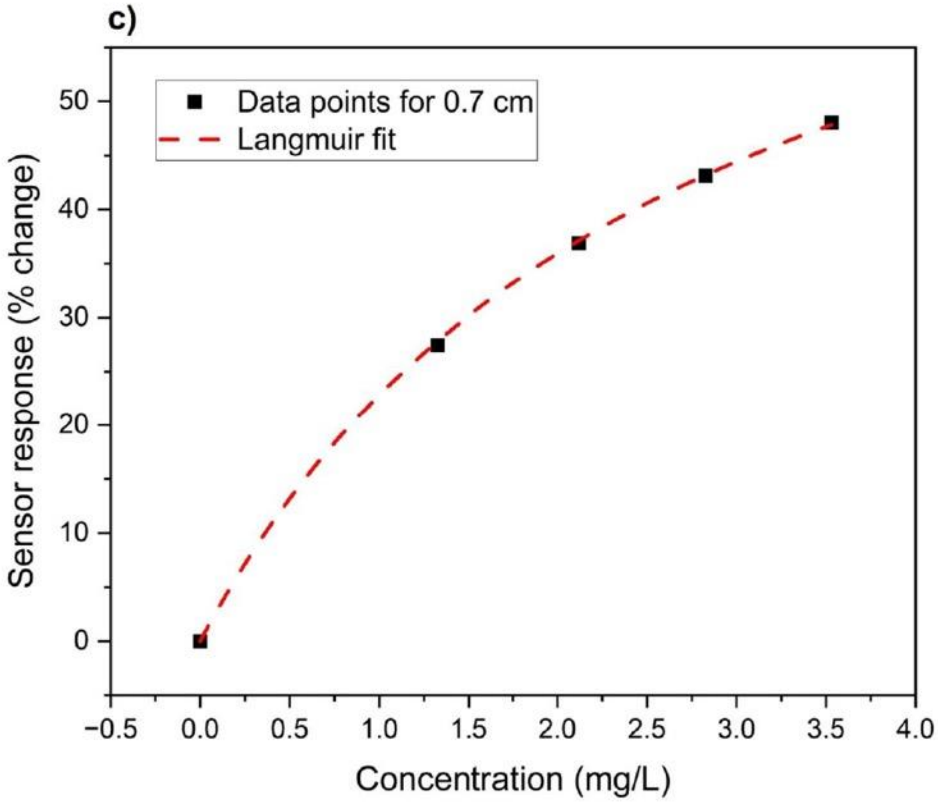

Figure S4. Calibration graphs of three blank sensors with different widths (distance between the contacts of the open area) in water with a background of NaCl and $NaHCO_3$ and at a pH of 8. a) is for 0.3 cm, b) is for 0.5 cm, and c) is for 0.7 cm wide openings. The sensor responses are shown as percent changes, and they are plotted against the free chlorine (FC) concentration. The percent changes for each concentration of the molecules are fitted with Langmuir adsorption isotherms. The dots are the actual data points, and the dashed lines are the Langmuir fits. The fitting parameters for 0.3 cm are $a = 30.84 \pm 1.11\%$ and $b = 0.42 \pm 0.03$ $mg^{-1}L$ for an R^2 value of 0.99; for 0.5 cm are $a = 44.87 \pm 1.97\%$ and $b = 0.49 \pm 0.05$ $mg^{-1}L$ for an R^2 value of 0.99; and for 0.7 cm are $a = 84.41 \pm 2.11\%$ and $b = 0.37 \pm 0.02$ $mg^{-1}L$ for an R^2 value of 0.99.

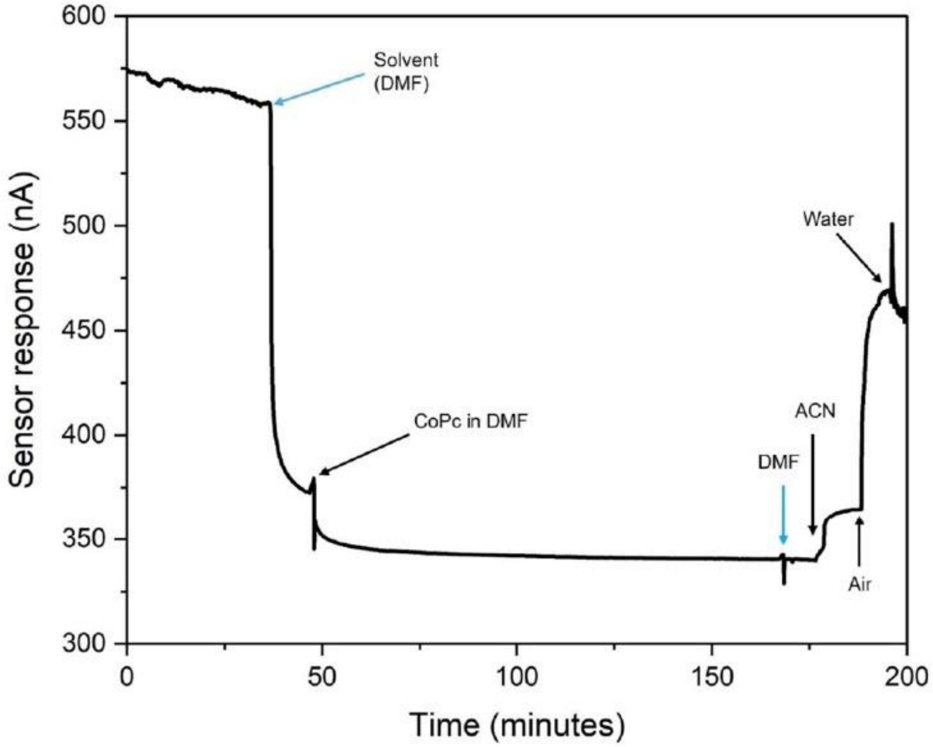

Figure S5. Functionalization of SWCNTs with CoPc in DMF. Sensor responses for different steps of the functionalization process were plotted against time.

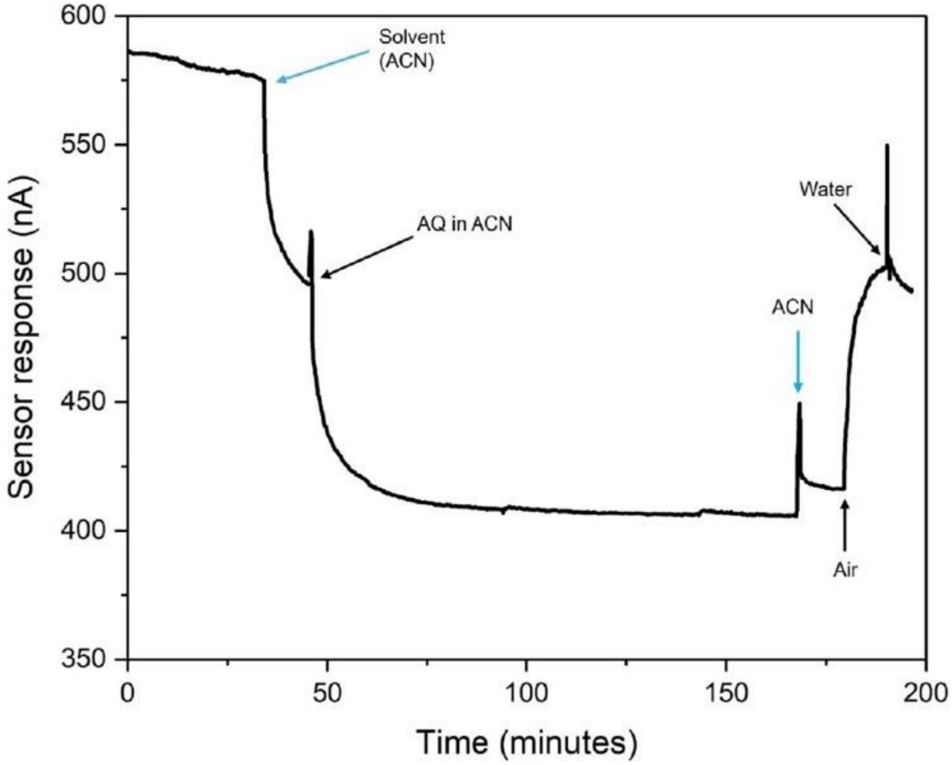

Figure S6. Functionalization of SWCNTs with AQ in ACN. Sensor responses for different steps of the functionalization process were plotted against time.

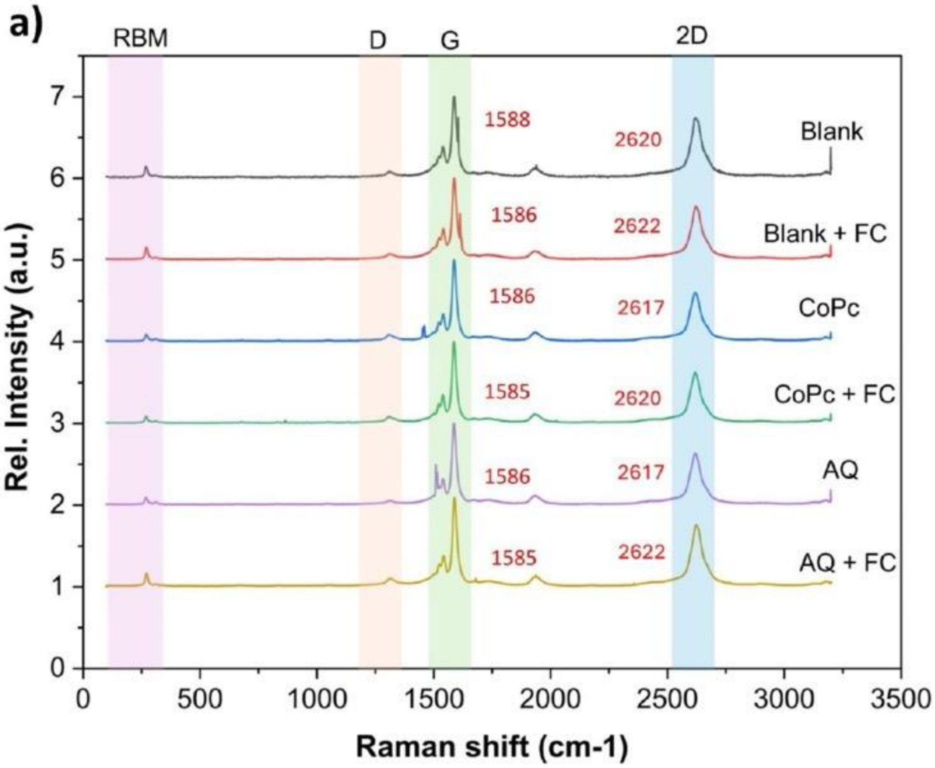
a)
RBM
D
G
2D
Rel. Intensity (a.u.)
0
1
2
3
4
5
6
7
Raman shift (cm-1)
0
500
1000
1500
2000
2500
3000
3500
1588
2620
Blank
1586
2622
Blank + FC
1586
2617
CoPc
1585
2620
CoPc + FC
1586
2617
AQ
1585
2622
AQ + FC

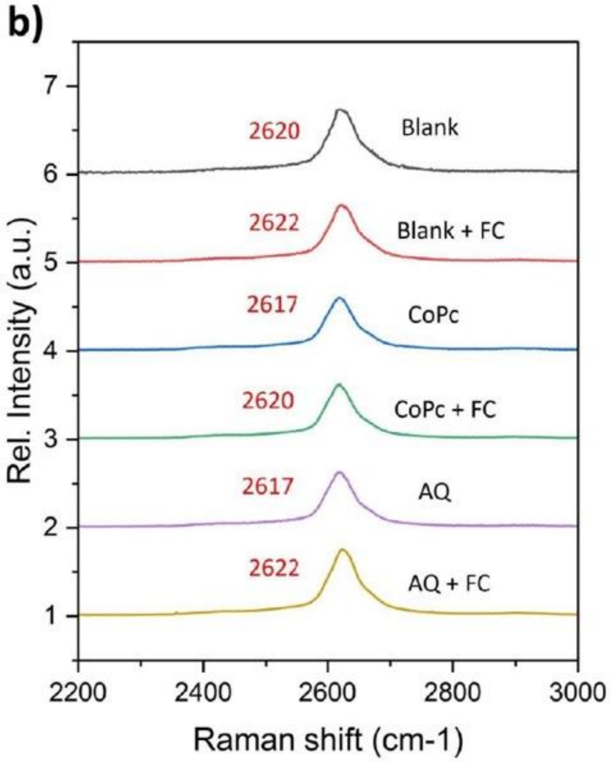

Figure S7. a) Raman spectra of the unfunctionalized SWCNT (blank) and functionalized SWCNT (CoPc and AQ) and their spectra after exposing to 4 mg/L of FC. Four distinct regions of SWCNT, radial breathing mode (RBM), D peak, G band and 2D peaks are highlighted colored boxes. 2D peak shifts are labeled with red color. In all three samples, the 2D peak showed upward shifts. The functionalized samples (CoPc and AQ) showed downward shifts relative to the blank sample. b) 2D peaks of the Raman spectra shown within the range of 2200 cm^{-1} to 3000 cm^{-1}.

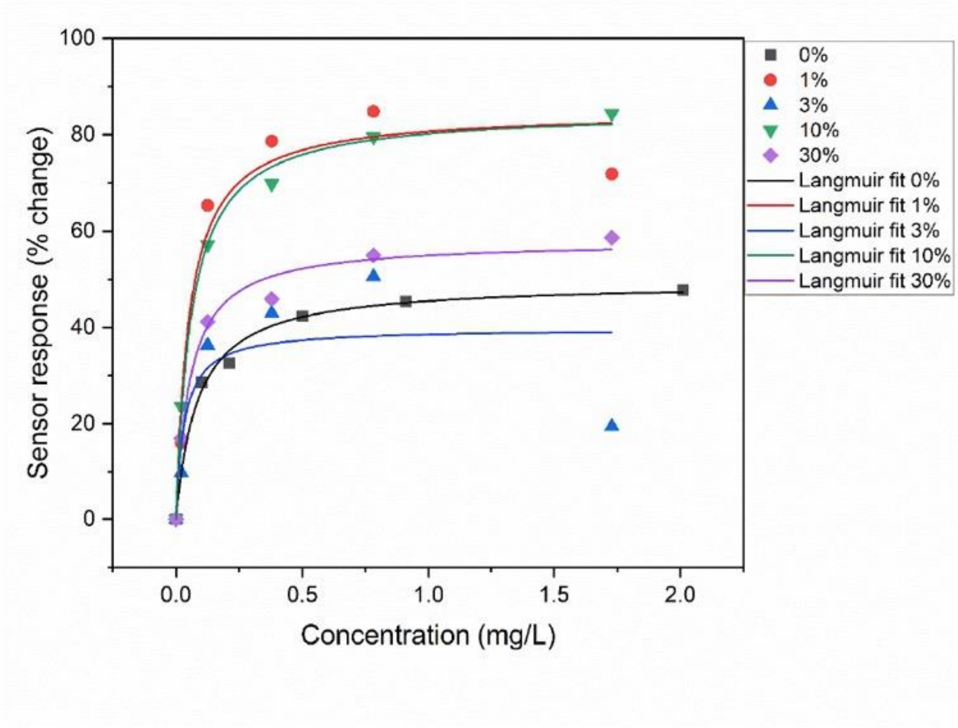

Figure S8. Sensor response of CoPc sensor as percent changes is plotted against concentration of FC. The four curves represent the CoPc concentrations (1%, 3%, 10%, and 30%) prepared in DMF from a saturated CoPc solution. The dots are the actual data point, and the lines represent Langmuir adsorption isotherm fits. The data points for CoPc concentration are fitted with Langmuir adsorption isotherms. The fitting parameters for 0% are a = 49.34±1.36% and b = 11.76±1.66 mg^{-1}L for an R^2 value of 0.99; 1% are a = 84.94±6.08% and b = 18.86±7.58 mg^{-1}L for an R^2 value of 0.96; for 3% are a = 39.79±8.48% and b = 30.55±40.58 mg^{-1}L for an R^2 value of 0.68; for 10% are a = 85.06±1.81% and b = 16.49±1.90 mg^{-1}L for an R^2 value of 0.0.99; and for 30% are a = 57.94±2.14% and b = 18.16±3.74 mg^{-1}L for an R^2 value of 0.99.

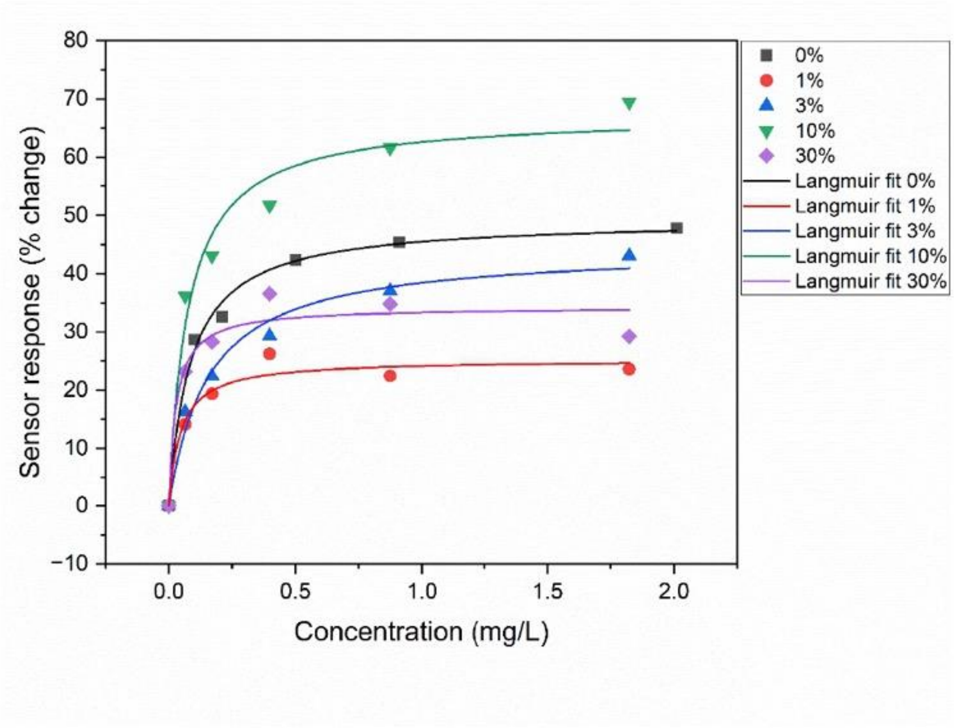

Figure S9. Sensor response of AQ sensor as percent changes is plotted against concentration of FC. The four curves represent the AQ concentrations (1%, 3%, 10%, and 30%) prepared in ACN from a saturated AQ solution. The dots are the actual data point, and the lines represent Langmuir adsorption isotherm fits. The data points for AQ concentration are fitted with Langmuir adsorption isotherms. The fitting parameters for 0% are a = 49.34±1.36% and b = 11.76±1.66 mg^{-1}L for an R^2 value of 0.99; 1% are a = 25.24±1.53% and b = 21.90±8.09 mg^{-1}L for an R^2 value of 0.96; for 3% are a = 44.35±2.58% and b = 6.47±1.44 mg^{-1}L for an R^2 value of 0.98; for 10% are a = 67.255±3.89% and b = 13.39±3.83 mg^{-1}L for an R^2 value of 0.97; and for 30% are a = 34.26±2.33% and b = 35.36±18.95 mg^{-1}L for an R^2 value of 0.95.

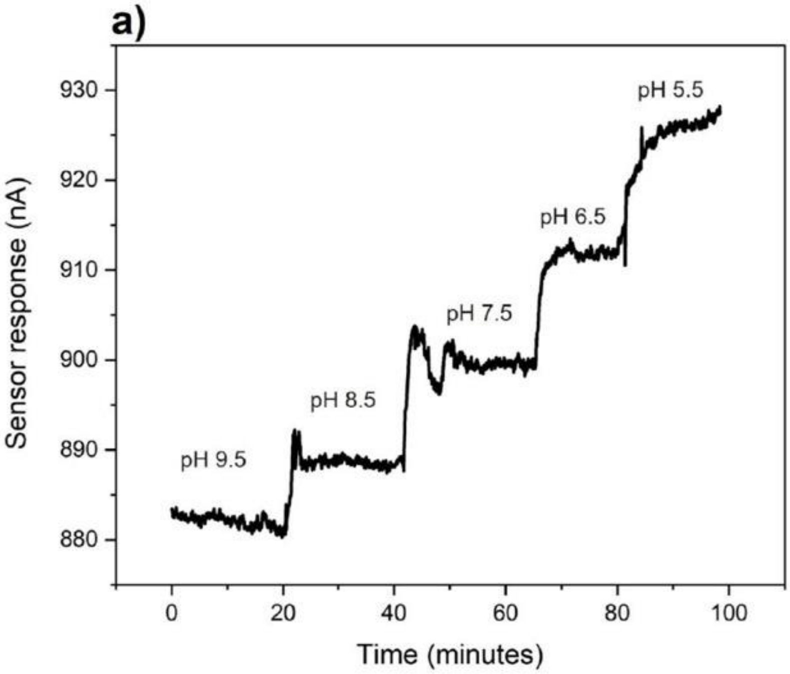
a)
pH 9.5
pH 8.5
pH 7.5
pH 6.5
pH 5.5
Sensor response (nA)
930
920
910
900
890
880
0
20
40
60
80
100
Time (minutes)

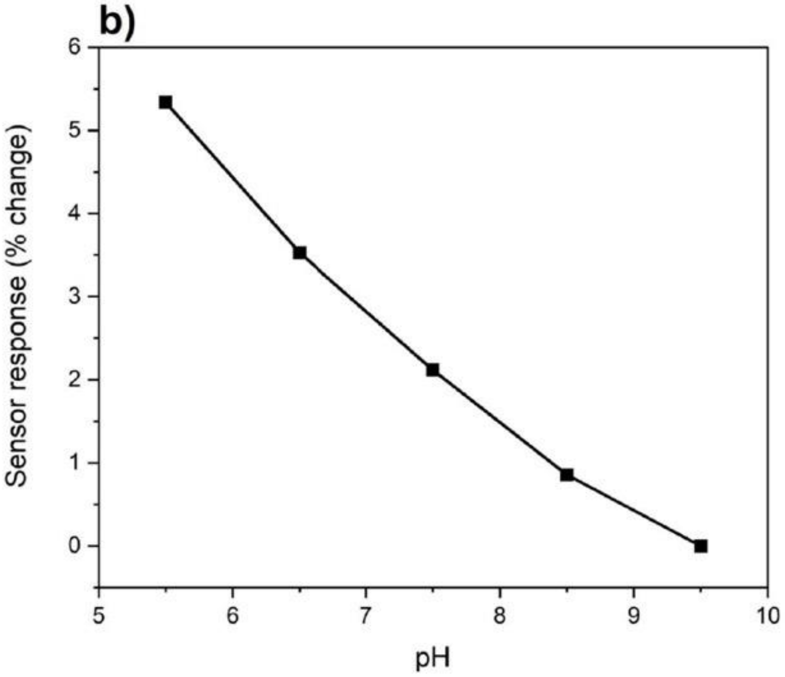
b)
Sensor response (% change)
pH
6
5
4
3
2
1
0
5
6
7
8
9
10

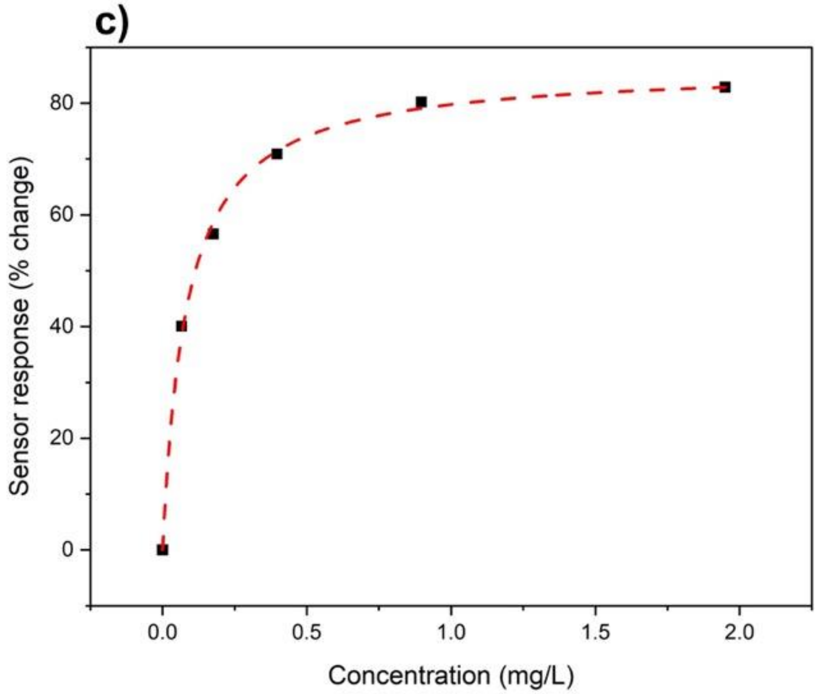

Figure S10. AQ sensor responses. (a) Raw sensor response of AQ sensor measured at pH 9.5 to 5.5. Current change is plotted against time. (b) Percent change of sensor response is plotted against different pHs. Percent change is calculated by setting the pH 9.5 response as baseline. (c) AQ sensor response as percent change plotted for different concentrations of FC. The dots are the actual data point, and the dashed line represents a Langmuir adsorption isotherm fit. The Langmuir adsorption isotherm model fitting parameters are a = 86.37±1.30% and b = 12.06±0.87 $mg^{-1}L$ for an R^2 value of 0.99.

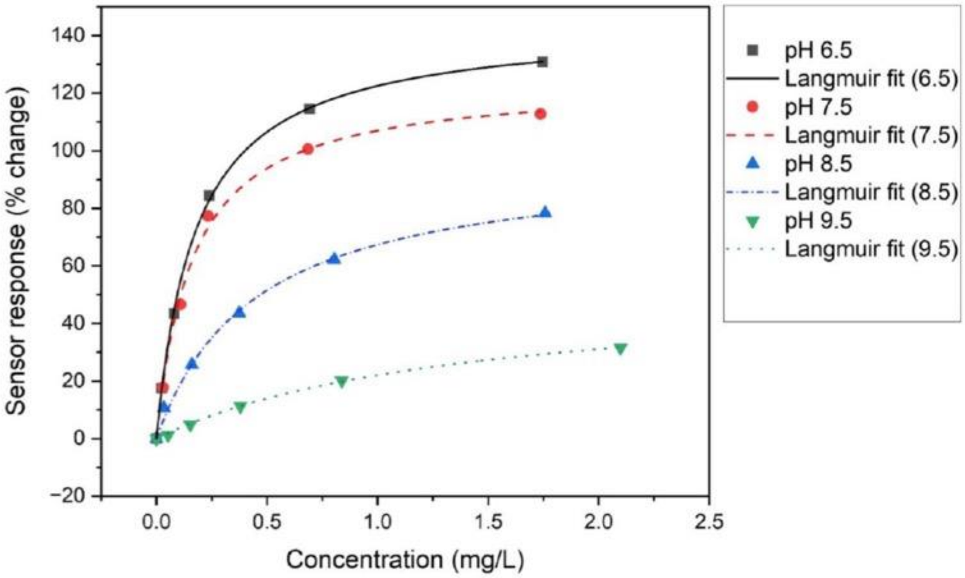

Figure S11. Calibration graphs of the blank sensor responses to a range of FC at 4 pH's (6.5, 7.5, 8.5, and 9.5). The data points are actual sensor responses as percent change and the lines represent the fitted Langmuir adsorption isotherms. The fitting parameters for the model: for pH 6.5, a = 144.23±1.20% and b = 5.64±0.17 mg^{-1}L; for pH 7.5, a = 124.34±2.96% and b = 6.16±0.52 mg^{-1}L; for pH 8.5, a = 97.39±4.0% and b = 2.25±0.25 mg^{-1}L; and for pH 9.5, a = 52.66±2.07% and b = 0.72±0.05. mg^{-1}L. All four fitted curves had R^2 value of 0.99.

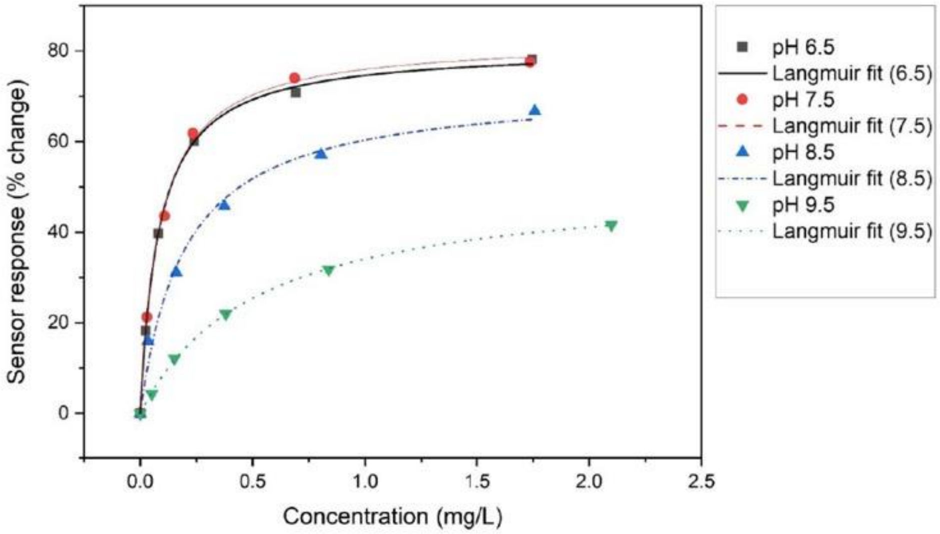

Figure S12. Calibration graphs of the AQ sensor responses to a range of FC at 4 pH's (6.5, 7.5, 8.5, and 9.5). The data points are actual sensor responses as percent change and the lines represent the fitted lines with Langmuir adsorption isotherms. The fitting parameters for the model: for pH 6.5, a = 80.82±0.77% and b = 12.0± 0.49 mg^{-1}L; for pH 7.5, a = 82.57±1.43% and b = 11.43±0.83 mg^{-1}L; for pH 8.5, a = 72.17±3.73% and b = 5.10±0.96 mg^{-1}L; and for pH 9.5, a = 51.72±0.61% and b = 1.93±0.06 mg^{-1}L. All four fitted curves had R^2 value of 0.99.

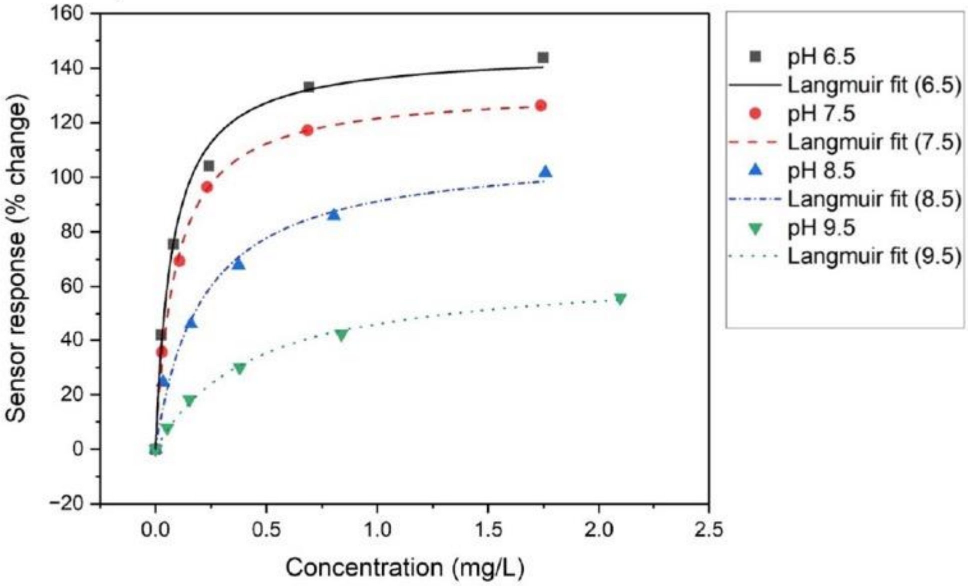

Figure S13. Calibration graphs of the CoPc sensor responses to a range of FC at 4 pH's (6.5, 7.5, 8.5, and 9.5). The data points are actual sensor responses as percent change and the lines represent the fitted lines with Langmuir adsorption isotherms. The fitting parameters for the model: for pH 6.5, $a = 146.32\pm4.54\%$ and $b = 13.38\pm1.82$ mg^{-1}L; for pH 7.5, $a = 132.42\pm2.1\%$ and $b = 11.15\pm0.74$ mg^{-1}L; for pH 8.5, $a = 110.22\pm6.7\%$ and $b = 4.79\pm1.03$ mg^{-1}L; and for pH 9.5, $a = 66.75\pm2.1\%$ and $b = 2.24\pm0.20$ mg^{-1}L. All four fitted curves had R^2 value of 0.99.

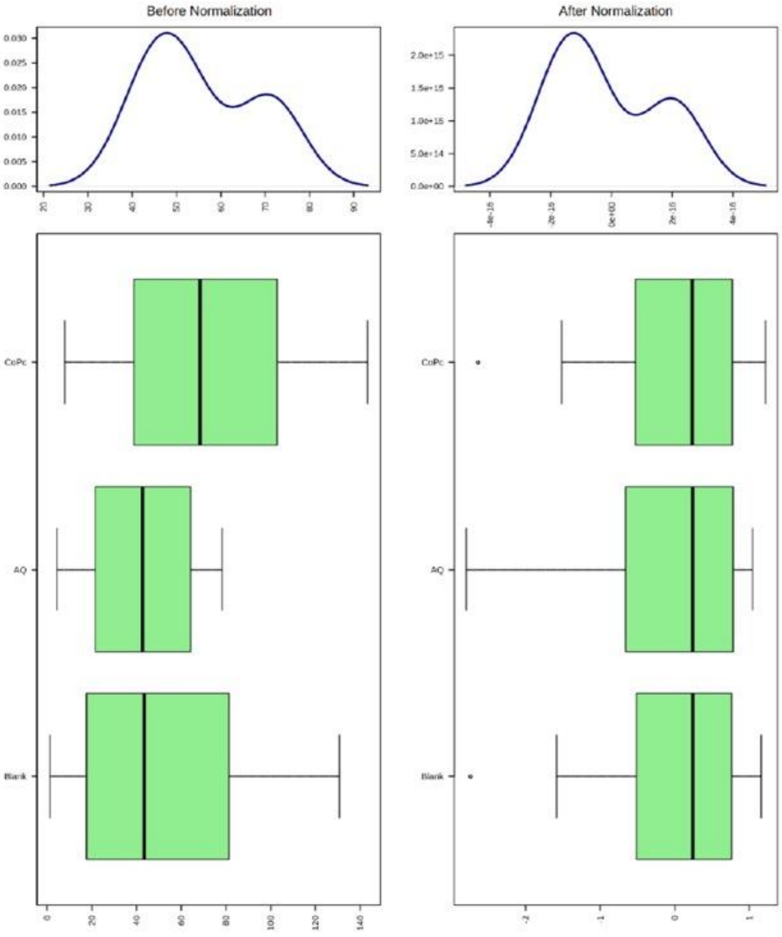

Figure S14. Normalization of the FC calibration dataset (shown in figure S9-S11) for the sensor array (blank, AQ, and CoPc). Autoscaling and log transformation methods were implemented to the three sensors array to achieve a uniform distribution of the dataset.

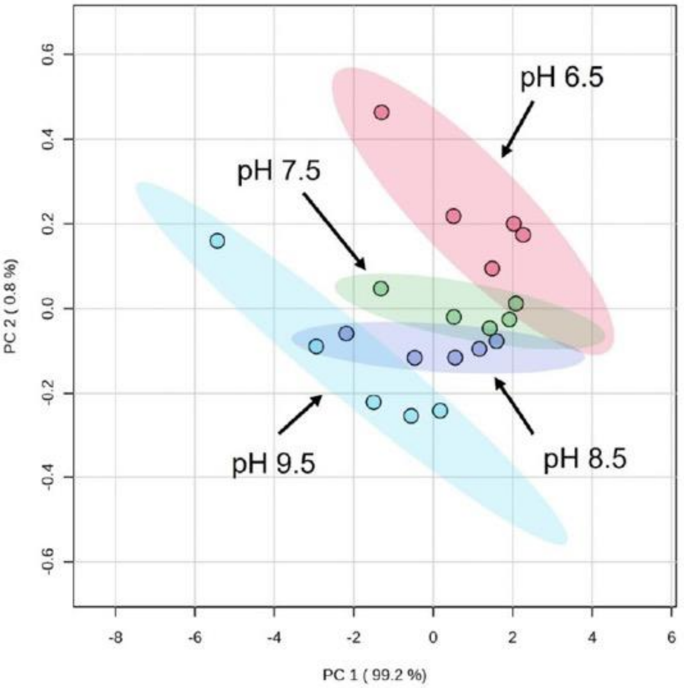

Figure S15. PCA score plot showing the different regions of pH tested. Only the CoPc and AQ sensors were used here to generate the scores.

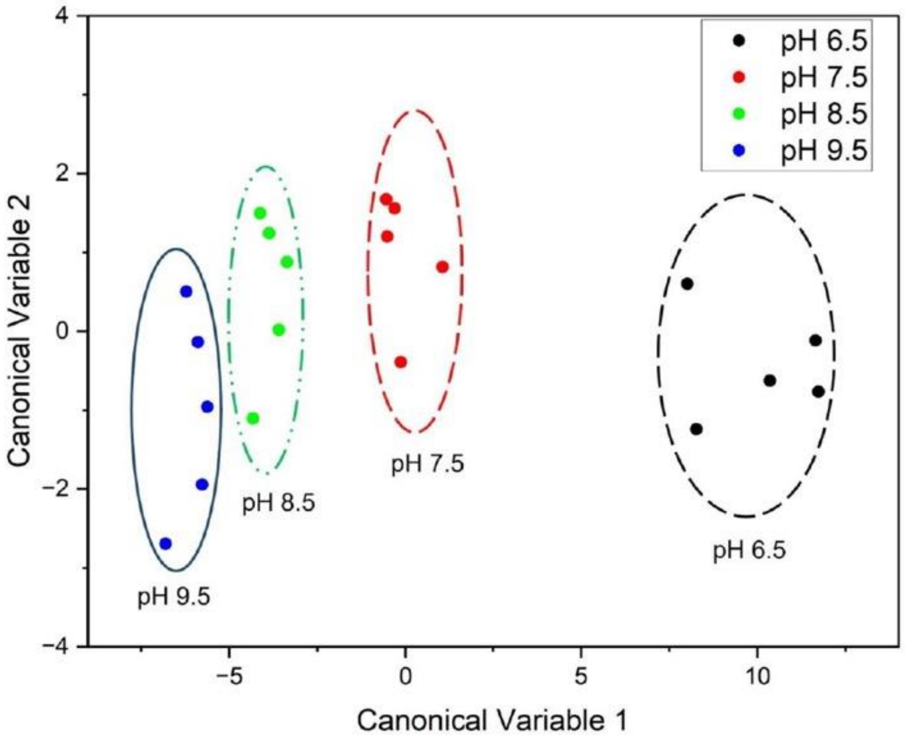

Figure S16. LDA canonical score plot for the first two variables generated from the array analysis. Raw sensor data of the three sensors (blank, AQ, and CoPc) were used to conduct the analysis. Each of the encircled regions represents a pH (labeled below) and the datapoints represent the observations. Each of the observations in a pH region represents a FC concentration.

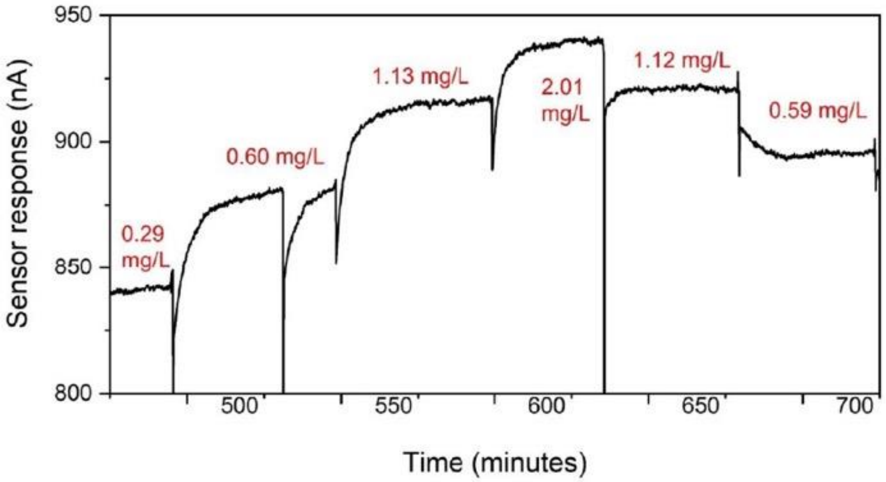

Figure S17. Electrical reset of the blank sensor in water. The sensor response is presented as current change against time. Each of the sharp current changes represents the reset pulse. The concentrations labeled above or below the curve represent the actual FC concentration measured by the commercial DPD reagent.

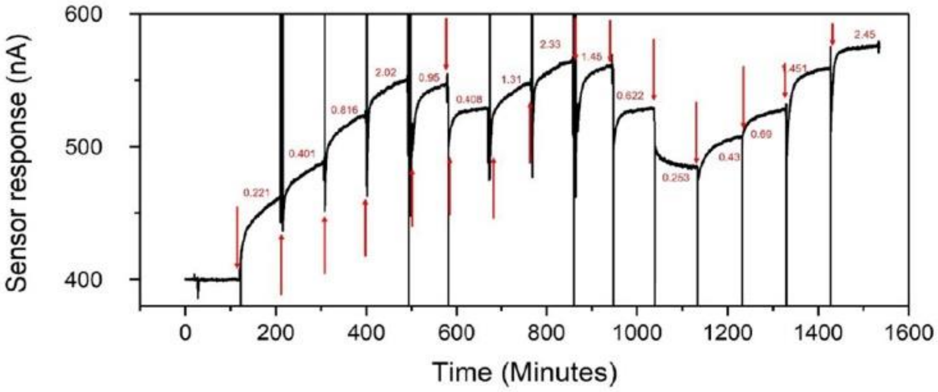

Figure S18. Continuous measurement of FC. Raw sensor response of AQ when exposed to varying concentrations of FC. The arrows represent the FC concentration change, and the concentration for each spike is labeled on top.

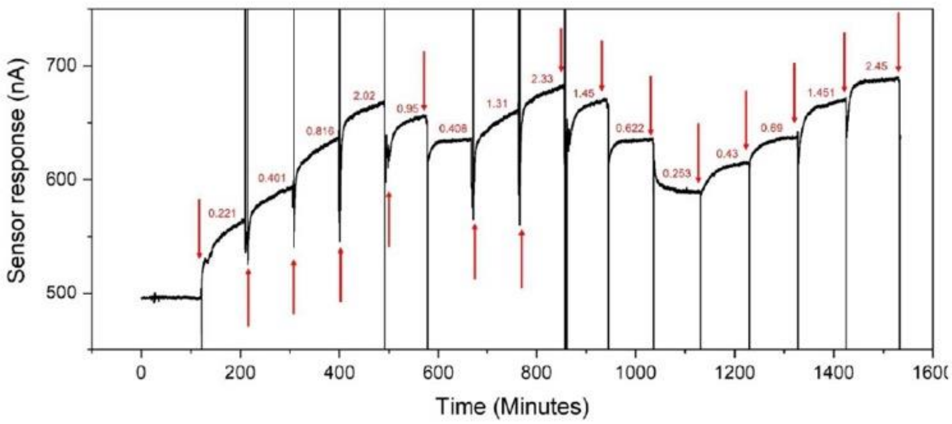

Figure S19. Continuous measurement of FC. Raw sensor response of blank when exposed to varying concentrations of FC. The arrows represent the FC concentration change, and the concentration for each spike is labeled on top.

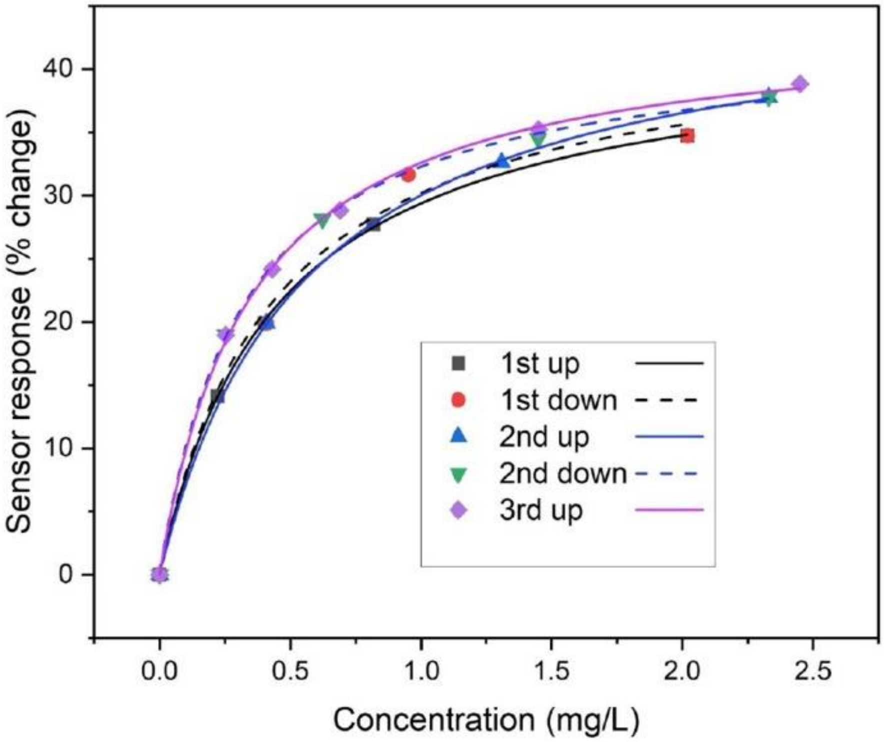

Figure S20. Calibration graphs of the blank sensors in simulated tap water from the responses in continuous measurement. Actual sensor responses (dots) are fitted with Langmuir adsorption isotherms. The fitted lines are presented as solid lines for the upward cycle and dashed line for the downward cycle.

Table S2. Fitting parameters of the Langmuir model of all three sensors (blank, CoPc, and AQ).

Blank				
Run	R^2	Adjusted R^2	a [%]	b [$mg^{-1}L$]
First up	0.99	0.99	42.51 ± 0.36	2.24 ± 0.05
First down	0.99	0.99	43.35 ± 3.57	2.98 ± 0.62
Second up	0.99	0.99	46.60 ± 0.37	1.81 ± 0.05
Second down	0.99	0.99	42.60 ± 0.42	3.13 ± 0.11
Third up	0.99	0.99	43.94 ± 0.49	2.87 ± 0.11

CoPc				
Run	R^2	Adjusted R^2	a [%]	b [$mg^{-1}L$]
First up	0.99	0.99	43.23 ± 1.85	3.80 ± 0.56
First down	0.99	0.99	41.68 ± 0.14	4.87 ± 0.81
Second up	0.99	0.99	46.21 ± 0.43	3.73 ± 0.16
Second down	0.99	0.99	47.60 ± 0.46	2.68 ± 0.10
Third up	0.99	0.99	47.37 ± 0.28	2.74 ± 0.05
Third down	0.99	0.99	47.15 ± 0.14	2.79 ± 0.03

AQ				
Run	R^2	Adjusted R^2	a [%]	b [$mg^{-1}L$]
First up	0.99	0.99	45.34 ± 0.88	2.46 ± 0.14
First down	0.98	0.97	46.24 ± 5.73	2.98 ± 0.62
Second up	0.99	0.99	50.17 ± 0.91	2.04 ± 0.13
Second down	0.99	0.99	47.51 ± 1.10	3.23 ± 0.29
Third up	0.99	0.99	49.65 ± 0.69	2.80 ± 0.13
Third down	0.99	0.99	49.75 ± 0.68	2.78 ± 0.12

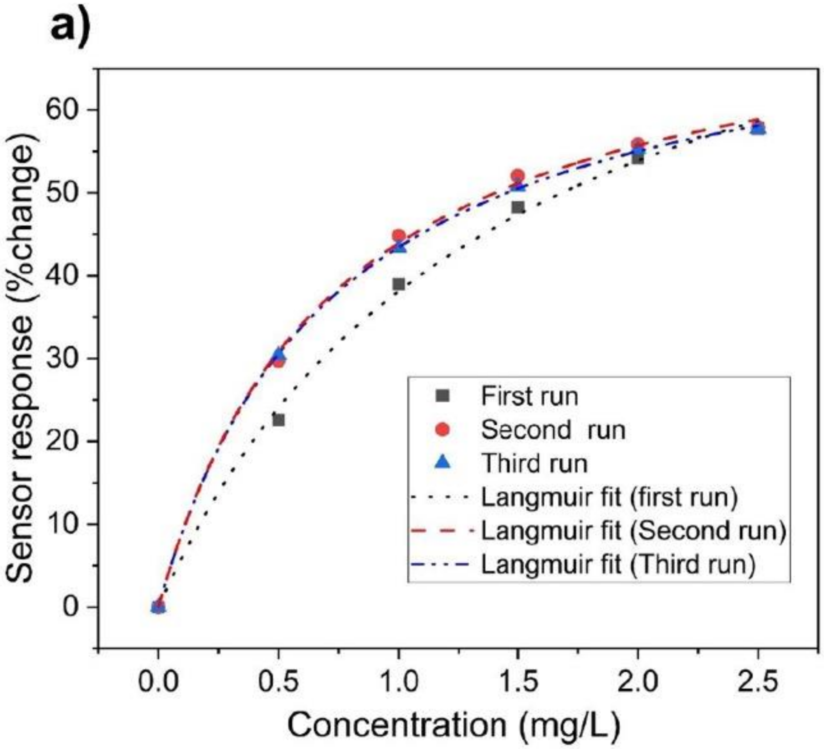
a)
Sensor response (%change)
Concentration (mg/L)
0
10
20
30
40
50
60
0.0
0.5
1.0
1.5
2.0
2.5
First run
Second run
Third run
Langmuir fit (first run)
Langmuir fit (Second run)
Langmuir fit (Third run)

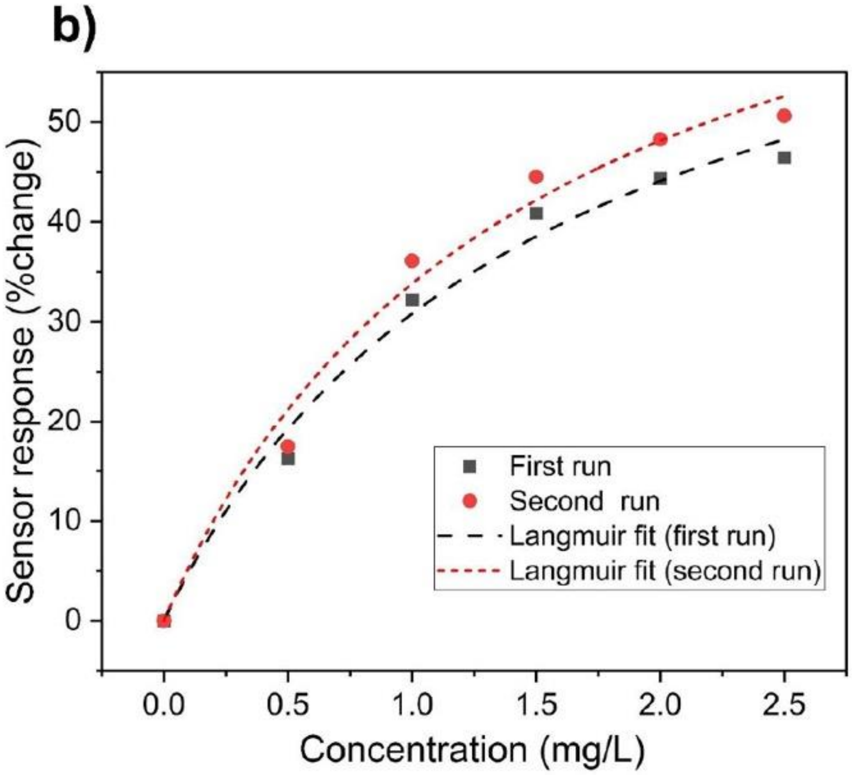
b)
Sensor response (%change)
Concentration (mg/L)
0
10
20
30
40
50
0.0
0.5
1.0
1.5
2.0
2.5
First run
Second run
Langmuir fit (first run)
Langmuir fit (second run)

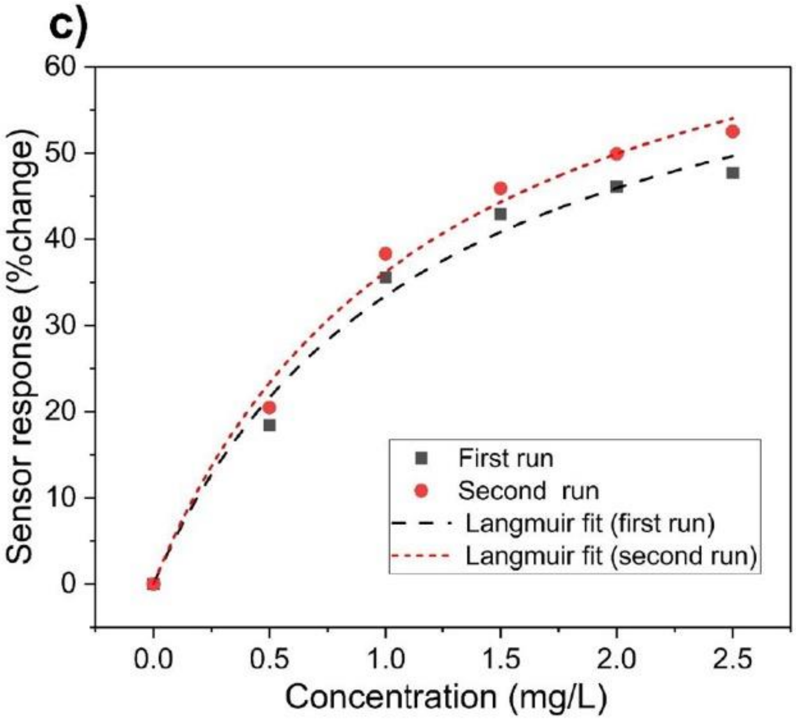

Figure S21. Sensor response of different blank sensor devices as percent changes is plotted against concentration of FC in NaCl and $NaHCO_3$ background. The dots are the actual data point, and the lines represent Langmuir adsorption isotherm fits. The data points for FC concentration are fitted with Langmuir adsorption isotherms. The parameters are reported and analyzed in Table S3.a) Three runs of sensor responses plotted against concentration of FC. b) Two runs of sensor responses plotted against concentration of FC. c) Two runs of sensor responses plotted against concentration of FC.

Table S3. Fitting parameters and standard deviation analysis of the sensor responses from sensors of different batches. Calibration data were shown in figure S21.

	Batch 1		Batch 2		Batch 3	
	a [%]	*b* [mg^{-1}L]	*a* [%]	*b* [mg^{-1}L]	*a* [%]	*b* [mg^{-1}L]
First run	91.80	0.71	77.50	0.66	73.37	0.84
Secon run	75.03	1.37	83.49	0.68	80.37	0.82
Third run	76.17	1.36				
Average and Std. deviation	81.00±7.65	1.15±0.31	80.50±3.00	0.67±0.01	76.87±3.50	0.83±0.01

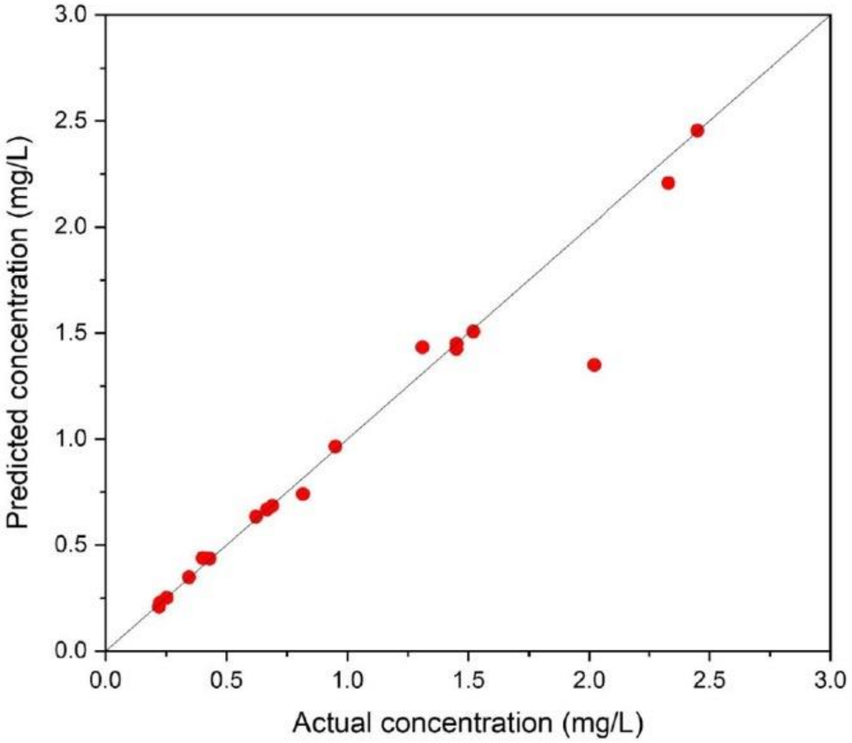

Figure S22. Regression graph for the simulated tap water measurements. Here all three cycles (1st, 2nd, and 3rd) of the CoPc and AQ sensors have been included. PLS model showing the predicted concentration from the model and actual concentration measured by the DPD colorimetric method. The dashed line represents the ideal comparison line. The R^2 value for the model is 0.988 and RMSELOOCV is 0.0822. The deviation from the linearity is due to variation in the measurement of the FC in the 1st cycle compared to the 2nd and 3rd cycles.

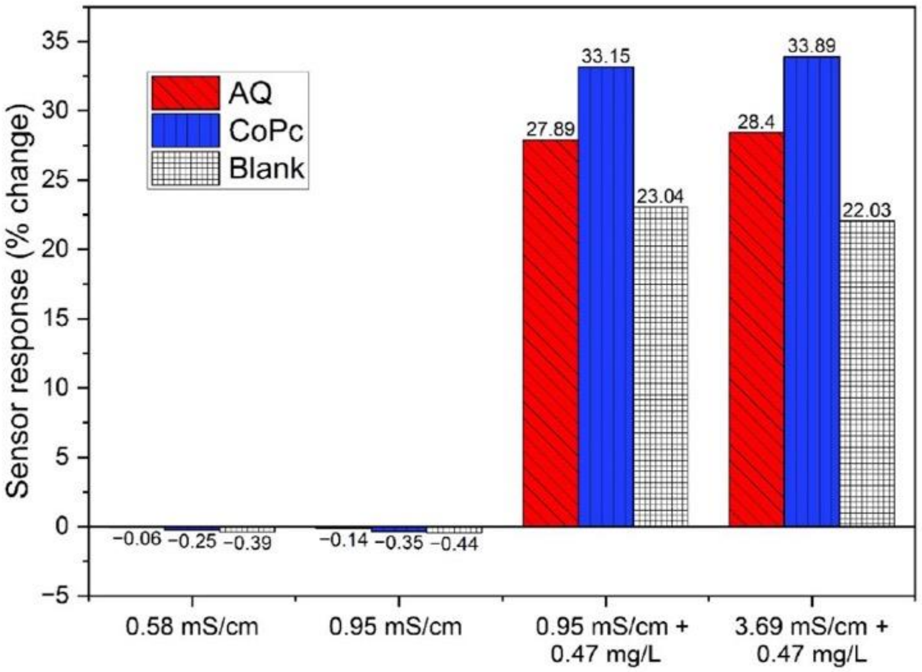

Figure S23. Blank, AQ, and CoPc sensor responses to various conductivity of aqueous solutions. The baseline responses of the sensors were measured in the simulated tap water (0.04 mmol KH_2PO_4, 0.6 mmol $CaCl_2$, 0.3 mmol $MgSO_4$, and 1 mmol $NaHCO_3$) background. NaCl was then added to achieve conductivities of 0.58 mS/cm and 0.95 mS/cm. 0.47 mg/L of FC was added when the conductivity of water was 0.95 mS/cm and in the next step NaCl was added to change the conductivity to 3.69 mS/cm in the presence of FC. The percent changes reported here were calculated by comparing the baseline response measured in the simulated tap water.

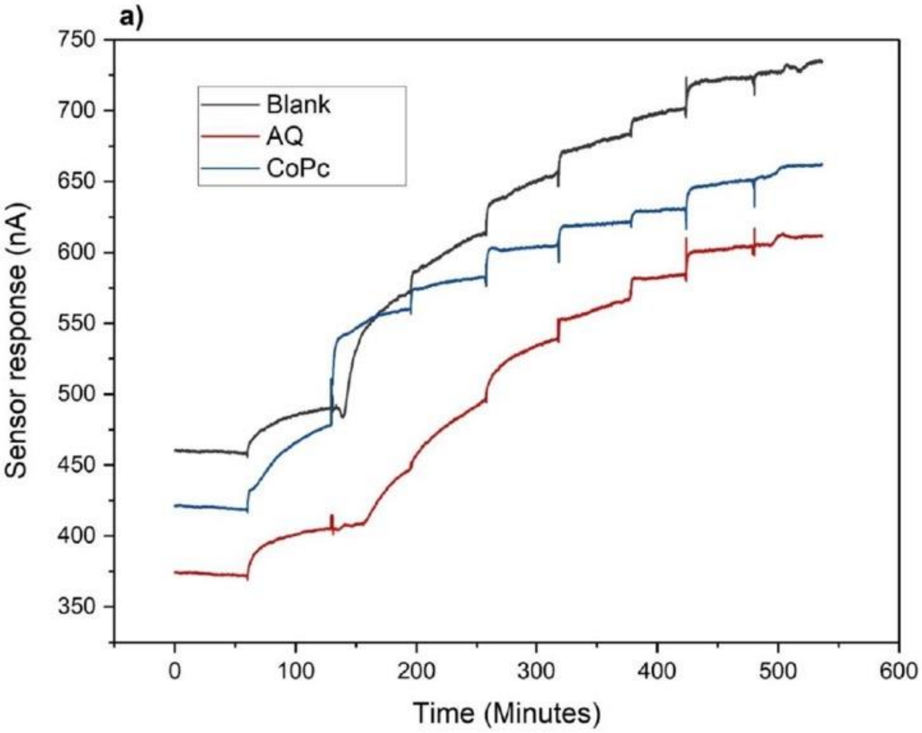
a)
Blank
AQ
CoPc
Sensor response (nA)
750
700
650
600
550
500
450
400
350
0
100
200
300
400
500
600
Time (Minutes)

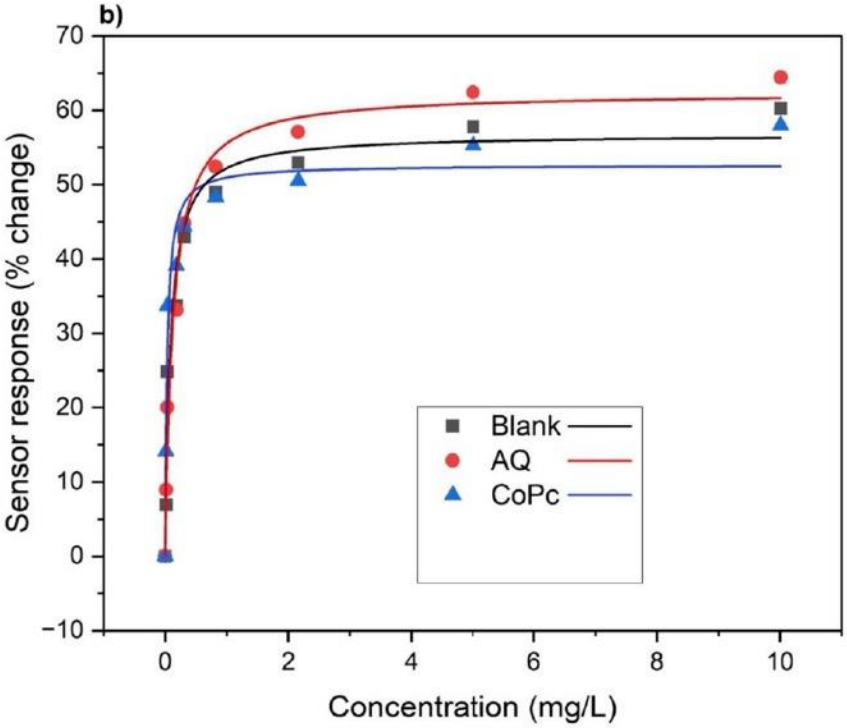
b)
Sensor response (% change)
70
60
50
40
30
20
10
0
−10
0
2
4
6
8
10
Concentration (mg/L)
Blank
AQ
CoPc

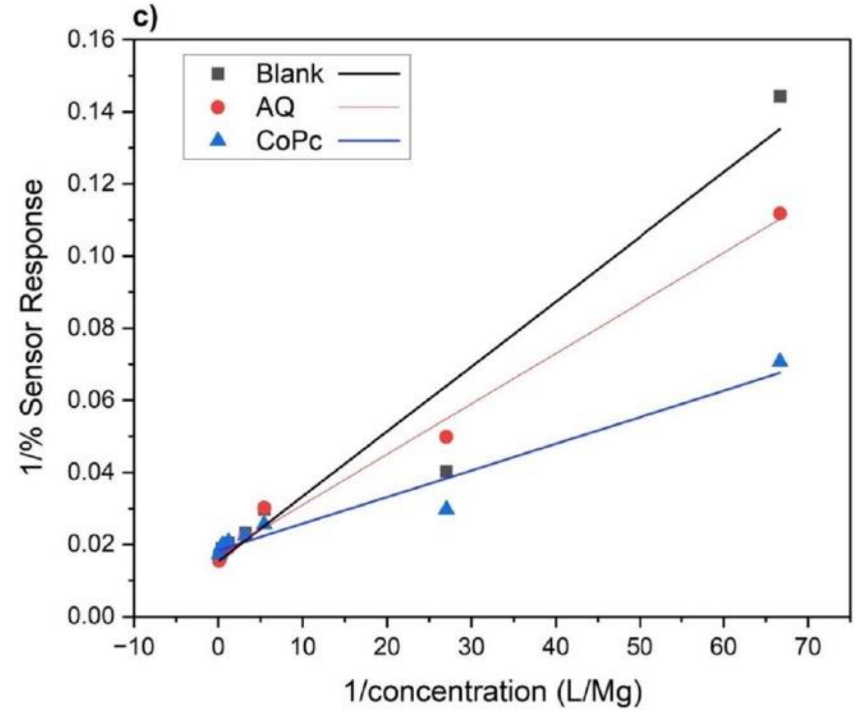

Figure S24. Dynamic range of the sensors fabricated with optimized design. a) Raw sensor response of the sensors when exposed to a range of FC concentrations (0.015 – 10 mg/L) in simulated tap water (0.04 mmol KH_2PO_4, 0.6 mmol $CaCl_2$, 0.3 mmol $MgSO_4$, and 1 mmol $NaHCO_3$). b) Fitted curves for the corresponding responses. Here Langmuir adsorption isotherms are used to fit the data points. Lines represent the actual fits. The fitting parameters for Blank are a = 56.77±2.31% and b = 11.46±2.71 $mg^{-1}L$ for an R^2 value of 0.97; for CoPc are a = 52.66±2.06% and b = 29.86±7.68 $mg^{-1}L$ for an R^2 value of 0.96; and for AQ are a = 62.38±1.93% and b = 8.11±1.35 $mg^{-1}L$ for an R^2 value of 0.98. These parameters and 3× standard deviations of the baseline were used to calculate the limit of detection (LOD) for the sensors. c) Linearized Langmuir adsorption isotherm of the model shown in Fig. S20b. The fitting parameters for AQ are a = 0.01706 and b = 0.0014 for an R^2 value of 0.99; for blank are a = 0.0154 and b = 0.0018 for an R^2 value of 0.94; and for CoPc are a = 0.0184 and b = 0.0007 for an R^2 value of 0.95.

Chapter 6 Identification and Quantification of Aqueous Disinfectants Using an Array of Carbon Nanotube-Based Chemiresistors

This chapter demonstrates an approach to identify and quantify multiple disinfectants in water using single-walled carbon nanotube (SWCNT) chemiresistive sensing arrays. Free chlorine and potassium permanganate were selected as model analytes. The arrays consisted of functionalized SWCNT devices alongside unfunctionalized reference sensors, enabling differentiation of the disinfectants based on their distinct response mechanisms. Sensor responses, collected across a range of concentrations and pH values, were fitted to Langmuir adsorption isotherms to describe the adsorption-driven interaction at each sensor type. Blank and functionalized devices responded through different pathways, producing complementary data that varied with concentration and pH. Chemometric methods were employed to analyze the multidimensional dataset: principal component analysis (PCA) revealed clear separation of the two disinfectants across five pH conditions (5.5, 6.5, 7.5, 8.5, and 9.5), while partial least-squares discriminant analysis (PLS-DA) provided robust classification and prediction, with Q^2 of 94.26% and R^2 of 95.67%. This proof-of-concept study demonstrates that solid-state SWCNT chemiresistive sensor arrays can be tailored for specific disinfectants and hold potential for deployment in water treatment and distribution monitoring. Reprinted with permission from *ACS Appl. Eng. Mater.* **2023**, *1*, 11, 3040–3052, Md Ali Akbar, Omar Sharif, P. Ravi Selvaganapathy, and Peter Kruse.
DOI: 10.1021/acsaenm.3c00505

ACS APPLIED ENGINEERING MATERIALS

Open Access

pubs.acs.org/acsaenm

Article

Identification and Quantification of Aqueous Disinfectants Using an Array of Carbon Nanotube-Based Chemiresistors

Md Ali Akbar, Omar Sharif, P. Ravi Selvaganapathy, and Peter Kruse*

Cite This: *ACS Appl. Eng. Mater.* 2023, 1, 3040−3052

Read Online

ACCESS | Metrics & More | Article Recommendations | Supporting Information

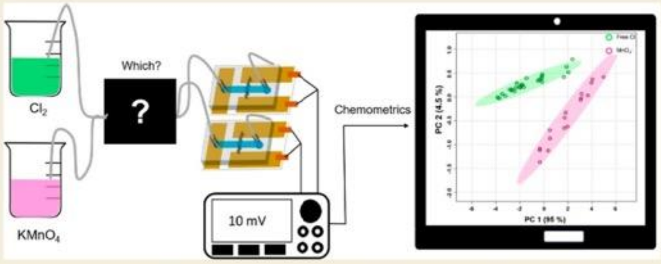

ABSTRACT: Disinfection of water is essential to prevent the growth of pathogens, but at high levels, it can cause harm to human health. Therefore, accurate monitoring of disinfectant concentrations in water is essential to ensure safe drinking water. The use of multiple disinfectants at different stages in water treatment plants makes it necessary to also identify the type and concentrations of all of the disinfectant species present. Here, we demonstrate an effective approach to identify and quantify multiple disinfectants (using the example of free chlorine and potassium permanganate) in water using single-walled carbon nanotube (SWCNT)-based reagent-free chemiresistive sensing arrays. Facile fabrication of chemiresistive devices makes them a popular choice for the implementation of sensor arrays. Our sensing array consists of functionalized and unfunctionalized (blank) SWCNT sensors to distinguish the disinfectants. The distinct responses from the different sensors at varying concentrations and pH can be fitted to the mathematical model of a Langmuir adsorption isotherm separately for each sensor. Blank and functionalized sensors respond through different mechanisms that result in varying responses that are concentration- and pH-dependent. Chemometric techniques such as principal component analysis (PCA) and partial least-squares-discriminant analysis (PLS-DA) were used to analyze the sensor data. PCA showed an excellent separation of the analytes over five different pHs (5.5, 6.5, 7.5, 8.5, and 9.5). PLS-DA provided excellent separability as well as good predictability with a Q^2 of 94.26% and an R^2 of 95.67% for the five pH regions of the two analytes. This proof-of-concept solid-state chemiresistive sensing array can be developed for specific disinfectants that are commonly used in water treatment plants and can be deployed in water distribution and monitoring facilities. We have demonstrated the applicability of chemiresistive devices in a sensor array format for the first time for aqueous disinfectant monitoring.

KEYWORDS: *carbon nanotubes, free chlorine, permanganate, chemiresistive sensor, water quality monitoring, disinfectant monitoring, principal component analysis, partial least-squares-discriminant analysis*

INTRODUCTION

Disinfectants are added to water to maintain hygiene. Disinfectants kill disease-causing pathogens by reacting with different components of the bacterial cells, thereby disrupting cellular processes.[1] In water treatment facilities, primary disinfection is carried out to remove pathogens using a strong disinfectant. Then, secondary disinfection is carried out in the distribution system by adding either the same disinfectant or a different one as a residual disinfectant to prevent the regrowth of the pathogens. Among the most commonly used disinfectants are free chlorine (pH-dependent mixture of OCl^-, HOCl, and Cl_2), chlorine dioxide (ClO_2), monochloramine (NH_2Cl), potassium permanganate ($KMnO_4$), hypobromous acid (HOBr), and hydrogen peroxide (H_2O_2).[2] The efficiency of the disinfectants at keeping water pathogen-free depends on the disinfectant levels in the water, which therefore need to be monitored.[3,4] Inadequate levels of disinfectants in water may lead to devastating events such as the Walkerton Tragedy in 2000 in Canada. 7 people died and 2300 others

Received: August 28, 2023
Revised: October 8, 2023
Accepted: October 17, 2023
Published: October 29, 2023

https://doi.org/10.1021/acsaenm.3c00505

became sick due to a pathogen outbreak in the water distribution system.[5,6] Water treatment plants sometimes use combinations of disinfectants for treating water.[4,7,8] Mixing disinfectants, however, will result in them reacting with each other, reducing efficacy and potentially running counter to the purpose of having disinfectant in water: keeping water safe by preventing the growth of pathogens. The importance of identifying disinfectants was highlighted during the 2016 Olympic Summer games in Rio de Janeiro (Brazil) when H_2O_2 was mistakenly added to a swimming pool that was previously disinfected with free chlorine.[9,10] The chemical reaction between H_2O_2 and free chlorine left the pool with little or no disinfection, resulting in the growth of microorganisms and the pool became green. Therefore, for effective disinfectant monitoring, it is not enough to know the disinfectant level, but it is also important to identify which disinfectant is present. Additionally, disinfectant identification is also very important for aquaculture, kidney dialysis,[11] hydroponics,[12] and brewing.[13] Due to interferences, most current monitoring devices require prior information on the identity of the disinfectant used for water treatment. Currently, there is no simple standard method for distinguishing different disinfectants present in water.

Current standard methods for measuring disinfectant concentrations are primarily colorimetric (*N*,*N*-diethyl-*p*-phenylenediamine, DPD for chlorine,[14] Lissamine Green B for chlorine dioxide,[15] and direct for $KMnO_4$[16]) and titrimetric (DPD ferrous for chlorine,[18] thiosulfate titration for H_2O_2,[19] and amperometric titration for chlorine[18]) techniques. Disinfectant monitoring is carried out on discrete samples at the treatment facilities and at several point locations within the distribution network, lacking information about the overall disinfectant dynamics. Discrete sampling and analysis are expensive and time-consuming, and most importantly, the requirement to add reagents is undesirable.[20−22] These methods need spectroscopic readout devices that are prone to interference from turbidity, other oxidizing species, and organic content present in water. Due to these shortcomings, colorimetric and titrimetric methods are not suitable for continuous disinfectant monitoring. Electrochemical methods are very promising for online disinfectant monitoring due to their reagent-free analysis and instantaneous read-out,[17−20] but they rely on reference electrodes which require frequent calibration,[21] degrade over time, and are susceptible to contamination. Disinfectants have distinct standard reduction potentials, and the oxidation reduction potential (ORP) of a disinfectant is often measured to quantify its oxidizing power in water. However, ORP measurements alone are not capable of distinguishing the disinfectants since the ORP is dependent on the concentration of disinfectant and the pH of the aqueous environment.[22−24] Disinfectant chemistry itself is also highly pH-dependent.[24,25] Therefore, there is a need for continuous disinfectant-monitoring methods which take pH into consideration and are reagent-free, inexpensive, and reliable.

We have previously reported chemiresistive sensors for continuous monitoring of free chlorine in drinking water utilizing nanocarbon-based films doped with redox-active aniline oligomers.[26,27] Facile fabrication, rapid prototyping, low cost, and availability of high precision resistance measurement circuits make chemiresistors a good choice for sensor applications.[28−30] Carbon nanotube (CNT) films are suitable chemiresistive substrates since their electrical properties are affected by the adsorption of electron-donating or electron-accepting species acting as dopants.[31−33] Redox-active molecules dope CNTs by forming charge-transfer complexes, the nature of which is susceptible to the oxidation state of the molecule.[34] Thus, the doping state of the CNTs is related to the oxidation state of the molecules.[35] Under ambient conditions, CNTs are inherently p-doped due to adsorbed molecular oxygen.[36,37] Oligoanilines in their fully reduced state (amino groups) n-dope CNTs, thus reducing the overall doping level and increasing the film resistance.[38] In the oxidized state (imine groups), they show p-doping, thus reducing the resistance of the CNT films. While these sensors show excellent sensitivity toward oxidants,[38,39] as individual sensors, they cannot distinguish disinfectants or separate disinfectant concentration from ORP.[9]

Here, we demonstrate the identification of two disinfectants using an array of single-walled CNT (SWCNT)-based chemiresistive sensors functionalized with redox-active molecules. As a proof-of-concept study, we report the differentiation and quantification of free chlorine and $KMnO_4$ over a relevant pH range. The sensor responses depend on the disinfectant's standard reduction potential and adsorbed redox active molecule's oxidation potential. CNT substrates are noncovalently functionalized with redox active molecules which introduce active sites on the CNT surfaces. Functional groups of these molecules then react with the disinfectant present in water. Molecules with different redox potentials create different active sites, resulting in distinct responses upon interaction with the analyte. Sensor arrays with six sensors (one blank and five functionalized) were constructed, and the responses were recorded by exposing them to two different analytes with a range of concentrations under environmentally relevant pH conditions. Principal component analysis (PCA) and partial least-squares-discriminant analysis (PLS-DA), two common chemometric techniques, have been applied to analyze the sensor responses. This proof of principle electronic tongue will provide a foundation for the development of arrays for other disinfectants and liquid analytes using functionalized chemiresistive sensors.

EXPERIMENTAL SECTION

Redox-Active Molecules

The redox-active molecules used for this study are phenyl-capped aniline tetramer (PCAT), anthracene-substituted phenyl-capped aniline tetramer (APCAT), *N*,*N*-diphenyl-*p*-phenylenediamine (DPPD), *N*,*N*′-diphenylbenzidine (DPB), and 4,4′,4″-methylidynetris (*N*,*N*-dimethylaniline) or leucocrystal violet (LCV). PCAT and APCAT were synthesized following known literature procedures (synthesis routes shown in S1 and S6).[40,41] DPPD, DPB, and LCV were purchased from Sigma-Aldrich and used as received. Details of the synthesis and characterization (UV−vis and ^{1}H NMR) of all oxidation states of all molecules are given in the Supporting Information (S3−S5 and S7−S15) to verify the identity and purity of the molecules. 20% saturated solutions of these molecules were prepared by diluting saturated solutions (referred to as 100%) of the molecules in the appropriate solvents; methanol was used for all molecules except DPB for which acetonitrile was used. The concentrations of the saturated solutions were measured as follows: 1.6 ± 0.14 mg/mL for PCAT, 1.72 ± 0.18 mg/mL for APCAT, 5.57 ± 0.18 mg/mL for DPPD, 1.12 ± 0.25 mg/mL for DPB, and 1.42 ± 0.1 mg/mL for LCV. Freshly prepared solutions were used for the functionalization of the sensors.

Cyclic Voltammetry and Differential Pulse Voltammetry

Cyclic voltammetry (CV) and differential pulse voltammetry (DPV) were performed in a nonaqueous medium using a 0.1 M tertbutyl

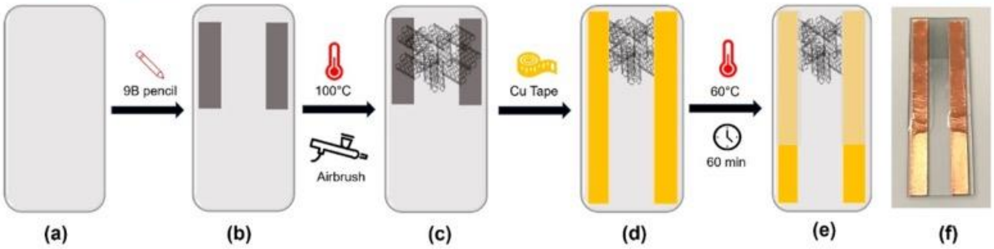

Figure 1. Schematic for the fabrication of the chemiresistive sensor. (a) Frosted glass slide is cleaned with methanol and dried. (b) Two thick pencil patches are drawn with a 9B pencil. (c) SWCNT suspension is airbrushed between the pencil patches at 100 °C. (d) Copper tape is attached lengthwise along the glass slide overlapping the pencil patch. (e) Copper tape is masked with PDMS and cured at 60 °C for an hour. (f) Photograph of a sensor device.

ammonium perchlorate supporting electrolyte with 0.02 mM diphenyl phosphate as a proton source in acetonitrile as a solvent. The working electrode was a platinum disk (0.785 mm^2 area), and a platinum wire was used as the counter electrode. A nonaqueous Ag/AgNO$_3$ electrode was prepared according to the literature and used as the reference electrode.[42] An EmStat potentiostat was used for potential control, and PSTrace software was used for data acquisition. For CV, a 0.1 V/s scan rate and a step size of 0.005 V were used. For DPV, E_{step} was 0.005 V, E_{pulse} was 0.1 V, and t_{pulse} was 0.05 s, and a scan rate of 0.01 V/s was applied. All experiments were performed under argon to prevent interference from air oxidation.

Single-Walled CNT Suspension

A methanolic suspension of SWCNT [chirality (6,5), average diameter 0.78 nm, 95% carbon basis, purchased from Sigma-Aldrich] was prepared by mixing 2−5 mg of SWCNT in 15 mL of methanol in a glass vial. The mixture was then sonicated in an Elmasonic P30H Ultrasonic Cleaner at 37 kHz for 6 h to facilitate the breakdown of the large nanotube bundles. The sonication system was set to sweep mode, and the temperature of the water bath was kept at 30 °C. The suspension was kept at room temperature and sonicated for an additional 30 min each time immediately before further use.

Sensor Fabrication

Figure 1 shows the schematic steps of the fabrication of the chemiresistive device. The frosted side of the glass slides (VWR VistaVision, 75 × 25 × 1 mm^3, Cat. no. 16004418) was used to prepare the substrate of the sensor. The glass slides were first cleaned with methanol and then dried in air. Two pencil patches were drawn on the frosted side using a 9B pencil. Slides were then placed on a hot plate to reach 100 °C. The SWCNT suspension was airbrushed over and between the pencil patches until a uniform film was achieved. The resistance of the film was kept in the range of 10−20 kΩ. After cooling the slides to room temperature, two pieces of adhesive copper tape (3M EMI Copper Foil Shielding Tape 1181, 1/4 in wide) were placed on the pencil patches. The contacts were masked with a thick layer of partially cured (5−6 h at room temperature) polydimethylsiloxane (PDMS—Sylgard 184 Silicon Elastomer from Dow Corning). The sensors were then cured at 60 °C for 1 h. A photograph of an actual device is shown in Figure 1f.

Characterization of the Molecules and Film

The molecules were dissolved in acetonitrile (0.5 mg/mL) and sonicated for 5 min. A Cary 100 UV−visible spectrometer was used for the spectroscopic analysis over a scanning window of 200−800 nm. Pure acetonitrile solvent was used to calibrate the blank, and quartz cuvettes were used for the analysis. Functionalized and nonfunctionalized SWCNT films have been characterized by a Renishaw inVia Raman spectrometer using a 633 nm HeNe laser (20× objective lens, 1.5 μm spot size, and 1% power) and a 1200 gr/mm grating at an accumulation rate of 15/s. The SWCNT films were airbrushed on the frosted side of a glass slide and then dipped into a 20% saturated solution of the relevant molecule. The samples were dried before Raman analysis. The spectra were normalized to the highest peak. Scanning electron microscopic (SEM) images were taken on a JEOL JSM-7000F microscope at 3.0 kV, 50,000×, and a working distance of 5.2 mm.

Functionalization of SWCNT Sensors

Functionalization was carried out with a freshly prepared batch of sensors following previously laid out procedures.[43,44] Six sensors with similar resistances were selected for each set of experiments, five of which were functionalized with redox-active molecules and one of which was used as a control (blank). Freshly prepared 20% saturated solutions of the redox-active molecules were prepared from fully saturated stock solutions. The substrate portion of the sensor was first dipped into the solvent for 5 min to wet and clean the SWCNT films. The sensors were then dipped into the corresponding molecule solutions for functionalization (Figure S36). The sensor response in the molecule solution was monitored, and the functionalization was carried out until a stable response was achieved. This process took about 2−5 h. After the doping process (molecule solution for five sensors and pure methanol for the blank), all six sensors were removed from the solutions and their films were rinsed three times with fresh batches of the same solvent to remove any excess molecules from the surface. This was done to ensure a thin, uniform layer of molecules on the SWCNT surface. The sensors were dried at room temperature to remove the solvent before being placed in water. From our previous work and data collected over the course of this study, we know that the sensors fabricated according to these procedures will remain stable for 8−10 weeks.[27,43,44]

Sensor Characterization

Several eDAQ Quad Multi-Function isoPod (EPU452) setups were used to acquire data for sensor testing. Up to two eDAQs can be connected to one computer, and each eDAQ has four channels. A 10 mV potential bias was applied across the sensor film, while the current was measured over time. The instrument was set to Biosensor mode (for sensors) with a data acquisition rate of 10 or 15 min^{-1} and a current range of 20 μA. A pH electrode (Fisherbrand Accumet Gel-Filled Polymer Body Single-Junction pH Combination Electrode) and an ORP electrode (Ionode IJ-64) were also connected in addition to six sensors for a two-eDAQ setup consisting of eight channels (Figure S36). For the electrodes, pH and ISE modes were used in eDAQ. The pH electrode was calibrated using two buffer solutions of pH 4 and 7 before every experiment. Then, all sensors and electrodes were placed in water (Type 1 ultrapure water obtained from a Millipore Simplicity UV system) with a phosphate buffer background. The buffer solutions were prepared either by dissolving phosphate-buffered saline (PBS) tablets (Sigma-Aldrich) or using a mixture of potassium phosphate monobasic and dibasic (purchased from Sigma-Aldrich). The sensors are left in buffered ultrapure water for 15−20 h before spiking with analytes (disinfectants). The glassware used for the experiments was pretreated with 0.1 ppm free chlorine before every experiment. Clean glassware was first soaked in a free chlorine solution for 1 h, followed by rinsing three times with ultrapure water.

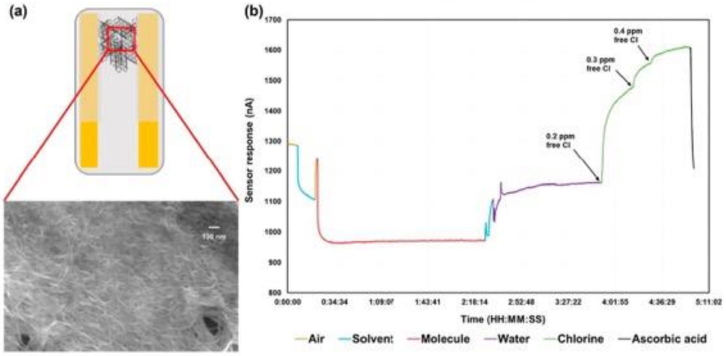

Figure 2. (a) Schematic of sensor geometry; the inset shows a SEM image of the CNT film. (b) Recorded sensor response as current (nA) over time for the different steps of the measurement. Solvent and molecule solution induces n-doping on the surface, while the oxidant (free chlorine) results in p-doping behavior. When exposed to ascorbic acid, the sensor showed a reset in the response due to analytes getting reduced by ascorbic acid.

Chlorine stock was prepared from a reagent-grade sodium hypochlorite solution (Sigma-Aldrich). The concentration of the chlorine solutions was measured using the DPD colorimetric method with a Hach Pocket Colorimeter II and a Thermo Scientific Orion Aquamate 8000 UV−vis spectrophotometer. The reagents used for the pocket colorimeter measurements were DPD-Free Chlorine Reagent Powder Pillows (Hach 1407099-CA) and for the benchtop Aquamate, Orion AC4P71 Powder Chemistry Packs. MnO_4^- stock was prepared by dissolving 99% $KMnO_4$ crystals (Sigma-Aldrich). Experiments were performed by keeping either the concentration or the pH of the solution constant and varying the other parameter. For the experiments at constant pH, sensors were exposed to several concentrations of free Cl (0, 0.25, 0.5, and 2 ppm) and $KMnO_4$ (as MnO_4^-) (0, 0.17 0.33, and 0.66, 1.33 ppm) at four different pH (6.5, 7.5, 8.5, and 9.5) resulting in a total of 40 experiments per sensor. Concentrated HCl (1 M) and NaOH (1 M) were used to achieve the desired pH of the PBS-buffered water. During the experiment, the pH of the solutions was kept constant by adding 0.1 M HCl and 0.1 M NaOH. Data are taken for a total of 33 min at each concentration. The first 3 min were taken to slowly add the concentrated stock solution (~630 ppm free chlorine and ~2000 ppm MnO_4^-) to change the concentrations of the solution. Concentrated free chlorine and permanganate were added to the center of the reaction vessel to prevent abrupt behavior due to interaction between the highly concentrated analyte and the surface. Even though the sensors reset with water, the complete resetting process from the highest concentration back down to 0 ppm takes about 24−48 h. Ascorbic acid (purchased from Sigma-Aldrich) was added to accelerate this process. After each experiment, the water with analyte was replaced with a freshly prepared 0.1 ppm aqueous solution of ascorbic acid for 15−30 min. For the experiments at constant concentration, different sets of sensors were used which were exposed to 1 ppm of free chlorine and 1 ppm MnO_4^- at 5 pHs ranging from 5.5 to 9.5. The required pH of the water solutions used for the experiments was achieved by using 0.05 M phosphate buffer and additions of 0.1 M HCl and 0.1 M NaOH solutions.

Data Analysis

Sensor responses were recorded as the current (nA). For further analysis, the last 2 min of data were averaged and compared with the baseline (I_0). The sensor response was calculated by dividing the change in current ($\Delta I = I - I_0$) by the baseline (I_0). The response data collected from six sensors at 1 ppm of analytes were subjected to machine-learning algorithms to extract further information. PCA was used as an unsupervised method, and PLS-DA was used as a supervised method to evaluate the separability of the array. MetaboAnalyst 5.0 and ProMV were used to perform multivariate analyses. Both of these two sources use the nonlinear iterative partial least-squares (NIPALS) algorithm to calculate the scores for both PCA and PLS-DA.[45] Normalization of the raw sensor responses was done by mean-centering and dividing each data point by the standard deviation of each variable (each sensor was treated as a variable in the array) before applying the NIPALS algorithm. Each of the sensor responses was inserted as the variable response for multivariate analyses.

■ RESULTS AND DISCUSSION

Sensing Mechanism

Chemiresistive sensors respond to changes in the chemical environment of the active element with changes in resistance. We utilized SWCNT networks to fabricate the active elements of our sensors. Figure 2a shows a representative SEM image of a thin layer of a SWCNT network. The surface of these SWCNT sensors adsorbs molecular oxygen from air and becomes inherently p-doped upon exposure to ambient conditions.[37] Therefore, holes are the primary charge carriers in the SWCNT sensors. Figure 2b shows the responses of a functionalized sensor when it is exposed to different chemical environments. When a dry sensor was transferred from air to pure liquid methanol, a decrease in the sensor response was observed. Charge transfer from the solvent to the SWCNTs leads to a decrease in the hole concentration and therefore a sharp decrease in conductivity. For the functionalized sensors, a further drop in hole concentration was observed when the sensor was introduced into the molecule (DPB) solution. This is due to the adsorption of molecules on the SWCNT surface through $\pi-\pi$ interactions. The formation of a self-assembled monolayer of molecules was facilitated by carrying out the doping process at sufficiently low concentrations and allowing enough time for the system to equilibrate. Excess molecules at the surfaces were removed by rinsing the film with a pure solvent at the end. After the doping process was completed, the sensors were immersed in pure water for a long time to achieve a stable baseline. The additions of either of the two oxidants, free chlorine (Figure 2b) and $KMnO_4$, resulted in increases of the chemiresistive current. This was observed in both the blank and functionalized sensors. Two sensing mechanisms have been reported to contribute to the sensor responses in these chemiresistive devices: electrostatic gating and charge trans-

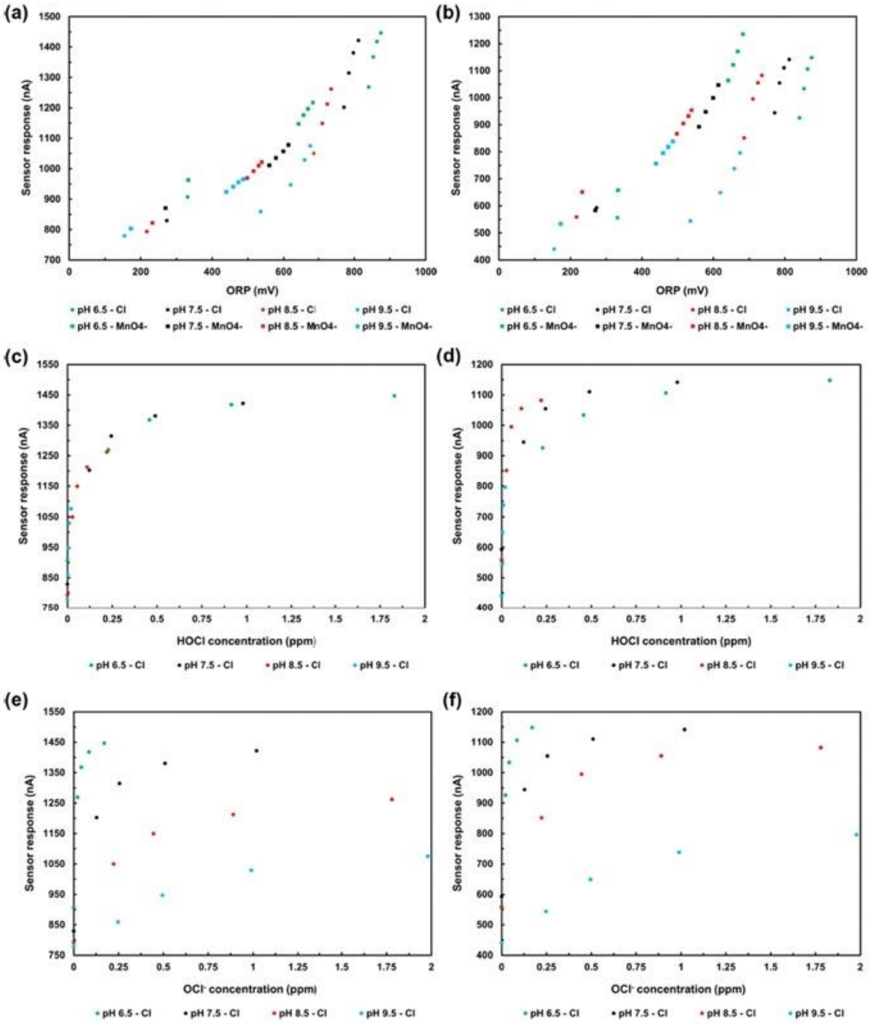

Figure 3. Raw sensor responses as current (nA) of blank (left column) and DPB (right column) sensors. (a,b) Responses for the two analytes in five concentrations over the four pHs (resulting in 2 × 4 × 5 = 40 data points for each sensor) plotted against the ORP (mV) of the solution. Similar sensor responses for the other four molecules (PCAT, APCAT, LCV, and DPPD) are provided in the Supporting Information (Figure S37). (c,d) Sensor responses against the free chlorine (as HOCl) concentration at four pHs. (e,f) Sensor responses against the free chlorine (as OCl^-) concentration at four pHs. HOCl and OCl^- concentrations were calculated from the free chlorine concentration.

fer.[46] The bare SWCNT sensors respond to the redox potential present at the surface due to the presence of oxidizing agents. The inherently p-doped nanotube surface gets further p-doped due to the presence of negatively charged hypochlorite (OCl^-) and permanganate (MnO_4^-) ions on the surface. These ions attract positively charged holes (primary carriers) to the surface of the film due to electrostatic gating. Consequently, the conductivity of the chemiresistive film increases. The increasing concentrations of the analytes result in a stepwise increasing response, which is later used for the calibration of the sensors.

Figure 3a represents the blank sensor response as current for both analytes covering a range of pHs and concentrations, which resulted in different magnitudes of ORP of the solution. It can be seen that the blank sensor responses appear to correlate reasonably well with the ORP of the solution. One possible reason for the imperfect correlation may be due to the presence of defects on the surface that interact with the analytes.[47,48] Most of the deviations occur for free chlorine at higher pHs (8.5 and 9.5). The pH-dependent nature of the different free chlorine species can result in the (co)presence of charged OCl^- or molecular HOCl and Cl_2. Below pH 4, Cl_2

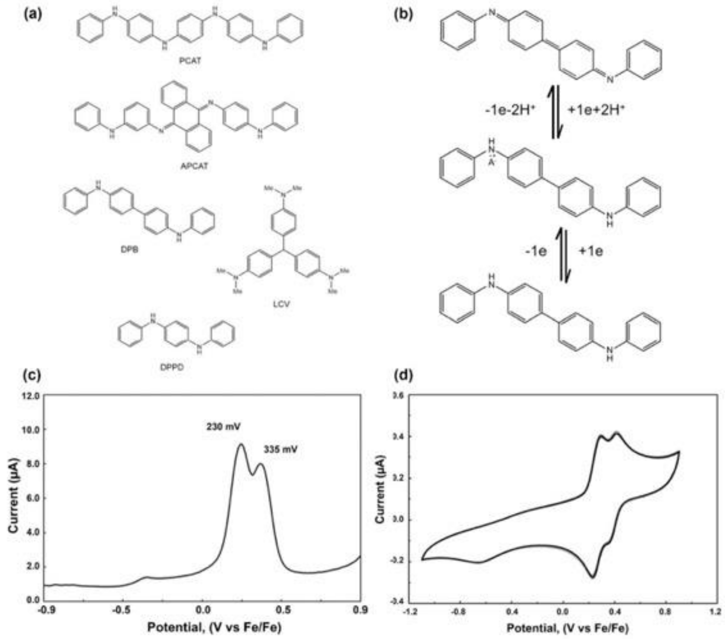

Figure 4. (a) Structures of the redox active molecules used for the array. PCAT, APCAT, DPB, LCV, and DPPD. (b) Reversible oxidation and reduction process steps of DPB. (c) CV of DPB. (d) DPV of DPB (oxidation scan).

exists as the sole component, while at pH range 6−9, OCl^- and HOCl exist together at different compositions depending on the level of pH. To better understand the mechanisms contributing to the sensor response, the individual amounts of HOCl and OCl^- content are plotted for the recorded sensor response. Figure 3c,e shows the data from the blank sensor for HOCl and OCl^- present in the solution. The HOCl and OCl^- amounts are calculated from the total free chlorine following the ratio of the species present at a certain pH. A pK_a of 7.58 (at 25 °C) was used for the calculation of the $HOCl/OCl^-$ equilibrium.[49−51] The HOCl concentrations at pH 6.5, 7.5, 8.5, and 9.5 were found to be 91.5, 55, 11, and 1% of the free chlorine, respectively.[51] It should be noted that the blue data points represent the HOCl at pH 9.5, which is only 1% of the total free chlorine as HOCl; hence such small values in Figure 3c,d. The remainder of the free chlorine is in the form of OCl^- at the corresponding pH's. The response of blank sensors to HOCl is correlated with the concentration of the HOCl species rather than pH, implying that it is directly due to HOCl molecules getting adsorbed onto the sensor film and completely unaffected by concurrently present OCl^- ions. This contrasts with the OCl^- (Figure 3e) response for the blank sensors which is also a function of pH. Since HOCl has a significantly higher disinfecting power (100 times) than OCl^-, this selective response to HOCl explains the close-to-ORP relationship in Figure 3a. In the blank sensor response (Figure 3c), HOCl showed asymptotic behavior at higher concentrations and the response can be fitted to an adsorption isotherm model. This suggests that the HOCl molecules adsorb on the CNT film and oxidize the surface in a charge-transfer process. The density of adsorbed molecules thus dominates the sensing response independent of pH. In contrast, OCl^- showed a pH-dependent sensing behavior (Figure 3e), which suggests a different mechanism. The interaction of negatively charged OCl^- on the surface with negatively charged defects is affected by the pH of the solution resulting in a higher response (Figure 3e) even for lower concentrations of OCl^-. Therefore, the ORP of the solution is a contributing factor here, and this is also seen from the correlation between ORP and MnO_4^- responses (Figure 3a).

Figure 3b shows the responses of a DPB-functionalized sensor for free chlorine and MnO_4^-. The sensor responses show a similar increasing trend with respect to ORP of the solution as the blank (Figure 3a); however, a noticeable difference can be seen as the molecules on the surface interact with the analytes. The amine groups in DPB (structure given in Figure 4a) are oxidized to imine groups in the presence of oxidizing agents. Figure 3c,d can be analyzed to understand the mechanism of HOCl interaction with the functionalized sensor. In contrast to the blank sensor (Figure 3c), the response of the doped sensor is not just a function of the HOCl concentration (Figure 3d). For example, three data points (red, green, and black) in Figure 3c,d at HOCl concentrations of approximately 0.25 ppm at three different pHs (and therefore, different total free chlorine concentrations) can be considered here: for the blank, HOCl responses were very close, whereas for DPB, the responses are far apart and pH-dependent. The red data point (pH 8.5) was in the presence of a higher amount of OCl^- (91%), followed by the black (45% at pH 7.5) and then green (8.5% at pH 6.5) data points. This dependence of the functionalized sensor response on OCl^- concentration present in solution

https://doi.org/10.1021/acsaenm.3c00505
ACS Appl. Eng. Mater. 2023, 1, 3040−3052

suggests that OCl^- interacted with the molecules through a redox reaction that resulted in additional p-doping of the surface which did not occur in the blank sensor. Figure 3e,f shows similar pH-dependent behavior of OCl^-. Overall, it is evident from the responses that molecules on the surface modulate the sensor responses to result in pH and disinfectant-dependent responses, and therefore, an array of selected molecules could help resolving disinfectant and pH information.

Redox-Active Molecules and Their Characterization

For the purpose of distinguishing disinfectants, five molecules were selected based on the requirements that they (a) adsorb well on the nanocarbon surface, (b) transmit reversible redox activity, and (c) have low reduction potentials. Figure 4a shows the structure of the molecules used in the array. Their planar conjugated structure facilitates adsorption on the CNT surface through $\pi-\pi$ interactions. Noncovalent functionalization of the sensors was chosen to avoid disrupting the electronic structure of the CNTs. Noncovalent functionalization of nanocarbon films with PCAT,[27] DPPD,[34] and LCV[30] has previously been studied by our group and found to modulate the electronic properties of the carbon structure. APCAT, an anthracene-substituted structure of PCAT, was selected since it is related to PCAT but with a larger conjugated system and lower redox potentials. Under ambient conditions, two of the four amine groups in APACT are already oxidized to imines; therefore, it starts from its half-oxidized form. DPB, has a structure similar to that of DPPD but with an additional benzene ring in the middle. Raman spectra of SWCNT functionalized with these molecules were analyzed to understand the effect of doping. Figure S38 shows the normalized Raman spectra for the bare and functionalized SWCNT sensors in the range of 500−2800 cm^{-1}. The characteristic peaks of the SWCNT for the D, G, and 2D bands were identified at around 1301, 1590, and 2595 cm^{-1}, respectively. The peak intensity ratios I_D/I_G and I_{2D}/I_G were examined to evaluate the doping effect of the molecules and the introduction of defects on the surface. I_D/I_G is often used to quantify the concentrations of defects in CNT films. The low I_D/I_G value (0.11) of the blank SWCNT film represents high-quality nanotubes with a low density of defects. For the functionalized SWCNT with the redox-active molecules, a higher range of I_D/I_G (0.16−0.20) was observed (shown in Table S3). Similarly, the I_{2D}/I_G ratio was found to be higher in the functionalized SWCNT films than that in the unfunctionalized one. Higher I_D/I_G and I_{2D}/I_G values in the functionalized sensors demonstrated that the molecules modulated the structure of the SWCNT films. This is an additional proof that the molecules remain on the CNT film, even after washing, and contribute to the sensor response (shown in Figure 3b). Another commonly used parameter to demonstrate the doping behavior is the 2D peak shifting in SWCNTs as shown by our group in previous reports.[37,52] These shifts were not observed clearly here because the sensor films were only surface-coated after film deposition. Previous Raman data (for some of the same molecules) had been obtained from thicker films prepared by sonicating CNTs together with the molecules, allowing for all nanotubes to be uniformly coated.[34] The molecules were further characterized electrochemically to understand the type of redox activity in the presence of oxidizing agents (disinfectants). Figure 4c shows the CV data for DPB in solution, which reveals the reversibility of the redox activity of the molecule. The oxidation of DPB is a two-electron process, and each redox couple can be associated with an individual one-electron oxidation process from the leucoemeraldine base (reduced state) to the pernigraniline base (oxidized state). Each of the amine groups of the molecule was oxidized in one of the steps by disinfectants. The differential pulse voltammogram of DPB (Figure 4d) also shows two peaks each in both the oxidation scan and the reduction scan. Figure 4b shows the reversible redox reaction of DPB. After comparison of the oxidation potentials of the molecules found from differential pulse voltammogram oxidation scans, they were ranked according to ease of oxidation, as summarized in Table S1. The full spectroscopic (mass spectroscopy, UV−vis, and NMR) and electrochemical data sets for all five molecules are available in the Supporting Information (S02−S35).

Calibration of the Sensors

Sensor responses (as percent change) were plotted as a function of the concentration of the analytes to establish the calibration graphs. Different mathematical models such as the Langmuir adsorption isotherm (eq 1), Freundlich adsorption isotherm (eq 2), and exponential decay (eq 3) have been applied to fit these responses. These three models satisfy the key requirement of no response at a 0 ppm concentration of the analytes. The Langmuir isotherm and exponential decay models have asymptotic behavior at higher concentrations (saturation of the sensor response at a maximum response value), which was observed in our sensor response. Surface science models like Langmuir and Freundlich isotherms are commonly implemented in explaining the adsorption of gas, liquid, and solid on solid surfaces. The Langmuir adsorption model assumes that a monolayer of molecules is adsorbed on the surface of the substrate, while the Freundlich adsorption model assumes that surface coverage will increase with increasing concentrations (no saturation of the response).

$$y = \frac{abx}{1 + bx} \tag{1}$$

$$y = mx^{1/n} \tag{2}$$

$$y = i(1 - e^{-jx}) \tag{3}$$

Here, y is the sensor response, and x is the concentration of the analyte. In eq 1, a is the saturation point or the maximum theoretical value of y; b is the Langmuir constant which is inversely related to the thickness of the chemiresistive sensor film.[22] The Freundlich parameter m (also known as the partitioning coefficient) refers to the maximum analyte adsorption capacity of the sensor film. A high value of m reflects a strong interaction of the analyte and film. The other parameter n (also known as the correction factor) is the measure of adsorption intensity of the substrate. The value of n can range from 0 to 1 where n close to 1 indicates a favorable adsorption condition and n when less than 1 indicates a less favorable condition. In eq 3, i is the maximum amount of the analyte adsorbed on the substrate and j is a constant related to the binding equilibrium. After fitting the responses with these three models (shown in Figure S39), the Langmuir isotherm model was found to best fit (higher R^2) the responses compared with the other two models. In this article, sensor responses are investigated as a function of concentration of the analytes at different pH. Other factors such as temperature and

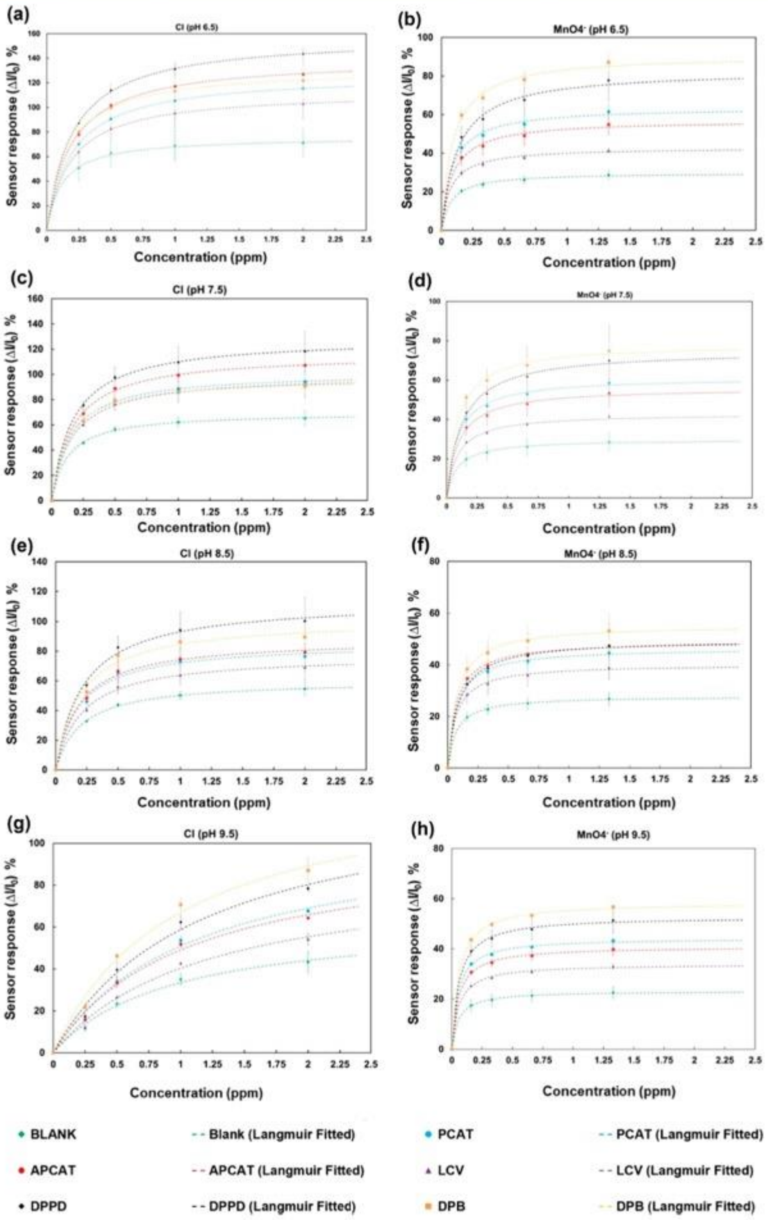

Figure 5. Calibration graphs of chlorine (left column) and permanganate (right column) responses from the sensors at pH 6.5, 7.5, 8.5, and 9.5. The error bars are given based on repeat runs for the same sensors. The dotted lines are the Langmuir isotherm fit, and the data points are the average of the two runs.

concentration of molecules for the functionalization can affect the sensor calibration. We observed that the sensors respond well to disinfectants in the practically relevant range of 15−35 °C. The use of relatively low concentrations of molecules in the functionalization solutions is necessary to prevent dimer formation on the SWCNT surface which could affect the performance of the sensors. Here, we employed room-temperature conditions and optimized concentrations of the redox-active molecules during functionalization in keeping with previously reported findings.[27,43]

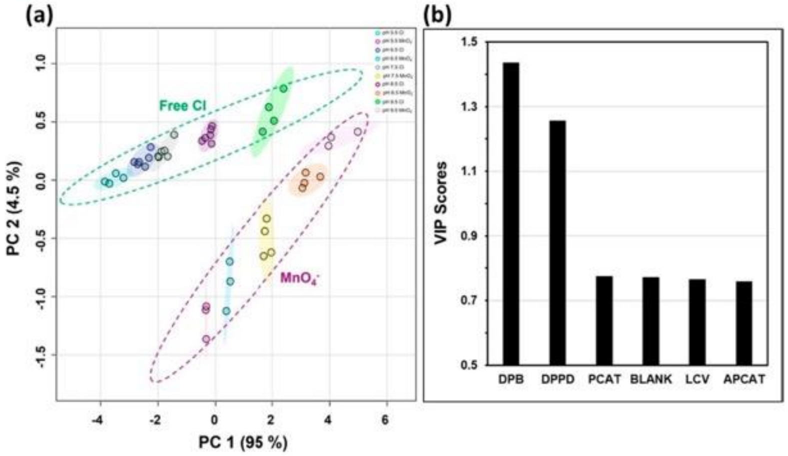

Figure 6. (a) PCA of the sensor responses for 1 ppm of analytes (free chlorine and permanganate) in five pHs (5.5, 6.5, 7.5, 8.5, and 9.5) of the chemiresistive sensor array. The dotted regions represent free chlorine and permanganate, and inside, the colored regions represent the pH regions for the corresponding analyte. The colored regions represent a 95% confidence level. (b) VIP plot from the PLS-DA model showing the contributions of the variable in differentiating the analytes.

Figure 5 shows the sensor response as a function of the concentration fitted to Langmuir isotherms (eq 1) for free chlorine (left column) and permanganate (right column). Each plot represents a specific pH and includes six curves representing six sensors. The fitting parameters are presented in a tabulated form in Table S4 of the Supporting Information. Increasing responses are observed with the addition of higher concentrations of HOCl/OCl$^-$ and MnO_4^-. Above a certain concentration, the sensor response saturates due to the establishment of an equilibrium between the disinfectant species in solution and at surfaces sites (e.g., dopant molecules). Doping of the films has successfully increased the sensitivity of the sensors as blank sensors give the lowest response in all experiments. For instance, blank gives responses of 67.81 and 27.70% for HOCl/OCl$^-$ and MnO_4^-, respectively, for 1 ppm at pH 6.5. For the same pH (6.5) and concentration (1 ppm), maximum responses were from the DPPD sensor (131.62%) for HOCl/OCl$^-$ and the DPB sensor (83.19%) for MnO_4^-.

The magnitudes of the responses from the functionalized sensors were found to vary depending on the analyte and pH of the solution. It was found that for the same type of sensor, free chlorine results in a higher sensor response than MnO_4^- for the same concentrations. For instance, DPPD gives a 131% response for free chlorine and a 73% response for MnO_4^- at the same concentration (1 ppm) and pH (6.5). The sensors showed a dependence on pH for both analytes: as the pH goes up, the sensor responses go down. The concentration of the buffer itself did not impact the sensing response within a range of 0.0025–0.02 M (Supporting Information, Figure S40). The small change in pH yields significantly higher change in sensing response compared to the change in buffer concentration, as shown in Figure S41. Hence, the pH sensitivity was not a result of varying phosphate species concentrations but rather due to changes in disinfectant effectiveness. The pH dependence of the sensor response to the disinfectants can be understood due to the involvement of protons in the corresponding redox reactions and thus the pH dependence of the redox potentials. The oxidation–reduction potential of an oxidant at an electrode can be calculated from the Nernst equation

$$E = E_0 + \frac{RT}{nF}\ln\frac{[\text{Oxidizer}]}{[\text{Reducer}]} \tag{4}$$

Here E, E_0, R, T, n, and F represent actual redox potential, standard redox potential, universal gas constant, temperature, number of electrons transferred, and the Faraday constant, respectively.

For HOCl reduction under acidic conditions at room temperature, the Nernst equation can be written as

$$\text{HOCl} + \text{H}^+ + 2\text{e}^- \rightarrow \text{Cl}^- + \text{H}_2\text{O} \tag{5}$$

$$E = E_{0,\text{HOCl}} + 29.58\ \text{mV}\cdot\log\frac{[\text{HOCl}]\cdot[\text{H}^+]}{[Cl^-]} \tag{6}$$

The Nernst equation for OCl$^-$ can be written as

$$\text{OCl}^- + \text{H}_2\text{O} + 2\text{e}^- \rightarrow \text{Cl}^- + 2\text{OH}^- \tag{7}$$

$$E = E_{0,\text{OCl}^-} + 29.58\ \text{mV}\cdot\log\frac{[\text{OCl}^-]}{[\text{Cl}^-]\cdot[\text{OH}^-]^2} \tag{8}$$

The standard redox potential of HOCl (+1.48 V) is higher than that of OCl$^-$ (+0.84 V) which explains the free chlorine responses at different pH. For 1 ppm of free chlorine, the blank sensor's response decreases from 68 to 33% when pH changed from 6.5 to 9.5, showing an effect of the redox potential on the sensor response. This effect is also visible in the functionalized sensors; for instance, the DPPD sensor also showed 59% sensor response for pH 9.5 and 132% for pH 6.5. The effect of pH on the sensor response to permanganate is similar, albeit to a lesser degree as compared with free chlorine, because permanganate is the only active species over the entire pH range. At pH 9.5, the blank sensor gives a 22% response for 1 ppm of MnO_4^- compared to a 28% response at pH 6.5. For the functionalized sensors, this change in sensor responses at two extreme pHs is even higher; the DPB sensor gives a 55% response at pH 9.5, while the sensor response reaches 83% for 1 ppm of MnO_4^-. The Nernst equation for permanganate reduction under acidic conditions can be written as

$$MnO_4^- + 4H^+ + 3e^- \rightarrow MnO_2 + 2H_2O \quad (9)$$

$$E = E_0 + 19.72\ \mathrm{mV} \cdot \log \frac{[MnO_4^-] \cdot [H^+]^4}{[MnO_2]} \quad (10)$$

Blank sensors respond to MnO_4^- in different pHs in a similar way to how they respond to free chlorine. Sensor responses increase with increasing pH, correlating with the ORP of the solution. This trend however differs for three of the functionalized sensors (PCAT, DPPD, and DPB), specifically for the sensor responses at pH 8.5 being lower than those at pH 9.5. Even though the sensors provide responses fitted in the model that could be used to quantify the level of known disinfectants, it is not immediately evident which disinfectant is present based on just the sensor response. To resolve this issue, multivariate analysis can be carried out to capture the pattern and important variables. Most importantly, it will help to visualize the data from six sensors in lower dimensions.

Chemometrics

Multivariate analysis of high-dimensional data is a common approach to reducing the dimensions of the data and differentiating analytes from the sensor array data.[53] PCA is commonly used as an unsupervised method where the label of the data set is not taken into consideration. Principal components (PCs) are generated from the analysis, which are uncorrelated variables presenting the maximum variance of the original data set. The data is first normalized using the auto scale method to get more uniformly distributed values; Figure S42 shows the distribution of the data before and after the normalization. After the normalization, PCA is carried out on the data set, and a 2D score plot is generated, as shown in Figure 6a. This score plot is generated from the PCA analysis from the array for the two analytes at five pHs (5.5, 6.5, 7.5, 8.5, and 9.5). Each of the data points on the score plot represents an observation coming from a total of six sensors (one blank and five functionalized with different molecules). The sensor responses are assumed to be independent of each other, so they constitute independent variables or dimensions. The six-dimensional data set that was collected from the six sensors is now presented in a 2D plot (Figure 6a). The first two PCs (PC1 and PC2) account for 99.5% of the total variation of the data set. This means 99.5% of the information is retained by these two dimensions; this illustrates a very good approximation of the original data set with six dimensions. Cross-validation, a criterion commonly used to cross-validate the PCA model, was used in the data set, finding a performance parameter of $Q^2 = 0.994$ for the first two PCs. This suggests that the two-component PCA model has a very good predictability for future data points. The cumulative R^2 of the PCA model for the first two components was 0.995. The colored highlighted regions represent the 95% confidence level of the corresponding pH. The two disinfectants were separated from each other in the score plot; therefore, the PCA model is capable of distinguishing free chlorine and permanganate. Further analysis of the same data set depicted in Figure 6 revealed 10 clusters representing 5 of the corresponding pHs of each analyte. The separation of the five pH regions in the free chlorine regions can be attributed to the ratio of the free chlorine species (HOCl and OCl^-) present at each pH. A larger separation indicates a greater difference in the properties of the analyte. Free chlorine regions are better separated at higher pHs (8.5 and 9.5) than at lower pHs (5.5, 6.5, and 7.5). This can be attributed to the increasing amount of OCl^- at higher pHs. MnO_4^- regions were well separated for the five pH regions. Both analytes show an increasing score along the PC 1 for increasing the pH of the solution. These scores can be calibrated for untested pHs of the solution. In addition to scores, loadings are another important component of a PCA model. Loadings represent the linear combination of the variables for specific PCs. Loadings plotted for a certain number of PCs that explain enough variation in the data set can present the type of trend among the variables. Loadings were plotted for two components which cumulatively explains 99.5% variance in the data (Figure S43). PCAT, APCAT, and blank showed the highest correlation among the six variables. LCV showed a slight variation due to its positive loading for the second component. DPB and DPPD however showed that they are not correlated, and the increased distances showed that these two sensors contribute the most to differentiating the analytes.

To get a better understanding of any data set, an unsupervised method (PCA) is often complimented with a supervised method (PLS-DA).[54] PLS-DA, unlike PCA, considers the labels of the observations, and PLS-DA is particularly helpful in the selection of features of the array in addition to dimension reduction. In this method, scores are calculated using the NIPALS algorithm (like PCA), known as PLS, and then discriminant analysis (DA) is carried out on the scores. Figure S44 shows the PLS-DA score plot for the data set. Since the data set was well separated in the PCA score plot, it was evident that PLS-DA would result in well-separated regions as supervised methods take the labels of the data set. The performance of the PLS-DA model was evaluated by calculating Q^2 and R^2. It was found that by increasing the number of components, the Q^2 and R^2 can be increased. The PLS-DA model was cross validated utilizing the leave-one-out (LOO) method that excludes one observation as testing set from the rest of the observations which is used as training data set. Q^2 and R^2 values for a two-component model were found to be 0.8978 and 0.9154, respectively; these two performance parameters increased to 0.9668 and 0.9778, respectively, when another component was added (Figure S45). PLS-DA was also implemented to evaluate the variable importance in projection (VIP). VIP plot shows the contribution of the variables (sensors in this case) in discriminating the analytes. From the VIP plot (Figure 6b), it was found that DPB and DPPD had the highest VIP scores of 1.43 and 1.26, respectively, for the two-component PLS-DA model. Therefore, DPB and DPPD are the two most important variables and thus the two most important sensors in the array in distinguishing free chlorine and permanganate. This can be used when designing an array with fewer sensors for a similar outcome. To evaluate the possibilities of having a smaller array for the same output, the same chemometric analysis was carried out using only three sensors. We chose DPB, DPPD, and the blank as a possible array. Figure S46 shows the PCA and PLS-DA score plots for the three-sensor array. Both figures show excellent separation for the two analytes. Therefore, it can be said that the functionalization of SWCNT sensors can be implemented for the identification of disinfectants.

■ CONCLUSIONS

Here, we have demonstrated a method to identify and quantify disinfectants and pH using a solid-state-reagent-free chemiresistive sensor array. Single-walled CNT sensors were functionalized with redox-active switchable dopant molecules. Six sensors (five functionalized and one bare) were incorporated into the array. The sensors respond to the free chlorine and permanganate solutions at different pH. The responses were fitted to the mathematical model of a Langmuir adsorption isotherm. pH-dependent responses were observed for each of the disinfectants. PCA and PLS-DA were used to separate the analyte responses from the data collected from the array. Both models were able to separate the analytes, demonstrating the efficacy of this sensing array. The cross-validation using two PCs showed a Q^2 value of 99.4% and an R^2 of 99.5%. DPPD and DPB sensors are found to be the most important sensors in the array from chemometric analyses. We have also evaluated the possibility of using a smaller array by including DPPD, DPB, and blank sensors. Chemometrics showed that only three sensors are enough to efficiently distinguish the two disinfectants. This proof-of-principle study shows the potential of using a functionalized SWCNT sensing array for the identification and quantification of disinfectants. PCA score plots generated from continuous measurement of the disinfectants can be used to monitor the disinfectant level of drinking water. It should be noted that this study represents a method to distinguish disinfectants based on their individual responses assuming that they will stay in the same form. In practice, disinfectant chemistry is complex due to its sensitivity to other factors, such as pH and temperature. Therefore, further testing is necessary for the identification of disinfectants from a mixture. Sensor stability is crucial for the long-term monitoring of analytes. The SWCNT sensors used for this study were found to be stable in water for at least 2 months of continuous use. The sensors were exposed to a wide range of pH (5.5−9.5) and oxidizing (free chlorine and permanganate) and reducing (ascorbic acid) agents. During that time, the functionalized sensors showed higher sensitivity toward the analytes compared to the blank sensors. This demonstrates that the molecular layer on the SWCNT surface remained stable for at least 8 weeks. In our previous study, we demonstrated that the chemiresistive sensors were not sensitive to commonly found ions in drinking water.[27] In addition, sensors were also found to be stable for the measurement of the analyte in local tap water background.[27] The cheap and reliable chemiresistive sensors hold excellent potential for water quality monitoring. This chemometrics-assisted chemiresistive array of sensors can be expanded for the identification of other commonly used disinfectants, as well as contaminants present in water.

■ ASSOCIATED CONTENT

Supporting Information

The Supporting Information is available free of charge at https://pubs.acs.org/doi/10.1021/acsaenm.3c00505.

> Synthesis procedures and full characterization via NMR, mass spectrometry, UV−vis spectroscopy, CV, differential pulse voltammetry of all molecules in their different oxidation states, and effect of buffer concentration and buffer pH on sensor measurements (PDF)

■ AUTHOR INFORMATION

Corresponding Author

Peter Kruse − *Department of Chemistry and Chemical Biology, McMaster University, Hamilton ON L8S 4M1, Canada;* orcid.org/0000-0003-4051-4375;
Email: pkruse@mcmaster.ca

Authors

Md Ali Akbar − *Department of Chemistry and Chemical Biology, McMaster University, Hamilton ON L8S 4M1, Canada;* orcid.org/0000-0002-1809-8232
Omar Sharif − *Department of Chemistry and Chemical Biology, McMaster University, Hamilton ON L8S 4M1, Canada*
P. Ravi Selvaganapathy − *Department of Mechanical Engineering and School of Biomedical Engineering, McMaster University, Hamilton ON L8S 4K1, Canada;* orcid.org/0000-0003-2041-7180

Complete contact information is available at:
https://pubs.acs.org/10.1021/acsaenm.3c00505

Notes

The authors declare no competing financial interest.

■ ACKNOWLEDGMENTS

We thank Dr. David Emslie and his research group (McMaster University) for technical assistance with the synthesis of PCAT and helpful discussion. We thank Dr. Jose M. Moran-Mirabal for granting access to the potentiostat. We thank Caroline Wojnas and Aditya Aryasomayajula for technical support. We thank Dr. Brandon Corbett, Dr. Anis M. Khokon, Johnson Dalmeida, Ritchie Ly, and M. Shafiqul Islam for assisting with the data analysis. Electron microscopy was performed at the Canadian Centre for Electron Microscopy (also supported by NSERC and other government agencies). Funding for this project was provided by NSERC through the Discovery Grant Program and a Collaborative Research and Development Grant, by 3M Canada, by the Ontario Centers of Excellence, as well as by a Canada First Research Excellence Fund project "Global Water Future".

■ REFERENCES

(1) Camper, A. K.; McFeters, G. A. Chlorine Injury and the Enumeration of Waterborne Coliform Bacteria. *Appl. Environ. Microbiol.* **1979**, *37* (3), 633−641.

(2) World Health Organization. *Guidelines for Drinking-Water Quality: Fourth ed. Incorporating the First Addendum*, 4th ed. + 1.; World Health Organization: Geneva, 2017.

(3) Sayre, I. M. International Standards for Drinking Water. *J. - Am. Water Works Assoc.* **1988**, *80* (1), 53−60.

(4) US Environmental Protection Agency—Office of Water. *Alternative Disinfectants and Oxidants Guidance Manual*, 1st ed.; US Environmental Agency: Washington, DC, 1999.

(5) Salvadori, M. I.; Sontrop, J. M.; Garg, A. X.; Moist, L. M.; Suri, R. S.; Clark, W. F. Factors That Led to the Walkerton Tragedy. *Kidney Int.* **2009**, *75* (112), S33−S34.

(6) Hrudey, S. E.; Payment, P.; Huck, P. M.; Gillham, R. W.; Hrudey, E. J. A Fatal Waterborne Disease Epidemic in Walkerton, Ontario: Comparison with Other Waterborne Outbreaks in the Developed World. *Water Sci. Technol.* **2003**, *47* (3), 7−14.

(7) Kouame, Y. A. O.; Haas, C. N. Inactivation of E. Coli by Combined Action of Free Chlorine and Monochloramine. *Water Res.* **1991**, *25* (9), 1027−1032.

(8) Betancourt, W. Q.; Rose, J. B. Drinking Water Treatment Processes for Removal of Cryptosporidium and Giardia. *Vet. Parasitol.* **2004**, *126*, 219−234.

(9) Kruse, P. Review on Water Quality Sensors. *J. Phys. D Appl. Phys.* **2018**, *51*, 203002.

(10) Sharif, O. Towards Identifying Disinfectants and Quantifying Disinfectant Levels in Water, Ph.D. Thesis, McMaster University, 2017.

(11) Hoenich, N. A. Disinfection of the Hospital Water Supply: A Hidden Risk to Dialysis Patients. *Crit. Care* **2009**, *13* (6), 1007.

(12) Van Os, E. A. Comparison of Some Chemical and Non-Chemical Treatments to Disinfect a Recirculating Nutrient Solution. *Acta Hortic.* **2009**, *843*, 229−234.

(13) Holah, J. T. Industrial Monitoring: Hygiene in Food Processing. In *Biofilms—Science and Technology*; Melo, L. F., Bott, T. R., Fletcher, M., Capdeville, B., Eds.; Springer, 1992; pp 645−659.

(14) Palin, A. T. The Determination of Free and Combined Chlorine in Water by the Use of Diethyl-p- Phenylene Diamine. *J.—Am. Water Works Assoc.* **1957**, *49* (7), 873−880.

(15) Pepich, B. V.; Dattilio, T. A.; Fair, P. S.; Munch, D. J.; Gordon, G.; Körtvélyesi, Z. An Improved Colorimetric Method for Chlorine Dioxide and Chlorite Ion in Drinking Water Using Lissamine Green B and Horseradish Peroxidase. *Anal. Chim. Acta* **2007**, *596*, 37−45.

(16) Mcbeath, S. T.; Wilkinson, D. P.; Graham, N. J. D. Analytical Quantification of Aqueous Permanganate: Direct and Indirect Spectrophotometric Determination for Water Treatment Processes. *Chemosphere* **2020**, *251*, 126626.

(17) Baranowska, I.; Bijak, K. Voltammetric Determination of Disinfectants at Multiwalled Carbon Nanotube Modified Glassy Carbon Electrode. *J. Anal. Chem.* **2013**, *68* (10), 891−895.

(18) Kumar, D. R.; Kesavan, S.; Nguyen, T. T.; Hwang, J.; Lamiel, C.; Shim, J. Polydopamine @ Electrochemically Reduced Graphene Oxide-Modified Electrode for Electrochemical Detection of Free-Chlorine. *Sens. Actuators, B* **2017**, *240*, 818−828.

(19) Jovic, M.; Cortés-Salazar, F.; Lesch, A.; Amstutz, V.; Bi, H.; Girault, H. H. Electrochemical Detection of Free Chlorine at Inkjet Printed Silver Electrodes. *J. Electroanal. Chem.* **2015**, *756*, 171−178.

(20) Salazar, P.; Martín, M.; García-García, F. J.; González-Mora, J. L.; González-Elipe, A. R. A Novel and Improved Surfactant-Modified Prussian Blue Electrode for Amperometric Detection of Free Chlorine in Water. *Sens. Actuators, B* **2015**, *213*, 116−123.

(21) Hanrahan, G.; Patil, G.; Wang, J.; Hanrahan, G. Electrochemical Sensors for Environmental Monitoring: Design, Development and Applications. *J. Environ. Monit.* **2004**, *6*, 657−664.

(22) Copeland, A.; Lytle, D. A. Measuring the Oxidation-Reduction Potential of Important Oxidants in Drinking Water. *J. - Am. Water Works Assoc.* **2014**, *106* (1), E10−E20.

(23) Kim, Y. H.; Hensley, R. Effective Control of Chlorination and Dechlorination at Wastewater Treatment Plants Using Redox Potential. *Water Environ. Res.* **1997**, *69* (5), 1008−1014.

(24) Suslow, T. V. *Oxidation-Reduction Potential (ORP) for Water Disinfection Monitoring, Control, and Documentation*; University of California, Agriculture and Natural Resources, 2004; p 8149.

(25) James, C. N.; Copeland, R. C.; Lytle, D. A. Relationships between Oxidation-Reduction Potential, Oxidant, and PH in Drinking Water. *AWWA Water Quality Technology Conference*, 2004; pp 1−13.

(26) Hsu, L. H. H.; Hoque, E.; Kruse, P.; Ravi Selvaganapathy, P. A Carbon Nanotube Based Resettable Sensor for Measuring Free Chlorine in Drinking Water. *Appl. Phys. Lett.* **2015**, *106*, 063102.

(27) Zubiarrain-Laserna, A.; Angizi, S.; Akbar, M. A.; Divigalpitiya, R.; Selvaganapathy, P. R.; Kruse, P. Detection of Free Chlorine in Water Using Graphene-like Carbon Based Chemiresistive Sensors. *RSC Adv.* **2022**, *12*, 2485−2496.

(28) Antony, C. E.; Gaana, K.; Praveen, S. G.; Jayakumar, A.; Yadav, A.; Sivakumar, N. S.; Kamath, N.; Suma, M. N.; Kamble, V. B.; Jaiswal-Nagar, D. Polyvinylpyrrolidone-Stabilized Palladium Nanocrystals as Chemiresistive Sensors for Low-Concentration Hydrogen Gas Detection. *ACS Appl. Nano Mater.* **2021**, *4* (2), 1643−1653.

(29) Zhang, J.; Liu, L.; Yang, Y.; Huang, Q.; Li, D.; Zeng, D. A Review on Two-Dimensional Materials for Chemiresistive- And FET-Type Gas Sensors. *Phys. Chem. Chem. Phys.* **2021**, *23* (29), 15420−15439.

(30) Patel, V.; Saha, D.; Kruse, P.; Selvaganapathy, P. R. Reagent-Free Hydrogen Peroxide Sensing Using Carbon Nanotube Chemiresistors with Electropolymerized Crystal Violet. *ACS Appl. Nano Mater.* **2022**, *5*, 3957−3966.

(31) Mondal, R. K.; Dubey, K. A.; Kumar, J.; Jagannath; Bhardwaj, Y. K.; Melo, J. S.; Varshney, L. Carbon Nanotube Functionalization and Radiation Induced Enhancements in the Sensitivity of Standalone Chemiresistors for Sensing Volatile Organic Compounds. *ACS Appl. Nano Mater.* **2018**, *1* (10), 5470−5482.

(32) Norizan, M. N.; Moklis, M. H.; Ngah Demon, S. Z.; Halim, N. A.; Samsuri, A.; Mohamad, I. S.; Knight, V. F.; Abdullah, N. Carbon Nanotubes: Functionalisation and Their Application in Chemical Sensors. *RSC Adv.* **2020**, *10* (71), 43704−43732.

(33) Patel, V.; Akbar, M. A.; Kruse, P.; Selvaganapathy, P. R. A Reagent-Free Phosphate Chemiresistive Sensor Using Carbon Nanotubes Functionalized with Crystal Violet. *Analyst* **2023**, *148*, 3551−3558.

(34) Hoque, E.; Chowdhury, T.; Kruse, P. Chemical in Situ Modulation of Doping Interactions between Oligoanilines and Nanocarbon Films. *Surf. Sci.* **2018**, *676*, 61−70.

(35) Klinke, C.; Chen, J.; Afzali, A.; Avouris, P. Charge Transfer Induced Polarity Switching in Carbon Nanotube Transistors. *Nano Lett.* **2005**, *5* (3), 555−558.

(36) Goniszewski, S.; Adabi, M.; Shaforost, O.; Hanham, S. M.; Hao, L.; Klein, N. Correlation of P-Doping in CVD Graphene with Substrate Surface Charges. *Sci. Rep.* **2016**, *6*, 22858.

(37) Moonoosawmy, K. R.; Kruse, P. Cause and Consequence of Carbon Nanotube Doping in Water and Aqueous Media. *J. Am. Chem. Soc.* **2010**, *132* (5), 1572−1577.

(38) Mohtasebi, A.; Broomfield, A. D.; Chowdhury, T.; Selvaganapathy, P. R.; Kruse, P. Reagent-Free Quantification of Aqueous Free Chlorine via Electrical Readout of Colorimetrically Functionalized Pencil Lines. *ACS Appl. Mater. Interfaces* **2017**, *9* (24), 20748−20761.

(39) Hoque, E.; Hsu, L. H. H.; Aryasomayajula, A.; Selvaganapathy, P. R.; Kruse, P. Pencil-Drawn Chemiresistive Sensor for Free Chlorine in Water. *IEEE Sens. Lett.* **2017**, *1* (4), 4500504.

(40) Wang, W.; MacDiarmid, A. G. New Synthesis of Phenyl/Phenyl End-Capped Tetraaniline in the Leucoemeraldine and Emeraldine Oxidation States. *Synth. Met.* **2002**, *129* (2), 199−205.

(41) Shao, Z.; Rannou, P.; Sadki, S.; Fey, N.; Lindsay, D. M.; Faul, C. F. J. Delineating Poly(Aniline) Redox Chemistry by Using Tailored Oligo(Aryleneamine)s: Towards Oligo(Aniline)-Based Organic Semiconductors with Tunable Optoelectronic Properties. *Chem.—Eur. J.* **2011**, *17* (44), 12512−12521.

(42) Sawyer, D. T.; Sobkowiak, A.; Roberts, J. L. *Electrochemistry for Chemists*, 2nd ed.; Wiley, 1995.

(43) Dalmieda, J.; Zubiarrain-Laserna, A.; Ganepola, D.; Selvaganapathy, P. R.; Kruse, P. Chemiresistive Detection of Silver Ions in Aqueous Media. *Sens. Actuators, B* **2021**, *328*, 129023.

(44) Dalmieda, J.; Zubiarrain-Laserna, A.; Saha, D.; Selvaganapathy, P. R.; Kruse, P. Impact of Surface Adsorption on Metal-Ligand Binding of Phenanthrolines. *J. Phys. Chem. C* **2021**, *125* (38), 21112−21123.

(45) Pang, Z.; Chong, J.; Zhou, G.; de Lima Morais, D. A.; Chang, L.; Barrette, M.; Gauthier, C.; Jacques, P. É.; Li, S.; Xia, J. MetaboAnalyst 5.0: Narrowing the Gap between Raw Spectra and Functional Insights. *Nucleic Acids Res.* **2021**, *49* (W1), W388−W396.

(46) Zubiarrain-Laserna, A.; Kruse, P. Review—Graphene-Based Water Quality Sensors. *J. Electrochem. Soc.* **2020**, *167* (3), 037539.

(47) Angizi, S.; Yu, E. Y. C.; Dalmieda, J.; Saha, D.; Selvaganapathy, P. R.; Kruse, P. Defect Engineering of Graphene to Modulate PH Response of Graphene Devices. *Langmuir* **2021**, *37* (41), 12163−12178.

(48) Angizi, S.; Huang, X.; Hong, L.; Akbar, M. A.; Selvaganapathy, P. R.; Kruse, P. Defect Density-Dependent PH Response of Graphene Derivatives: Towards the Development of PH-Sensitive Graphene Oxide Devices. *Nanomaterials* **2022**, *12*, 1801.

(49) Deborde, M.; von Gunten, U. Reactions of Chlorine with Inorganic and Organic Compounds during Water Treatment-Kinetics and Mechanisms: A Critical Review. *Water Res.* **2008**, *42* (1–2), 13–51.

(50) Choi, H.; Chatterjee, P.; Lichtfouse, E.; Martel, J. A.; Hwang, M.; Jinadatha, C.; Sharma, V. K. Classical and Alternative Disinfection Strategies to Control the COVID-19 Virus in Healthcare Facilities: A Review. *Environ. Chem. Lett.* **2021**, *19* (3), 1945–1951.

(51) Spencer, M. *Water Quality Instrumentation*, 1st; Water Environment Federation: Alexandria, 2022.

(52) Moonoosawmy, K. R.; Kruse, P. To Dope or Not to Dope: The Effect of Sonicating Single-Wall Carbon Nanotubes in Common Laboratory Solvents on Their Electronic Structure. *J. Am. Chem. Soc.* **2008**, *130* (40), 13417–13424.

(53) Qian, X.; Gargalo, C. L.; Gernaey, K. V.; Stadler, B. Distinguishing Commercial Beers Using a Solution-Based Sensor Array Derived from Nanoscale Polydiacetylene Vesicles. *ACS Appl. Nano Mater.* **2020**, *3* (4), 3439–3448.

(54) Sharifi, H.; Tashkhourian, J.; Geramizadeh, B.; Ghohestani, E.; Zangouri, V.; Asadian, F.; Hemmateenejad, B. Metallic Nanocluster-Based Sniffing Device for Identification of Malignancy in Gastric Cancer Tissues. *ACS Appl. Nano Mater.* **2023**, *6* (7), 5578–5590.

Supporting Information for

Identification and Quantification of Aqueous Disinfectants Using an Array of Carbon Nanotube-Based Chemiresistors

Md Ali Akbar[1], Omar Sharif[1], P. Ravi Selvaganapathy[2], Peter Kruse[1,*]

[1]Department of Chemistry and Chemical Biology, McMaster University, Hamilton, ON L8S 4M1, Canada

[2]Department of Mechanical Engineering, McMaster University, Hamilton, ON L8S 4K1, Canada

[3]School of Biomedical Engineering, McMaster University, Hamilton, ON L8S 4K1, Canada

* E-mail: pkruse@mcmaster.ca

Synthesis and Characterization

Phenyl Capped Aniline Tetramer (PCAT)

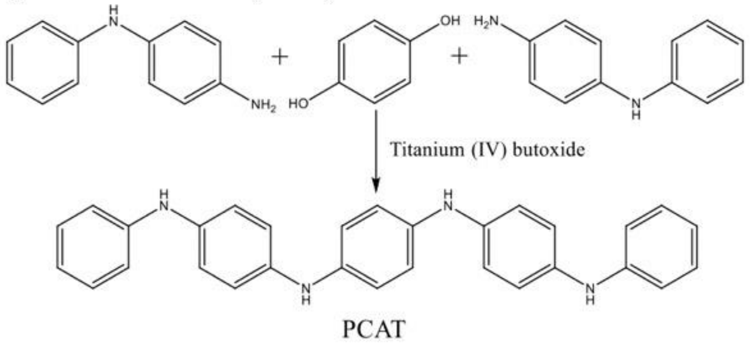

Figure S1. Synthesis of the phenyl-capped aniline tetramer in its leucoemeraldine state.

N^1,$N^{1'}$-(1,4-phenylene)-bis(N^4-phenyl benzene-1,4-diamine) was synthesized by a coupling reaction of N-Phenyl-p-phenylenediamine and hydroquinone in a controlled argon atmosphere in presence of titanium (IV) butoxide as a coupling agent. The synthesis was followed as reported by MacDiarmid [Wang, W.; MacDiarmid, A. G. New Synthesis of Phenyl/phenyl End-Capped Tetraaniline in the Leucoemeraldine and Emeraldine Oxidation States. *Synth. Met.* **2002**, *129*, 199–205] with slight modification. Toluene was used instead of benzene for this synthesis, as benzene is a designated substance and has regulated use. N-Phenyl-p-phenylenediamine, hydroquinone, titanium(IV) butoxide, anhydrous toluene and DMF all were purchased from Sigma-Aldrich. A 250 mL round bottom flask was equipped with a Teflon stirring bar and water-cooled reflux condenser capped with a rubber septum. 9.2 g (0.050 moles) solid N-Phenyl-1,4-phenylenediamine was added to the flask. The reaction flask was purged with argon and kept under a positive pressure using argon balloons. The flask was heated to 70 °C in an oil bath on a magnetic stirring plate. 100ml anhydrous toluene was added with a syringe through the septum, a black solution was formed. Another 100 mL round bottom flask was equipped with Teflon stirring bar and rubber septum. 1.38 g (0.0125 moles) hydroquinone was added to the flask and the flask was purged with argon. The flask environment was protected it with argon balloons connected through a rubber septum. The flask was placed in a preheated 70 °C oil bath on a magnetic stirring plate. 40 ml anhydrous toluene was added through a syringe to the flask. Hydroquinone doesn't dissolve in the toluene immediately. 25.6 ml colorless liquid titanium (iv) n-butoxide was added to the flask using a syringe, an orange solid formed in the solution. Hydroquinone and titanium (iv) n-butoxide were stirred for 30 minutes and an orange-red solution was formed. The orange-red solution was then added to the black solution of N-Phenyl-p-phenylenediamine using a cannula transfer. The empty bottle of the orange-red solution was washed with 10 ml anhydrous toluene and added to the final reaction mixture. The reaction system was then stirred for 16 hours at 70 °C under in an argon atmosphere.

A crystalline precipitate formed during this time. The reaction flask was then cooled to room temperature under argon. White needle-shaped microscopic crystals were collected on a fritted Buchner funnel by vacuum filtration using an air pump. The precipitate was washed with laboratory grade toluene until the dark-brown red filtrate become colorless. Around 650 ml toluene was used. After washing the precipitate was kept under suction for 10 minutes. The precipitate was then dissolved in 120 ml of DMF and stirred for 10 min, a dark blue solution formed. The solution was vacuum filtrated on a Buchner funnel (~4.25 cm) with #1 Whatman filter paper using an air pump. The filtrate was added to 1200 ml deionized water in a 2000 ml beaker drop by drop during 2 hours. The solution was stirred for 15 hours. A greenish precipitate formed. The precipitate was collected on a Buchner funnel (~9 cm) with a #1 Whatman filter paper by vacuum filtration. The precipitate was washed with 100 mL deionized water. After washing, the solution remains under suction for 10 minutes. The precipitate was then transferred on the filter paper to a desiccator and kept under vacuum for 48 hours at room temperature. The dry precipitate was pulverized by mortar and pestle into a fine powder and was further dried under vacuum for another 48 hours. As prepared aniline tetramer was found in its leucoemeraldine base form.

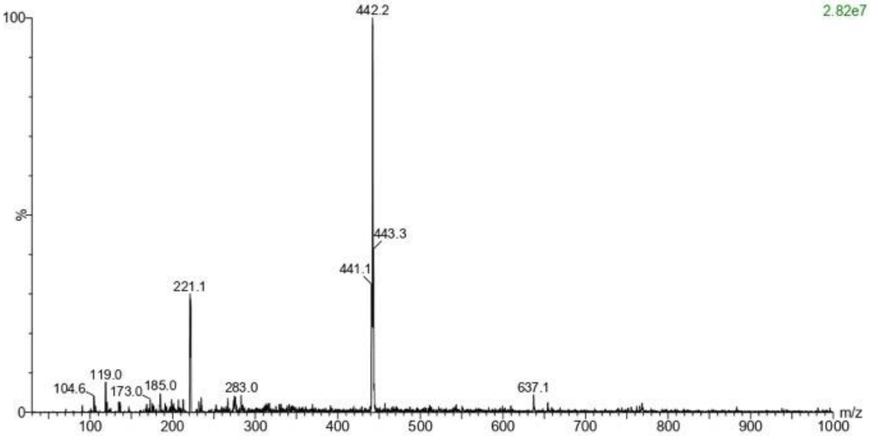

Figure S2. Mass spectrum of PCAT leucoemeraldine base.

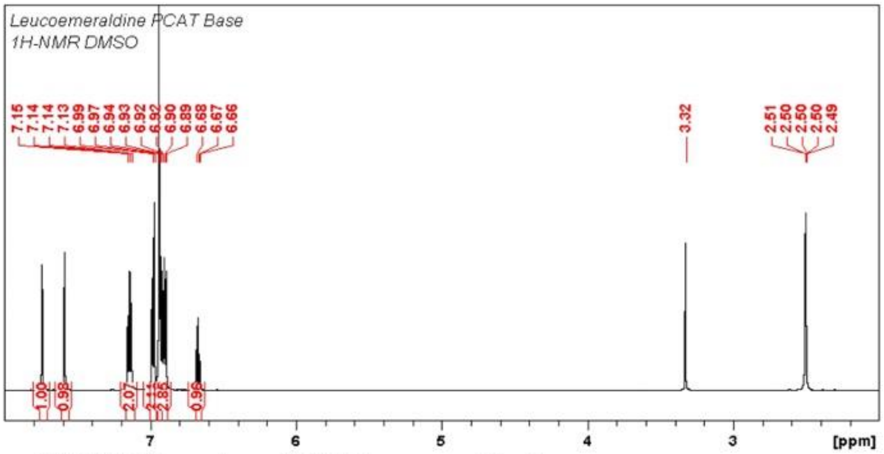

Figure S3. ^{1}H NMR spectrum of PCAT leucoemeraldine base.

The leucoemeraldine base form was characterized using mass spectrometry and nuclear magnetic resonance spectroscopy. The calculated mass is 442.2157 and the mass found was 442.2. The mass spectrum and NMR spectrum are shown above. NMR spectrum for leucoemeraldine base found ^{1}H NMR (600MHz, DMSO)δ: 7.74(2H^b,s), 7.59(2H^a,s), 7.14(4H^d,t), 6.97(4H^e,d), 6.94(12H^{f,g},m), 6.67(2H^c,t)ppm.

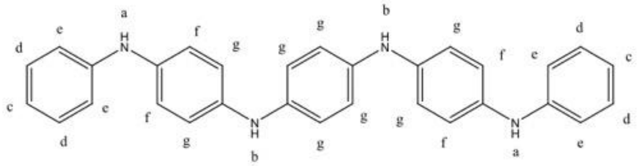

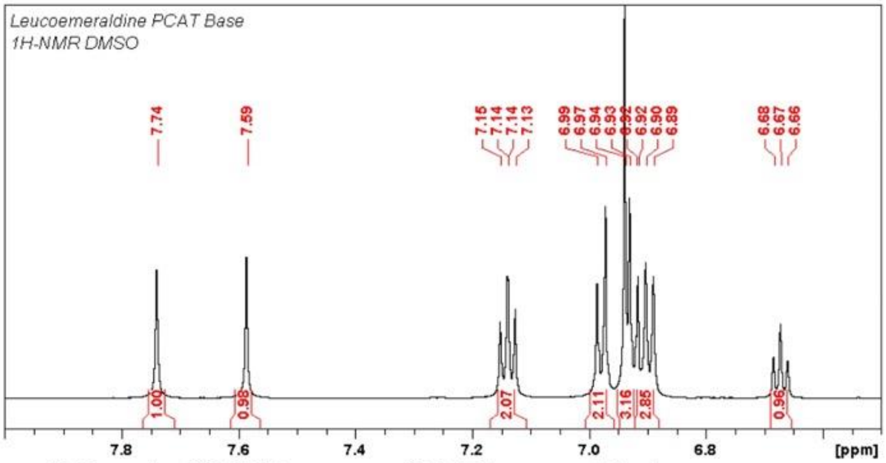

Figure S4. Zoom-in of ^{1}H NMR spectrum of PCAT leucoemeraldine base.

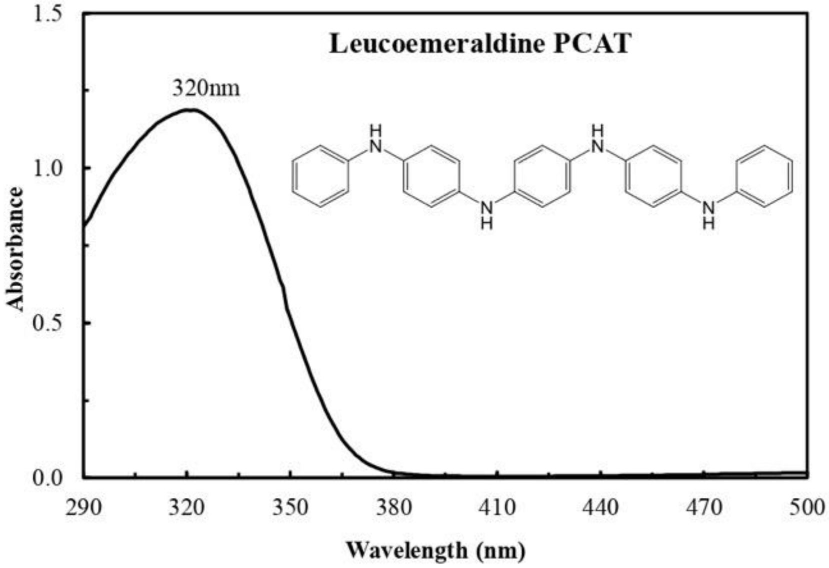

Figure S5. UV-Vis spectrum of leucoemeraldine base of PCAT in acetonitrile.

The observed spectrum of reduced PCAT is shown in Fig. S5. λ_{max} for PCAT is found at 320 nm and the calculated HOMO-LUMO gap for the electronic transition is 3.87 eV.

N^1,N$^{1'}$-(anthracene-9,10-diyl)-bis (N^4-phenyl benzene-1,4-diamine) (APCAT)

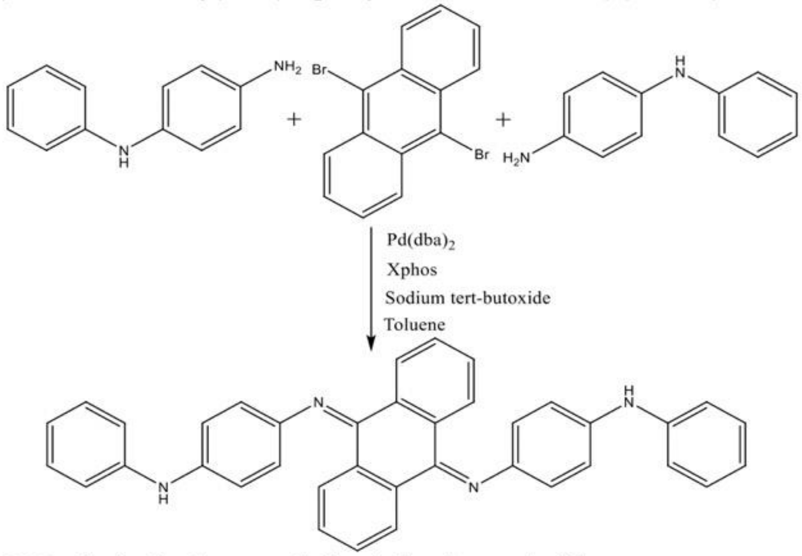

Figure S6. Synthesis of anthracene substituted phenyl capped aniline tetramer.

N^1,N$^{1'}$-(anthracene-9,10-diyl)-bis (N^4-phenyl benzene-1,4-diamine) (APCAT) was synthesized by Buchwald-Hartwig Amination of N-Phenyl-p-phenylenediamine and 9,10-Dibromoanthracene. A 250 mL round bottom flask with a magnetic stirrer was loaded with 9,10-dibromoanthracene (0.877 g, 2.61 mmol, 1 equivalent), N-Phenyl-p-phenylenediamine (1.05 g, 5.74 mmol, 2.2 equivalent), Pd(dba)2 (0.09 g, 0.16 mmol, 6 mol%), Xphos (0.12 g, 0.23 mmol, 9 mol%) and sodium tert-butoxide (0.75 g, 7.83 mmol, 3 equivalent). The round bottom flask was fitted with a water-cooled reflux condenser and sealed with a rubber septum. The round bottom flask was then purged with argon for 15 minutes and 40 mL anhydrous toluene was added to the flask using a syringe. The flask was then placed in a 100 °C preheated oil bath. The reaction flask was protected by argon balloons. The progress of the reaction was monitored by doing TLC. The reaction was run for 36 hours until the absence of 9,10-dibromoanthracene was seen in TLC. The reaction was cooled to room temperature and 50ml ethanol and 200ml water were added to the reaction mixture and stirred for 10 hours. The product was separated out as a dark orange precipitate. After the filtration, the product was washed 3 times with a 20% ethanol in water solution. The precipitate was then dried in a desiccator under vacuum for 48 hours.

The APCAT product was characterized by mass spectroscopy and NMR spectroscopy. Chemical Formula: $C_{38}H_{30}N_4$, Exact Mass = 542.25, Molecular Weight = 542.69. The mass spectrum shows the $M+H^+$ peak for 541 which indicates that APCAT was synthesized in its half-oxidized state.

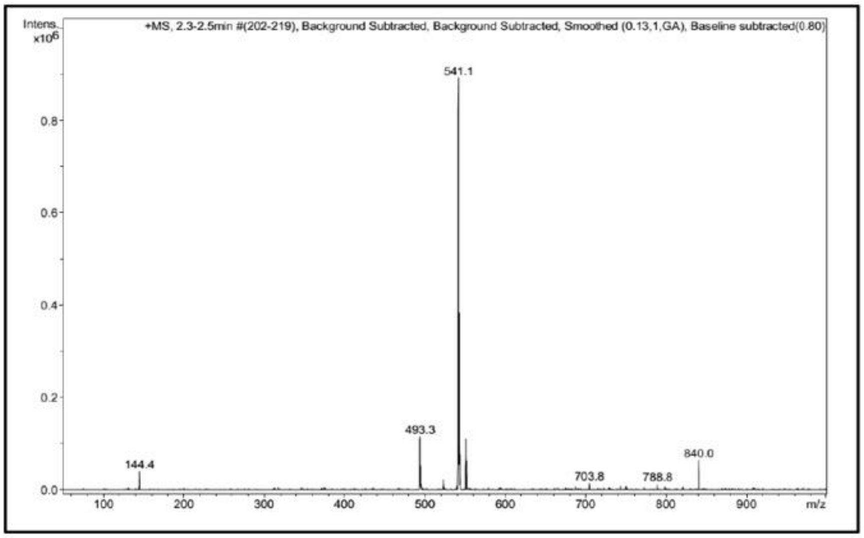

Figure S7. Mass spectrum of synthesized APCAT.

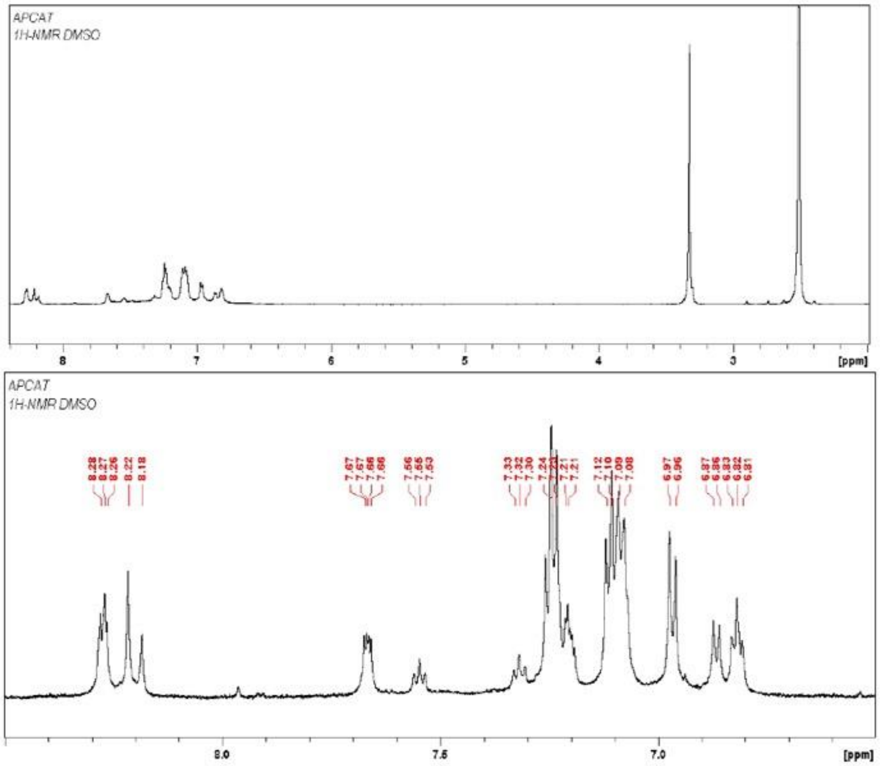

Figure S8. ^{1}H NMR spectrum of synthesized APACT.

The APACT NMR spectrum indicates that the synthesized product is indeed a mixture. From the PCAT emeraldine base, we have seen that it consists of two isomers. It is most likely that the APCAT is in its emeraldine base form and a mixture of isomers. The emeraldine base was tried to reduce with ascorbic acid, formic acid, and phenyl hydrazine but without success. This might be due to the easy air oxidation of APACT leucoemeraldine base to emeraldine base.

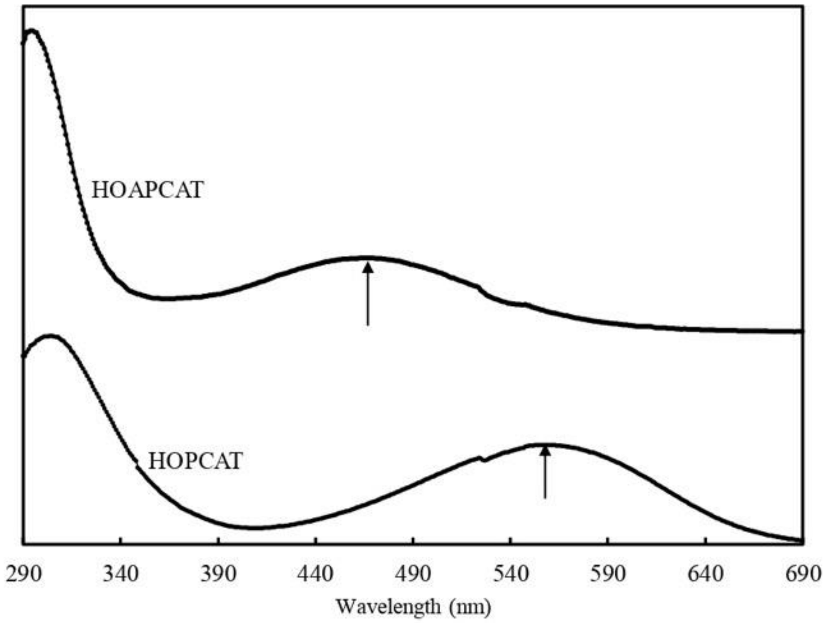

Figure S9. UV spectra of PCAT and APCAT emeraldine bases.

In comparison to the PCAT emeraldine base, APCAT emeraldine base also shows a similar peak for quinoid formation. The anthraquinoid peak is seen at 470 nm for the APCAT molecule. Overall, mass spectrometry, NMR spectroscopy, and UV-Vis spectroscopy strongly indicate that the synthesized product is the APCAT emeraldine base.

N, N-Diphenyl-p-phenylenediamine (DPPD)

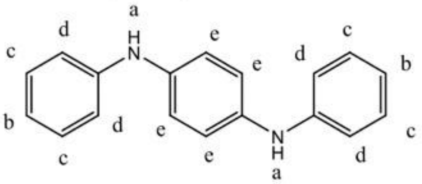

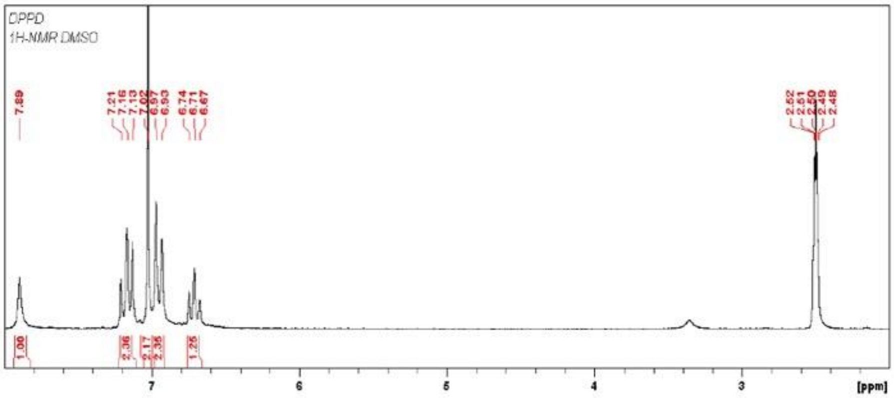

Figure S10. ^{1}H NMR spectrum of DPPD. (600 MHz, DMSO) δ: 7.89(2H^a,s), 7.21(4H^c,t), 7.02(4H^d,d), 6.97(4H^e,d), 6.71(2H^b,t)ppm.

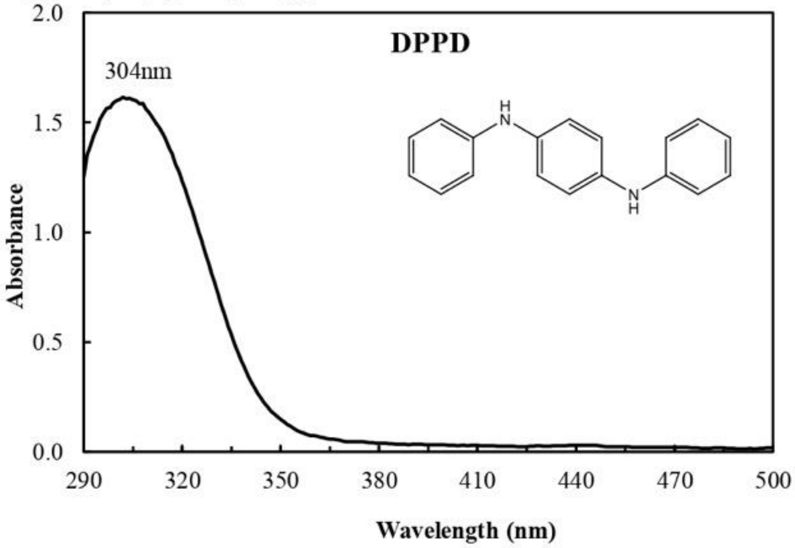

Figure S11. UV-Vis spectrum of DPPD in acetonitrile.

The observed spectrum of DPPD is shown in Figure S-11. The λ_{max} is found at 304 nm for DPPD. The calculated HOMO-LUMO gap is 4.07 eV from the electron transition at 304 nm.

N,N'-Diphenyl-4,4'-biphenylenediamine (DPB)

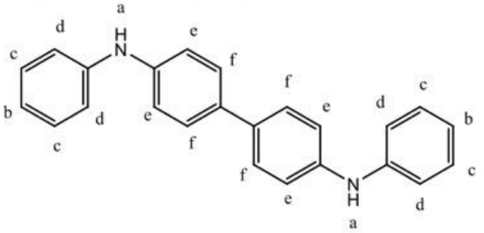

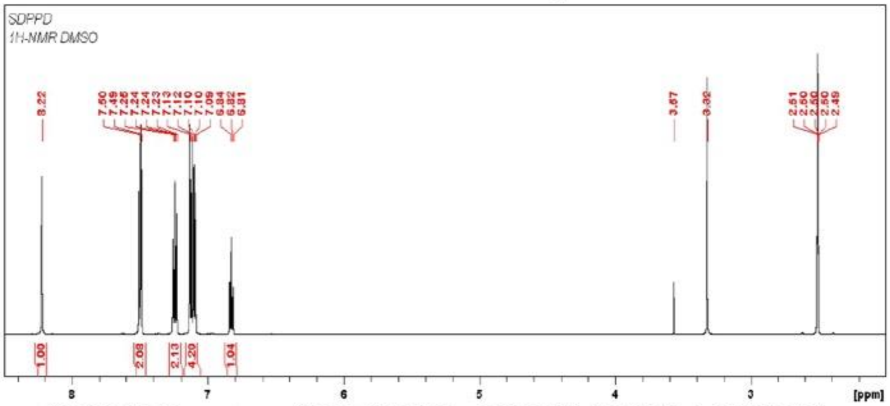

Figure S12. ^{1}H NMR spectrum of DPB (600 MHz, DMSO) δ: 8.22(2H^a,s), 7.50(4H^f,d), 7.24(4H^c,t), 7.13 (4H^e,d), 6.10(4H^d,d), 6.82(2H^b,t) ppm.

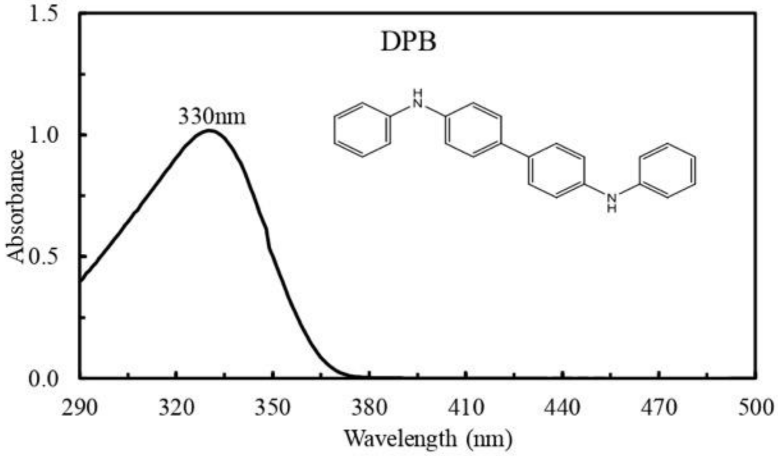

Figure S13. UV-Vis spectrum of DPB in acetonitrile.

The observed UV-Vis spectrum of DPB in acetonitrile is shown in Fig. S13. One extra conjugation at the middle ring of DPPD results in a red shift and the λ_{max} is found at 330 nm. The calculated HOMO-LUMO gap from the electron transition is 3.75 eV.

Crystal Violet

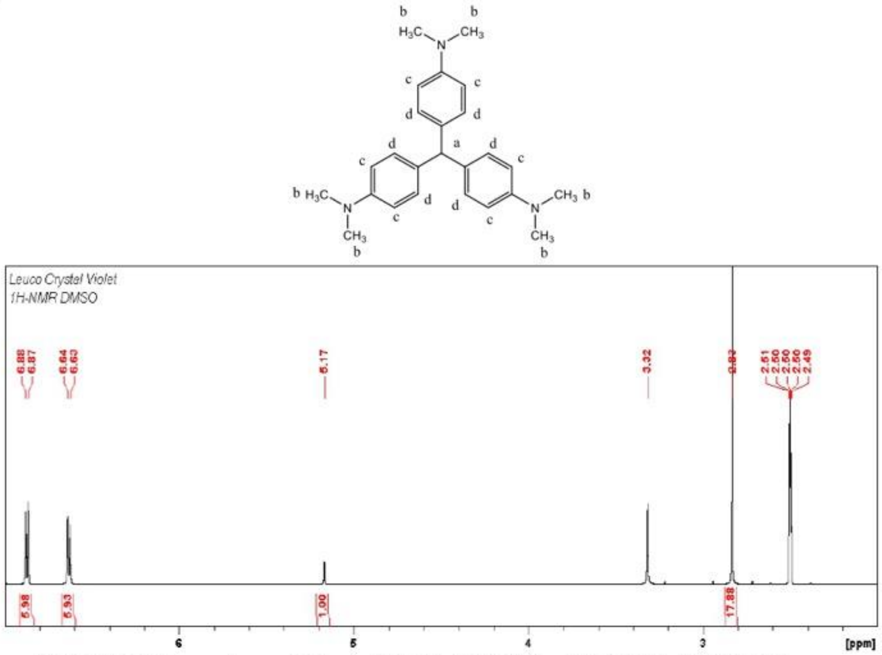

Figure S14. ^{1}H NMR spectrum of Crystal Violet (600 MHz, DMSO) δ: 6.88(6H^d,d), 6.64(6H^c,d), 5.17(1H^a,s), 2.83(18H^b,s)ppm.

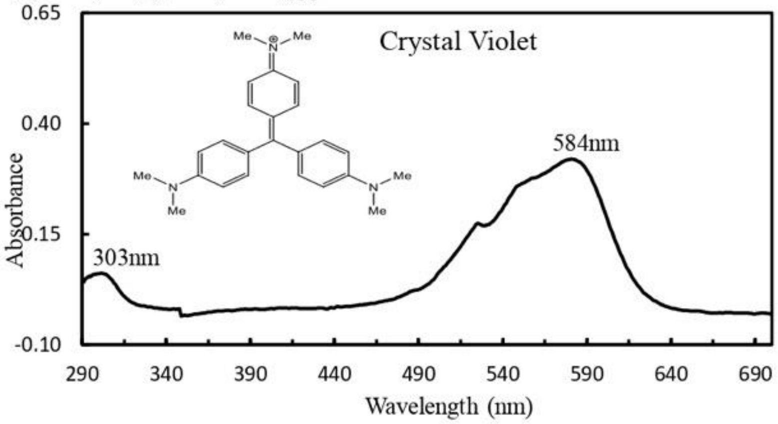

Figure S15. UV-Vis spectrum of crystal violet in acetonitrile.

The observed crystal violet spectrum is shown in Fig. S15. The characteristic absorption of visible light at 586 nm for crystal violet is seen with one shoulder at 550 nm. A minor absorption peak is at 303 nm. The λ_{max} at 584 nm has a calculated HOMO-LUMO gap of 2.12 eV.

Electrochemical Characterization

The electrochemical properties of redox-active molecules are discussed here based on the cyclic voltammogram and differential pulse voltammogram. All the voltammograms are reported relative to internal ferrocene standard. The CV and DPV show a ferrocene redox peak at 0.0975 V relative to the Ag/AgNO$_3$ reference electrode. All the CV and DPV measurements were done in 0.1 M tertbutyl ammonium perchlorate (TBAP) supporting electrolyte and 0.02 mM diphenyl phosphate as a proton source in acetonitrile solvent. For cyclic voltammetry, a scan rate of 0.1 V/s was used. For DPV an E$_{pulse}$ of 0.1 V and a scan rate of 0.01 V/s was applied.

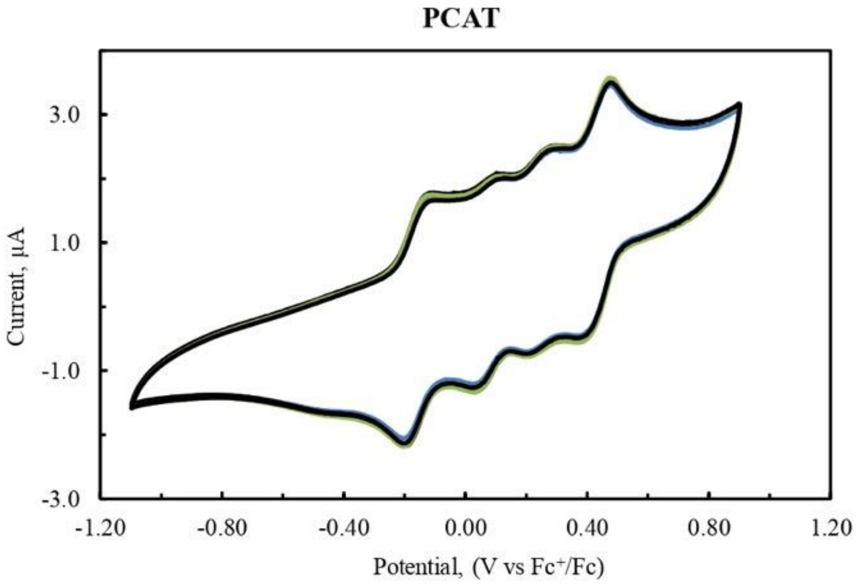

Figure S16. Cyclic voltammogram of PCAT in acetonitrile.

From the cyclic voltammetry data for PCAT, four induvial peaks are seen, and the oxidation-reduction process is reversible. The oxidation of PCAT is a four-electron process and each peak can be associated with an individual one electron process from leucoemeraldine base oxidizing to the pernigraniline base. The voltammogram found is consistent with the literature and can be explained by four individual one electron processes.[Shao, Z.; Rannou, P.; Sadki, S.; Fey, N.; Lindsay, D. M.; Faul, C. F. J. Delineating Poly(Aniline) Redox Chemistry by Using Tailored Oligo(Aryleneamine)s: Towards Oligo(Aniline)-Based Organic Semiconductors with Tunable Optoelectronic Properties. *Chem. Europ. J.* **2011**, *17*, 12512–12521.] The redox mechanism in Fig. S17 shows the oligoaniline oxidation from the amine to imine.

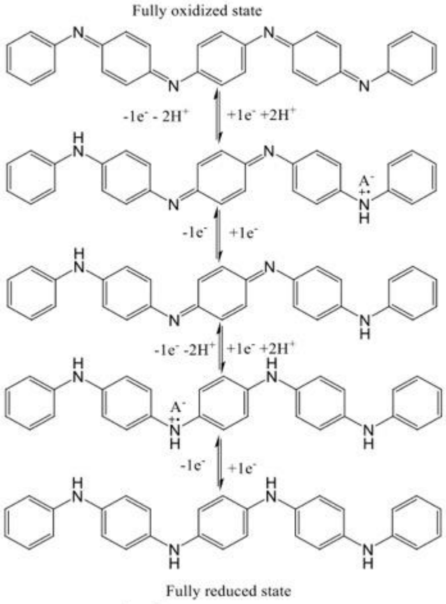

Figure S17. PCAT redox process mechanism.

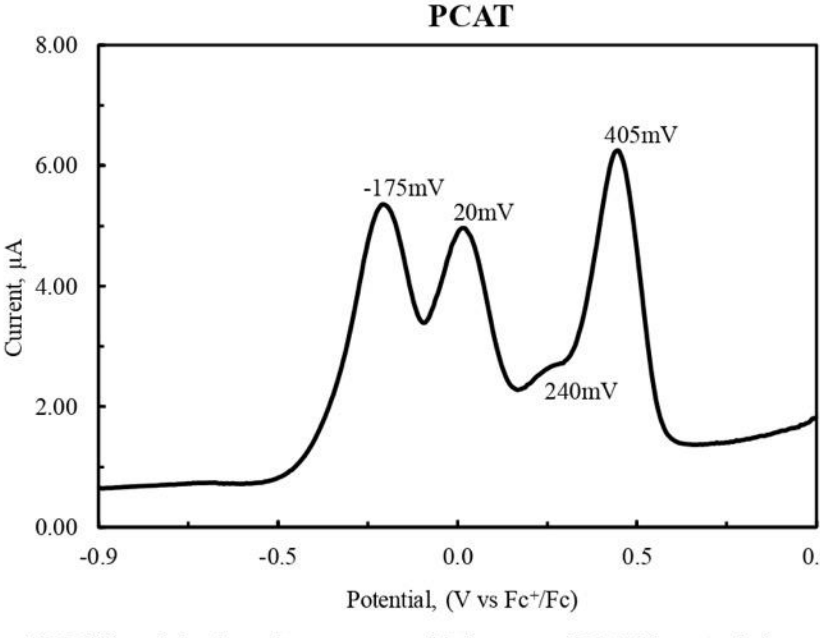

Figure S18. Differential pulse voltammogram oxidation scan of PCAT in acetonitrile.

The differential pulse voltammogram of PCAT shows four peaks in the oxidation scan. Four oxidation peaks are found to be at -175 mV, 20 mV, 240 mV, and 405 mV. Each individual peak can be assigned to a one electron process from PCAT being gradually oxidized from leucoemeraldine base to pernigraniline base.

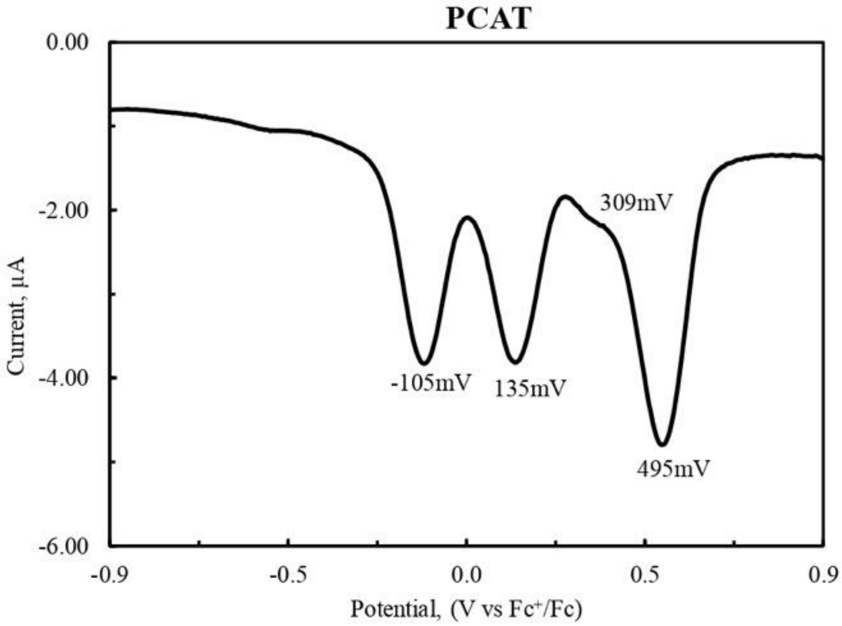

Figure S19. Differential pulse voltammogram reduction scan of PCAT in acetonitrile

The reduction scan of PCAT shows four reduction peaks at 495 mV, 420 mV, 220 mV and -9 mV. The oxidation reduction peaks show a 100 mV peak difference which is due to the E_{pulse} of 100 mV. The voltammogram shows that as the reducing voltage is applied to the PCAT in its pernigraniline base, it gets reduced to the leucoemeraldine base. The four peaks can be associated with four one electron processes during PCAT reduction.

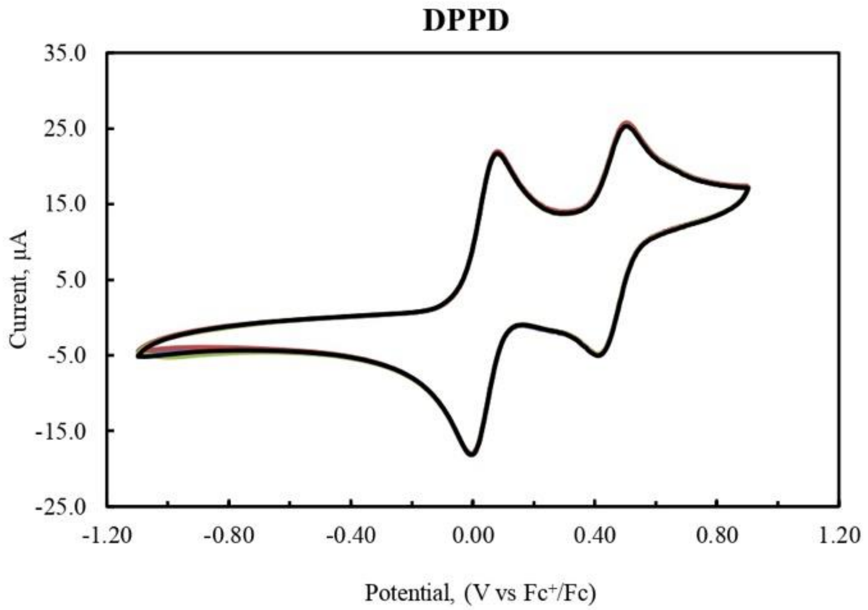

Figure S20. Cyclic voltammogram of DPPD in acetonitrile.

The reversible oxidation and reduction of DPPD is a two-electron process and the cyclic voltammogram shows two reversible peaks. The peaks can be associated with the DPPD being reversibly oxidized from reduced state amine to oxidized state imine. The proposed mechanism of the DPPD redox process is given in Fig. S21. It shows that reduced DPPD first converts into the intermediate semiquinoid form which is then converted into the imine base. Each process is a single electron process thus we can see two individual peaks for DPPD.

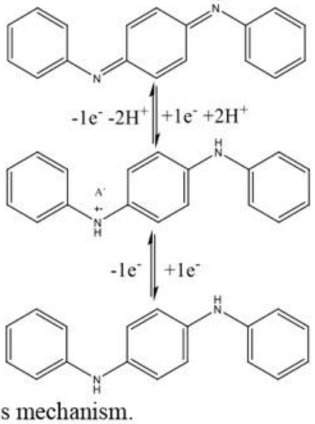

Figure S21. DPPD redox process mechanism.

The oxidation scan of DPPD shows two oxidation peaks at 0 mV and 415 mV. The peak difference in Fig. S22 suggests a highly stable semiquinoid intermediate and the full oxidation occurs at a higher potential similar to PCAT oxidation.

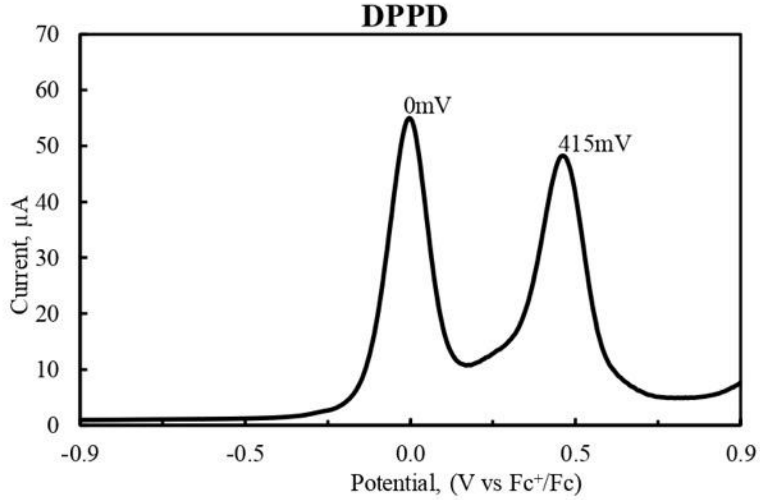

Figure S22. Differential pulse voltammogram oxidation scan of DPPD in acetonitrile.

The DPPD reduction scan shows two reduction peaks at 85 mV and 510 mV.

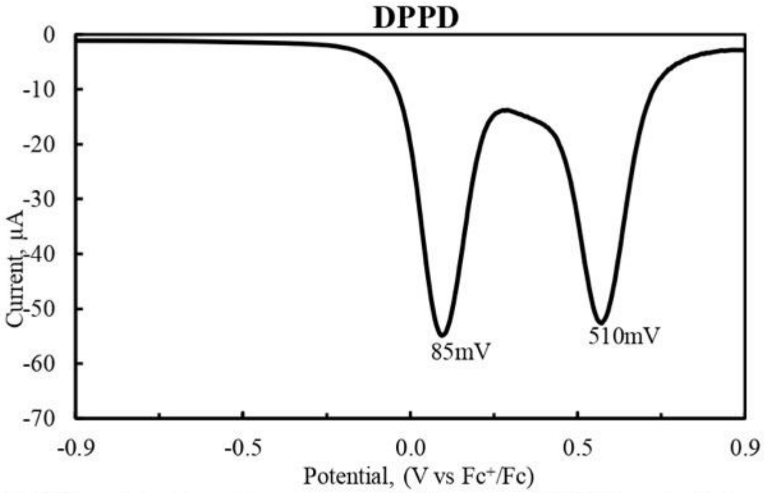

Figure S23. Differential pulse voltammogram reduction scan of DPPD in acetonitrile.

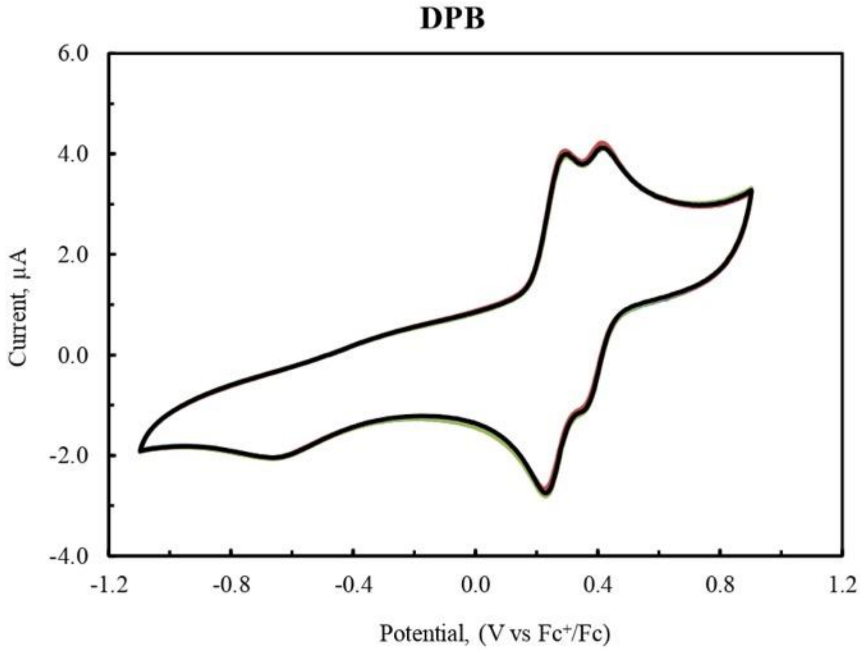

Figure S24. Cyclic voltammogram of DPB in acetonitrile.

The DPB molecule is similar to DPPD, but with two benzene rings in the middle. Adding one extra benzene ring should decrease the HOMO-LUMO gap of the molecule and it was expected to be easier to oxidize. Even though the full oxidation potential of DPB is lower than that of DPPD, the first redox couple of DPB is higher than DPPD. This might be due to the more stable structure of a conjugated molecule which increases the potential of the first redox couple. For DPB two reversible oxidation-reduction peaks are seen around 0.3V and a broad peak is seen at -0.6V which diminishes in the differential pulse voltammogram. The reduction peak at -0.6V might come from the dissolved oxygen. The proposed redox mechanism of DPB is given in Fig. S25.

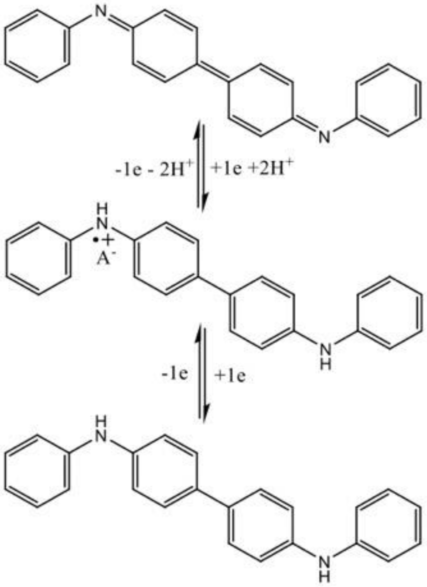

Figure S25. DPB redox process mechanism.

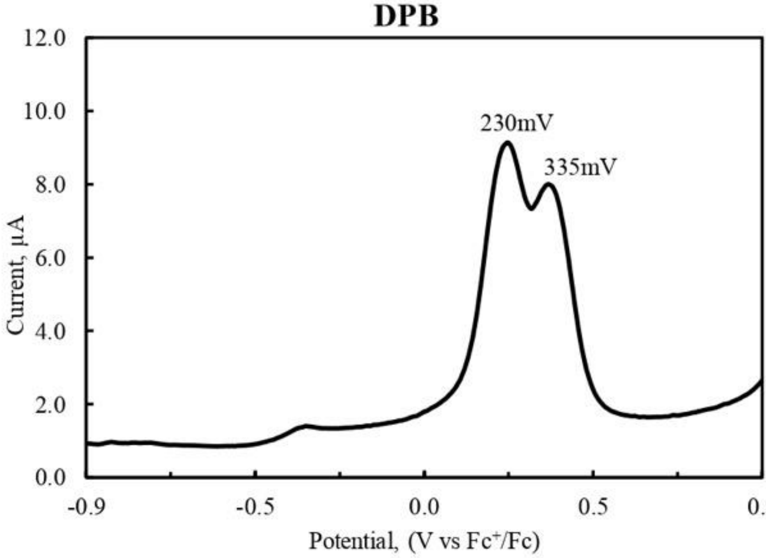

Figure S26. Differential pulse voltammogram oxidation scan of DPB in acetonitrile.
From the differential pulse voltammogram of DPB, two oxidation peaks are seen at 230 mV and 335 mV. The two peaks are associated with the two-electron process oxidation of DPB.

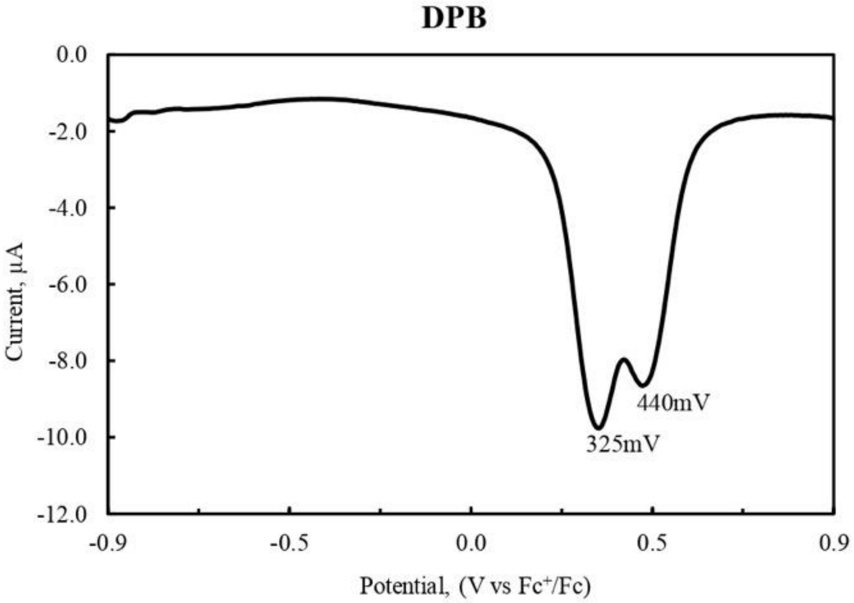

Figure S27. Differential pulse voltammogram reduction scan of DPB in acetonitrile.

The DPB reduction scan voltammogram shows two peaks at 440mV and 325mV. The two peaks represent the two electron process reduction of DPB from its oxidized state to its reduced state.

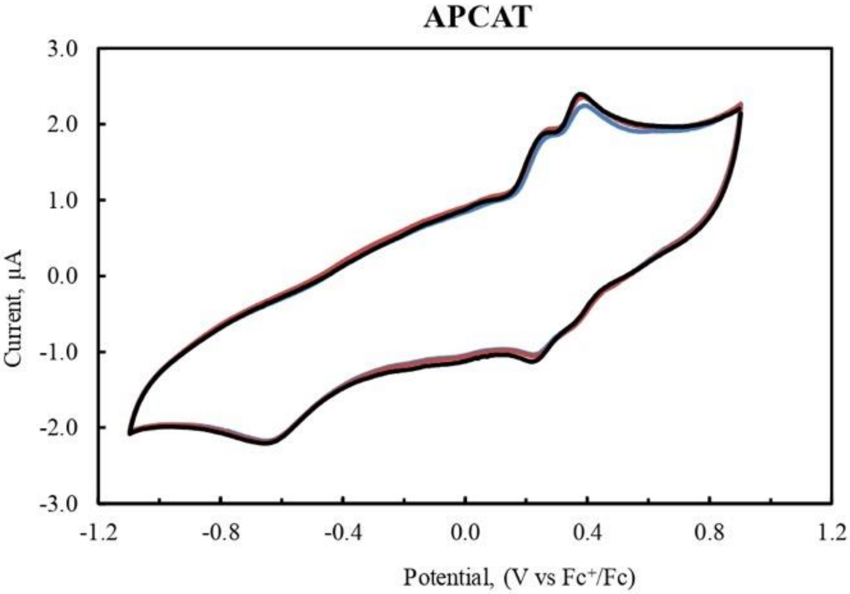

Figure S28. Cyclic voltammetry of APCAT in acetonitrile.

The APCAT cyclic voltammogram is shown in Fig. S28. The APCAT CV data alone doesn't give the complete information about the redox properties of the molecule. Taking into consideration DPV data, we can get a more complete picture of the redox properties of APCAT. The APCAT molecule shows similar redox properties to PCAT. Its electron transfer process is expected to be similar to PCAT because of their same structural configuration. From the CV data, we can clearly see that APCAT shows two redox couple at 0.3 V and one broader peak at around -0.6 V. The voltammetry resolution is not very good due to the starting compound being already half oxidized and there might be some other impurities present. Overall, the DPV gives us better information to understand the redox properties of APCAT.

The DPV oxidation scan of APCAT shows four oxidation peaks at -575 mV, -215 mV, 335 mV, and 435 mV. Four peaks can be associated with the four-electron process oxidation from leucoemeraldine to the pernigraniline base. The first two oxidation peaks are much smaller compared to the second pair of oxidation peaks. We started from the half-oxidized molecule which is emeraldine base, so the abundance and peak height are expected to be higher for a molecule being oxidized from the emeraldine to the pernigraniline state.

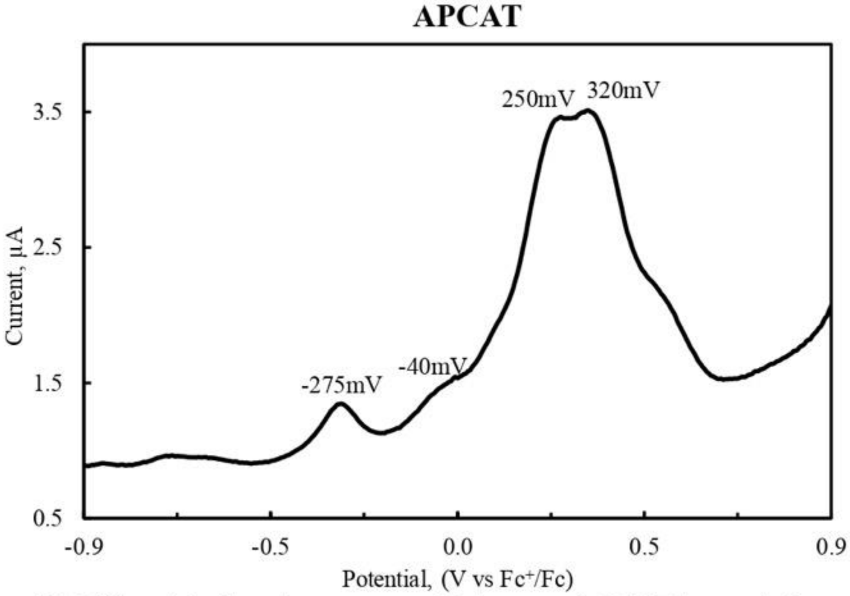

Figure S29. Differential pulse voltammogram oxidation scan of APCAT in acetonitrile.

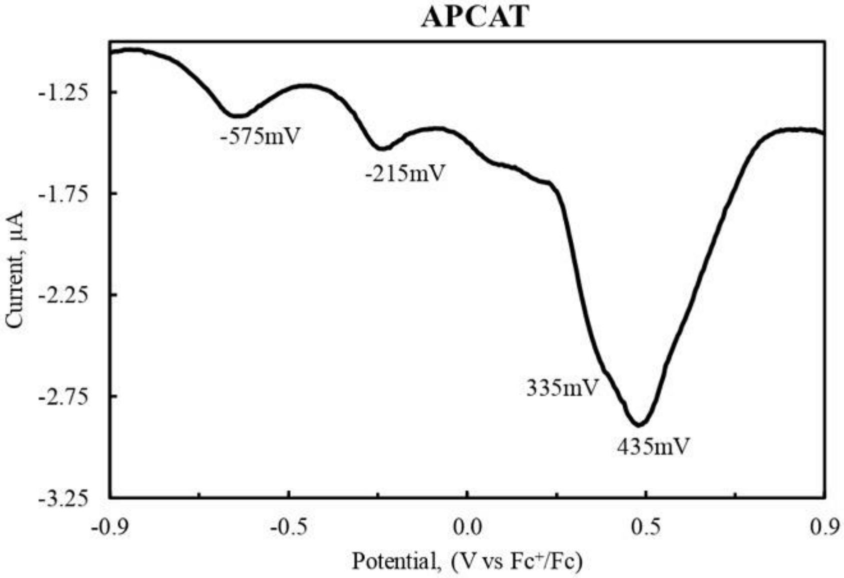

Figure S30. Differential pulse voltammogram reduction scan of APCAT in acetonitrile.

The APCAT DPV reduction scan voltammogram shows four reduction peaks at 530 mV, 440 mV, -150 mV and -480 mV. The voltammogram represents the molecule being reduced from the pernigraniline base to the emeraldine base and then subsequently getting reduced to the leucoemeraldine base.

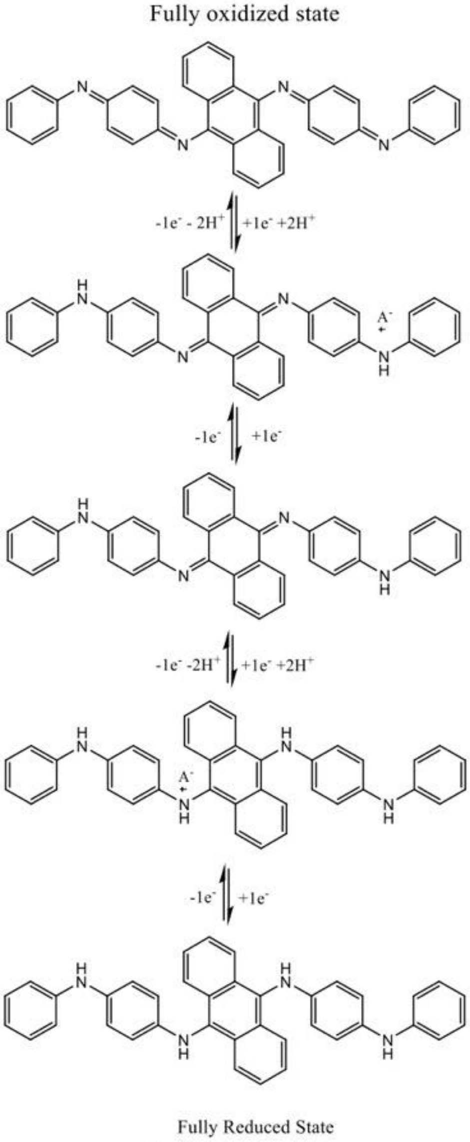

Figure S31. APCAT redox process mechanism.

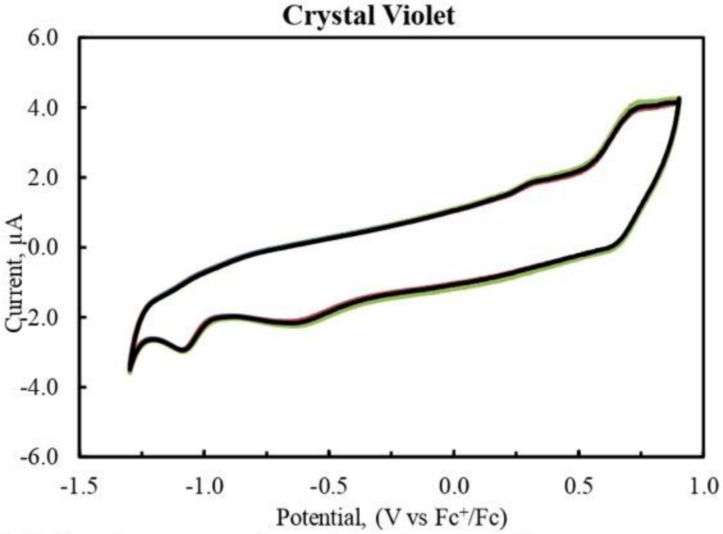

Figure S32. Cyclic voltammogram of crystal violet in acetonitrile.

The redox properties of crystal violet are somewhat different from the aniline oligomers due to the structural differences. Structurally, aniline oligomers are long conjugated molecule while crystal violet is a short triaryl methane molecule. The CV data shows that crystal violet has one reversible oxidation-reduction and one irreversible reduction. The reversible redox process is at around 0.7V which makes crystal violet harder to oxidize in comparison to the selected aniline oligomers.

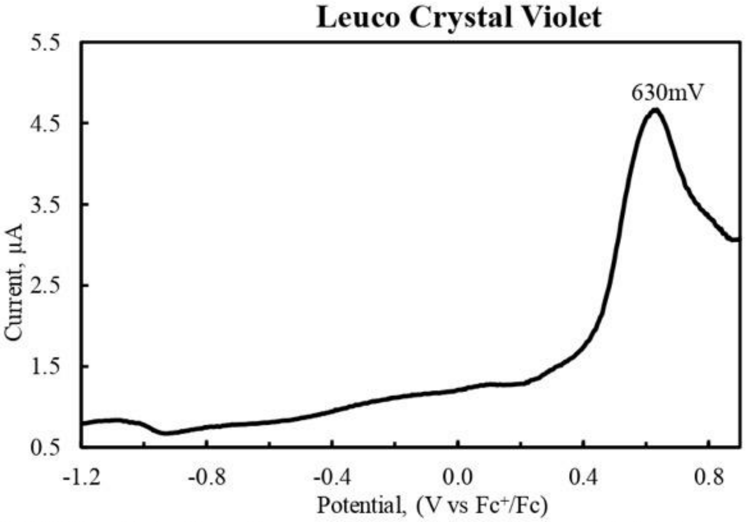

Figure S33. Differential pulse voltammogram oxidation scan of crystal violet in acetonitrile.

Crystal violet has one oxidation peak at 630 mV. The DPV scanning window was selected from -1.2V to +1V and all the parameters were kept same as described experimental procedure.

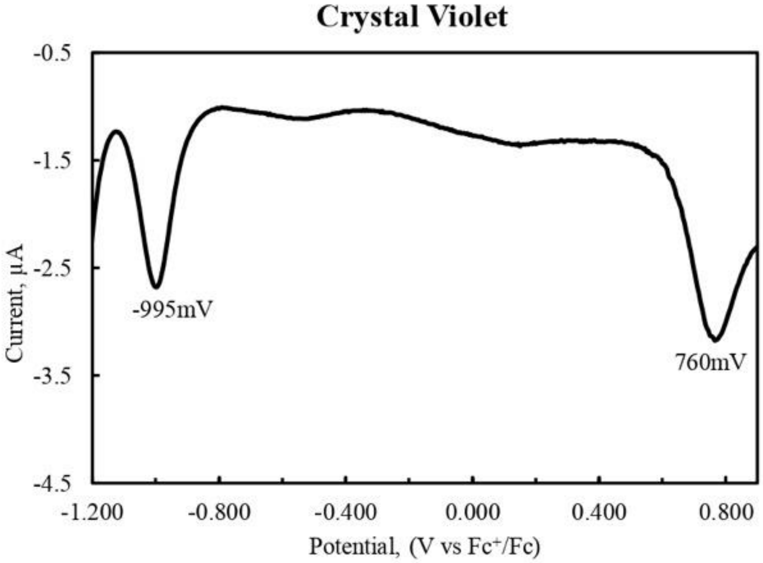

Figure S34. Differential pulse voltammogram oxidation scan of crystal violet in acetonitrile.

Two reduction peaks are seen in the reduction scan of crystal violet in DPV, one of which is a reversible reduction at 865 mV and another is an irreversible reduction at -900 mV. This is maybe due to the leucoemeraldine form being further reduced to a very reactive anion at higher reduction potential and thus we see an irreversible reduction peak. The mechanism for the reversible peak is shown below in Fig. S35 which shows a one electron process.

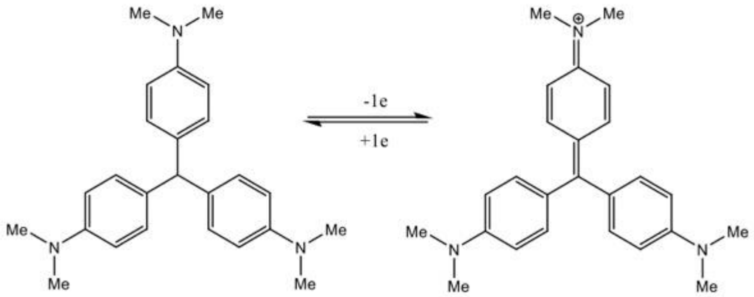

Figure S35. Crystal violet redox process mechanism.

Ranking of Molecule by Ease of Oxidation and Reduction

Considering the DPV peaks for oxidation and reduction we can now rank molecules by the ease of oxidation and reduction. The oxidation reduction potential is calculated from the peak potential.

Table S1. Differential pulse voltammetry peaks for different redox active molecule.

	Oxidation Potential ($E_{1/2}$)				**Reduction Potential ($E_{1/2}$)**			
PCAT	-125	70	290	455	445	260	85	-155
APCAT	-225	10	300	370	385	285	-245	-625
DPPD	50	465			460	35		
SDPPD	280	385			390	275		
C. Violet	680				710			

Table S2. DPV data from oxidation scan for five redox active molecules.

	Oxidation Potential [mV] *vs.* Fc^+/Fc			
Molecule	$E°_1$	$E°_2$	$E°_3$	$E°_4$
PCAT	-125	70	290	455
APCAT	-225	10	300	370
DPPD	50	465		
DPB	280	385		
LCV	680			

Figure S36. Experimental setup of the experiment (top) and functionalization of the sensors with redox-active molecules (bottom). The molecule solutions exhibit the following coloration: PCAT appears as a deep blue, APCAT appears as red, LCV is a pale blue, DPPD is a deep black, and DPB is white.

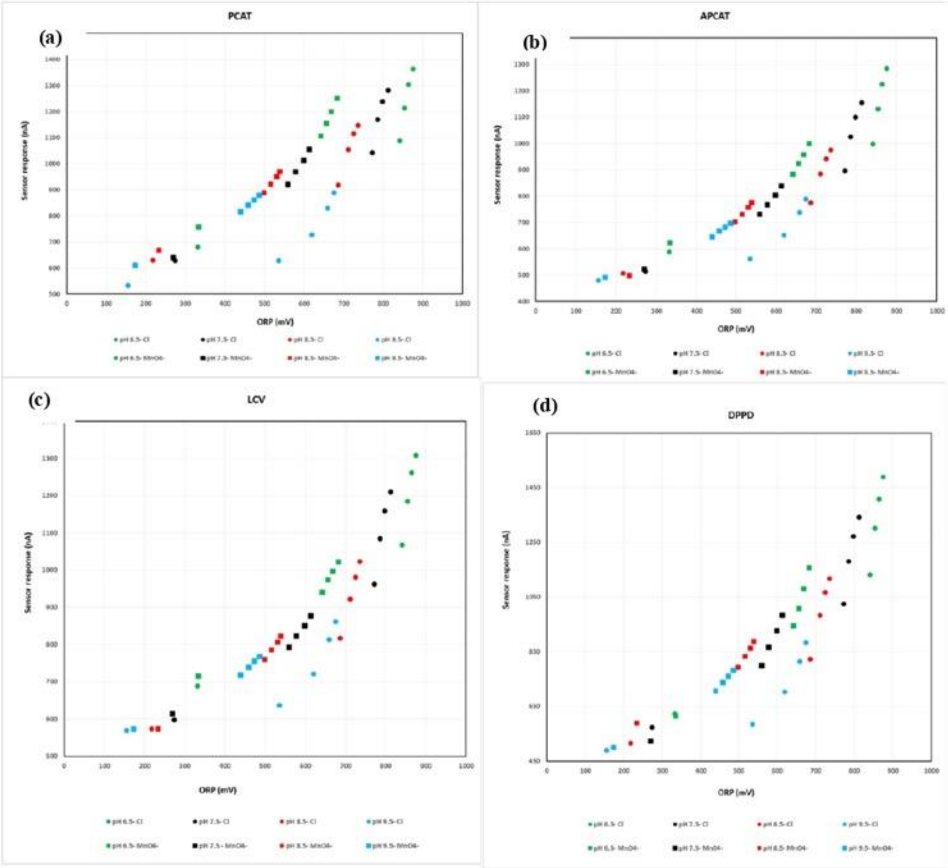

Figure S37. Raw sensor responses as current (nA) of PCAT (a), APCAT (b), LCV (c), and DPPD (d) sensors. Each figure shows the responses for the two analytes in 5 concentrations over the 4 pHs (resulting in 2*4*5 = 40 data points for each sensor) plotted against the ORP (mV) of the solution.

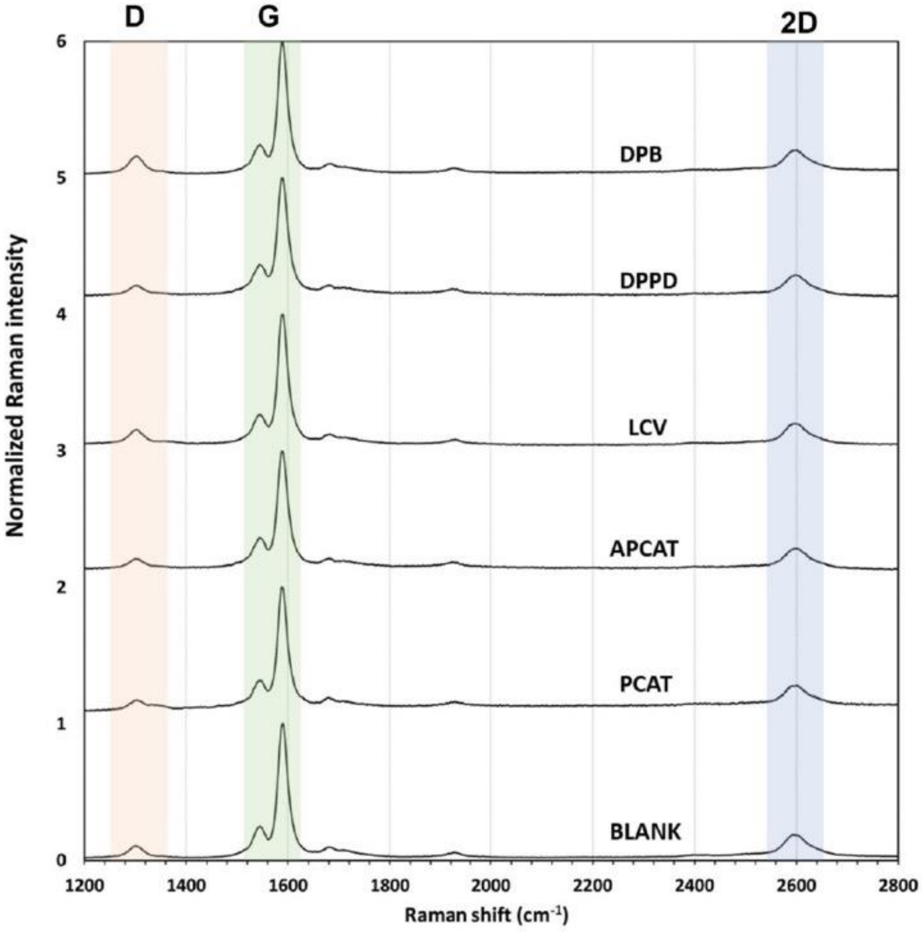

Figure S38. Raman spectra of the Blank and redox-active molecules doped SWCNT sensors. D, G, and 2D peaks are highlighted on the figure.

Table S3. I_D/I_G and I_{2D}/I_G calculations using the D, G, and 2D peak intensities. The standard deviation represented (if there is any) showed the variation in different spots of the same sample.

	BLANK	PCAT	APCAT	LCV	DPPD	DPB
I_D/I_G	0.11	0.20±0.03	0.18±0.03	0.16	0.19±0.02	0.16
I_{2D}/I_G	0.19	0.30±0.02	0.28±0.01	0.20	0.27±0.02	0.21

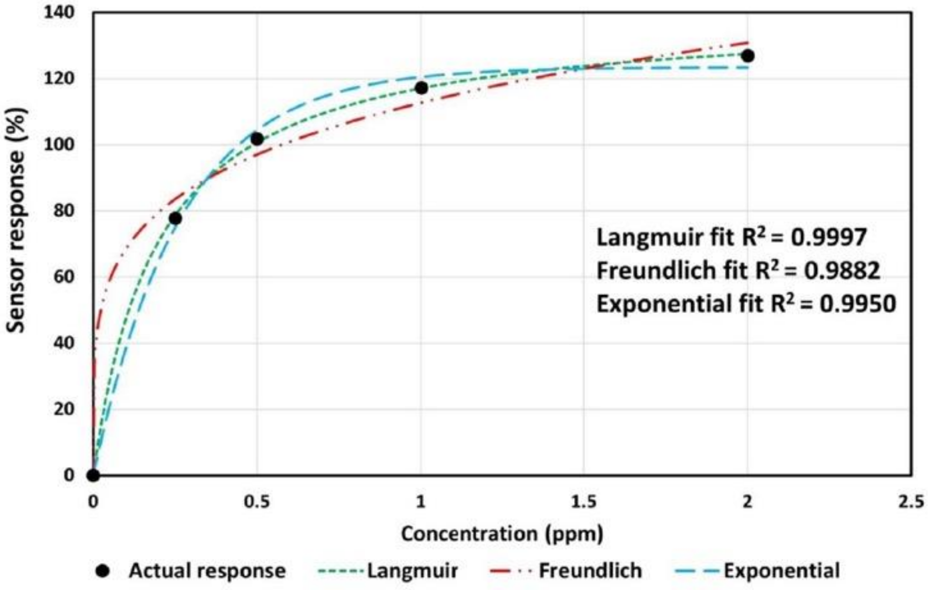

Figure S39. Sensor response from plotted for a range of concentration of free chlorine. Langmuir adsorption isotherm, Freundlich adsorption isotherm, and exponential decay have been fitted to the actual responses (black dots). Here APCAT sensor responses for pH 6.5 was used.

Table S4. Langmuir isotherm curve fitting parameters for the data presented in Figure 5.

Analyte	Sensor name	pH 6.5		pH 7.5		pH 8.5		pH 9.5	
		A	B	A	B	A	B	A	B
Free Cl	BLANK	0.76	8.28	0.7	7.84	0.6	4.96	0.65	1.08
	PCAT	1.27	4.95	1.02	6.76	0.86	5.24	1.07	0.91
	APCAT	1.4	5.13	1.16	6.01	0.88	5..30	1.00	0.96
	LCV	1.13	5.28	1.00	6.27	0.77	4.73	0.88	0.84
	DPPD	1.58	4.99	1.29	5.84	1.14	4.49	1.26	0.87
	DPB	1.32	6.14	0.97	7.86	1.02	5.01	1.33	1.01
MnO_4^-	BLANK	0.30	12.74	0.30	11.57	0.28	14.48	0.23	18.03
	PCAT	0.64	11.82	0.61	11.01	0.46	13.74	0.44	19.60
	APCAT	0.57	11.25	0.56	10.31	0.49	14.11	0.41	17.88
	LCV	0.43	13.60	0.43	11.14	0.40	14.68	0.34	17.55
	DPPD	0.83	7.88	0.75	8.02	0.50	11.25	0.53	16.99
	DPB	0.91	10.95	0.78	10.96	0.55	13.47	0.59	17.79

Effect of Buffer

Since 0.005 M phosphate buffer was used for analyte preparation, it is necessary to account for the effect of the buffer on the sensor. Four different buffer concentrations from 0.0025 M to 0.02 M were tested. The change in conductivity of a DPPD sensor for different buffer concentrations is shown in Fig. S36. The conductivity change is almost negligible for different concentrations.

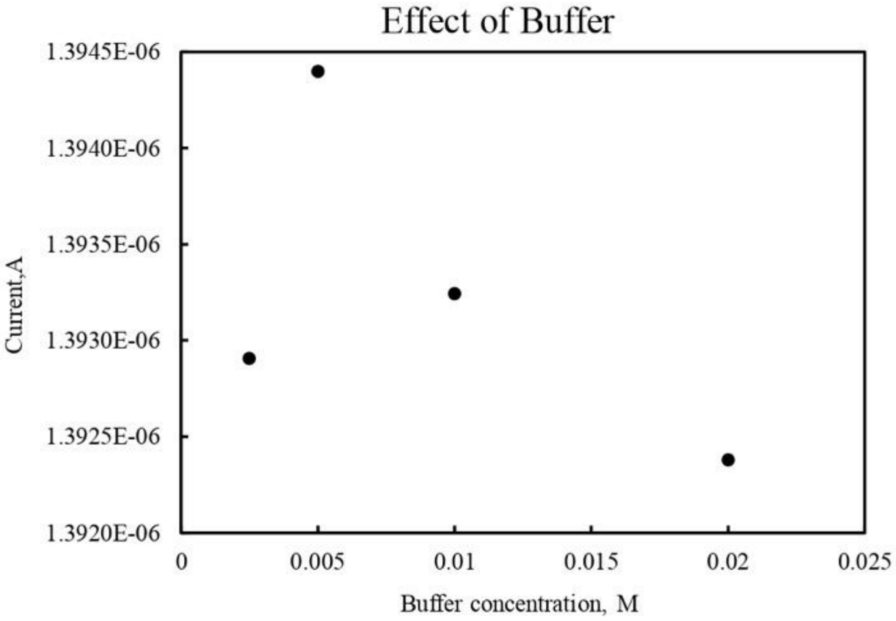

Figure S40. Current measurement for different buffer concentration.

The comparison of the sensor response for a simple pH change and a buffer concentration change is shown in Fig. S37. A change in pH from 7.42 to 7.12 results in a sensor response of about 0.39%. On the other hand, a change in concentration of the buffer from 0.0025 M to 0.2 M gives just 0.04%. In conclusion, an 8-fold change in concentration has almost negligible consequence for the sensor response. Therefore, the sensor is selective to pH and oxidizing agents only, not to the buffer concentration.

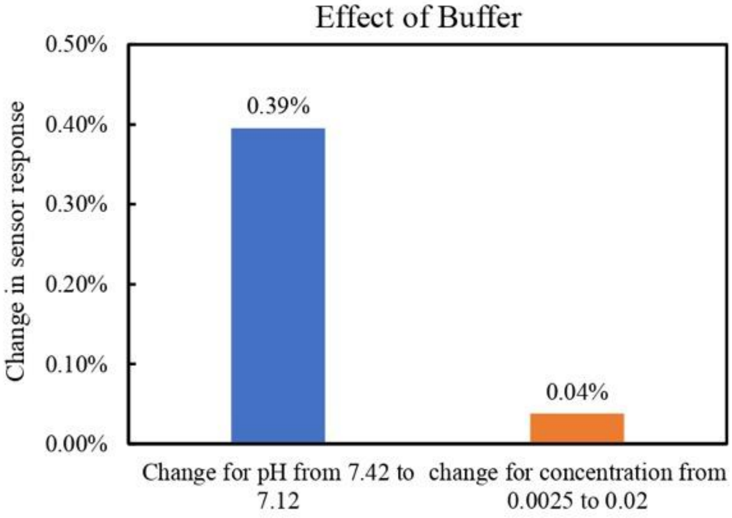

Figure S41. Comparison of sensing response as percent change for pH and buffer concentration.

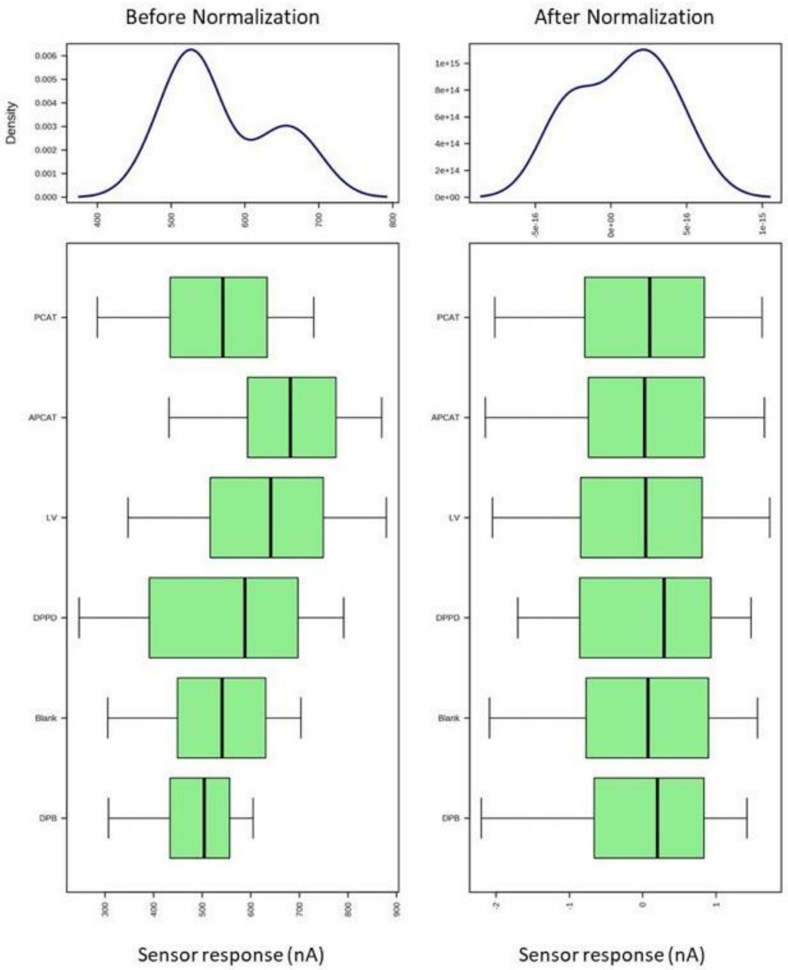

Figure S42. Normalization of the array data. Left column shows the distribution before the normalization and right column shows the distribution after the normalization.

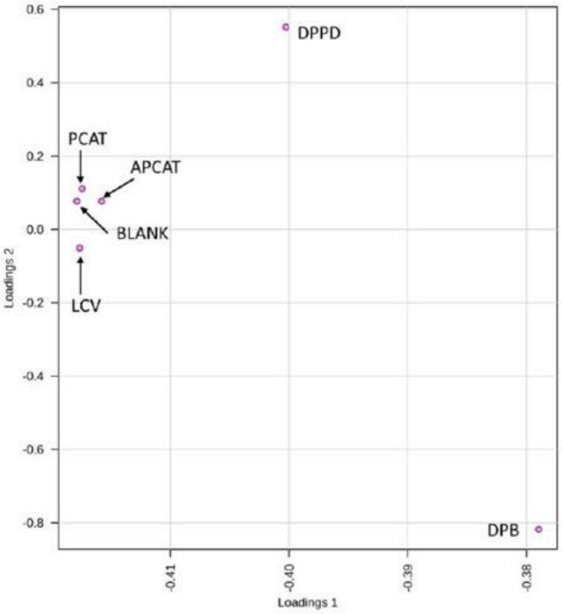

Figure S43. Loadings for the first two components are plotted. Six sensors are labeled on the graph. PCAT, APCAT and Blank show the most correlation while LCV shows little variation. DPPD and DPB show that these two variables are not correlated as one of them has positive loadings for the second component and the other has negative loadings.

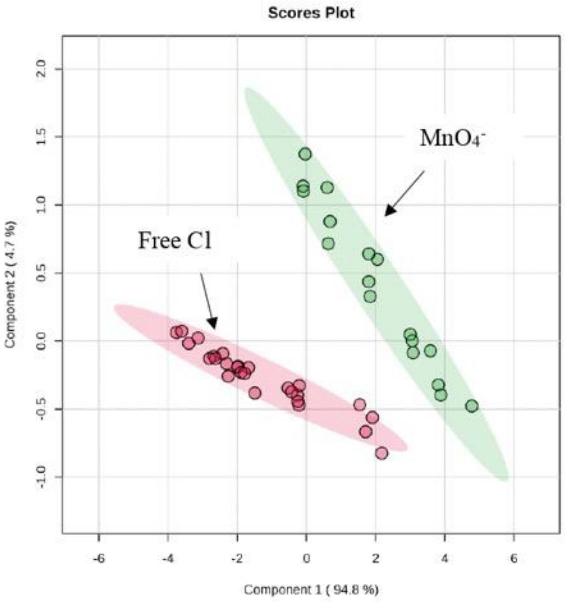

Figure S44. PLS-DA score plot for the responses of 6 sensors. Here first two components are shown for the score plots. The two analytes (free chlorine and MnO_4^-) are well separated.

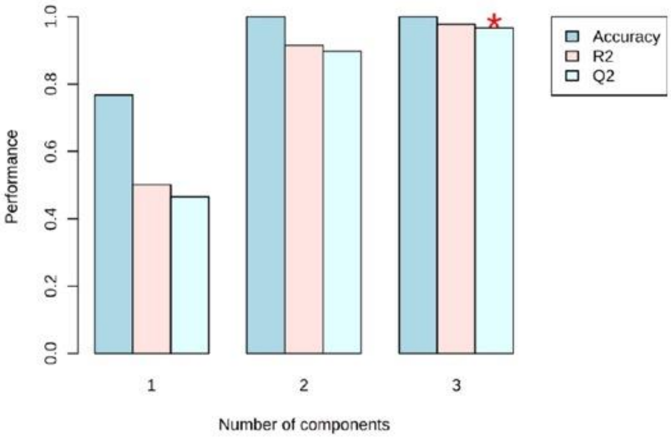

Figure S45. Performance parameters for the PLS-DA model. Here three components are shown.

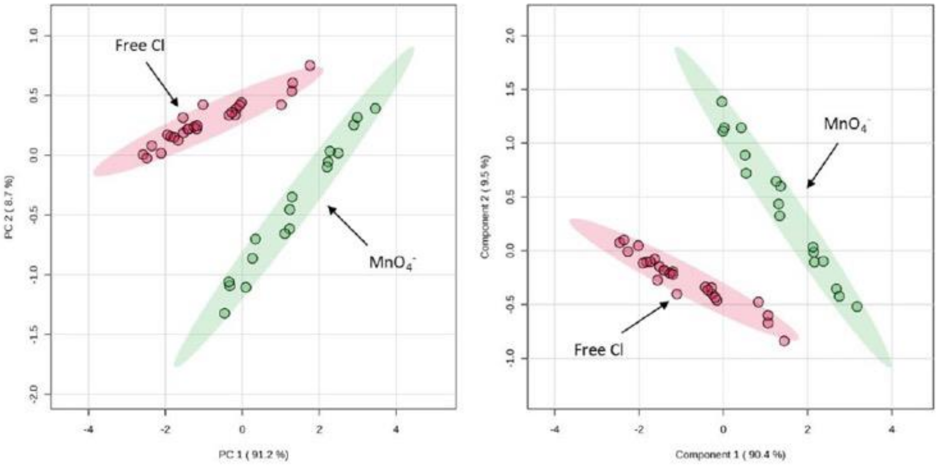

Figure S46. PCA (left) and PLS-DA (right) score plots generated from the responses of the three sensors (blank, DPB, DPPD).

Chapter 7 Continuous Monitoring of Monochloramine in Water, and Its Distinction from Free Chlorine and Dichloramine Using a Functionalized Graphene-Based Array of Chemiresistors

This chapter presents a solid-state, reagent-free method for monochloramine (MCA) sensing using an array of few-layer graphene (FLG) chemiresistors. The devices were fabricated from exfoliated FLG and functionalized with redox-active molecules designed to provide differential responses to MCA, free chlorine (FC), and dichloramine (DCA) across a range of concentrations. Chemometric analysis was applied to separate overlapping responses and to construct multivariate calibration models for quantitative detection. A minimum of three sensors within the array was required to preserve full functionality. The array was demonstrated to quantify MCA in both buffered solutions and tap water, providing a low-cost and reagent-free approach for continuous monitoring.

Reprinted with permission from the journal of *ACS ES&T Water* **2024**, *4*, 9, 4041-4051, Md Ali Akbar, Ponnambalam Ravi Selvaganapathy, and Peter Kruse.

DOI:10.1021/acsestwater.4c00341

ACS ES&T Water

pubs.acs.org/estwater

Article

Continuous Monitoring of Monochloramine in Water, and Its Distinction from Free Chlorine and Dichloramine Using a Functionalized Graphene-Based Array of Chemiresistors

Md Ali Akbar, Ponnambalam Ravi Selvaganapathy, and Peter Kruse*

Cite This: *ACS EST Water* 2024, 4, 4041−4051

Read Online

ACCESS | Metrics & More | Article Recommendations | Supporting Information

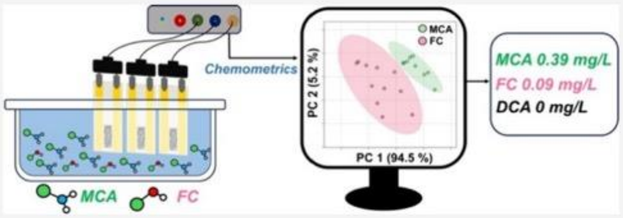

ABSTRACT: Monochloramine (MCA) is commonly added to drinking water as a disinfectant to prevent pathogen growth. The generation of MCA at the treatment plant requires tight control over both pH and the ratio of free chlorine (FC) to ammonia to avoid forming undesirable byproducts such as dichloramine (DCA) and trichloramine (TCA), which can impart odor and toxicity to the water. Therefore, continuous monitoring of MCA is essential to ensuring drinking water quality. Currently, standard colorimetric methods to measure MCA rely on the use of reagents and are unsuitable for online monitoring. In addition, other oxidants can interfere with MCA measurement. Here, we present a solid-state, reagent-free MCA sensing method using an array of few-layer graphene (FLG) chemiresistors. The array consists of exfoliated FLG chemiresistors functionalized with specific redox-active molecules that have differential responses to MCA, FC, and DCA over a range of concentrations. Chemometric methods were employed to separate the analytes' responses and to generate multivariate calibration for quantification. A minimum of three sensors are required in the array to maintain full functionality. The array has been demonstrated to quantify MCA in buffered and tap water as a low-cost, reagent-free approach to continuous monitoring.

KEYWORDS: *chloramine, free chlorine, graphene, solid state sensor, chemiresistive sensor, disinfectant monitoring, electronic tongue, water quality sensor*

■ INTRODUCTION

The lower reactivity and longer disinfection capacity of chloramine have made it a popular alternative to free chlorine (FC) as a residual disinfectant in drinking water distribution systems.[1−3] Chloramine is formed by reacting FC with an ammonia source after primary disinfection as the water leaves the treatment plant. FC in the presence of ammonia or nitrogen compounds forms one or more chloramines such as monochloramine (MCA, NH_2Cl), dichloramine (DCA, $NHCl_2$), and nitrogen trichloride (TCA, NCl_3) depending on the pH and Cl to N ratio.[4,5] Only MCA is desirable for disinfection purposes since DCA tends to create odor- and taste-related problems in drinking water, and TCA induces pronounced irritations of the eyes and respiratory system.[6−8] Typically, 0.5−2 mg/L (or ppm) of monochloramine is maintained in the water distribution system to prevent pathogen growth in water.[5,9] Therefore, monitoring the level of MCA is crucial. Even though there is no U.S. EPA-approved direct method to measure MCA,[3] indirect amperometric titration and colorimetric methods can be used to measure total and free chlorine in water.[2] Amperometric titration methods can distinguish three common forms of chlorine (Cl_2/HOCl/OCl^-, NH_2Cl, and $NHCl_2$) but are demanding in operator skill and maintenance.[2,10] In the simpler and more popular *N*,*N*-diethyl-*p*-phenylenediamine (DPD) methods (ferrous and colorimetric), the MCA concentration is calculated as the difference between free and total chlorine, assuming that no DCA and TCA are present. DPD methods are subject to interferences (copper, oxidized manganese,

Received: April 21, 2024
Revised: August 5, 2024
Accepted: August 5, 2024
Published: August 8, 2024

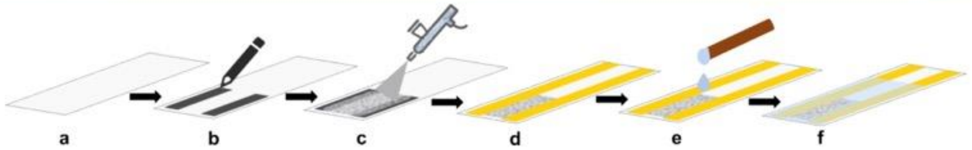

Figure 1. Schematic of FLG chemiresistive sensor fabrication steps: (a) clean glass slide, (b) drawing the pencil contacts using 9B pencil, (c) airbrushing the FLG solution in between the pencil contacts, (d) placing Cu tape on the pencil contacts, (e) deposition of PDMS on the Cu tape, and (f) fully fabricated sensor.

iodide, chromate[3]) and unsuitable for continuous monitoring of monochloramine.[2,10,11]

Membrane introduction mass spectrometry (MIMS),[12−14] chromatographic,[15,16] and spectrophotometric[9,17,18] methods have also been proposed to detect MCA, including Hach's Monochlor F reagent-based colorimetric method.[19,20] The use of reagents and/or complex instrumentation for these methods limits their utility for continuously monitoring MCA in a distribution network. Electrochemical methods have the potential for simple, reagent-free, online monitoring of MCA;[21] however, they require reference electrodes. Chemiresistors are solid-state electrical sensors that convert a chemical signal into an electrical signal, namely, a change in conductance.[22] Typically, a small bias voltage is applied between the contacts of a chemiresistor and then the change in conductivity of the sensing element is monitored as a function of changes in the chemical environment.[22] Carbon-based materials such as carbon nanotubes,[23] graphene,[24,25] graphene-like carbon,[26] and graphite[27] have been used as the transducing element for monitoring pH,[28] heavy metals,[24] and disinfectants[26,29] in water. Single-element disinfectant sensors are effective when only one disinfectant with a known identity is present. We have recently demonstrated that an array of functionalized carbon nanotubes can be implemented to distinguish multiple disinfectants (e.g., free chlorine and potassium permanganate) in water.[30] Graphene-based chemiresistive substrates can be obtained from inexpensive source materials.[25,27,31] We have studied few-layer graphene (FLG) exfoliated from graphite for pH[28,32] and heavy metal[24,33] sensing and found that this substrate is less susceptible to interferences than carbon nanotubes and is easily modified for the selective detection of desired analytes through functionalization.

Here, we propose a functionalized FLG sensor array to monitor MCA concentrations in water and distinguish it from FC and DCA. The proposed array consists of four FLG sensors functionalized with redox active molecules and a bare FLG sensor. The sensors responded to these three analytes in a similar trend, with an increase in conductivity. With chemometrics, the multivariate responses were fit into principal component analysis (PCA), partial least-squares discriminant analysis (PLS-DA), linear discriminant analysis (LDA), and partial least-squares regression (PLSR) models for the speciation and quantification of the disinfectants, both of which could provide the complete picture of drinking water disinfection efficacy. We showed that the number of sensors in the array can be reduced to three to efficiently monitor MCA in water. We demonstrated the continuous monitoring of MCA and FC in water. We also evaluated the operation of the sensor array in tap water as a real sample.

EXPERIMENTAL SECTION

Chemicals. Graphite powder (99.99%) was purchased from Alfa Aesar, Haverhill, MA, USA. Isopropanol (IPA), 2,3-diaminophenazine (DAP), 1-aminopyrene (APy), 9,10-phenanthrenequinone (PQ), *N*,*N*′-diphenylbenzidine (DPB), sodium hypochlorite (NaOCl) solution (reagent grade, 10–15%), ammonium chloride (NH_4Cl), potassium phosphate dibasic (K_2HPO_4), potassium phosphate monobasic (KH_2PO_4), sodium bicarbonate ($NaHCO_3$), sodium chloride (NaCl), calcium chloride dihydrate ($CaCl_2.2H_2O$), magnesium sulfate ($MgSO_4$), and acetonitrile were purchased from Sigma-Aldrich. Type 1 ultrapure water was obtained from a Millipore Simplicity UV water purification system.

Sensor Fabrication. FLG was first exfoliated from graphite powder using a modified procedure of a previously reported study.[24] Briefly, 40 mg of graphite powder was added to 4.5 mL of IPA and 10.5 mL of deionized (DI) water in a 20 mL capped vial. Then, the resulting suspension was sonicated for 6 h using an Elmasonic P60H ultrasonic cleaner set at 100% power and sweep mode at 37 kHz. Subsequently, two-step centrifugation of the suspension was carried out using an Eppendorf MiniSpin Plus microcentrifuge at 14,000 rpm (13,149 × *g*). In the first step, the suspension was centrifuged for 5 min, and the supernatant was collected, thus removing unexfoliated graphite. In the second step, the supernatant was centrifuged for 15 min, and from this step, the retentate was collected as the final product. The final product was airbrushed for sensor fabrication within an hour.

Figure 1 shows the steps for the fabrication of the sensors (actual photographs of the sensors are shown in Figure S1). The frosted end of a glass microscope slide (VWR VistaVision, 75 × 25 × 1 mm^3, cat. no. 16004418) was first rinsed with acetone and methanol to remove any contaminants. After the slide was dried in the air, two 9B pencil patches were drawn as contact pads on the two sides of the frosted end of the microscope slide. Exfoliated FLG was then carefully airbrushed using 10–15 psi of N_2 on the frosted side at 150 °C until a uniform continuous network of FLG flakes was achieved connecting the pencil contact pads (targeting a resistance range of 10–15 kΩ). This resistance range was selected based on previous studies[24,32] where we found that a resistance range of 10–20 kΩ in our particular sensor geometry provides the optimal thickness of the film for aqueous sensing. Here, we chose a narrower range to reduce sensor variation due to fabrication artifacts. The film resistance between the contact pads was monitored during the airbrushing process by using a multimeter. Then two copper tapes were attached on top of the pencil contacts covering the full length of the glass slide as shown in Figure 1 and Figure S1; the top end gets connected via alligator clips to the potentiostat. Finally, the copper tape (3M EMI Copper Foil Shielding Tape 1181, 1/4 in. wide) was masked with a thin layer of polydimethylsiloxane (PDMS

Sylgard 184 Silicon Elastomer from Dow Corning) making sure to cover the edges of the FLG film. The PDMS was cured at 60 °C for an hour. The sensor was then cooled on the hot plate at room temperature.

Functionalization of FLG Sensors. A set of sensors with similar resistance were noncovalently functionalized with selective molecules. The sensing molecule solutions were prepared by dissolving 2,3-diaminophenazine (DAP), 1-aminopyrene (APy), 9,10-phenanthrenequinone (PQ), N,N′-diphenylbenzidine (DPB) in acetonitrile (ACN). The structures of the molecules used for functionalization are shown in Figure 2. These molecules were selected due to their small size, conjugated structure, low reduction potential, and reversible redox behavior. Their conjugated structure facilitates the adsorption of the molecules on the graphene surface through π−π interactions. The smaller size of the molecules enables a closer packing due to self-assembly during adsorption on the surface, which increases selectivity, prevents nonspecific interactions, and creates more reactive sites for analytes to interact. The lower redox potential facilitates interactions with the oxidizing analytes. Finally, the reversible redox behavior is essential for the sensors to respond to not only oxidizing but also to reducing environments. The desired concentrations (10% DAP, 10% PQ, 20% DPB, 20% APy) of molecule solutions were prepared by diluting from a stock of 100% saturated solutions. The sensors were immersed in the molecule solutions for ∼8 h keeping a constant volume of the solution.

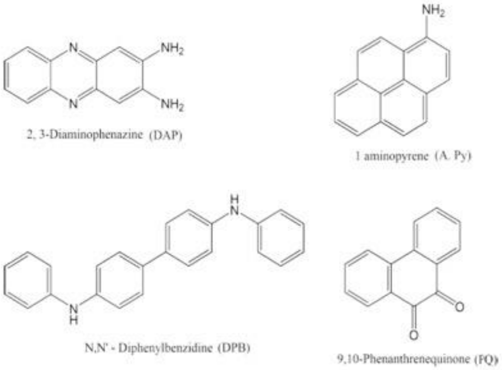

Figure 2. Structures of the molecules used for the functionalization of FLG chemiresistive sensors. 2,3-diaminophenazine (DAP), 1-amino pyrene (APy), *N,N*′-diphenyl benzidine (DPB), and 9,10-phenanthrenequinone (PQ).

Characterization of the Film. Exfoliated FLG film samples (bare and doped) were characterized by Raman spectroscopy to verify the quality of the graphene. A Renishaw inVia Raman spectrometer was used for the characterization. A 532 nm solid state continuous wave laser was focused with a 50× objective lens on the sample to collect the spectra over a range of 100−3500 cm^{-1} (2 cm^{-1} resolution). The 50 mW laser was kept at 5% power. The samples were prepared on Whatman membrane filters (PTFE, supported) of 0.45 μm pore size and 47 mm diameter (GE Healthcare Life Science). The morphology of the FLG film was also examined using a JEOL JSM7000F scanning electron microscope (SEM) at a 3 kV beam energy. The samples were prepared by airbrushing FLG on a Si wafer according to a similar procedure as a sensor, and the final resistance of the film was 10 kΩ.

Chloramine Synthesis and Quantification. For this study, only MCA and DCA were chosen for the analyte characterization in addition to FC. TCA was not considered since it is the least stable chloramine and forms only at a pH below 3.7. MCA stock solution was prepared before conducting experiments in phosphate-buffered water (PBW) using a published recipe.[34] PBW was prepared by mixing 94 mL of 1 M K_2HPO_4 and 6 mL of 1 M KH_2PO_4 and then diluted with ultrapure water to 1 L and kept in the refrigerator for further use. 11 mg of NH_4Cl were placed in a 20 mL vial and then dissolved in 9.95 mL of PBW. 50 μL of 10% NaOCl was then slowly added to the stirring solution. The solution was left stirring for 10 more minutes after the addition of NaOCl was complete. The vial was then kept in a refrigerator for 30 min to stabilize the MCA solution.

AQUAfast chlorine (total and free) DPD reagent powder packs were used to quantify MCA in the solution following the ATP EPA-approved Orion Methods AC4P72 (total chlorine) and AC4P71 (free chlorine). The testing was carried out using a Thermo Scientific Orion Aquamate 8000 UV−vis spectrophotometer and AQUAfast 24 mm round vials (Cat. No. AC2V24). The total chlorine amount represents all forms of chlorine (bound and free) in water. The formation of bound chlorines like MCA, DCA, and TCA depends on the pH of the

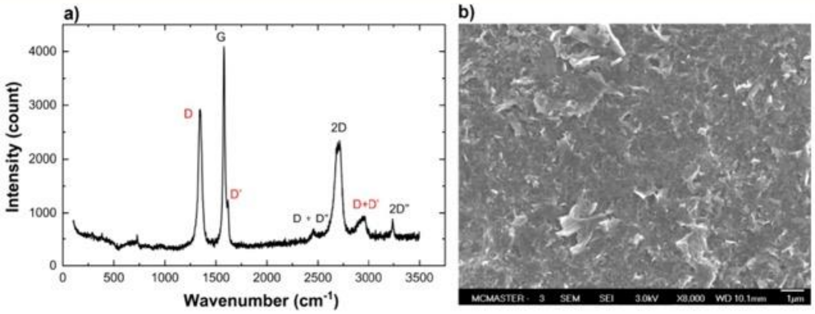

Figure 3. Characterization of exfoliated FLG. (a) Raman spectra of the airbrushed FLG film on a glass slide collected using a 532 nm laser. (b) SEM image of the FLG film.

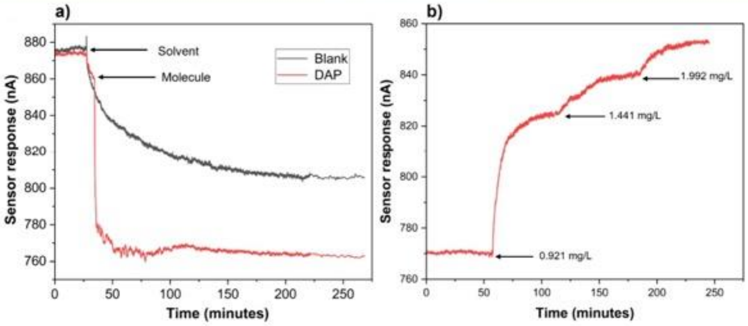

Figure 4. (a) Doping characteristics of the SAM of DAP on the FLG film. Current responses of sensor in solvent and molecule solution. (b) Sensor response to monochloramine. Actual concentrations of the MCA measured by DPD method are labeled with the arrow; the arrow represents the time for the MCA spiking.

solution. Since the pH of PBW was above 8, it can be assumed that all the bound chlorines were MCA. Therefore, the subtraction of free chlorine from total chlorine would provide the amount of MCA in the solution. Here, we followed this to calculate the amount of MCA in the solution.

DCA was synthesized utilizing a commonly reported approach[35,36] by lowering the pH of the MCA solution to 3.7 which ensures the transformation of MCA to DCA. After lowering the pH, the solution was given an hour to complete the reaction. Then, the amount of DCA was measured by the same method described above for MCA. In this case, the subtraction of total and free chlorine yielded the amount of DCA.

Sensor characterization and data analysis methods used in this article are explained in the Supporting Information.

RESULTS AND DISCUSSION

Characterization of the Chemiresistive Transducing Film. Carbon-based materials such as graphene (single layer and few layer), graphene oxide, and carbon nanotubes (single-walled and multiwalled) are some of the best substrates that have been demonstrated for transducer films in aqueous chemiresistive sensing.[23,24,28,37] Fabrication of a stable and uniform film is the key requirement for sensitive chemiresistive sensing, as the film directly interacts with water and any analyte present in the solution. FLG from the exfoliation of graphite presents a simple and economical way of producing resistive films. Sonication-assisted exfoliation contributes to the defectivity of FLG as shown previously.[32] Raman spectra were evaluated to verify the quality of the FLG films. Figure 3a shows the Raman spectrum of an FLG film. The characteristic D (~1350 cm^{-1}), G (~1590 cm^{-1}), 2D (~2680 cm^{-1}), and 2D′ (~3250 cm^{-1})[38] peaks of FLG were observed. The G band represents the in-plane vibrational mode of the sp^2 hybridization, and the D band originates from lattice defects. The intensity ratio of these two bands (I_D/I_G) can be used as a measure of the concentration of defects in the material. The presence of FLG was confirmed from the 2D peak since this peak is missing the characteristic graphite shoulder. The D, D′, and D + D (red colored in the graph) peaks show that defects were introduced during the exfoliation process. The peaks exhibited here are in good agreement with previously reported FLG characterization.[24,32] SEM images of the film show a continuous film and horizontal orientation of the graphene flakes. We note that airbrushing the FLG suspension for the sensor fabrication resulted in a more uniform coverage for the desired resistance (~10 kΩ). No visible gaps are present in the airbrushed film, unlike previously reported drop-cast films.[24]

Functionalization of the Sensors. Functionalization or doping of graphene is a common approach to modify the properties of graphene for sensing analytes. Covalent and noncovalent approaches have been extensively researched to introduce selectivity.[39] Noncovalent functionalization avoids disrupting the conjugation of graphene sheets, thereby preserving the electronic properties of the graphene material. During the doping, the molecules are adsorbed onto the FLG surface through $\pi-\pi$ stacking. Figure 4a shows the characteristics of the sensor during the doping procedure. The blank sensor is only exposed to the solvent (ACN) while the doped ones are exposed to the molecules dissolved in ACN. The FLG surface of the sensors starts off being p-doped as a result of accumulating oxygen functionalities as defects during the exfoliation process.[40] As the sensors were dipped in ACN a decrease in current was observed, as the inherent p-doping of the FLG surface is partially counteracted by n-doping due to charge transfer from the solvent. For the functionalized sensor (DAP), the current across the chemiresistive film sharply drops when the molecule solution is introduced. This is due to the molecules being adsorbed onto the graphene layer. As the molecules donate electrons to the FLG surface, the hole density decreases, further counteracting the p-doping of the film. Stabilization of the current represents the completion of surface coverage by the molecules. Further rinsing with pure solvent ensures that only a monolayer of molecules remains at the surface by removing any aggregates of molecules. The counteracting of the p-doping of the film due to n-doping by the molecules used to functionalize the FLG film was further characterized by Raman spectroscopy. Blank and functionalized samples were prepared, and the 2D peak shifts were evaluated to gauge the degree of doping of FLG samples when functionalized by DAP, PQ, DPB, and APy. A down-shift in the 2D peak represents diminished p-doping, while an upshift results from enhanced p-doping of the substrate.[41,42] The 2D peaks for all functionalized samples were downshifted relative to the blank sample (shown in Figure S3). The largest downshift shift was obtained for the DPB sample ($\Delta\omega_{2D} \approx 11$ cm^{-1}). The smallest downshifts were present for the DAP and PQ samples ($\Delta\omega_{2D} \approx 5$ cm^{-1}). This confirms that the

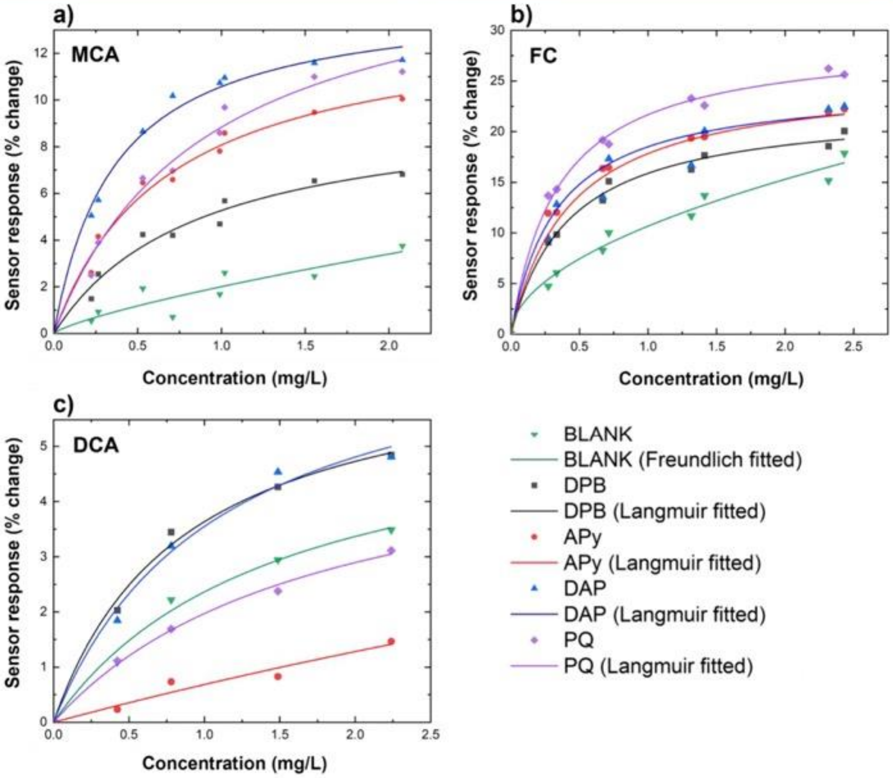

Figure 5. Calibration graphs of the sensors. The percent change of each spiking of analytes were plotted against the actual concentration of the solution. The colored dots represent the actual data points, and the corresponding lines represent the fits of the mathematical models. Three graphs represent monochloramine (a), free chlorine (b), and dichloramine (c).

functionalization of the FLG was successful. The concentration of the molecule solution plays an important role in the functionalization of the FLG film and therefore the responses coming from the sensor.[24] We previously found that molecule solutions at 4% of the saturation concentration result in a more uniform molecule deposition on the FLG film.[24] However, the concentration of each molecule solution must be optimized for the best surface coverage. All four molecules' concentrations were optimized for MCA sensing by testing freshly fabricated sensors in 5, 10, 20, and 40% DAP, DPB, PQ, and APy solutions prepared relative to the fully saturated corresponding solution. The percent change graphs for each concentration are provided in the Supporting Information (Figures S4−S7). Sensors doped with 10% solutions of DAP and PQ showed the most sensitivity and stability, while for DPB and APy, the optimized concentrations were found to be 20%. The optimized concentrations were used for all of the subsequent experiments.

Figure 4b shows the chemiresistive current response of a functionalized sensor (DAP) as a function of time. The DAP-functionalized sensor shows a clear response to the addition of MCA to the buffer. The solution was spiked with consecutive additions of freshly prepared MCA stock solution, and the standard colorimetric method (DPD) measured the solutions to be 0.921, 1.441, and 1.992 mg/L. As an oxidizing agent, MCA withdraws electrons from the FLG surface. Due to the loss of electrons from the surface, the hole density increases, and the sensors exhibit an increase in current. The stepwise increase in current can be attributed to the increasing interaction of MCA molecules with the surface.

Calibration Graphs. Raw sensor responses for the three analytes (MCA, FC, and DCA) were analyzed to calibrate the sensors for each of the analytes. Figure 5 presents three graphs for five sensors' responses plotted as percent current change against the concentration of the corresponding analytes. The percent change of the sensor response for each concentration is calculated by dividing the change in current due to the sensor response by the baseline (0 ppm) current. To further analyze the data from raw sensor responses, we plotted the percent current change as a function of concentration for each of the analytes. The sensor responses were fitted to the Langmuir absorption isotherm model as in eq 1.

$$y = \frac{abx}{1 + bx} \tag{1}$$

$$y = mx^{1/n} \tag{2}$$

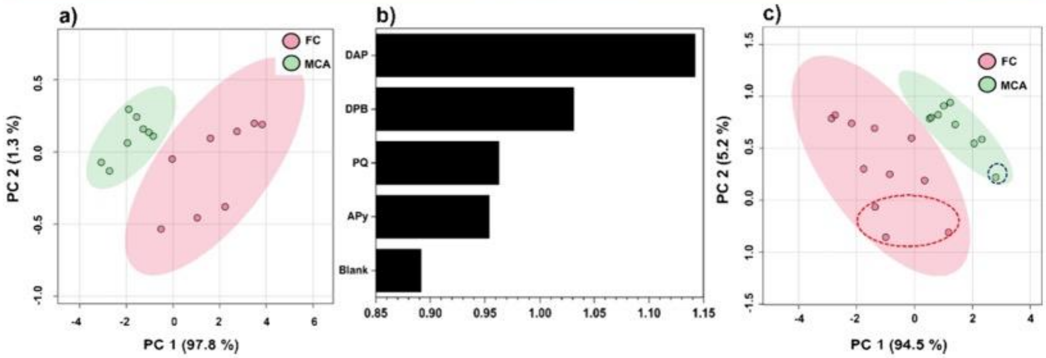

Figure 6. Chemometric analysis of the calibration data set. (a) PCA score plot showing the responses of the array for varied concentrations of MCA (green region) and FC (red region). The colored ellipses represent 95% confidence level. (b) VIP plot showing the scores for the contribution of the sensors in separating the analytes. (c) PCA score plot for the calibration data set and mixture of analytes generated from the three important variables selected from the VIP plot. Red and green ellipses represent the FC and MCA regions, respectively. Dotted circles represent the data points taken for different Cl_2:N ratios.

Here, y represents the sensor response, x is the concentration of the analyte, a is the saturation point or the maximum theoretical value of y, and b is the Langmuir constant, which relates to the equilibrium between the density of adsorbed molecules on the surface and the concentration of the molecules in the bulk solution. For chemiresistive sensors, a can be referred to as the maximum theoretical response for a sensor and b is related to the binding constant of the analyte to the sensing element. Both parameters combined can explain the sensitivity of the sensor to a particular analyte. This model assumes that the adsorption of analyte molecules is limited to a monolayer. Equation 2 is for a Freundlich isotherm, which is also commonly used for chemiresistive sensing of disinfectants.[29] This model does not assume adsorption to be limited to a monolayer and can, therefore, accommodate a response that does not saturate. m is referred to as the partitioning coefficient and n is a correction factor. We have previously evaluated these two mathematical models along with exponential decay.[30] Table S1 provides the R^2, adjusted R^2, and the model parameters for the sensors.

Figure 5a shows the responses of the five sensors in the array to MCA. The DAP sensor shows the largest response in the array; 11.72% sensor response is recorded for 2.08 mg/L of MCA. The blank sensor provides the lowest responses (3.75%) out of all the sensors for the same concentration of MCA. The model parameters for the DAP sensor are $a = 14.44 \pm 0.53\%$ and $b = 2.73 \pm 0.32$ mg^{-1} L for an R^2 value of 0.99. The range of concentrations tested here covers the commonly desired MCA level in drinking water.[5,9] The saturation value for the DAP sensor is 14.44% which at 95% of the maximum response (fitting parameter a) can measure 7 mg/L of MCA. The linearized fit of the Langmuir equation (eq 1) for the DAP sensor from the concentrations tested and the theoretical values for 95% saturation of the sensor response demonstrate that the sensors can potentially be used for higher concentrations of MCA (figure S8). The lower limit of detection (LoD) for the DAP sensor is calculated to be 0.027 mg/L. Electron-donating amine groups lower the redox potential of phenazine-based molecules.[43] High responses from DAP could be attributed to the small size and two amine groups present in the molecule. The small molecules will adsorb more densely on the graphene surface, therefore increasing the density of the amine groups. These amine groups interact with the analytes. As shown previously, amine groups interact with oxidizing agents to enhance the responses from the functionalized sensors compared to the blank sensor.[26,30] The blank sensor responded with a steady increase for a maximum of 3.75% for the 2.08 mg/L MCA. However, the sensor showed high variation for the MCA measurement, as shown in Figure 5a. The model parameters for the Langmuir fit of the blank sensor are $a = 10.55 \pm 9.55\%$ and $b = 0.24 \pm 0.29$ mg^{-1} L. We have found that all functionalized sensors fit the Langmuir model better (in terms of R^2) for MCA and FC, while the blank sensor fits the Freundlich model better (Figures S9 and S10). For both MCA and FC, the blank sensor gives the lowest response, further demonstrating that functionalization improved the sensitivity. Functionalization also improved the stability of the sensors during MCA sensing as the blank sensor showed the most variation in measurements leading to a lower R^2 value (0.83), whereas all the others are above 0.97. PQ, being the second most responsive sensor, has the potential to measure much higher concentrations of MCA since it has a much smaller value for b (1.09 ± 0.20) and only saturates at $a = 16.89 \pm 1.44\%$. These differences in responses from the functionalized sensors can be exploited during data analysis.

Among the functionalized sensors in the FC (Figure 5b) measurement, PQ ($a = 29.20 \pm 0.67\%$, $b = 2.88 \pm 0.25$ mg^{-1} L) shows the highest sensitivity followed by DAP ($a = 25.56 \pm 1.82\%$, $b = 2.31 \pm 0.55$ mg^{-1}L), APy ($a = 24.71 \pm 0.51\%$, $b = 2.98 \pm 0.23$ mg^{-1} L), and DPB ($a = 22.59 \pm 0.76\%$, $b = 2.37 \pm 0.27$ mg^{-1} L). The appearance of the blank sensor response in Figure 5a,b is indicative of a different mechanism compared with the functionalized sensors. The b parameter for the blank sensor when fitted to the Langmuir model is the smallest for both MCA and FC (Table S1). DCA responses for the sensors are shown in Figure 5c. The sensors are found to be less sensitive to DCA than to the other two analytes. The responses for DCA should not be compared with those for MCA and FC since the DCA measurements were carried out at a pH of ~3.8 compared to the measurement carried out at basic pH for the other two. However, we demonstrate that the sensor array is capable of measuring DCA with distinct trends from those of each of the sensors.

Classification of the Disinfectants. As discussed in the calibration section, the disinfectants generate different magnitudes of responses for the five sensors without any sensors showing selectivity for a particular disinfectant. Five variables make it complicated to visualize the responses and distinguish the analytes. Multivariate methods are commonly used to monitor, differentiate, and identify analytes in water from complex data sets.[44−47] In a recent study, we introduced chemometric approaches such as PCA and PLS-DA to distinguish FC and $KMnO_4$ at different pHs using an array of six sensors.[30] Here, we analyzed the MCA and FC data using chemometric methods. A brief description of the chemometric methods is provided in the Supporting Information. Normalization of the data by the autoscaling method gives a uniform distribution (Figure S11) of the sensor data. The 5 × 16 response matrix includes five sensor array responses for eight spiked concentrations of each of the analytes (MCA and FC). PCA reorganizes the data to maximize the variance and identify five principal components (PC). The top three PCs explained 99.9% of the data set, as shown in the scree plot (Figure S12). The pairwise score plots (Figure S13) show that the analyte responses can be separated using the first two PCs with PC1 explaining 97.8% and PC2 explaining 1.3%. The observations from the array are then projected in a 2D score plot using PC1 and PC2 in Figure 6a. Each of the 16 data points represents the observations measured by the array, and a clear separation in the MCA and FC regions demonstrates that the array generates distinct responses for the two analytes. To understand the contribution of the sensors in the separation of the two disinfectants, the loading plot (Figure S14a) and biplot (Figure S14b) are investigated. Loading represents the weights or coefficients assigned to each of the sensors in the construction of the PC and the values show the contributions of the sensors in the PC. All the sensors were positively correlated along loading 1 while along loading 2, only the DAP-functionalized sensor was positively correlated. This represents a larger contribution from DAP to PC2. Additionally, a greater angle for the DAP sensor than the other ones represents its somewhat different correlation. A supervised PLS-DA model of the same data set shows better separation in the score plot (Figure S15a) than the PCA model. This is due to the consideration of class information along with the variance in the data (like PCA). The R^2 value of the model with two components is 0.874; this represents a good fit of the model to the data set. Predictive performance Q^2 is measured by the leave-one-out cross-validation (LOOCV) method to be 0.815; a high value such as this indicates the level of predictive accuracy of the PLS-DA model. The variable importance in the projection (VIP) plot from the PLA-DA model is often used to determine the important variables in a model as shown in Figure 6b. DAP and DPB are considered the most important sensors in the array as their VIP scores are more than 1.00. These two sensors contribute the most to the separation of the responses for MCA and FC. Therefore, an array consisting of less than five sensors can be implemented in the identification of the analytes. Figure S15b,c shows that removing the blank and APy-functionalized sensors does not affect the separation of MCA and FC. Therefore, excellent separation of the analytes can be achieved by only DAP, DPB, and PQ, demonstrating the potential of using a three-sensor array with lower cost, simpler design, and reduced power consumption. Finally, cross-validation carried out by LDA shows 100% accuracy in the classification of the data set. This validates that the array can differentiate between FC and MCA.

Monitoring of MCA in the Presence of FC. Chloramines (MCA, DCA, TCA) are not commercially sold since their stability depends on the type of chloramine and temperature of the solution. The formation of the type of chloramine relies on the ratio of the reactants and the pH of the solution. In water treatment plants, MCA is generated by reacting chlorine and an ammonia source.[48] HOCl is formed when chlorine is added to water.

$$Cl_2 + H_2O \rightarrow HOCl + H^+ + Cl^- \tag{3}$$

At pH above 3, this reaction completes, forming HOCl. This HOCl is a weak acid and forms OCl^-.

$$HOCl \rightarrow H^+ + OCl^- pKa = 7.6 \tag{4}$$

HOCl and OCl^- are both powerful oxidants, and their proportions are pH-dependent. At pH 7.0 to 8.5, FC quickly reacts with ammonia to form chloramines in a series of competing reactions 5−7:

$$NH_3 + HOCl \rightarrow NH_2Cl + H_2O \tag{5}$$

$$NH_2Cl + HOCl \rightarrow \mathit{N}HCl_2 + H_2O \tag{6}$$

$$NHCl_2 + HOCl \rightarrow HCl_3 + H_2O \tag{7}$$

These reactions are primarily dependent on pH and the chlorine to ammonia weight ratio (Cl_2:N); to a lesser degree, on temperature and contact time. MCA is the dominating chloramine when the ratio of Cl_2:N is kept less than 5:1 at a basic pH. When the Cl_2:N ratio is in the range of 5:1 to 7.6:1, DCA is formed and the residual chlorine level decreases. The DCA formation is acid-catalyzed, and at low pH, MCA transforms into DCA. If the ratio is above 7.6:1, only TCA is formed at low pH. A previous study[49] concluded that both FC and MCA can be present in water; to evaluate the sensor performance, a similar situation is created for the array to analyze the two disinfectants. The sensors are exposed to various Cl_2:N ratios at pH 8, which were obtained by spiking FC in NH_4Cl solution. The steady pH of 8 ensures the absence of DCA and TCA. It is found that below 5:1 (Cl_2:N) only MCA is present in the solution. At a higher ratio, both FC and MCA are present simultaneously. PCA is then carried out on the sensor responses for different ratios along with the calibration data set. The raw sensor responses of all the sensors are provided in the Supporting Information (figure S16). Figure S17a shows the scores generated from the five sensors, and Figure S17b is for four sensors after excluding the Blank. Figure 6c shows the PCA score plot for the three sensors that scored the highest in the VIP plot. The circled samples in colored ellipses represent the experimental data points with different ratios of Cl_2:N. The sample with the blue circle represents the response for the Cl_2:N < 5:1. This sample had only MCA in the solution, it falls in the MCA region. The data point appeared at a more negative PC2 region of the ellipse due to a lower concentration of MCA (0.108 mg/L) than the concentrations of MCA in the other data points. Data points in the dotted red circle represent a higher Cl_2:N ratio than 5:1 and in these three cases, both FC and MCA are present in the solution. For the first spike in Cl_2:N, which was targeting a 6:1 ratio, the FC concentration was measured to be

0.09 mg/L while the MCA concentration was 0.39 mg/L. The data points fall in the FC region in the score plot; this could be because the FC is the predominant chlorine residual in water after the breakpoint.[50] As the FC concentration increased, we noticed a decrease in PC1 values, which was also noticed with the calibration data set. Cross-validation analysis was then carried out on the same data set using LDA where calibration data was used as training data and the circled data points as testing data. The analysis showed that the three-sensor array performs the best with 100% accuracy in classifying the analytes. To summarize, this chemometrics-assisted sensor array can detect a sample with MCA and projects a mixture of MCA and FC (a higher Cl_2:N ratio) as FC.

Tap Water Testing. To evaluate its performance, the sensor array was tested in a real water matrix. The City of Hamilton (Ontario, Canada) uses MCA as the residual disinfectant, and the sample was collected from Hamilton.[48] Before unknown levels of MCA were tested using the sensor array, the sensor array was calibrated using the tap water background to remove the matrix effect from the sensor responses. The calibration of the sensors was conducted by spiking a range of concentrations (0−1.715 mg/L) in a tap water background. The PCA method is then employed to generate PC scores. The first and second PCs explained 97.9 and 1.2% of the total variation of the data set, respectively (Figure S18). The PCA model performs well in separating the FC and MCA samples. It can be noticed that MCA samples in tap water fall in the region of MCA despite the difference in background, validating that an array can differentiate MCA in different matrices. We then used the PLSR model, a commonly used chemometric modeling technique for quantification of analytes to quantify MCA levels from the array.[51] This model is known to perform well with unknown/testing data since it considers the concentration in building the model rather than just the responses. Three tap water samples were collected from the same source and tested within 1 h of collection. The MCA concentration of the tap water was measured before the sensors were placed and after the 2 h mark. The latter measurement was used as the actual concentration to compare to the data from the sensor array. Figure 7 shows the PLSR model; the red dots are the spiked MCA samples in the tap water background, while the white dots represent the tap water sample with MCA. The concentrations predicted by the model were very close to the actual measured concentrations; hence, the three tap water samples were very close to the ideal comparison line. The model parameters, R^2, and root mean squared error value using leave-one-out cross-validation (RMSELOOCV) values are 0.99 and 0.012 for this PLSR model, representing good fit and prediction ability. The recovery rate for the MCA concentration has been calculated by comparing the actual concentration measured by the DPD method and predicted concentrations from the PLS model. An average recovery of 98 ± 7.72% has been found for the concentration predicted by the array. This demonstrates that the array can be used to quantify unknown concentrations after calibrating in the same background as the testing data.

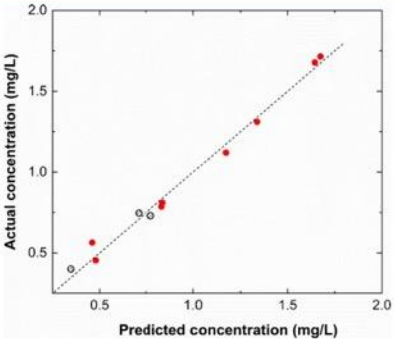

Figure 7. Regression graph from the PLS model showing the predicted concentration from the model and actual concentration measured by the DPD method. The solid red dots represent the training data set from the known spiking of MCA in tap water. The open circles represent the testing data set for three unknown tap water samples. The dashed line represents the ideal comparison line.

Though the sensors remain stable and respond well in the tap water background, an interference study with ions commonly present in tap water has been conducted to provide insight into the selectivity of the sensors to MCA. The following concentrations of potentially interfering ions were added: KH_2PO_4 (0.04 mmol), $CaCl_2$ (0.6 mmol), $MgSO_4$ (0.3 mmol), and $NaHCO_3$ (1 mmol), followed by a dose of MCA to verify the sensor response. This reflects the concentrations of major ions (phosphate, chloride, sulfate, bicarbonate, sodium, potassium, calcium, and bicarbonate) typically present in the drinking water supply of the City of Hamilton, Ontario, Canada (maximum concentrations reported in the water quality report).[48] The chemicals were added one at a time, at 1 h intervals. Finally, 0.95 mg/L MCA was added to compare the MCA response to commonly found interferent chemicals. Figure S19 shows the raw responses of the sensors when chemicals were added. The responses to the salt solutions were negligible compared to the MCA responses (shown in Figure S20). It was found that none of the sensors showed more than a 0.7% change when the ions were added, while the addition of 0.95 mg/L MCA resulted in a 4.82% response for unfunctionalized and 4.97−11.49% response for the functionalized sensors. Considering the relative sensor responses to typical (if at the higher end) concentrations of different ions compared to MCA, we can conclude that the sensors are stable in tap water and in the presence of commonly found ions in water.

CONCLUSIONS

We have introduced a novel approach to address the challenges associated with MCA monitoring through the development of a solid-state, reagent-free MCA sensing array of few-layer graphene (FLG) chemiresistors functionalized with redox-active molecules. The performance of the sensor array was thoroughly characterized with MCA, FC, and DCA across a range of concentrations, achieving distinct responses for the three analytes. Multivariate methods such as PCA, PLS-DA, and LDA were applied to demonstrate the effective separation of the analytes. The array was also evaluated for nonideal scenarios where MCA and FC could be present together. The stability of the chemiresistive sensors is largely dependent on the durability of the FLG film and the molecules attached to it. The sensors tested for characterization were exposed to oxidizing agents (MCA, FC, and DCA). Sensors were also exposed to solutions with a wide pH range (3.8−8.0) in the presence of the oxidizing agents. Stability can be gauged by the sensitivity and reproducibility of the sensor response.

Table 1. Comparison of the Performance of the Array with the Other Previously Reported Methods for the Determination of MCA

detection type	dynamic range	LOD/LOQ	differentiation from FC	suitability for online monitoring	reference
electrochemical sensor (amperometric detection)	1−10 mg/L	0.03 mg/L	no	yes	21
membrane introduction mass spectrometry (MIMS)	0.1−10.3 mg/L	0.034 mg/L	no	yes	53
colorimetry	0.06−0.25 mg/L	0.01 mg/L	no	no	4
liquid chromatography coupled to electrospray ionization-tandem mass spectrometry (LC-ESI-MS/MS)	4×10^{-5}−1×10^{-2} mg/L	4×10^{-5} mg/L	not reported	no (toxic reagent, instability of indophenol, complexity of the procedure)	15
salicylate-spectrophotometric method	0−4 mg/L		not reported	yes (by adding flow-injection technique)	54
chlorine microelectrode	0.1−30 mg/L		no	not reported	55
derivatization-chromatographic separation	0.03−7.1 mg/L	0.01 mg/L	No	yes	16
electrical (chemiresistive)	0.22−7 mg/L	0.027 mg/L	yes	yes	this work

Functionalized sensors showed higher sensitivity and less variability in sensor responses than the blank sensor due to the presence of molecules on the graphene film. The variation in the blank sensor response can be attributed to nonspecific adsorbate interactions (fouling) at the sensor surface. The stability of the functionalized sensors is the result of the successful functionalization of the graphene film, rendering it inert to nonspecific interactions. Sensors remained stable during the testing period (5 weeks). Real tap water characterization of the sensors for the analytes demonstrated that the FLG sensors are stable to commonly found ions in drinking water. Furthermore, in a previous study with FLG-based chemiresistors, we showed that the sensors (in the presence of DI water and real matrix) could be stably used to detect analytes in the presence of commonly found ions.[24]

The FLG chemiresistive array has been demonstrated in the continuous monitoring of MCA in tap water, highlighting its potential for real-time applications. This chemiresistive array offers a low-cost, reagent-free solution for the continuous monitoring of MCA in drinking water, overcoming the limitations of the standard DPD method. The array can also be employed to differentiate FC and MCA in a continuous monitoring format (Supporting Information Figures S21 and S22).

We have demonstrated the applicability of an electrical sensing technique for the monitoring of MCA. We have tested the sensors for the monitoring of MCA in both buffered and tap water. Chemometric analysis showed that the array can be used to monitor MCA. A simple PCA plot can be used to monitor the type and concentration of MCA in water. Our findings also show that removing the blank sensor improves the separation of MCA responses from FC responses, emphasizing the importance of functionalization of the sensors as the bare FLG surface is more susceptible to interferents. We also find that the three sensors modified with DAP, DPB, and PQ are the most important sensors in the array and their use is sufficient to distinguish the two disinfectants.

Table 1 compares other reported methods for MCA detection with those presented here. The common approaches like chromatographic and mass spectrometric methods provide excellent limits of detection. However, these methods need expensive instrumentation and training of the operator. The only electrochemical sensor reported for MCA detection did not show the differentiation from FC. Electrical transduction-based sensors such as chemiresistive sensors can be incorporated into a continuous monitoring system for online detection of MCA, for example in the water treatment plant to monitor the MCA dosing process or in the water distribution system. There is a risk of the MCA in water being converted to its undesirable counterpart DCA at low pH and high Cl:N ratios, and in this study, we have demonstrated a way to monitor the various disinfectant species in water continuously within a practically relevant dynamic range. In a relevant setting, the sensor array can be placed in water, and in the presence of MCA, the array will respond through a current change. The sensor electronics then records the current changes from all sensors and enters them into the PCA algorithm to generate a corresponding score. The score can be compared with the calibrated samples to determine the type of analyte. To measure the MCA concentration, multivariate regression analysis such as PLS can be carried out on the responses. During this process, the sensors remain immersed and deliver continuous data as desired. Furthermore, this method holds the potential to be expanded to other platforms such as ion-selective chemiresistive platforms for robust sensing of analytes.[41,52]

■ ASSOCIATED CONTENT

Supporting Information

The Supporting Information is available free of charge at https://pubs.acs.org/doi/10.1021/acsestwater.4c00341.

> Additional experimental details, including photographs of sensors and the experimental setup, sensor data, fitting parameters, and details on the chemometric analysis (PDF)

■ AUTHOR INFORMATION

Corresponding Author

Peter Kruse − *Department of Chemistry and Chemical Biology, McMaster University, Hamilton, Ontario L8S 4M1, Canada;* orcid.org/0000-0003-4051-4375; Email: pkruse@mcmaster.ca

Authors

Md Ali Akbar − *Department of Chemistry and Chemical Biology, McMaster University, Hamilton, Ontario L8S 4M1, Canada;* orcid.org/0000-0002-1809-8232

Ponnambalam Ravi Selvaganapathy − *Department of Mechanical Engineering and School of Biomedical*

Engineering, McMaster University, Hamilton, Ontario L8S 4L7, Canada; orcid.org/0000-0003-2041-7180

Complete contact information is available at:
https://pubs.acs.org/10.1021/acsestwater.4c00341

Author Contributions

CRediT: **Md Ali Akbar** conceptualization, formal analysis, investigation, methodology, writing-original draft, writing-review & editing; **Ponnambalam Ravi Selvaganapathy** methodology, writing-review & editing; **Peter Kruse** conceptualization, funding acquisition, methodology, supervision, writing-review & editing.

Notes

The authors declare no competing financial interest.

■ ACKNOWLEDGMENTS

We thank Dr. Shayan Angizi for fruitful discussions on the functionalization of FLG. We also thank Dr. Dipankar Saha for the discussion on preparing samples for SEM and Jhoynner Martinez from CCEM for the assistance with the imaging. Electron microscopy was performed at the Canadian Centre for Electron Microscopy (also supported by NSERC and other government agencies). The authors acknowledge financial support from the Natural Sciences and Engineering Research Council of Canada through the Discovery Grant Program (award numbers RGPIN-2018-06145 and RGPIN-2023-04927).

■ REFERENCES

(1) Engelhardt, T. L.; Malkov, V. B. *Chlorination, Chloramination and Chlorine Measurement*. Hach Company: Loveland, CO, 2015.

(2) US Environmental Protection Agency - Office of Water. *Alternative Disinfectants and Oxidants Guidance Manual*, 1st Ed.; US Environmental Agency: Washington, DC, 1999.

(3) Health Canada *Chloramines in Drinking Water - Guideline Technical Document for Public Consultation*; 2018.

(4) Nguyen, T. H.; Chevallier, E.; Garcia, J.; Nguyen, T. D.; Laurent, A. M.; Beaubestre, C.; Karpe, P.; Tran-Thi, T. H. Innovative Colorimetric Sensors for the Detection of Nitrogen Trichloride at Ppb Level in Swimming Pools. *Sensors Actuators, B Chem.* **2013**, *187*, 622–629.

(5) World Health Organization *Monochloramine in Drinking-Water. Background Document for Development of WHO Guidelines for Drinking-Water Quality*, 4th edn.; 2011.

(6) Wang, A. Q.; Lin, Y. L.; Xu, B.; Hu, C. Y.; Gao, Z. C.; Liu, Z.; Cao, T. C.; Gao, N. Y. Factors Affecting the Water Odor Caused by Chloramines during Drinking Water Disinfection. *Sci. Total Environ.* **2018**, *639*, 687–694.

(7) Jacobs, J. H.; Spaan, S.; van Rooy, G. B. G. J.; Meliefste, C.; Zaat, V. A. C.; Rooyackers, J. M.; Heederik, D. Exposure to Trichloramine and Respiratory Symptoms in Indoor Swimming Pool Workers. *Eur. Respir. J.* **2007**, *29*, 690–698.

(8) Hery, M.; Hecht, G.; Gerber, J. M.; Gendre, J. C.; Hubert, G.; Rebuffaud, J.; Rebuffaud, J. Exposure to Chloramines in the Atmosphere of Indoor Swimming Pools. *Ann. Occup. Hyg.* **1995**, *39* (4), 427–439.

(9) Nguyen, T. H.; Mugherli, L.; Rivron, C.; Tran-Thi, T. H. Innovative Colorimetric Sensors for the Selective Detection of Monochloramine in Air and in Water. *Sensors Actuators, B Chem.* **2015**, *208*, 622–627.

(10) Jenkins, S. H. *Standard Methods for the Examination of Water and Wastewater*; 1982; Vol. *16*.

(11) World Health Organization *Guidelines for Drinking-Water Quality: Fourth ed. Incorporating the First Addendum*, Fourth edi.; World Health Organization: Geneva, 2017.

(12) Kotiaho, T.; Lister, A. K.; Hayward, M. J.; Cooks, R. G. On-Line Monitoring of Chloramine Reactions by Membrane Introduction Mass Spectrometry. *Talanta* **1991**, *38* (2), 195–200.

(13) Shang, C.; Blatchley, E. R. Differentiation and Quantification of Free Chlorine and Inorganic Chloramines in Aqueous Solution by MIMS. *Environ. Sci. Technol.* **1999**, *33*, 2218–2223.

(14) Roumiguières, A.; Kinani, S.; Bouchonnet, S. Tracking Monochloramine Decomposition in MIMS Analysis. *Sensors* **2020**, *20* (1), 247.

(15) Kinani, S.; Layousse, S.; Richard, B.; Kinani, A.; Bouchonnet, S.; Thoma, A.; Sacher, F. Selective and Trace Determination of Monochloramine in River Water by Chemical Derivatization and Liquid Chromatography/Tandem Mass Spectrometry Analysis. *Talanta* **2015**, *140*, 189–197.

(16) Chehab, R.; Coulomb, B.; Boudenne, J. L.; Robert-Peillard, F. Development of an Automated System for the Analysis of Inorganic Chloramines in Swimming Pools via Multi-Syringe Chromatography and Photometric Detection with ABTS. *Talanta* **2020**, *207*, No. 120322.

(17) Tao, H.; Chen, Z.-L.; Li, X.; Yang, Y.-L.; Li, G.-B. Salicylate-Spectrophotometric Determination of Inorganic Monochloramine. *Anal. Chim. Acta* **2008**, *615* (14), 184–190.

(18) Hossain, S.; Chow, C. W. K.; Hewa, G. A.; Cook, D.; Harris, M. Spectrophotometric Online Detection of Drinking Water Disinfectant: A Machine Learning Approach. *Sensors* **2020**, *20* (22), 6671.

(19) Harp, D. L. *Current Technology of Chlorine Analysis for Water and Wastewater, Technical Information Series*. Hach Co. Inc, USA Bookl. 2002, No. *17*, 34.

(20) Kinani, S.; Richard, B.; Souissi, Y.; Bouchonnet, S. Analysis of Inorganic Chloramines in Water. *TrAC - Trends Anal. Chem.* **2012**, *33*, 55–67.

(21) Seymour, I.; O'Sullivan, B.; Lovera, P.; Rohan, J. F.; O'Riordan, A. Elimination of Oxygen Interference in the Electrochemical Detection of Monochloramine, Using in Situ PH Control at Interdigitated Electrodes. *ACS Sensors* **2021**, *6* (3), 1030–1038.

(22) Kruse, P. Review on Water Quality Sensors. *J. Phys. D. Appl. Phys.* **2018**, *51*, 203002.

(23) Patel, V.; Akbar, M. A.; Kruse, P.; Selvaganapathy, P. R. A Reagent-Free Phosphate Chemiresistive Sensor Using Carbon Nanotubes Functionalized with Crystal Violet. *Analyst* **2023**, *148*, 3551–3558.

(24) Dalmieda, J.; Zubiarrain-Laserna, A.; Ganepola, D.; Selvaganapathy, P. R.; Kruse, P. Chemiresistive Detection of Silver Ions in Aqueous Media. *Sensors Actuators, B Chem.* **2021**, *328*, No. 129023.

(25) Wu, R.; Gilavan, M. T.; Akbar, M. A.; Fan, L.; Selvaganapathy, P. R. Direct Transformation of Polycarbonate to Highly Conductive and Superhydrophobic Graphene/Graphitic Composite by Laser Writing and Its Applications. *Carbon N. Y.* **2024**, *216*, No. 118597.

(26) Zubiarrain-Laserna, A.; Angizi, S.; Akbar, M. A.; Divigalpitiya, R.; Selvaganapathy, P. R.; Kruse, P. Detection of Free Chlorine in Water Using Graphene-like Carbon Based Chemiresistive Sensors. *RSC Adv.* **2022**, *12*, 2485–2496.

(27) Hoque, E.; Hsu, L. H. H.; Aryasomayajula, A.; Selvaganapathy, P. R.; Kruse, P. Pencil-Drawn Chemiresistive Sensor for Free Chlorine in Water. *IEEE Sensors Lett.* **2017**, *1* (4), 4500504.

(28) Angizi, S.; Huang, X.; Hong, L.; Akbar, M. A.; Selvaganapathy, P. R.; Kruse, P. Defect Density-Dependent PH Response of Graphene Derivatives: Towards the Development of PH-Sensitive Graphene Oxide Devices. *Nanomaterials* **2022**, *12*, 1801.

(29) Patel, V.; Saha, D.; Kruse, P.; Selvaganapathy, P. R. Reagent-Free Hydrogen Peroxide Sensing Using Carbon Nanotube Chemiresistors with Electropolymerized Crystal Violet. *ACS Appl. Nano Mater.* **2022**, *5* (3), 3957–3966.

(30) Akbar, M. A.; Sharif, O.; Selvaganapathy, P. R.; Kruse, P. Identification and Quantification of Aqueous Disinfectants Using an Array of Carbon Nanotube-Based Chemiresistors. *ACS Appl. Eng. Mater.* **2023**, *1* (11), 3040–3052.

(31) Pan, S.; Deen, M. J.; Ghosh, R. Low-Cost Graphite-Based Free Chlorine Sensor. *Anal. Chem.* **2015**, *87* (21), 10734−10737.

(32) Angizi, S.; Yu, E. Y. C.; Dalmieda, J.; Saha, D.; Selvaganapathy, P. R.; Kruse, P. Defect Engineering of Graphene to Modulate PH Response of Graphene Devices. *Langmuir* **2021**, *37* (41), 12163−12178.

(33) Dalmieda, J.; Zubiarrain-Laserna, A.; Saha, D.; Selvaganapathy, P. R.; Kruse, P. Impact of Surface Adsorption on Metal-Ligand Binding of Phenanthrolines. *J. Phys. Chem. C* **2021**, *125* (38), 21112−21123.

(34) Donlan, Rodney; Murga, R.; Carpenter, J.; Brown, E.; Besser, R.; Fields, B. Monochloramine Disinfection of Biofilm-Associated Legionella Pneumophila in a Potable Water Model System. In *Legionella*; Marre, R.; Kwaik, Y. A.; Bartlett, C.; Cianciotto, N. P.; Fields, B. S.; Frosch, M.; Hacker, J.; Lück, P. C., Eds.; American Society for Microbiology: Washington, DC, 2001; pp 406−410.

(35) Schreiber, I. M.; Mitch, W. A. Influence of the Order of Reagent Addition on NDMA Formation during Chloramination. *Environ. Sci. Technol.* **2005**, *39*, 3811−3818.

(36) Lee, H.-J.; Halali, M. A.; Sarathy, S.; de Lannoy, C.-F. The Impact of Monochloramines and Dichloramines on Reverse Osmosis Membranes in Wastewater Potable Reuse Process Trains: A Pilot-Scale Study. *Environ. Sci.: Water Res. Technol.* **2020**, *6*, 1336−1346.

(37) Angizi, S.; Selvaganapathy, P. R.; Kruse, P. Graphene-Silicon Schottky Devices for Operation in Aqueous Environments: Device Performance and Sensing Application. *Carbon N. Y.* **2022**, *194*, 140−153.

(38) Hong, J.; Park, M. K.; Lee, E. J.; Lee, D.; Hwang, D. S.; Ryu, S. Origin of New Broad Raman D and G Peaks in Annealed Graphene. *Sci. Rep.* **2013**, *3*, 2700.

(39) Georgakilas, V.; Otyepka, M.; Bourlinos, A. B.; Chandra, V.; Kim, N.; Kemp, K. C.; Hobza, P.; Zboril, R.; Kim, K. S. Functionalization of Graphene: Covalent and Non-Covalent Approaches, Derivatives and Applications. *Chem. Rev.* **2012**, *112* (11), 6156−6214.

(40) Ryu, S.; Liu, L.; Berciaud, S.; Yu, Y. J.; Liu, H.; Kim, P.; Flynn, G. W.; Brus, L. E. Atmospheric Oxygen Binding and Hole Doping in Deformed Graphene on a SiO2 Substrate. *Nano Lett.* **2010**, *10* (12), 4944−4951.

(41) Darestani-Farahani, M.; Mendoza Montealegre, I.; Tavakkoli Gilavan, M.; Kirby, T.; Selvaganapathy, P. R.; Kruse, P. A Highly Sensitive Ion-Selective Chemiresistive Sensor for Online Monitoring of Lead Ions in Water. *Analyst* **2024**, *149* (10), 2915.

(42) Sugawara, M.; Watanabe, T.; Einaga, Y.; Koh, S. Impact of Gate Electrode on Free Chlorine Sensing Performance in Solution-Gated Graphene Field-Effect Transistors. *RSC Adv.* **2024**, *14* (11), 7867−7876.

(43) Tian, B.; Ding, Z.; Ning, G. H.; Tang, W.; Peng, C.; Liu, B.; Su, J.; Su, C.; Loh, K. P. Amino Group Enhanced Phenazine Derivatives as Electrode Materials for Lithium Storage. *Chem. Commun.* **2017**, *53* (20), 2914−2917.

(44) Li, J.; Wang, X.; Tang, J.; Li, F.; Wang, X.; Muhammad, T. A. D.; Hu, Z.; Wang, D.; Gong, Z.; Fan, M. Fingerprinting and Differentiation of Landfill Leachate and Domestic Sewage in Surface Water with Machine Learning Based Surface Enhanced Raman Spectroscopy. *ACS ES&T Water* **2024**, *4* (3), 1146−1154.

(45) Newhart, K. B.; Klanderman, M. C.; Hering, A. S.; Cath, T. Y. A Holistic Evaluation of Multivariate Statistical Process Monitoring in a Biological and Membrane Treatment System. *ACS ES&T Water* **2024**, *4* (3), 913−924.

(46) Saito, T.; Nishi, S.; Amano, Y.; Beppu, H.; Miyakawa, K. Origin of Dissolved Organic Matter in Deep Groundwater of Marine Deposits and Its Implication for Metal Binding. *ACS ES&T Water* **2023**, *3* (12), 4103−4112.

(47) Yessenbayeva, K.; Turdiyeva, K.; Ramazanova, E.; Lee, W. Water Chemistry, Source Identification, and Health Risk Assessment in Surface Water of the Ural River. *ACS ES&T Water* **2024**, *4* (4), 1620−1628.

(48) City of Hamilton *Drinking Water Systems Annual Water Quality and Summary Report*; 2021.

(49) Kouame, Y.; Haas, C. N. Inactivation of E. Coli by Combined Action of Free Chlorine and Monochloramine. *Water Res.* **1991**, *25* (9), 1027−1032.

(50) Health Canada *Guidelines for Canadian Drinking Water Quality - Summary Table*; Water and Air Qality Bureau, Healthy Environments and Consumer Safety Branch: Ottawa, Ontario, 2017.

(51) Felmy, H. M.; Lackey, H. E.; Medina, A. S.; Minette, M. J.; Bryan, S. A.; Lines, A. M. Leveraging Multiple Raman Excitation Wavelength Systems for Process Monitoring of Nuclear Waste Streams. *ACS ES&T Water* **2022**, *2* (3), 465−473.

(52) Darestani-Farahani, M.; Ma, F.; Patel, V.; Selvaganapathy, P. R.; Kruse, P. An Ion-Selective Chemiresistive Platform as Demonstrated for the Detection of Nitrogen Species in Water. *Analyst* **2023**, *148* (22), 5731−5744.

(53) Hu, W.; Lauritsen, F. R.; Allard, S. Identification and Quantification of Chloramines, Bromamines and Bromochloramine by Membrane Introduction Mass Spectrometry (MIMS). *Sci. Total Environ.* **2021**, *751*, No. 142303.

(54) Tao, H.; Chen, Z. L.; Li, X.; Yang, Y. L.; Li, G. B. Salicylate-Spectrophotometric Determination of Inorganic Monochloramine. *Anal. Chim. Acta* **2008**, *615*, 184−190.

(55) Lee, W. H.; Pressman, J. G.; Wahman, D. G.; Bishop, P. L. Characterization and Application of a Chlorine Microelectrode for Measuring Monochloramine within a Biofilm. *Sensors Actuators, B Chem.* **2010**, *145* (2), 734−742.

Supporting Information

Continuous Monitoring of Monochloramine in Water, and Its Distinction from Free Chlorine and Dichloramine Using a Functionalized Graphene-Based Array of Chemiresistors

Md Ali Akbar[1], Ponnambalam Ravi Selvaganapathy[2, 3], Peter Kruse[1]*

[1]Department of Chemistry and Chemical Biology, McMaster University, Hamilton, Ontario, Canada

[2]Department of Mechanical Engineering, McMaster University, Hamilton, Ontario, Canada

[3]School of Biomedical Engineering, McMaster University, Hamilton, Ontario, Canada

* Email: pkruse@mcmaster.ca

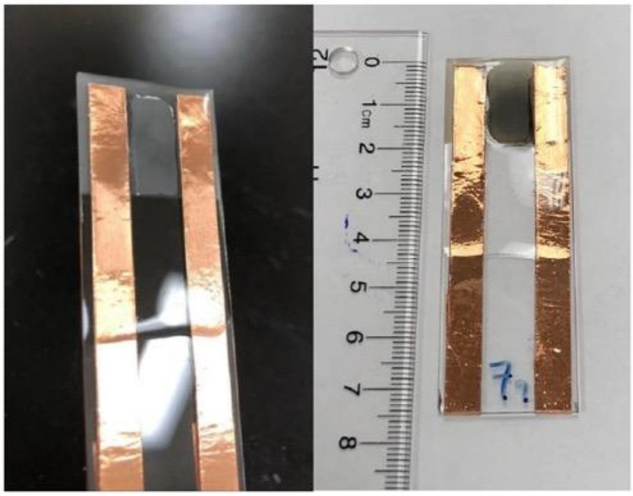

Figure S1. Photographs of actual chemiresistive devices.

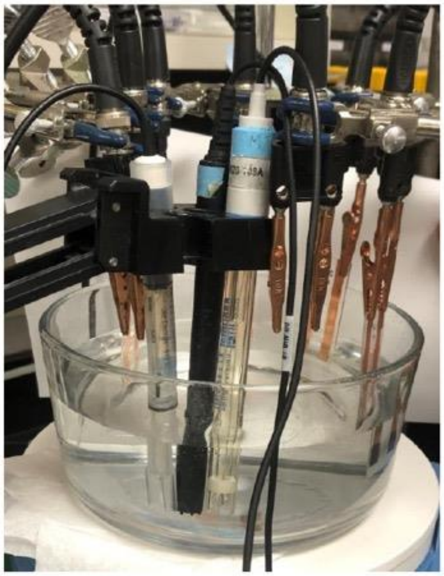

Figure S2. Experimental setup for the sensor characterization.

Sensor characterization. Sensor testing data was acquired using multiple eDAQ Quad Multi-Function isoPod™ (EPU452) configurations. Each of these setups allows for the connection of up to two eDAQs to a single computer. Each eDAQ comprises four individual channels. During the testing, a 10 mV potential bias was employed across the sensor film, while monitoring the temporal variation of the current in Biosensor mode. For a more comprehensive analysis, a pH electrode (Fisherbrand™ accumet™ Gel-Filled Polymer Body Single-junction pH Combination Electrode) and an ORP electrode (Ionode IJ-64) were included alongside six sensors as shown in figure S2. The pH and ORP electrodes were connected to eDAQ channels set to pH and ISE (Ion-Selective Electrode) modes respectively. Ahead of each experiment, the pH electrode underwent calibration using two buffer solutions: for acidic testing pH 4 and 7 and for basic testing pH 7 and 10 were used.

Testing of the sensors was carried out in a background of 100 mg/L of NaCl and 100 mg/L of $NaHCO_3$ to simulate tap water conditions.[1] MCA, FC and tap water testing was done at pH ~8 and DCA was used in pH ~3.7. Tap water was collected from McMaster University (Hamilton, Ontario). For the background calibration experiment the tap water was collected on a Monday morning after the tap had not been run for at least 2 full days, so the MCA concentration was low enough for the spiking of a known amount of MCA. For the actual testing of MCA, tap water was collected after running the tap for ~15 minutes so fresh water is used with a higher level of MCA. The pH of the tap water was found to be ~8. FC sensing was done by adding aliquots of FC stock of ~3000 mg/L. MCA and DCA testing were done from freshly prepared MCA stock (~400 mg/L). Considering the stability issues of chlorine-based disinfectants, the concentrations of the stock solutions were measured immediately before use. Sensors and electrodes were submerged in the background solution for ~24 hours to achieve a stable baseline before starting the experiment.

Data analysis. The raw responses gathered from the sensors as current (I) are first normalized by the baseline current (I_o) according to the following equation:

$$Response\ (\%\ change) = \frac{I - I_o}{I_o} \times 100\% \qquad (1)$$

For the I and I_o, the last two minutes of data are averaged for the analysis. The responses as percentage change are used for further analysis. Chemometric techniques were implemented to analyze the array responses collected from the five sensors. The sensor responses were considered variable responses for chemometric analysis. For the clustering of MCA and FC, the sensor responses were analyzed by PCA (unsupervised) and PLS-DA (supervised) methods using MetaboAnalyst 6.0. Nonlinear iterative partial least-squares (NIPALS) algorithm is employed by MetaboAnalyst for the calculation of the scores for both PCA and PLS-DA.[2] Linear Discriminant Analysis (LDA) was implemented using OriginPro 10.0 as a supervised method to carry out the validation analysis of the data set. For the quantification of analytes, partial least square regression (PLSR) method was used to quantify unknown tap water samples. OriginPro 10.0 was used to carry out the PLSR analysis. Before applying the NIPALS algorithm, autoscaling is carried out as a preprocessing technique of the sensor responses that involves adjusting variables by subtracting their mean and then dividing by their standard deviation. It centers the data around its average and normalizes it by its spread. To measure the predictive performance of the supervised models, Leave-One-Out Cross-Validation (LOOCV) is employed. LOOCV involves utilizing all data points, except one, for training the model, while reserving a single data point for validation. This procedure is iteratively applied to each data point in the dataset, and the model's performance is assessed based on its capability to predict the excluded data point.

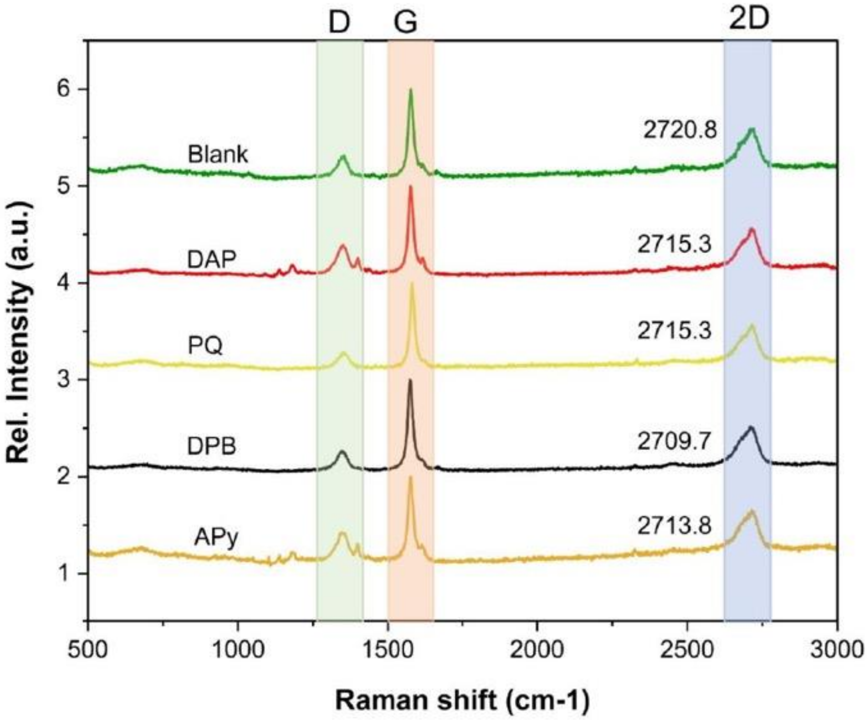

Figure S3. Raman spectra of the unfunctionalized (blank) and functionalized (DAP, PQ, DPB, and APy) FLG sample on membrane filter. The spectra were collected using a 532 nm laser. The position of the 2D peak is labeled on the figure.

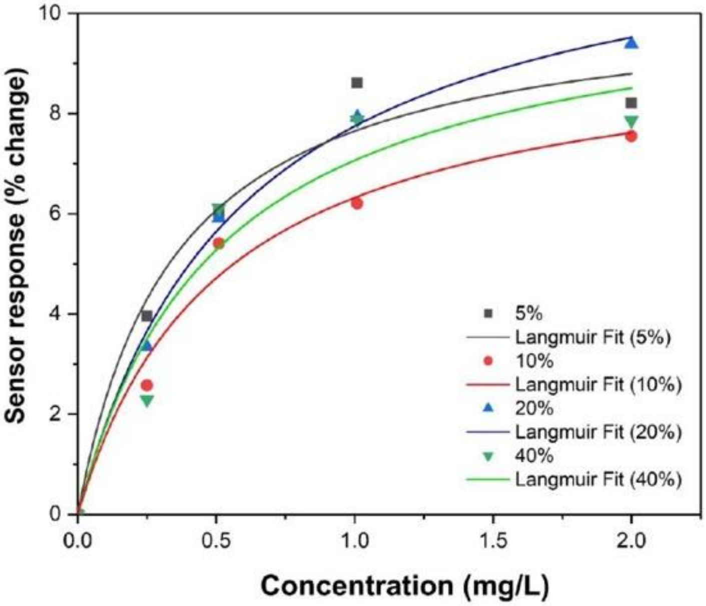

Figure S4. 1-Aminopyrene (APy) functionalization optimization curves. The sensor responses are shown as percent changes (data points) and they are plotted against the monochloramine (MCA) concentration. The data points for each concentration of the molecules are fitted with Langmuir absorption isotherm model. The fitting parameters for 5% are a = 10.34±1.11% and b = 2.84±0.99 $mg^{-1}L$ for an R^2 value of 0.97; for 10% are a = 9.58±1.04% and b = 1.94±0.58 $mg^{-1}L$ for an R^2 value of 0.98; for 20% are a = 12.35±0.57% and b = 1.68±0.20 $mg^{-1}L$ for an R^2 value of 0.99; and for 40% are a = 10.69±2.12% and b = 1.95±1.07 $mg^{-1}L$ for an R^2 value of 0.94.

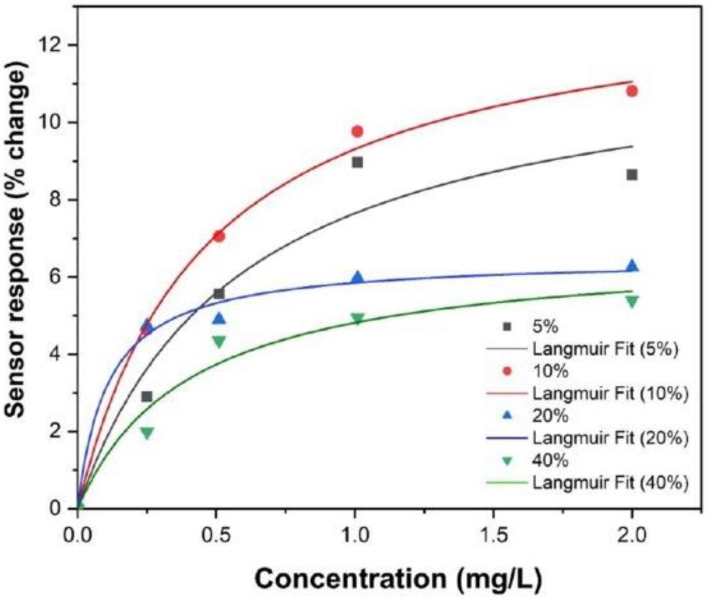

Figure S5. 2,3-Diaminophenazine (DAP) functionalization optimization curves. The sensor responses are shown as percent changes (data points) and they are plotted against the monochloramine (MCA) concentration. The data points (sensor responses) for each concentration are fitted with Langmuir absorption isotherm model. The fitting parameters for 5% are a = 12.12±2.19% and b = 1.71±0.81 mg^{-1}L for an R^2 value of 0.95; for 10% are a = 13.61±0.59% and b = 2.16±0.27 mg^{-1}L for an R^2 value of 0.99; for 20% are a = 6.49±0.33% and b = 9.08±2.82 mg^{-1}L for an R^2 value of 0.99; and for 40% are a = 6.77±0.90% and b = 2.46±1.00 mg^{-1}L for an R^2 value of 0.96.

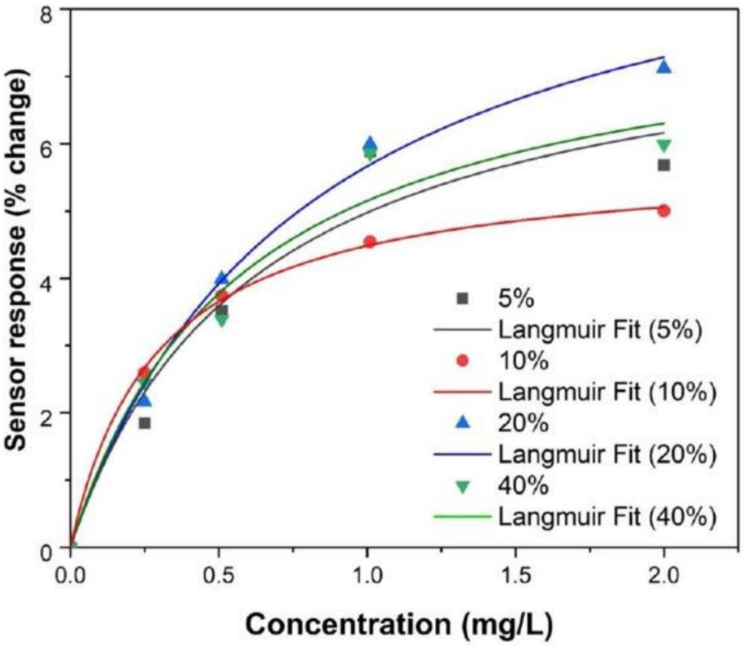

Figure S6. N, N'-Diphenyl benzidine (DPB) functionalization optimization curves. The sensor responses are shown as percent changes (data points) and they are plotted against the monochloramine (MCA) concentration. The data points (sensor responses) for each concentrations of the molecule is fitted with Langmuir absorption isotherm model. The fitting parameters for 5% are a = 8.09±1.57% and b = 1.59±0.79 $mg^{-1}L$ for an R^2 value of 0.95; for 10% are a = 5.80±0.10% and b = 3.41±0.21 $mg^{-1}L$ for an R^2 value of 0.99; for 20% are a = 10.21±0.74% and b = 1.24±0.21 $mg^{-1}L$ for an R^2 value of 0.99; and for 40% are a = 8.12±1.13% and b = 1.74±0.64 $mg^{-1}L$ for an R^2 value of 0.97.

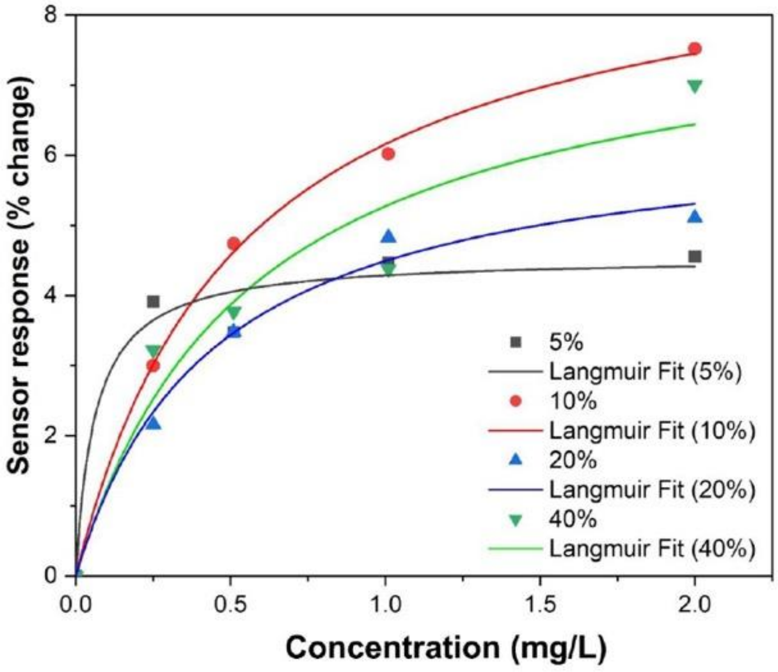

Figure S7. 9,10-Phenanthrenequinone (PQ) functionalization optimization curves. The sensor responses are shown as percent changes (data points) and they are plotted against the monochloramine (MCA) concentration. The data points (sensor responses) for each concentration of the molecule is fitted with Langmuir absorption isotherm model. The fitting parameters for 5% are a = 4.55±0.38% and b = 16.07±12.51 $mg^{-1}L$ for an R^2 value of 0.97; for 10% are a = 9.43±0.26% and b = 1.88±0.14 $mg^{-1}L$ for an R^2 value of 0.99; for 20% are a = 6.48±0.46% and b = 2.25±0.47 $mg^{-1}L$ for an R^2 value of 0.99; and for 40% are a = 8.28±1.67% and b = 1.75±0.94 $mg^{-1}L$ for an R^2 value of 0.93.

Table S1. Fitting parameters of the Langmuir model of all sensors (20% APy, 10% PQ, 10% DAP, and 20% DPB) for three analytes.

MCA				
Sensor	R^2	Adjusted R^2	a [%]	b [$mg^{-1}L$]
Blank	0.8293	0.8049	10.55 ± 9.55	0.24 ± 0.29
APy.	0.9851	0.9829	13.51 ± 0.88	1.48 ± 0.24
PQ	0.9829	0.9805	16.89 ± 1.44	1.09 ± 0.20
DAP	0.9904	0.9890	14.44 ± 0.53	2.73 ± 0.32
DPB	0.9729	0.9690	9.81 ± 1.01	1.16 ± 0.27

FC				
Sensor	R^2	Adjusted R^2	a [%]	b [$mg^{-1}L$]
Blank	0.9757	0.9723	24.18 ± 2.34	0.87 ± 0.19
APy	0.9955	0.9948	24.71 ± 0.51	2.98 ± 0.23
PQ	0.9945	0.9937	29.20 ± 0.67	2.88 ± 0.25
DAP	0.9586	0.9527	25.56 ± 1.82	2.31 ± 0.55
DPB	0.9904	0.989	22.59 ± 0.76	2.37 ± 0.27

DCA				
Sensor	R^2	Adjusted R^2	a [%]	b [$mg^{-1}L$]
Blank	0.9893	0.9857	5.86 ± 0.83	0.68 ± 0.19
DAP	0.9901	0.9868	7.44 ± 0.82	0.91 ± 0.23
DPB	0.9936	0.9915	6.76 ± 0.52	1.16 ± 0.22
PQ	0.9962	0.9949	5.445 ± 0.51	0.567 ± 0.1
APy	0.9478	0.9305	10.09 ± 23.23	0.073 ± 0.19

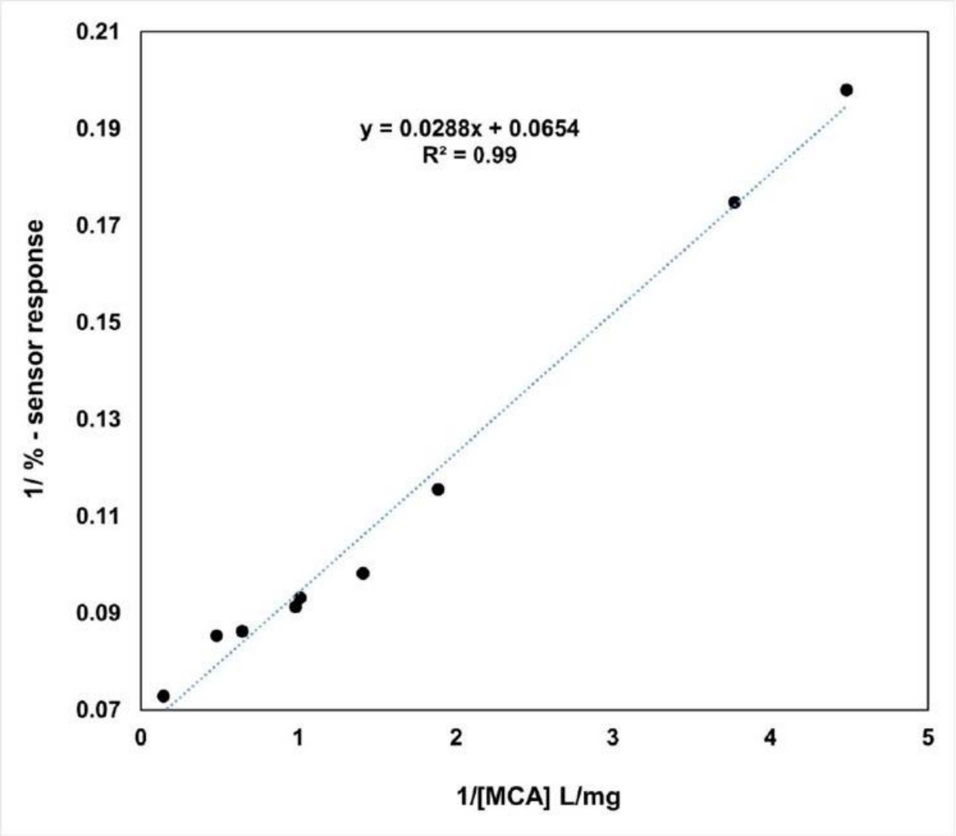

Figure S8. Linearized fit of the MCA responses from DAP sensor. 1/(% sensor response) is plotted against 1/(MCA concentration) to linearize the Langmuir absorption isotherm model. The solid dots include tested MCA concentrations and the maximum concentration calculated for 95% of the saturated response.

Dynamic range and limit of detection calculation: To estimate the dynamic range of MCA sensing a linearized Langmuir absorption isotherm model is implemented by plotting 1/(% sensor response) *vs.* 1/(MCA concentration). We only tested the sensors for a range of MCA that are more found in the water distribution system. However, a higher concentration of MCA can be detected. To calculate the maximum concentration the sensors can detect, we use the Langmuir parameter *a* which refers to the maximum response that can be achieved. Assuming 95% of *a* is achieved coverage a maximum concentration (x) is then calculated using the following Langmuir absorption isotherm equation.

$$y = \frac{abx}{1 + bx} \qquad (2)$$

For the DAP sensor, *a* parameter is 14.44%, which represents the maximum sensor response. 95% if this yields a concentration of 6.96 mg/L. A linear fit of the measured concentrations along with this maximum concentration gives an R^2 value of 0.99. From equation 2, detection limit of MCA is calculated for the DAP sensor using 3 times the standard deviation of the last 30 points (two minutes) of the baseline before spiking with MCA. For the DAP sensor, the limit of detection is measured to be 0.0275 ± 0.0007 mg/L.

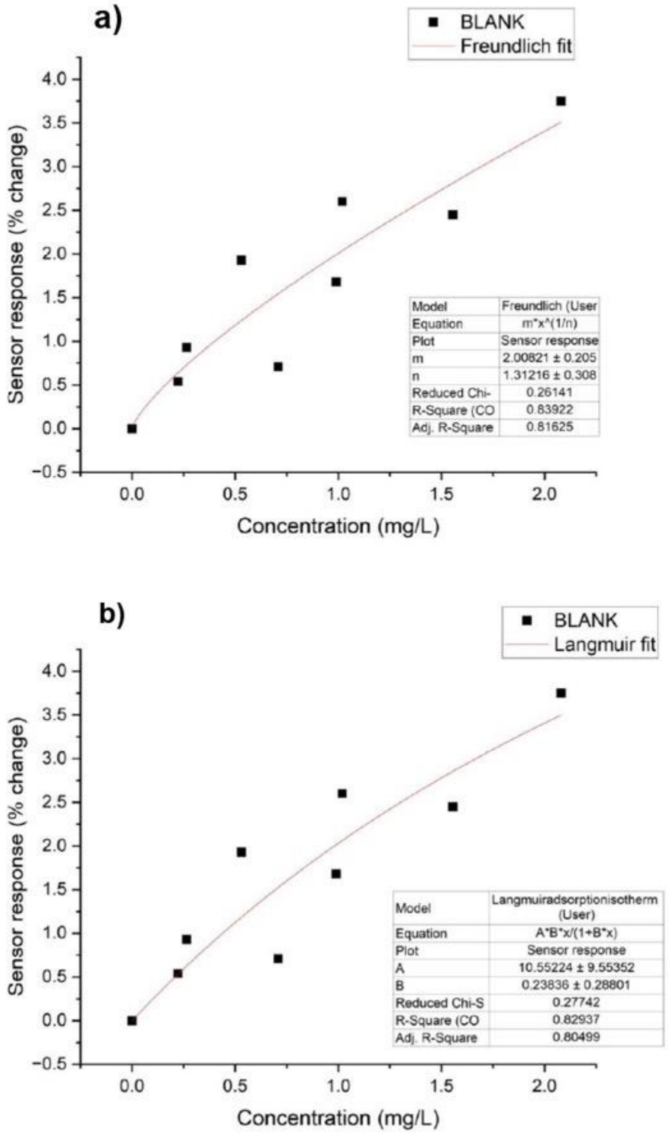

Model	Freundlich (User
Equation	m*x^(1/n)
Plot	Sensor response
m	2.00821 ± 0.205
n	1.31216 ± 0.308
Reduced Chi-	0.26141
R-Square (CO	0.83922
Adj. R-Square	0.81625

Model	Langmuiradsorptionisotherm (User)
Equation	A*B*x/(1+B*x)
Plot	Sensor response
A	10.55224 ± 9.55352
B	0.23836 ± 0.28801
Reduced Chi-S	0.27742
R-Square (CO	0.82937
Adj. R-Square	0.80499

Figure S9. Blank or bare sensor responses to MCA in buffered water fitted to Freundlich (a) and Langmuir (b) absorption isotherm model.

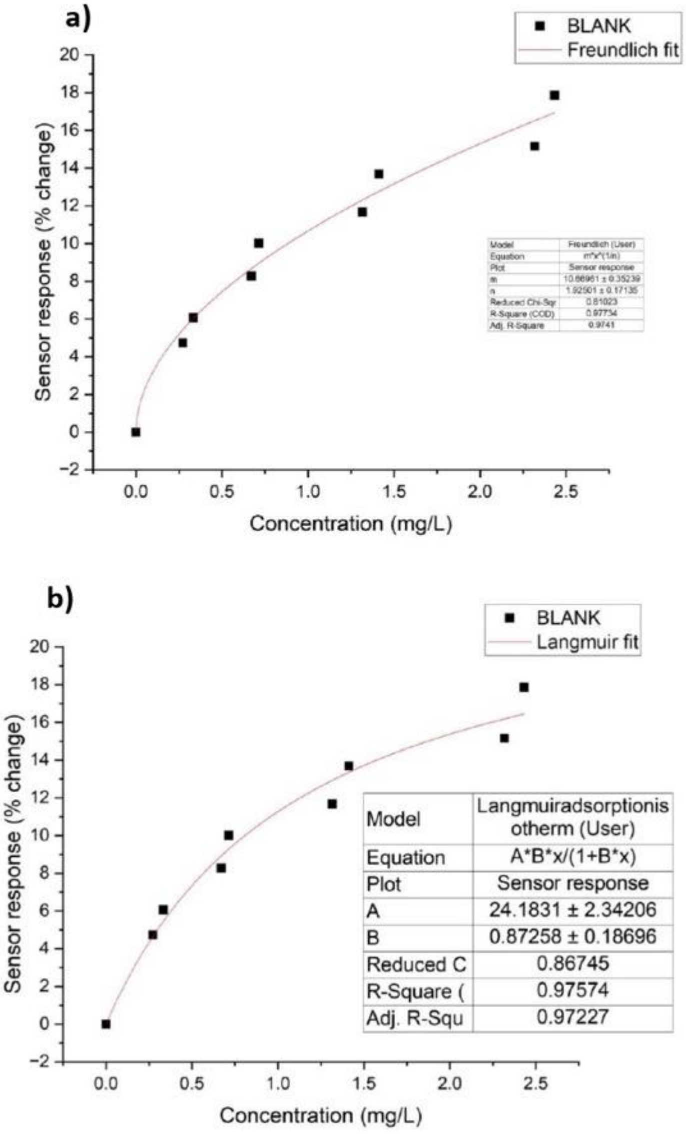

Model	Freundlich (User)
Equation	m*x^(1/n)
Plot	Sensor response
m	10.66961 ± 0.35239
n	1.92501 ± 0.17135
Reduced Chi-Sqr	0.81023
R-Square (COD)	0.97734
Adj. R-Square	0.9741

Model	Langmuiradsorptionisotherm (User)
Equation	A*B*x/(1+B*x)
Plot	Sensor response
A	24.1831 ± 2.34206
B	0.87258 ± 0.18696
Reduced C	0.86745
R-Square (	0.97574
Adj. R-Squ	0.97227

Figure S10. Blank or bare sensor responses to FC in buffered water fitted to Freundlich (a) and Langmuir (b) absorption isotherm model.

Chemometrics: Chemometrics refers to the statistical and mathematical methods that can be applied to a data set to explain underlying chemical information. This includes a range of qualitative techniques such as Principal Component Analysis (PCA), Partial Least Squares-Discriminant Analysis (PLS-DA), and Linear Discriminant Analysis (LDA). The Partial Least Square Regression (PLS-R) model is commonly used in multivariate calibration of sensing array data.[3] PCA is a powerful dimensionality reduction technique that allows for the extraction of useful information from complex sensor responses. By identifying and emphasizing the most significant patterns and reducing the data to a more manageable size, PCA simplifies the interpretation and analysis of large sensor datasets. In a PCA plot, scores refer to the positions of each sample (or observation) in a new coordinate system that PCA creates. Scores depict where each sample stands in terms of the identified patterns and each score represents how much a particular sample contributes to the overall variability in the dataset. In addition to dimension reduction, PCA score plots can be utilized for process monitoring[3] and pattern recognition.[4] Scores can also be used to carry out PCR for the quantification of the analyte; this is done by adding a linear regression step to the score values, often to the principal component (PC) that explains the greatest variation of the total dataset.[5]

In this study, we have extensively used PCA (score plot, loadings and biplot) to visualize the data to show the differentiation of the analyte. We have also employed the PLS-R model which tries to maximize the relationship of the sensors' responses (used as independent variables) and concentrations (used as dependent variables) for each response coming out of the array. In our dataset, we had 5 independent variables from 5 sensors and one dependent variable from the concentration of the analyte in that observation. In addition to PCA, we used two supervised methods PLS-DA and LDA to support PCA; these two methods take the class labels of the observations into account. These two methods are known to perform better in separation and classification of analytes.[6,7] PLS-DA is an extension of partial least square regression (PLS-R) and specifically designed for categorical variables. We have used the score plots to visualize the separation of the responses and the variable importance in projection (VIP) plot as a tool for variable (sensor) selection for the array. The VIP score for each variable represents contribution of that variable to the model and the VIP score is calculated by adding the squared weights of each variable, scaled by the percentage of variance explained by each latent variable in the model. Lastly, (LDA) is used to show the accuracy of estimation of the analytes based on the sensor responses. Cross validation is carried out to show the accuracy of the analytes.

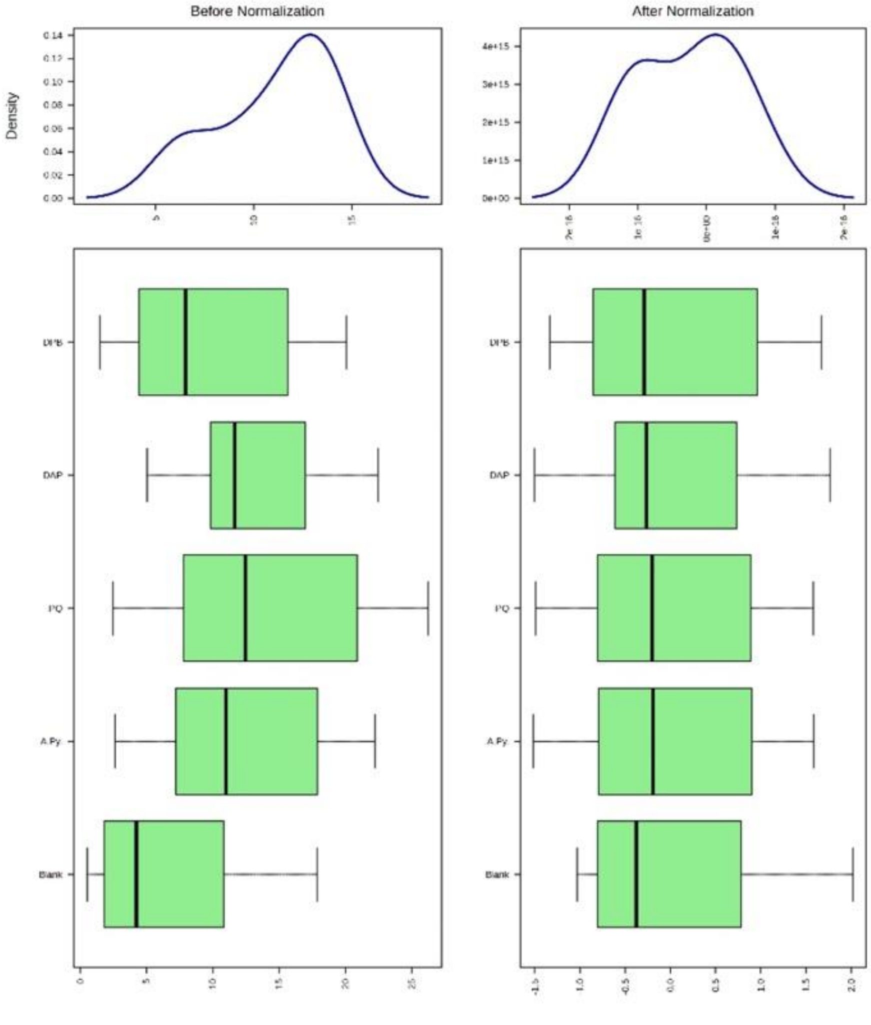

Figure S11. Normalization of the MCA and FC calibration dataset (shown in figure 5) for the sensor array. Autoscaling method is implemented to the five sensors array to achieve a uniform distribution of the dataset.

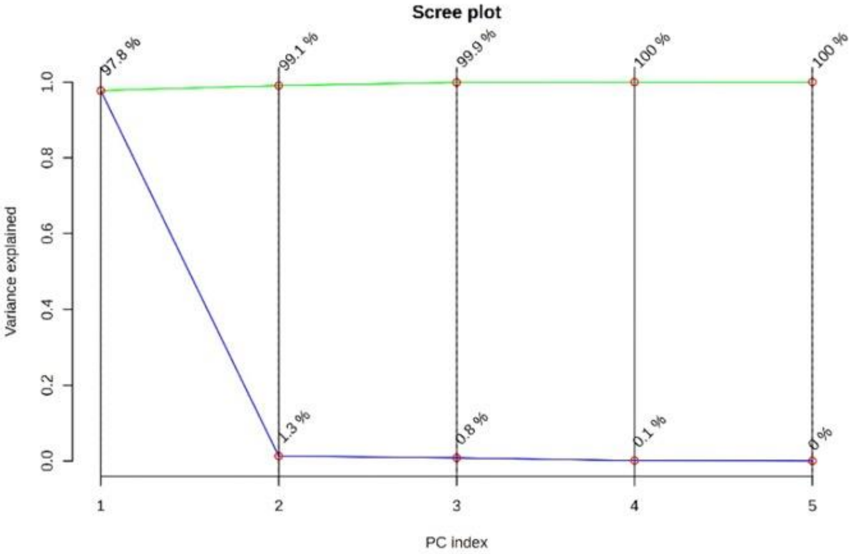

Figure S12. Scree plot showing the variance explained by the principal components (PC) generated from the PCA analysis for the MCA and FC calibration dataset shown in figure 5.

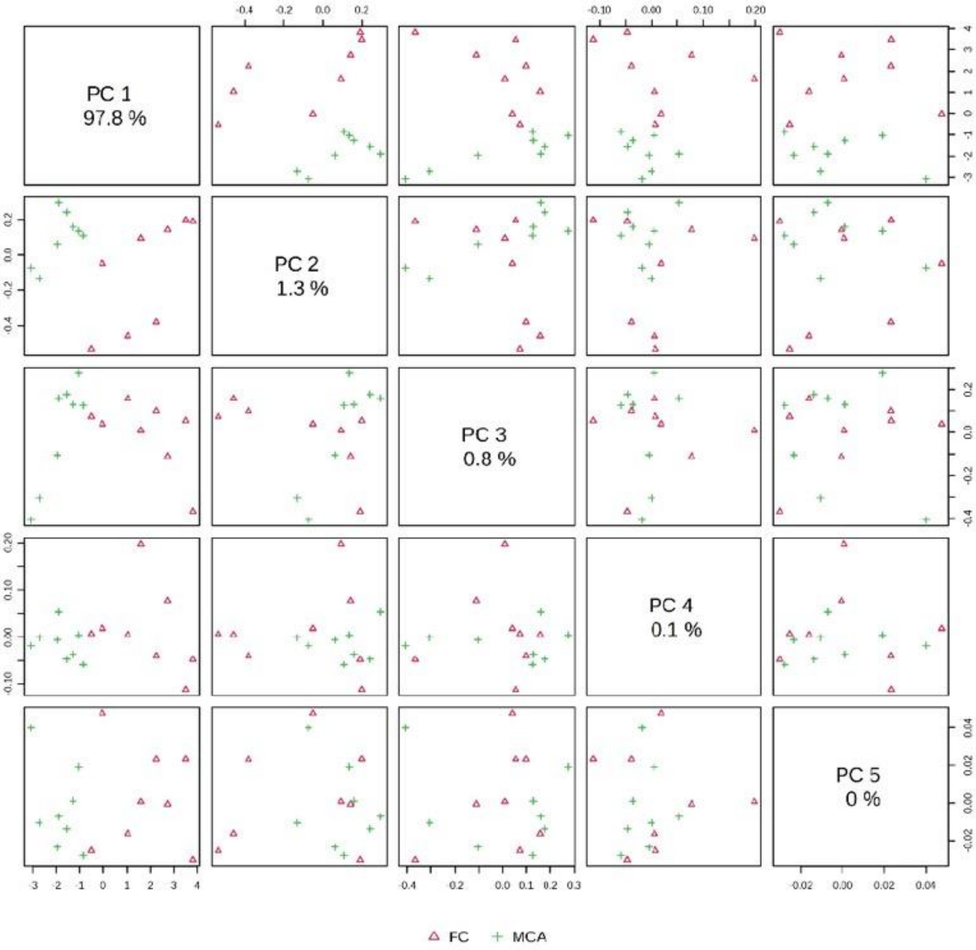

Figure S13. Pairwise score plots generated from the calibration dataset of MCA and FC (also shown in figure 5).

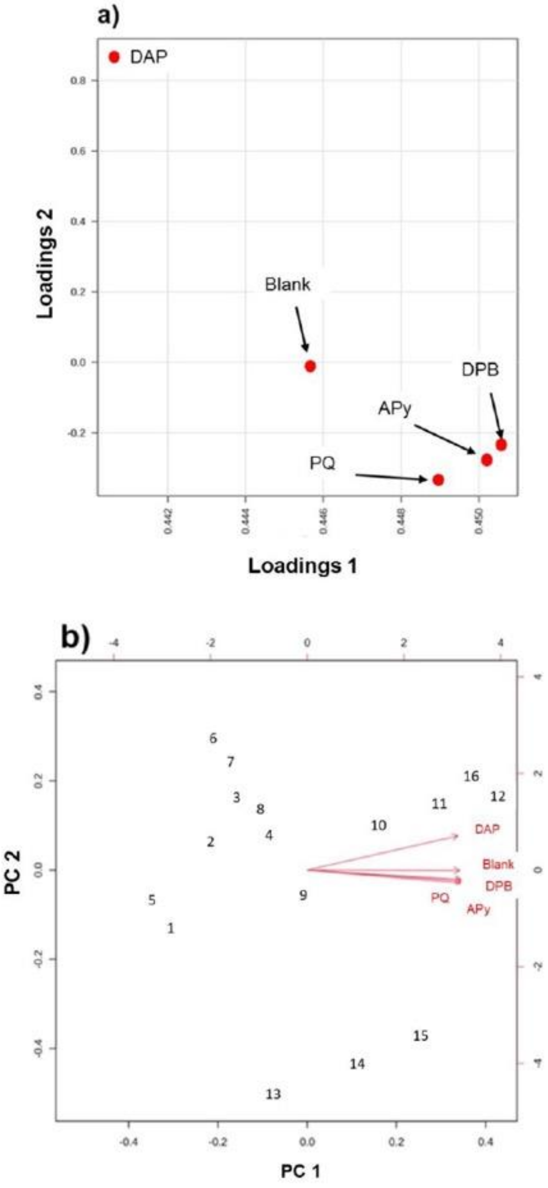

Figure S14. Scatter plot (a) of loading 1 *versus* loading 2PCA biplot (b) of the first two components generated from the calibration dataset of MCA and FC.

a)

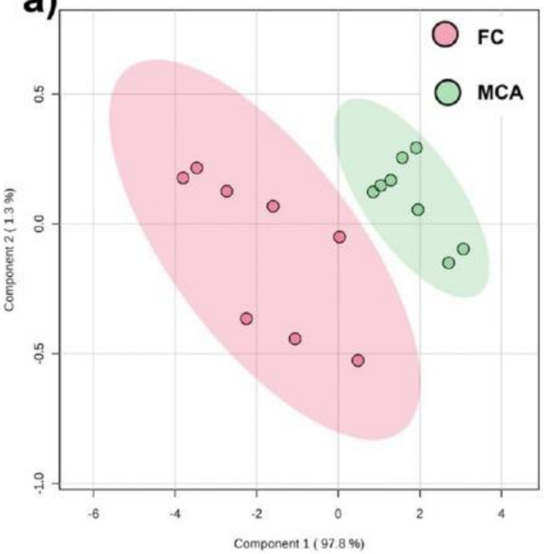
FC
MCA
Component 2 (1.3 %)
0.5
0.0
-0.5
-1.0
-6
-4
-2
0
2
4
Component 1 (97.8 %)

b)

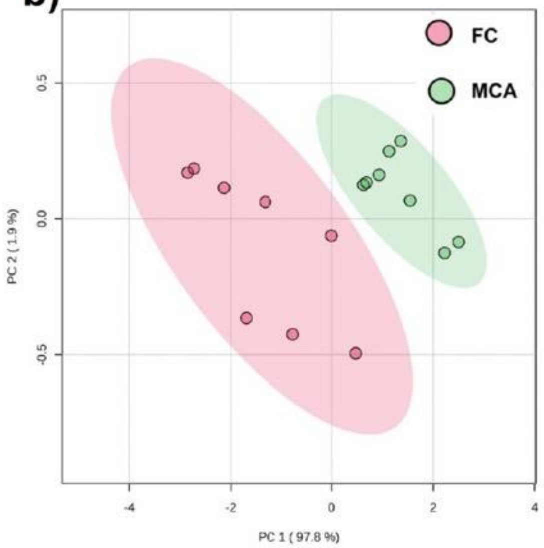
FC
MCA
PC 2 (1.9 %)
0.5
0.0
-0.5
-4
-2
0
2
4
PC 1 (97.8 %)

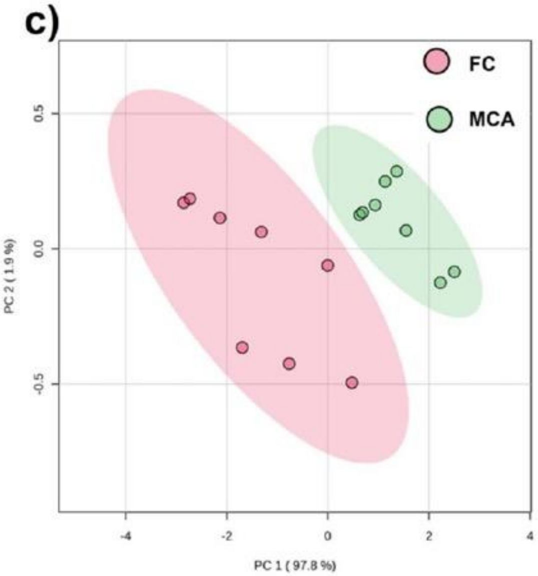

Figure S15. Evaluation of the sensors for the separation of analytes. MCA is shown as green region and FC as red region. The colored ellipses represent the 95% confidence level. (a) PLS-DA score plot of the classification dataset. (b) The PCA score plot is generated from all the functionalized sensors (DAP, DPB, PQ, APy). This can be seen that the speciation gets improved (compared to the one shown in 6a) after removing the blank for the analysis. This is due to the removal of noise in the data set that was introduced by the Blank sensor. (c) PCA score plot for three sensors (DAP, DPB, and PQ) calculated to be the top three sensors with highest VIP scores.

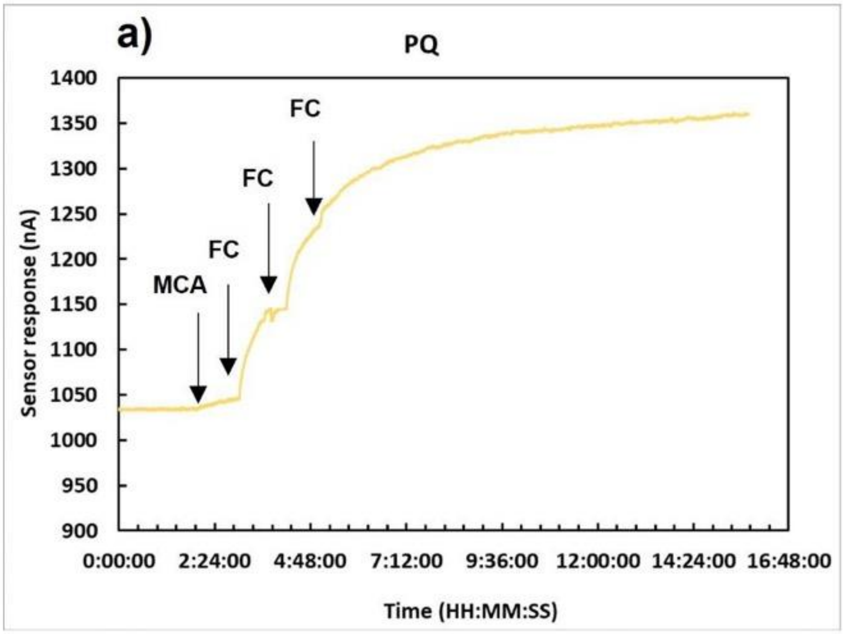
a)
PQ
Sensor response (nA)
1400
1350
1300
1250
1200
1150
1100
1050
1000
950
900
MCA
FC
FC
FC
0:00:00
2:24:00
4:48:00
7:12:00
9:36:00
12:00:00
14:24:00
16:48:00
Time (HH:MM:SS)

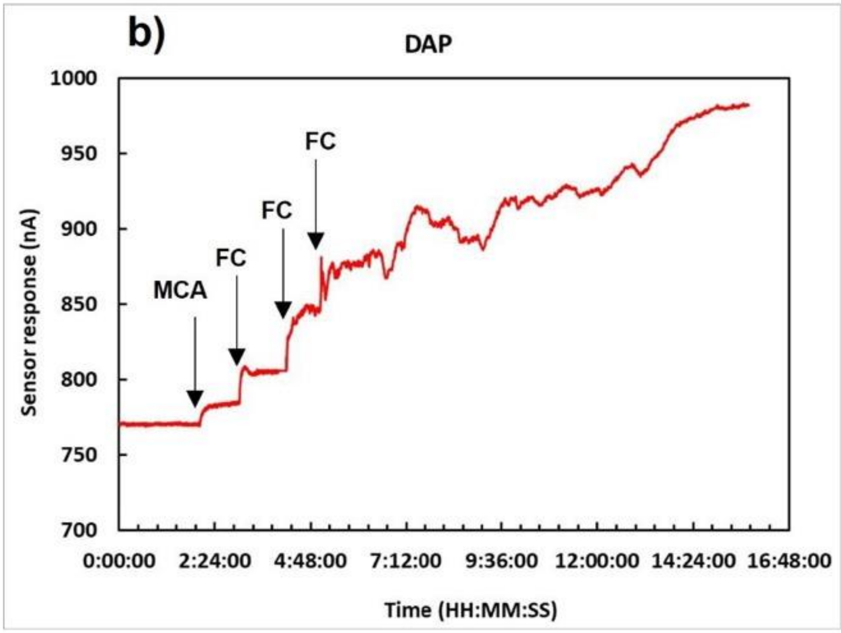
b)
DAP
Sensor response (nA)
1000
950
900
850
800
750
700
MCA
FC
FC
FC
0:00:00
2:24:00
4:48:00
7:12:00
9:36:00
12:00:00
14:24:00
16:48:00
Time (HH:MM:SS)

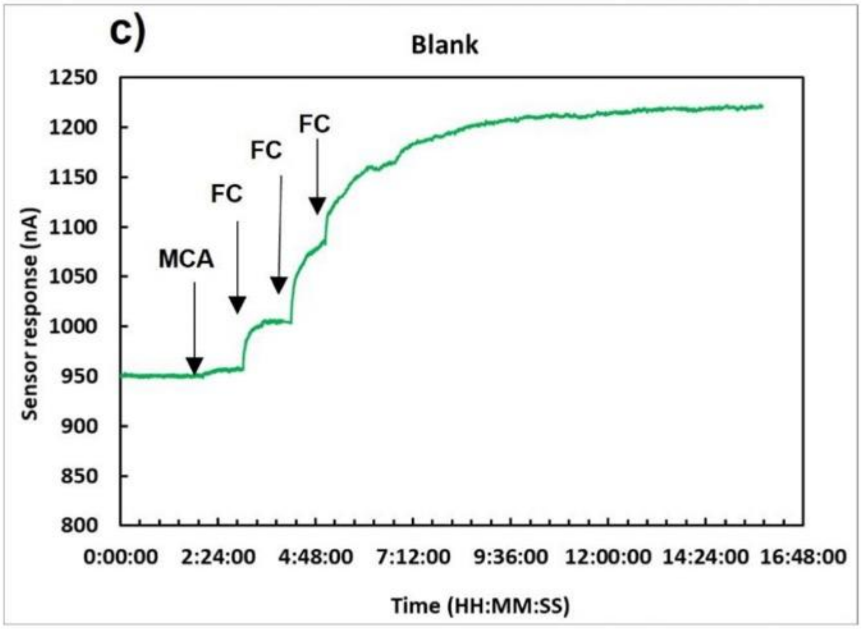
c)
Blank
Sensor response (nA)
1250
1200
1150
1100
1050
1000
950
900
850
800
MCA
FC
FC
FC
0:00:00
2:24:00
4:48:00
7:12:00
9:36:00
12:00:00
14:24:00
16:48:00
Time (HH:MM:SS)

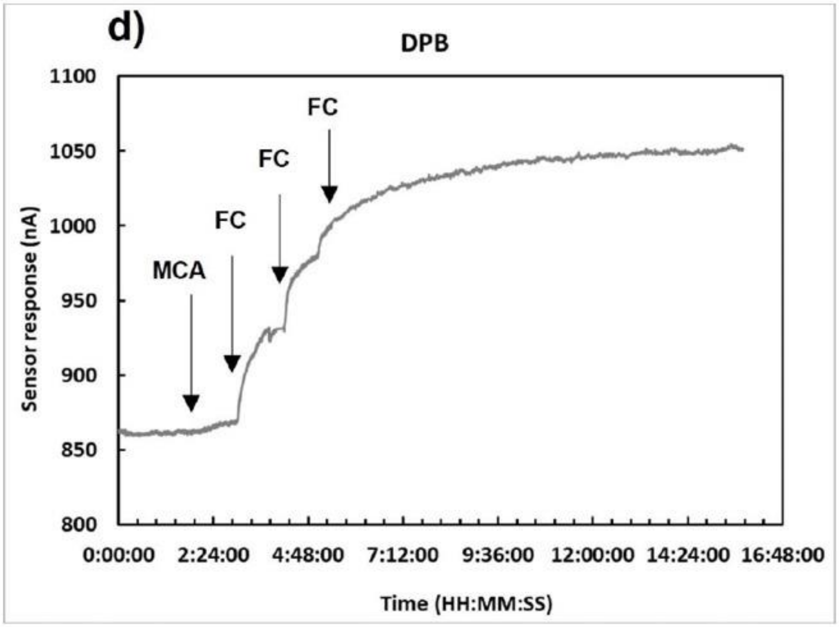
d)
DPB
Sensor response (nA)
1100
1050
1000
950
900
850
800
MCA
FC
FC
FC
0:00:00
2:24:00
4:48:00
7:12:00
9:36:00
12:00:00
14:24:00
16:48:00
Time (HH:MM:SS)

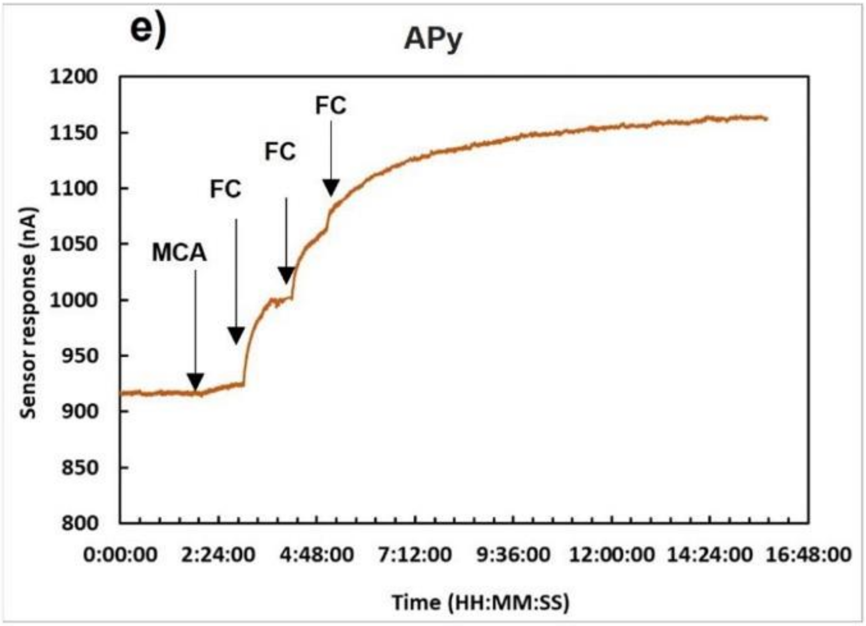

Figure S16. Raw sensor responses of the five sensors (PQ, DAP, Blank, DPB, and APy) for the monitoring of MCA in the presence of FC. Each spike with MCA and FC is labeled with the arrow. At the end of each measurement the concentrations of free chlorine (FC) and total chlorine (TC) were measured with DPD reagent.

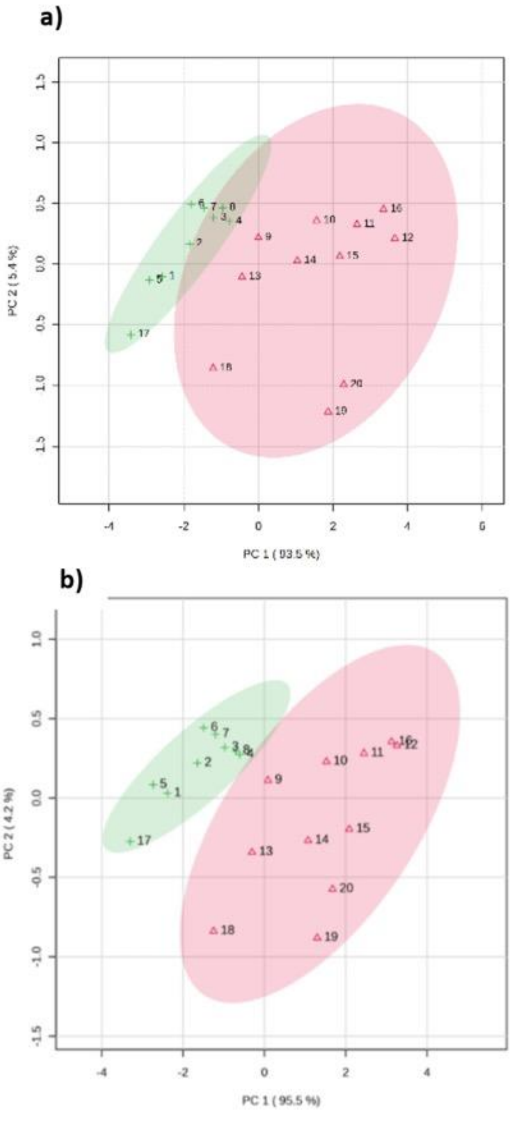

Figure S17. PCA score plots showing the separation of FC and MCA. Sample 1-16 represent the calibration dataset and 17-20 represent samples with different Cl_2: N ratio. PCA plots represent scores generated from array of all 5 sensors (top) and 4 functionalized sensors (bottom)

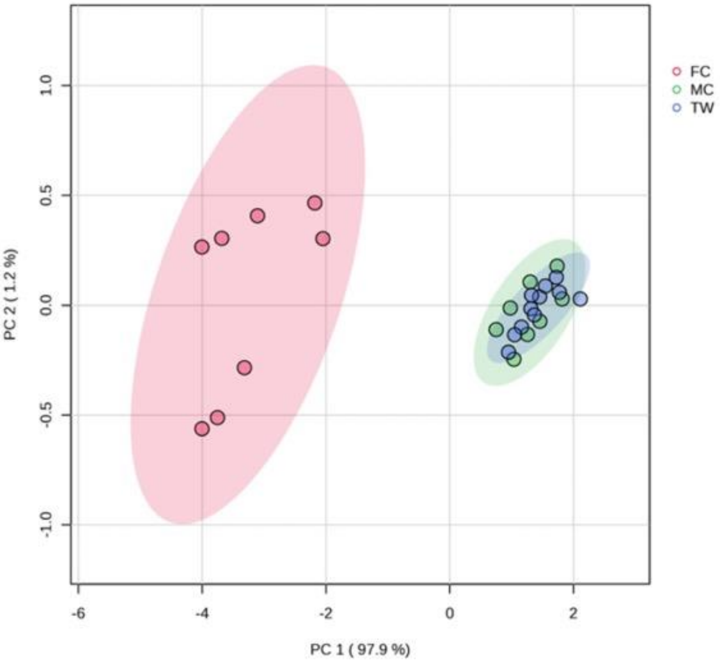

Figure S18. Chemometrics. The analysis on the MCA, FC data in buffered water background and MCA in tap water background (labeled as TW). PCA score plot showing the two main regions: MCA (green and blue) and FC (red). The colored ellipses represent the 95% confidence level. MCA region shows an overlap of MCA characterization in buffered water (green) and in tap water (blue). FC region shows FC characterization in buffered water.

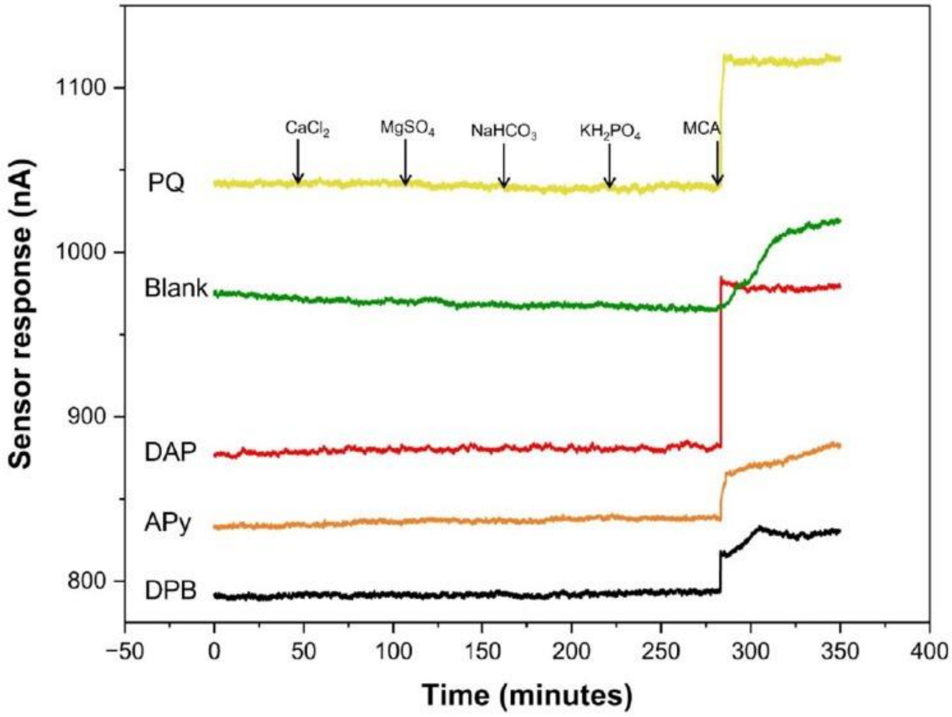

Figure S19. Raw sensor response as current change measured for the interference study. Concentrations of interferents added : $CaCl_2$ (0.6 mmol), $MgSO_4$ (0.3 mmol), $NaHCO_3$ (1 mmol), and KH_2PO_4 (0.04 mmol). Arrow shows the point when the interferent was added to the tap water background. MCA was measured (DPD method) to be 0.94 mg/L.

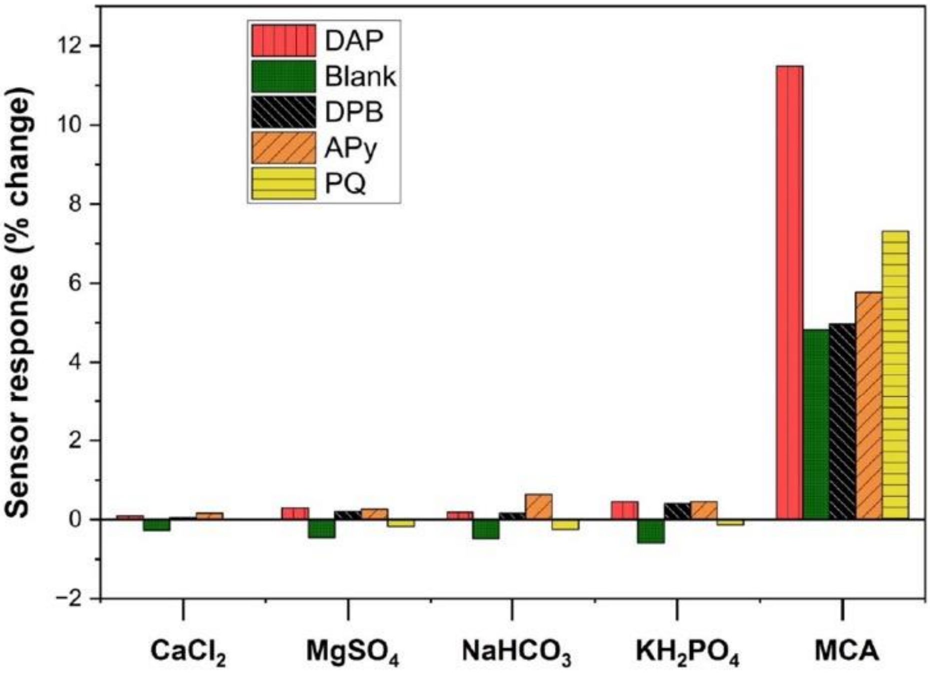

Figure S20. Bar graph showing the comparative sensor response as percent current change calculated for the interference study. Concentrations of interferents added : $CaCl_2$ (0.6 mmol), $MgSO_4$ (0.3 mmol), $NaHCO_3$ (1 mmol), and KH_2PO_4 (0.04 mmol). MCA was measured (DPD method) to be 0.94 mg/L.

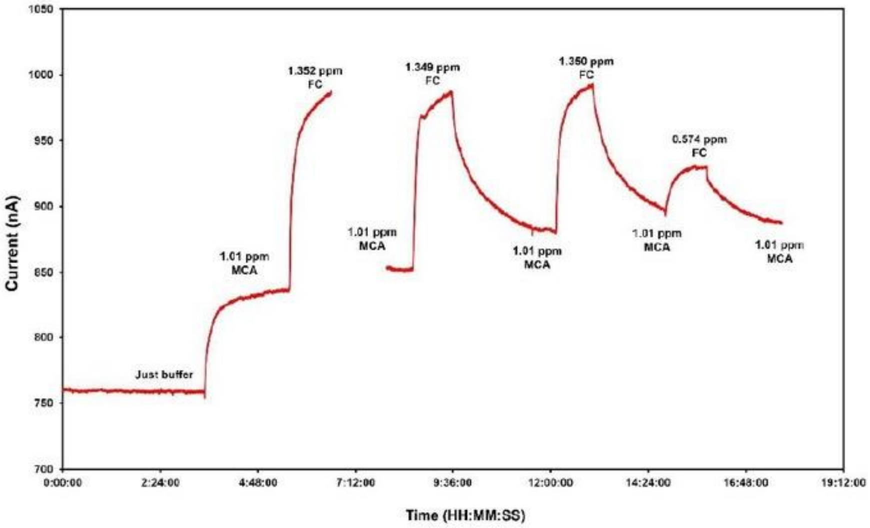

Figure S21. DAP sensor responses for the continuous monitoring of MCA and FC.

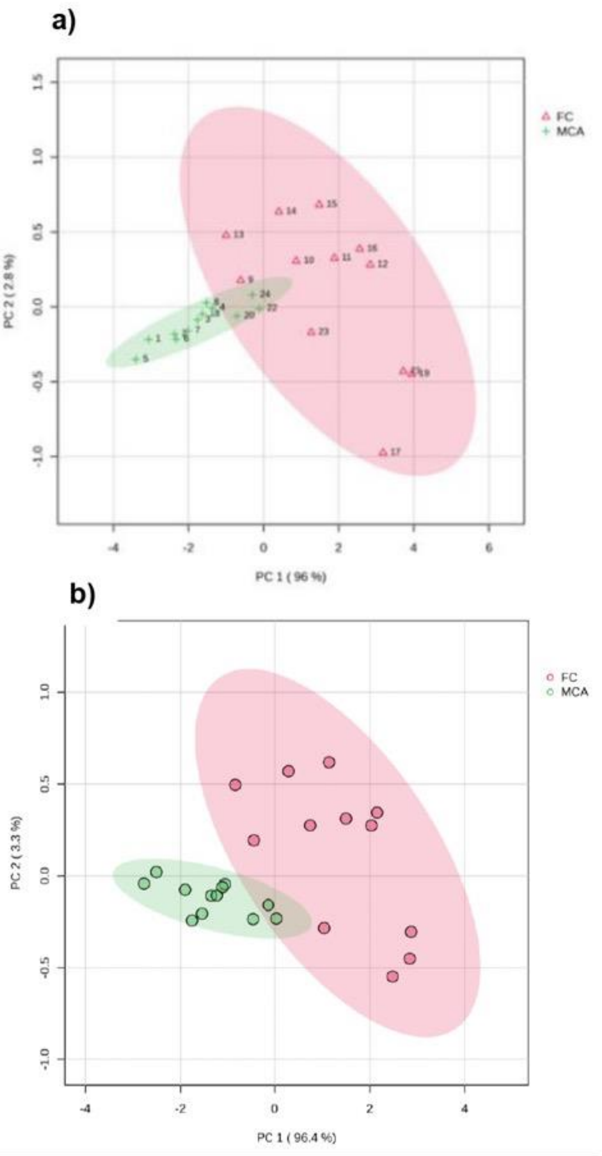

Figure S22. (a) PCA score plots from all 5 sensors. (b) PLS-DA score plot for all the sensor responses.

Continuous monitoring of MCA and FC: Continuous monitoring of analytes in water is beneficial to evaluate the water quality in real time. Here we have demonstrated the characterization of the sensors for continuous monitoring of MCA and FC in buffer solution. After stabilizing the sensors in water for 8 hours, MCA (1.01 ppm) was added to the solution. After the response for MCA stabilizes, sensors were exposed to FC (1.352 ppm) solution to assess if the array would be able to detect the change. Figure S18 shows the MCA and FC raw responses for a DAP-functionalized sensor with the concentrations labelled on top of the curve. The DAP sensor responded to both disinfectants, however the magnitude of the responses varied due to the concentration and type of the disinfectant. FC being the stronger oxidant gave a higher sensor response compared to MCA. The sensor showed reversible responses with the two disinfectants. It should be noted that the MCA responses took longer to stabilize than the FC responses. The FC responses are higher in magnitude than MCA. Figure S19a shows the PCA plot for the dataset collected from continuous monitoring of MCA and FC. The PCA score plot shows some overlap which gets s reduced in the PLS-DA score plot (figure S19b). To further evaluate the responses, LDA analysis was carried out to cross-validate the model, and LDA analysis of the data reported here shows that sensor array with four functionalized sensors could predict with 100% accuracy to the continuous monitoring data.

References

(1) Zubiarrain-Laserna, A.; Angizi, S.; Akbar, M. A.; Divigalpitiya, R.; Selvaganapathy, P. R.; Kruse, P. Detection of Free Chlorine in Water Using Graphene-like Carbon Based Chemiresistive Sensors. *RSC Adv.* **2022**, *12*, 2485–2496.

(2) Pang, Z.; Chong, J.; Zhou, G.; De Lima Morais, D. A.; Chang, L.; Barrette, M.; Gauthier, C.; Jacques, P. É.; Li, S.; Xia, J. MetaboAnalyst 5.0: Narrowing the Gap between Raw Spectra and Functional Insights. *Nucleic Acids Res.* **2021**, *49* (W1), W388–W396.

(3) Newhart, K. B.; Klanderman, M. C.; Hering, A. S.; Cath, T. Y. A Holistic Evaluation of Multivariate Statistical Process Monitoring in a Biological and Membrane Treatment System. *ACS ES&T Water* **2024**, *4* (3), 913–924.

(4) Barreira, J. C. M.; Casal, S.; Ferreira, I. C. F. R.; Peres, A. M.; Pereira, J. A.; Oliveira, M. B. P. P. Supervised Chemical Pattern Recognition in Almond (Prunus Dulcis) Portuguese PDO Cultivars: PCA- and LDA-Based Triennial Study. *J. Agric. Food Chem.* **2012**, *60* (38), 9697–9704.

(5) Bro, R.; Smilde, A. K. Principal Component Analysis. *Anal. Methods* **2014**, *6* (9), 2812–2831.

(6) Bohrer, F. I.; Colesniuc, C. N.; Park, J.; Ruidiaz, M. E.; Schuller, I. K.; Kummel, A. C.; Trogler, W. C. Comparative Gas Sensing in Cobalt, Nickel, Copper, Zinc, and Metal-Free Phthalocyanine Chemiresistors. *J. Am. Chem. Soc.* **2009**, *131* (2), 478–485.

(7) Brereton, R. G.; Lloyd, G. R. Partial Least Squares Discriminant Analysis: Taking the Magic Away. *J. Chemom.* **2014**, *28* (4), 213–225.

Chapter 8 Conclusions and Outlook

In this thesis, carbon-based substrates such as carbon nanotube and graphene have been used to fabricate chemiresistive sensors for water quality applications, specifically disinfectant monitoring. The chemiresistive sensors have been functionalized with planar, conjugated, redox active molecules. The single-walled carbon nanotube sensor surface was optically characterized and optimized for sensing of permanganate in aqueous solution. We have furthered our studies to multivariate disinfectant sensing of free chlorine at various pH's with successful application of nanotube-based arrays with functionalized chemiresistive sensors. We have shown that sensor arrays can distinguish free chlorine and permanganate. Finally, we demonstrated that these arrays can be extended to a different material (graphene) and to a practical scenario where multiple disinfectant species are present together.

The summary of the main findings of the 4th chapter is given below:

- SWCNT percolation networks with different resistances have been fabricated for the purpose of optical, microscopic, and electrical characterization.
- The density of the percolation network was optimized for chemiresistive devices.
- The devices fabricated with the highest resistance (~25 kΩ) can detect lower range concentrations of permanganate (0.01− 0.1 mg/L) with a limit of detection (LoD) of 0.0001 mg/L.
- Medium resistance devices (~15 kΩ) were shown to detect mid-range concentrations of permanganate (0.2 −1.6 mg/L) with a LoD of 0.002 mg/L.
- Low resistance devices (~5 kΩ) were shown to detect high range concentrations of permanganate (1− 8 mg/L) with a LoD of 0.03 mg/L.
- SWCNT networks were successfully functionalized with N, N-Diphenyl-1,4-phenylenediamine (DPPD).
- It was found that the functionalization improved the sensitivity and repeatability of the chemiresistive devices.

The summary of the main findings of the 5th chapter is given below:

- An array of single-walled carbon nanotube (SWCNT) chemiresistors was fabricated to monitor FC in a continuous manner at different pHs.
- The SWCNT chemiresistors were non-covalently functionalized with cobalt phthalocyanine and anthraquinone.
- The array was successfully applied to differentiate FC concentrations ranging from 0.03 mg/L to 2.1 mg/L within a pH range of 6.5 to 9.5. Chemometric analysis (PCA) was carried out to assess the sensor array performance to differentiate FC in the pH's tested.
- The SWCNT chemiresistive sensor design has been improved from our previous devices to incorporate components to facilitate mass fabrication. Silver contacts and parafilm dielectric have been adopted to the fabrication process.
- The new sensor design was tested over a wide range (0.015–10 mg/L) of FC. The LoD of the sensor was calculated to be 0.001 mg/L.
- An electronic reset function was successfully incorporated into the sensors to be able to continuously monitor the concentration of FC for both upward and downward changes.
- The sensors were tested in simulated tap water over an extended FC concentration range (0.015 – 10 mg/L).
- Chemometric analysis (PLS) was carried out to assess the model's performance.

The summary of the main findings of the 6th chapter is given below:

- An array of SWCNT sensors comprising of functionalized (PCAT, APCAT, DPPD, DPB, and LCV) and unfunctionalized (blank) sensors were used to distinguish different disinfectants (free chlorine and potassium permanganate).
- The molecules were electrochemically characterized and the functionalization of SWCNT with the molecules was characterized by Raman spectroscopy.
- PCA and partial least squares-discriminant analysis (PLS-DA) were used to analyze the sensor data. PCA showed excellent separation of the analytes over five different pHs (5.5, 6.5, 7.5, 8.5, and 9.5). PLS-DA provided excellent separability as well as

good predictability with Q^2 of 94.26%. and R^2 of 95.67% for the 5 pH regions of the two analytes.

- Chemometrics showed that only three sensors were enough to distinguish and quantify free chlorine and potassium permanganate over a range of pH values.

The summary of the main findings of the 7th chapter is given below:

- Few-layer graphene (FLG) has been selected to demonstrate the broader applicability of disinfectant-based sensing.
- An array of FLG chemiresistors were fabricated and functionalized with 2,3-diaminophenazine (DAP), 1-aminopyrene (APy), 9,10- phenanthrenequinone (PQ), and N,N'-diphenylbenzidine (DPB).
- These devices were used for detecting monochloramine (MCA), free chlorine (FC), and dichloramine (DCA).
- The sensor responses were separated by chemometric approaches such as PCA and PLS.
- Simultaneous detection of MCA and FC has been demonstrated.
- Predictive detection of MCA has been demonstrated by using the training dataset collected from a tap water background and utilizing PLS regression.

The following section explores some of the ideas that can be carried out in future:

1. As the work advances, emphasis should be placed on refining the sensing layer of chemiresistive sensors. While SWCNT-based devices demonstrated stability over repeated measurements for several weeks, the proportion of sensors that maintained reliable performance remained low. Few-layer graphene (FLG) substrate was effective in transmitting functionalizing behavior in the sensor array. These substrates also exhibited a higher density of defects compared to SWCNT networks. Therefore, facile fabrication of FLG can be adopted and controlled experiments can be carried out by intentionally introducing defects to the substrate. Then functionalization of the substrate can be conducted to gauge the level of sensor array output for better combination of the sensors. For large-scale applications, graphene-like carbon (GLC) substrates offer a promising route for mass production. As a continuation, a set of

molecules can be selected from the work presented here. GLC sheets of larger surface can be functionalized to introduce better repeatability between the sensors. Different thicknesses should be tested to gain better understanding of the functionalization process. These improvements can take this sensing platform to a better level than the currently used colorimetric disinfectant analyzer where reagents are added.

2. Array based sensing methods for other analytes such as disinfectants that are used in advanced oxidation (AOP) processes such as hydrogen peroxide, ozone, and peracetic acid. Multivariate detection of heavy metals can be explored using functionalized sensor array since their simultaneous detection is necessary. For example, hydrogen peroxide and free chlorine array can be useful where free chlorine is used to quench excess peroxide after the disinfection process.
3. Substrates designed for sensing disinfectants: Metal–organic frameworks (MOFs) and covalent–organic frameworks (COFs) are attractive because of their ordered pores, high surface areas, and tunable chemistry. Their functional groups can be tailored to interact with specific disinfectants, making them good candidates for selective sensing. In some cases, MOFs and COFs on their own can act as sensing platforms. They may show changes in conductivity, dielectric behavior, or redox activity when exposed to oxidants. These intrinsic responses make the idea of all-framework chemiresistive sensors promising, but the frameworks must be engineered to remain stable in water and to support reliable charge transport. MOFs and COFs can also be combined with conductive nanomaterials such as CNTs or graphene. In such hybrids, the porous and chemically tunable frameworks bring selectivity and pre-concentration, while the carbon materials provide fast and stable conductivity. This combination often results in better sensitivity and signal transduction. Future work should compare the two approaches: stand-alone frameworks versus hybrids. This will help us understand where each performs best and what trade-offs exist between porosity, water stability, and conductivity. The biggest challenge will remain the stability of these systems, whether framework-only or hybrid, for long-term, flow-through sensing in real water treatment environments.

4. Machine learning based chemiresistive sensors with training data gathered for complex samples over long duration. Chemiresistive sensors often show signal drift as time goes on. This can happen because of fouling, changes in the environment, or gradual shifts in the sensor surface itself. Standard calibration methods usually do not deal well with these long-term issues. The challenge is even greater in real water systems, where many oxidants, background ions, and natural organic matter are present at the same time. Machine learning (ML) offers a way forward by finding patterns in large amounts of data and adjusting as sensor behavior changes. One clear step for future work is to build training datasets that mirror actual operating conditions. These should include changes in pH, temperature, ionic strength, and mixtures of disinfectants, collected over long periods. If sensor arrays are exposed to this kind of complexity in both laboratory and pilot-scale studies, ML models can be trained to separate overlapping responses and reduce background noise. Such datasets also make it possible to develop predictive models that catch small shifts in sensor output before they build up into major baseline drift. In this way, long-term reliability of sensors in the field can be improved.
5. Long term stability and fouling resistance can be explored to facilitate commercialization of chemiresistive sensors. Incorporation of ultrathin zwitterionic or perfluorinated coatings that repel biofilms while sensing analyte to the CNT network can be studied. Another approach could be to integrate low frequency electrothermal or electrochemical regeneration cycles to burn off organic foulants without disassembling the sensor. Selective membranes can also be incorporated on the sensors developed in this thesis to increase the durability of the sensors. The devices need to undergo month-long chlorine stress tests (≥ 2 mg L^{-1} as Cl_2) and temperature cycling to quantify drift mechanisms and predict service lifetimes.